Charles University in Prague

Faculty of Science

PhD program: Molecular and Cellular Biology, Genetics and Virology

Ivana Kopová, MSc.

The biocompatibility and potential cytotoxicity of materials for joint replacement manufacturing and coating

PhD Thesis

Supervisor: Lucie Bačáková, MD, PhD, Assoc. Prof.

Institute of Physiology of the Czech Academy of Sciences

Prague

2016

Declaration

I hereby declare that this thesis is the result of my own work and effort. The containing material has not been previously submitted for the purpose of obtaining the same or any other academic degree. All literature sources have been properly cited.

Prague 1.8.2016 ……

Ivana Kopová

Acknowledgements

I would like to sincerely thank my supervisor Lucie Bacakova for the opportunity to work in her laboratory and for her enthusiastic guidance and support. Many thanks are also owed to my colleagues and external co-workers for their help and for the stimulating atmosphere they have created.

Special gratitude is due to my family and friends for their patience, emotional support, and never-ending belief in me.

Paula Solon is gratefully acknowledged for the language revision of this thesis.

This research would not have been possible without the financial support from the Czech Academy of Sciences (grant No. KAN400480701), Grant Agency of the Czech Republic (projects No. P107/11/1856, P107/12/1025, P108/12/1168 and P108/12/G108) and Technology Agency of the Czech Republic (grant No. TA01011141).

Abstract

Currently used prostheses for total joint replacement still have numerous disadvantages: extreme stiffness or elastic modulus of the bulk metallic material; insufficient integration of the implant into the host bone; and a high wear and corrosion rate, which causes an accumulation of mostly metallic or polymeric wear debris. Because of these reasons, many patients experience increasing local pain, swelling, allergic reactions, and inflammation resulting in bone loss and the aseptic loosening of the implant leading to the need for painful and expensive revision surgery.

To address the mechanical issues of commonly used orthopaedic alloys, this thesis presents the development of the new β-type titanium alloy Ti-35Nb-7Zr-6Ta-2Fe-0.5Si with a relatively low elastic modulus (up to 85 GPa), increased tensile strength (880 MPa), and enhanced biocompatibility and osteoconductivity.

Considering the generally low osteoinductivity of metallic implants, various surface modifications and coatings have been developed to improve the cell-material interaction, e.g. carbon-based coatings. Among these coatings, C_{60} fullerene layers have emerged as a great candidate for coating orthopaedic implants due to their therapeutic potential in arthritis. The potential cytotoxicity and DNA damage response of fullerenes have been evaluated. Although the fresh C_{60} coating has attenuated the adhesion and proliferation of cells, no DNA damage or signs of cytotoxicity have been found. The biocompatibility of C_{60} films has improved with the increasing age of these films or by co-deposition of C_{60} molecules with Ti atoms, thanks to changes in their physicochemical properties (such as fragmentation, oxidation, polymerization and graphitization).

In order to minimize the wear and corrosion of the Co-Cr-Mo alloy, the diamond-like-carbon (DLC) coating of this alloy with a titanium gradient adhesive interlayer has been used. The wear analysis has revealed no visible wear or delamination of the DLC coating after 3 million cycles of increasing loading force of up to 2.5 kN. Moreover, no proof of any cytotoxicity of the potential wear debris has been found.

In the last project of this thesis, a biocompatible, fully optically transparent diamond-based planar biosensor for the non-invasive (label-free), real-time monitoring of cell cultivation has been successfully invented. The main advantage of this sensor is its transparency, which enables microscopic native cell observation and the wide frequency range of the sensor allowing the detailed study of different cellular processes.

Abbreviations

53BP1	p53-binding protein
C_{60}	fullerene with 60 carbon atoms
CFRPEEK	carbon-fiber-reinforced polyetheretherketone
DLC	diamond-like-carbon
DOI	digital object identifier
ECM	extracellular matrix
gamma-H2AX	phosphorylated histone H2AX
HA	hydroxyapatite
IF	impact factor
PE	polyethylene
PMMA	polymethyl methacrylate, bone cement
SS (316L)	stainless steel
THF	tetrahydrofuran
TJR	total joint replacement
TNZT	Ti-Nb-Zr-Ta
UHMWPE	ultra-high-molecular-weight polyethylene
XPS	X-ray photoelectron spectroscopy

Table of contents

1 Introduction

1.1 Bone tissue engineering

The aging population together with the increasing demand for a longer, more active, and healthier lifestyle brings new challenges to regenerative medicine. Bone and joint degenerative or inflammatory problems (such as osteoarthritis, rheumatoid arthritis) affect several hundred million people worldwide. Furthermore, one in every three women over 50 years of age suffers a fracture caused by bone loss (osteoporosis). Alarmingly, according to the predictions, there is going to be a sharp increase due to the predicted doubling in the number of people over age 50 by the year 2020 (web page: bjdonline.org). These large bone defects caused by diseases or different traumas (like bone fractures, infections, and tumours) often cannot be healed properly and require a surgical approach, including transplantation or total joint replacement (TJR, also called arthroplasty).

Traditionally, bone grafts have been used to fill the bone loss. Autologous grafts, the patient's own tissues, are preferentially used due to their immunocompatibility, osteoconductivity (i.e. supporting cell adhesion, proliferation, and extracellular matrix formation), as well as osteoinductivity (i.e. promoting new bone formation by the recruitment and differentiation of progenitor cells). Moreover, autografts contain autologous cells that take part in bone regeneration. Unfortunately, the quality and quantity of bone tissue for harvesting is quite limited and decreases with the increasing age of the patient. The second option is an allograft (tissues from another human donor) or a xenograft (tissues from an animal donor). Xenografts are more available than autografts, and avoid the need for a second surgical intervention. However, patients must often endure long waits for allograft transplantation, sometimes even several years. In addition, allografts, like xenografts, pose a risk of disease transmission from the donor to the patient and may cause an immune response leading to subsequent graft failure [1].

Consequently, over the past decades, the concept of using artificial materials as bone graft substitutes for filling large bone defects emerged in the formation of a new field called "bone tissue engineering". Tissue engineering has been defined as an interdisciplinary field which applies the principles and methods of life sciences, materials science, and bioengineering for the development of biological substitutes that restore, maintain, or improve the biological function of tissues or whole organs [2].

1.2 The composition and mechanical properties of bone

The mechanical properties of an ideal orthopaedic implant should match host bone properties; thus, it is important to understand the basic mechanics of the bone itself. Human bone is a dynamic heterogeneous highly complex structure composed of different cell types and bone extracellular matrix (ECM). Osteoblasts are responsible for the synthesis and secretion of the organic components of ECM (bone formation), whereas osteocytes and osteoclasts are involved in bone resorption, a process critical for the maintenance, repair, and remodelling of bone tissue (Fig. 1; [3, 4]).

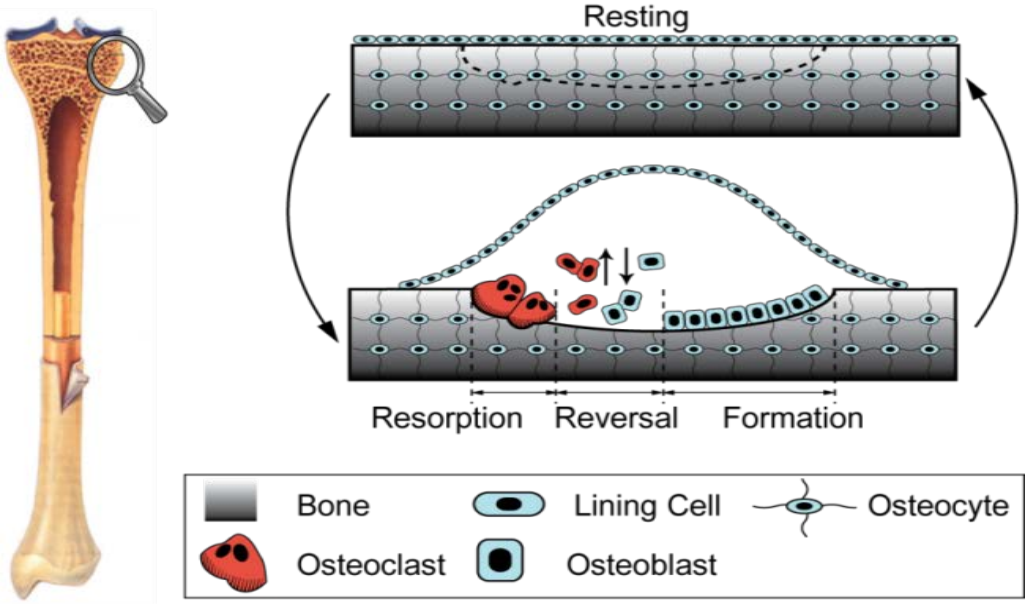

Fig. 1: A simplified scheme of bone dynamics [4]

Bone matrix is a composite consisting of about 30 % organic materials (proteins synthetized by cells) and 70 % inorganic mineral phase (salts). The most abundant component of bone ECM is inorganic hydroxyapatite (HA) occurring in the form of elongated crystals generated by the interaction of calcium phosphate and calcium hydroxide. Bone also contains smaller amounts of other minerals such as magnesium, fluoride, and sodium. The inorganic part of the ECM gives bone its characteristic rigidity and hardness resulting in the ability to resist compression, described by compressive strength [5].

About 90 % of the organic matrix consists of type I collagen. Collagen I is a fibrous protein organised into long crosslinked rope-like fibrils which provide the bone's flexibility and

enables its resistance to stretching, twisting, or fractures [5]. This elastic deformation of bone can be described and quantified by its tensile strength, fracture resistance, or elastic modulus. Thus, organic and inorganic phases together create a composite material with excellent tensile and compressive strength, which can bend under strain and recover its shape without generating permanent damage. Forces that exceed the capacity of bone elasticity may cause failure, typically bone fractures (stress above breaking point). In addition, there are about 300 different proteins involved in the cell adhesion, signalling, binding, and arranging of the other macromolecules. These proteins together with collagen I are crucial for proper ECM matrix organization and subsequent mineralization [6].

Table 1 shows a review of the mechanical properties of bone. The most important parameters are the compressive strength of the cortical and cancellous bone in the range 100–230 and 2–12 MPa, and Young's modulus (also called the elastic modulus) varying between 7–30 and 0.5–0.05 GPa, respectively [7]. These large variations in mechanical properties make it difficult to design a universal artificial bone or even a universal orthopaedic prosthesis.

Property	Cortical bone	Cancellous bone
Compressive strength (MPa)	100–230	2–12
Flexural, tensile strength (MPa)	50–150	10–20
Strain to failure (%)	1–3	5–7
Fracture toughness ($MPam^{1/2}$)	2–12	–
Young's modulus (GPa)	7–30	0.5–0.05

Table 1: The mechanical properties of cortical and cancellous bone [7]

1.3 Requirements for orthopaedic prostheses

1.3.1 Mechanical properties

Orthopaedic implants are medical devices constructed to support a damaged bone or to replace a missing joint or bone. Nowadays, various orthopaedic implants are available for the hip, knee, shoulder, and elbow with different requirements. Orthopaedic implants are required to have high tensile and compressive strength to prevent prostheses fractures and improve their functional stability. The response of the material to the repeated cyclic loads or strains is determined by the fatigue strength of the material, and this property determines the long-term success of an implant subjected to cyclic loading.

In addition, sufficient elasticity (a low elastic modulus) is also needed to ensure the uniform distribution of stress on the implant and to minimize the relative movement at the implant-bone interface. If the elastic modulus of the prosthesis is too high, the load which is normally applied to the bone is carried by the stiff implant, and the bone tissue atrophies due to lack of mechanic stimulation (this process is called stress shielding). Consequent osteoporosis results in fractures of the surrounding bone or loosening of the implant [8]. On the other hand, an excessively low elastic modulus causes large amounts of shear motion between the implant and the bone, leading to the formation of fibrous tissue and ultimately implant failure [9]. Thus, a material with an excellent combination of a high strength and low but sufficient elastic modulus should be used for implantation to avoid loosening of the implant and the need for a revision surgery.

1.3.2 Non-mechanical properties

1.3.2.1 Corrosion and wear resistance

Since the artificial bone implants are made of different, mostly metallic materials, high corrosion resistance is also required. Corrosion is the physicochemical interaction between a metal and its environment causing the release of metallic ions from the metal surface to the surrounding environment. These material changes result in a roughening of the surface, a weakening of the restoration and the eventual impairment of the prosthesis function [10]. Similarly, materials for total joint replacement need to also be wear resistant to avoid debris formation from the friction of contact surfaces. The potential accumulation of metallic ions from corrosion or wear of the prosthesis causes allergic reactions, inflammation and bone resorption that may eventually lead to the implant loosening [11]. Unfortunately, it is not only metallic debris, but also polymeric or ceramic debris which causes adverse biological reactions

[12]. In order to reduce both the volume of wear and the corrosion of the prostheses, different approaches for surface modification including various implant coatings have been investigated.

1.3.2.2 Biocompatibility

Apart from the mechanical properties, the main requirement for orthopaedic prostheses is their biocompatibility. The biocompatibility of the material is described as its ability to support normal cellular activity without any local and systematic toxic effects to the host tissue [13]. Therefore, biocompatibility depends on both material composition (the potential cytotoxicity of the metallic, ceramic, or polymeric compounds used), its physicochemical properties (like stiffness), as well as its surface properties such as surface roughness, charge, wettability, corrosion, and wear resistance (Table 2).

Bulk material composition, micro- (or nano)-structure, morphology
Crystallinity and crystallography
Elastic constants
Water content, hydrophobic–hydrophilic balance
Macro-, micro-, nano-porosity
Surface chemical composition, chemical gradients, surface molecular mobility
Surface topography
Surface energy
Surface electrical/electronic properties
Corrosion parameters, ion release profile, metal ion toxicity (for metallic materials)
Degradation profile, degradation product form and toxicity (for polymeric materials)
Leachables, additives, catalysts, contaminants and their toxicity (for polymeric materials)
Dissolution/degradation profile, degradation product toxicity (for ceramic materials)
Wear debris release profile

Table 2: Material properties affecting material biocompatibility [13]

In addition, biomaterials (defined as any matter, surface, or construct that interacts with living systems) could be either passively tolerated by the host body or they could actively stimulate specific desired cellular responses. Materials which are able to promote cell behaviour such as cell adhesion, migration, proliferation, secretion of various molecules, or differentiation into a specific cell type are called “bioactive”. These bioactive biomaterials should mimic the

functions of original bone tissue and act as an analog of natural ECM, which should facilitate implant integration into the surrounding host tissue [14].

1.3.2.3 Osseointegration

The ability of an implant to integrate with the adjacent bone and other tissues is also very important for the longevity of the prosthesis inside the human body. Osseointegration (i.e. the process of new bone formation during bone healing) is the clinical goal of implant surgery. A higher degree of osseointegration improves the mechanical stability of the implant, which decreases the probability of implant loosening. To achieve this, bone cells' adhesion, proliferation, and differentiation leading to ECM formation are needed. When the implant is not well integrated with the host bone, a fibrous tissue is formed between the bone and the implant [15]. There are many factors responsible for good osseointegration including implant composition, surface wettability, and electrostatic charges (surface chemistry), as well as the surface roughness and topography [16-18].

1.4 Materials of orthopaedic prostheses

The stems of load-bearing orthopaedic implants like total hip replacement are mainly fabricated from metallic alloys due to their superior mechanical properties (hardness, stiffness, etc.). However, other materials such as ceramics and polymers can be used for constructing the articular surfaces of joint prostheses. The artificial bearing surfaces of the prosthesis replace the natural ball-and-socket structure of the joint and for the hip implant are called femoral head (ball) and acetabular cup or shell (socket). A common implant composition for total hip and knee replacement is shown in Fig. 2.

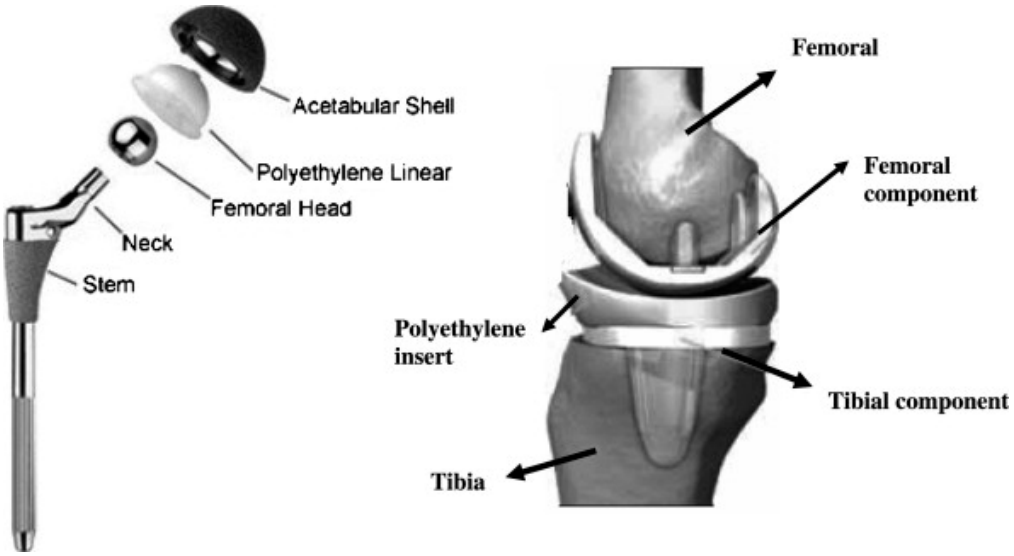

Fig. 2: Prostheses for total hip (left) and knee (right) replacement [19]

Several categories of TJR prostheses which consider bearing surfaces have been developed. Aside from the most common metal-on-metal, ceramic-on-ceramic, and metal-on-plastic (Fig. 3) models, other combinations like ceramic-on-plastic are available on the market.

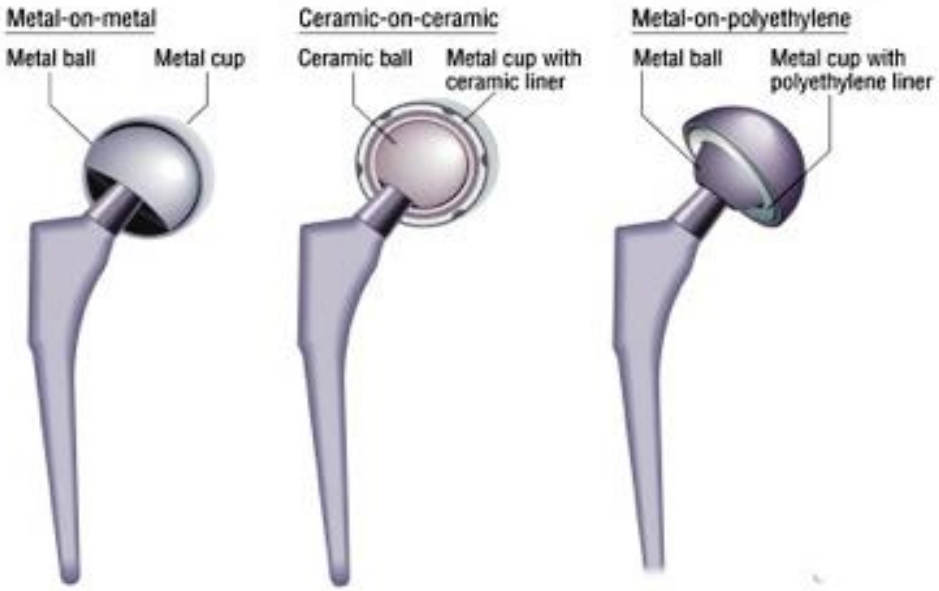

Fig. 3: A schematic composition of the most commonly used hip replacement prostheses (http://maxcurehospitals.com/nizamabad/hip-replacement-surgery)

The bearing surfaces of current artificial hip replacements are usually made out of ultra-high-molecular-weight polyethylene (UHMWPE), cobalt-chromium-molybdenum (Co-Cr-Mo) alloy or ceramics (alumina or zirconia). However, all of these combinations have their advantages as well as disadvantages; therefore, the choice of a suitable metallic implant depends on several factors including the patient's age, sex or individual illness.

1.4.1 Metallic materials

Metals have biomechanical properties which make them suitable for manufacturing TJR prostheses. Aside from their excellent hardness, they are also easy to process and have a good finish. Great malleability and ductility (the ability to draw out metal in the shape of wire) allow the shaping of metal into prostheses as well as intramedullary rods, screws, and long stems. By combining several metallic elements together, alloys with improved properties beyond those of a single element are made. Metallic implants can be sterilized by common sterilization procedures which make them easy to use. Despite a large number of metallic medical devices in use today, orthopaedic prostheses are manufactured of only a few metals such as 316L stainless steel, cobalt chromium alloys, and titanium-based alloys. Each of these materials has its own advantages as well as disadvantages and limitations.

1.4.1.1 Stainless steel (SS)

Stainless steel has the longest history of metallic materials used in orthopaedics dating back to the 30s [20]. Surgical stainless steel (also known as grade 316 SS) is an iron-based alloy with varying amounts of nickel, chromium, and molybdenum. These additions make the alloy stronger and more resistant to corrosion in comparison with common steel. The low carbon content (less than 0.03%, grade 316L SS) is added into 316 SS to decrease the corrosion rate, adverse tissue responses, and metal allergies. The main advantages of 316L SS are its great strength and affordable price. Unfortunately, this alloy has a relatively poor fatigue strength, low wear resistance, high corrosion rate, and high elastic modulus causing stress shielding (around 200 GPa). A comparison of the main mechanical properties including the tensile strength and elastic modulus of different metallic materials for TJR are shown in Table 3.

	Tensile strength (MPa)	Elastic modulus (GPa)
Stainless steel 316L (Fe-Cr-Ni-Mo-(C))	465-950	200-210
Co-Cr-Mo	275-1585	200-230
pure Ti (grade 4)	240-550	100
Ti-4Al-6V	850-965	115
Ti-6Al-7Nb	900-1050	110
Ti–5Al–2.5Fe	1000-1030	110
Ni-Ti	755-960	20-110
Ti-13Nb-13Zr	970-1030	79-85
Ti-15Zr-4Nb-4Ta	880-1030	90-100
Ti-29Nb-13Ta-4.6Zr	900	65
Ti-35Nb-7Zr-5Ta	590	55

Table 2: The mechanical properties of metallic materials used or investigated for TJR (adapted from [14, 19, 21 and 22])

However, the major concern in using stainless steel for implants is its high nickel content, which has been reported as a toxic substance to the human body [23]. Studies have shown that 316L SS implants often failed because of the implant's corrosion in bodily fluids leading to the release of harmful metallic elements like nickel [24, 25]. It is well known that nickel is the most frequent cause of the metal allergy, causing skin irritation, swelling, and inflammation. Current knowledge about the molecular mechanism of a nickel-induced allergy is reviewed in [26]. Nickel ions have also been reported to cause DNA damage and apoptosis in human T cells [27, 28]. Studies on rats have demonstrated tumour formation after the injection of nickel compounds [29, 30]. Similarly, a higher incidence of lung and nasal cancers in nickel refinery workers has been described, especially after co-exposure with tobacco smoking [31, 32]. *In vitro* and *in vivo* studies have shown that Ni containing nanoparticles are more toxic than microparticles [33, 34]. Epigenetic mechanisms (including alterations in DNA methylation, histone modifications such as acetylation, methylation, or ubiquitination, structural chromatin

changes, and alteration in transcription factors activity) are now considered to be responsible for nickel carcinogenicity [35, 36].

Another reason for implant failure could be an infection at the site of the surgery. Iron and chromium have been reported to have the poorest antimicrobial activity when compared with other metal-like titanium and cobalt [37]. Altogether, stainless steel implants have exhibited tendencies to fail after long-term use due to various reasons such as a high elastic modulus compared with that of bone, low wear and corrosion resistance, and insufficient biocompatibility, which makes SS an unsuitable material for manufacturing permanent implants. However, due to its low-cost aspect, 316L SS is still utilized for internal fixation devices (e.g. wires, pins, screws, plates, and intramedullary nails or rods) that are not meant to be load bearing for an extended period of time.

1.4.1.2 Cobalt-chromium-based alloys

In the last few decades, cobalt-chromium-based alloys have replaced stainless steel in clinics for use in TJR. Two main types of Co-Cr-based alloys, varying significantly in composition, are utilized for surgical implant purposes; nevertheless, the trade designation of “Vitallium” (or "Stellite" in Britain) is often applied to both types. The wrought alloy type is a cobalt-chromium-nickel alloy and has a better ductility and ultimate strength than the cast type composed of cobalt, chromium, and molybdenum. As in the case of stainless steel, the wrought alloy has a high nickel content and therefore exhibits lower corrosion resistance and biocompatibility than the cast cobalt-chromium-molybdenum alloy [38].

Co-Cr-based alloys are superior to stainless steel in fatigue strength as well as wear and corrosion resistance, and thus the cast Co-Cr-Mo alloy is currently used as the main material for metal-on-metal total hip and knee arthroplasty. Unfortunately, these alloys also have their disadvantages including a high elastic modulus (similar to that of stainless steel; Table 3) causing stress shielding. In addition, they are more difficult to manufacture and hence more expensive when compared with stainless steel [14].

Despite the generally good wear and corrosion resistance of Co-Cr alloys, ion release and accumulation is still of some concern in all metallic implants. Although the overall wear is reduced, significantly elevated metal concentrations in body fluids of patients with Co–Cr alloy metal-on-metal bearing hip implants have been repeatedly reported [39-41]. Moreover, the widespread dissemination of metallic debris from Co-Cr prostheses to the lymph nodes, bone marrow, liver, and spleen, along with the associated necrosis and fibrosis of lymphoid tissue

has been observed [42]. Like nickel, in the last few decades, numerous studies have described the potential allergenicity, cytotoxicity, and carcinogenicity of cobalt and chromium ions. Both metals have been found to induce a wide range of immunological reactions including irritant-type skin toxicity and contact dermatitis [43]. Cobalt or chromium compounds and cobalt-chromium nanoparticles have also been able to cause DNA damage [44-47]. In addition, chromium salts have been reported to have higher genotoxic effects than nickel salts [48].

The mutagenicity and genotoxicity of cobalt and chromium ions in patients with Co-Cr alloy implants have also been described [49]. Furthermore, tumorigenicity after Co-Cr alloy implantation in rats has been demonstrated [50]. Similarly, the production of malignant tumours in rats after cobalt powder injection occurred [51, 52]. However, other studies have not been able to confirm the adverse effects of cobalt and chromium compounds or only in much higher concentrations than those that occurred in patients with Co-Cr implants [53-57]. A recent review summarizing and interpreting around 80 of these studies has not found clear evidence that Co-Cr-containing hip implants are associated with an increased risk of systemic cancers [58].

Whether it is because of the increasing concentration of specific ions or because of any wear debris accumulation, the fact remains that many patients experience increasing local pain, swelling, and inflammation causing osteolysis and aseptic loosening of the implant leading to the need for painful and expensive revision surgery. Therefore, the current research is focused on the development of new alloys with a lower elastic modulus and better biocompatibility (the aim of publication I of this thesis, for more information, see chapter 1.4.1.3). Another approach is to minimalize the wear of currently used prostheses by the employment of biocompatible coatings with different additional functions (the purpose of the manuscript of this thesis, for more information, see chapter 1.4.2).

1.4.1.3 Pure titanium and Ti-based alloys

Pure titanium

Except for Co-Cr-based alloys, commercially pure titanium and its alloys are also widely used in orthopaedics as bone fixation materials, craniofacial or dental implants, as well as TJR prostheses for hip, knee, shoulder, and other joints. This wide variety of applications can be attributed to the excellent mechanical properties of titanium including its relatively high strength and its concurrently low density (high strength per density) and lower elastic modulus (up to 115 GPa when alloyed) in comparison with stainless steel and Co-Cr alloys (Table 3;

[14]). Moreover, titanium has superior biocompatibility and corrosion resistance thanks to the spontaneous formation of an adhesive titanium dioxide layer at its surface [59].

Another advantage of titanium-based biomaterials is their high rate of integrity with the host bone. This osteoinductive property significantly improves the long-term behaviour of the prostheses, decreasing the risks of implant loosening and failure. Titanium is one of the few materials without calcium phosphate that has been reported to calcify when exposed to simulated body fluid and is therefore expected to undergo a similar calcification *in vivo* [60]. Indeed, a histological and ultrastructural study on a retrieved forearm bone-anchored titanium prosthesis and surrounding tissue revealed a high degree of osseointegration, with the mature, mineralized, and remodelled bone in direct contact with the implant surface after being in use for more than 11 years [61]. In accordance with these publications, the titanium alloy Ti-6Al-4V implanted into the medullary space of the distal femur of rabbits has shown higher mineralization at the bone–implant interface than Co-Cr alloy [62].

Despite all the favourable properties of titanium, the strength of pure Ti (up to 550 MPa, depending on grade number 1-4; Table 3) is not sufficient for its use in total joint replacement. Thus, commercially pure Ti is currently employed only for implants without extensive demands for strength like small orthopaedic fixation implants and dental implants. For total joint replacement, titanium in the form of a stronger alloy must be used.

Alpha–beta titanium alloys

Titanium alloys are classified into four types called α, near α, α+β, and β alloys depending on their chemical composition, the content and nature of alloying elements, and the resulting microstructure [63]. The most common titanium alloy used in orthopaedics is Ti-6Al-4V with a biphasic alpha–beta microstructure. Aluminium together with O, N, C and Sn belongs into α–stabilizers, while V as well as Mo, Nb, Ta, Fe, W, Cr, Si, Ni, Co, Mn and H belongs to β-stabilizers. Alpha–beta alloys exhibit higher strength than α and near α alloys (such as commercially pure grades of titanium; Table 3) due to the presence of both α and β phases. Thus, aluminium and vanadium alloying elements improve the mechanical properties by doubling the ultimate strength values in relation to commercially pure Ti, which makes the Ti-6Al-4V alloy more suitable for prostheses manufacturing [59, 63].

Unfortunately, the long-term performance of this alloy has raised a concern due to Al and V release and their potential cytotoxicity. The toxicity and tumorigenicity of vanadium have been investigated because of the therapeutic potential of vanadium derivatives in diabetes and

cardiovascular diseases. However, numerous side effects consisting mainly of digestive problems including loss of appetite, a significant reduction of body weight, weakness, nose bleeding, vomiting, diarrhoea and dehydration, have been observed in rats or humans. Furthermore, the inhalation of vanadium compounds has been reported to cause rhinitis, pharyngitis, chronic productive cough, tracheobronchitis, bronchopneumonia or even the formation of lung neoplasms in rats [64]. Similar to nickel, vanadium ions have also been described to cause DNA damage and apoptosis in human T cells [27, 28]. Hence, other alpha–beta titanium alloys with similar properties to Ti-6Al-4V but without V content, like Ti–6Al–7Nb and Ti–5Al–2.5Fe alloys, have been developed [65, 66]. These alloys nevertheless, still contain aluminium. Numerous studies have reported the negative contribution of aluminium to neurodevelopmental and age-related neurodegenerative diseases such as autism spectrum disorders in infants, amyotrophic lateral sclerosis, and Alzheimer's disease in the elderly [67]. Moreover, studies on rats have shown that aluminium can be accumulated in the bone and causes decreased bone mineralization resulting in bone loss [68]. The mechanical properties of bone like its elastic modulus and strength have also been found to reduce after Al administration in rats [69] - an occurrence which should definitely be avoided in patients after prosthesis implantation.

In vitro studies comparing the wear particles of Ti-6Al-4V, Ti-6Al-6Nb, and pure Ti have revealed a higher activation of monocytes and phagocytes together with a significantly higher release of proinflammatory and bone-resorbing agents including interleukin-1, interleukin-6, tumour necrosis factor, and prostaglandin E2 when cultivated with Ti-6Al-4V particles [70, 71]. Accordingly, human fibroblasts exposed to Ti-6Al-4V wear particles isolated from the soft-tissue membrane of a failed total hip arthroplasty became activated and released proinflammatory mediators that influenced bone metabolism [72]. Furthermore, an *in vivo* study evaluating the tumorigenicity of Ti-6Al-4V and Co-Cr-Mo alloys on rats has shown a higher incidence of implant-associated tumours after Ti-6Al-4V implantation [50].

Apart from the potential cytotoxicity of Al and V, another major issue of Ti-6Al-4V alloy is its high wear rate (higher than that of SS or Co-Cr alloys; [73, 74]) and still too high elastic modulus (around 115 GPa) that may lead to the prosthesis loosening. *In vivo* studies have revealed that the healing and bone formation of rabbit femur have been twofold higher when an implantation of Ti-Mo alloy with a lower elastic modulus and better biocompatibility was used instead of Ti-6Al-4V [75]. Similarly, the new bone formation has been found to increase over time after the implantation of a biocompatible Ti-Zr alloy into the maxilla of miniature

pigs, while in the case of the Ti-6Al-4V implant, a decrease in the bone formation has been observed [76]. Aside from the Al and V toxicity and high elastic modulus, another possible explanation has been suggested: Ti and V ions leaking from the implant inhibit the hydroxyapatite formation and mineralization of adjacent tissues [77].

Beta titanium alloys

Because of the above-described disadvantages of the currently used Ti-6Al-4V alloy, the development of a new alloy with better biocompatibility and a lower elastic modulus is necessary. Of the different types of titanium alloys, β phase titanium alloys tend to satisfy most of the requirements for an orthopaedic implant application in contrast to the previously described α-β phase alloy Ti-6Al-4V. In the 60s, β phase nitinol alloys with a very low elastic modulus appeared [78]. Nitinol alloys are Ni-Ti alloys, which can exhibit an elastic modulus as low as 20 GPa (very similar to that of cortical bone). Moreover, nitinol alloys belong to the group of shape-memory alloys, which are able to "remember" and restore their original shapes in response to changing temperature or loading. Thanks to their super elasticity and the ability to deliver a uniform compressive stress, their use in load-bearing applications seemed very promising. However, there is the issue with the high nickel content (above 50 %) described in chapter 1.4.1.1.

In order to overcome this problem, other β phase Ni-free Ti alloys specifically tailored for biomedical applications are still under investigation. As already mentioned, the use of harmful elements including Ni, Co, Cr, V and Al should be avoided in implant development. Other elements such as Mo, Pd, and Sn have also been reported not to exhibit sufficient biocompatibility [59]. Based on these considerations, the recently developed biomedical alloys consist mainly of new beta titanium alloys with non-toxic alloying elements like Nb, Ta, and Zr [79]. A binary alloy consisting of Ti and 8 at.% Zr is already in clinical use and has shown good biocompatibility and osseointegration; nevertheless, long-term clinical evaluation is still lacking [76]. Apart from Ti-based alloys, current research is also focused on Ta, Nb or Zr-based alloys.

To create a purely biocompatible alloy with a minimal elastic modulus without compromising strength, numerous alloys with various Ti, Nb, Zr and Ta composition have emerged. These alloys consist entirely of biocompatible elements and they should prevent bone atrophy while enhancing the bone remodelling thanks to their relatively low elastic modulus (Table 3). Apart from lowering the elastic modulus, the presence of Ta and Nb improves the corrosion resistance

of the alloy. A comparative study on the corrosion behaviour of Ti–Ta and Ti-6Al-4V alloys has revealed that the addition of Ta remarkably reduces the concentration of metal release [80]. Correspondingly, the corrosion resistance of the Ti-Ta alloy in fluoridated acidified saliva was better when compared with the Ti-6Al-7Nb alloy [81]. The better corrosion resistance of alloys with Ta content was attributed to the presence of a more stable Ta_2O_5 passive film strengthening the TiO_2 passive layer. Similarly, Nb and Zr additions have been reported to increase the wear resistance of the Ti alloys thanks to the formation of Nb_2O_5 and ZrO_2 passive films, which possess very good lubricating properties [82, 83]. Indeed, the wear and corrosion rate comparison of the Ti-6Al-4V, Ti-6Al-7Nb and Ti-13Nb-13Zr alloys have shown the best behaviour of the Ti-13Nb-13Zr alloy, while the Ti-6Al-4V alloy exhibited the lowest wear and corrosion resistance [84]. Another study has proven the lowest metal release *in vitro* from the Ti-15Zr-4Nb-4Ta alloy when compared with the Ti-6Al-4V and Ti-6Al-7Nb alloys [85].

The effect of low modulus of implants made of Ti–15Zr–4Nb–4Ta and Ti-29Nb-13Ta-4.6Zr alloys on bone fracture healing, bone atrophy, and bone remodelling has been investigated in animal models. Intramedullary rods or plates of Ti-29Nb-13Ta-4.6Zr (elastic modulus up to 65 GPa) implanted into fracture models in the tibiae of rabbits were compared with Ti–6Al–4V and stainless steel implants with a much higher elastic modulus of around 115, and 200 GPa, respectively. The best bone remodelling with the lowest bone atrophy was observed after Ti-29Nb-13Ta-4.6Zr implantation. Moreover, the highest bone absorption occurred in the case of the intramedullary rod made of stainless steel [86, 87]. Another *in vivo* study also performed on rabbits has shown comparable or higher bone mineral density and better new bone formation around Ti-15Zr-4Nb-4Ta implants in comparison with Ti-6Al-4V implants [88]. Similar results had previously been observed in rats when the same alloy composition was used. In addition, the corrosion of the Ti-6Al-4V implant tended to increase with longer implantation times [89]. A recent study has proven comparable osseointegration of the Ti–10.1Ta–1.7Nb–1.6Zr alloy to commercially pure titanium grade 4, which is still regarded as a state-of-the-art material for bone anchoring, with an even lower inflammatory response in rats [90].

One of the lowest elastic moduli achieved in β Ti alloys has been found in alloy with the composition Ti-3Nb-7Zr-5Ta (TNZT). However, a significant disadvantage of this and other above-described low-rigidity alloys is their relatively low strength (up to 550 MPa for TNZT; Table 3), which makes them undesirable for use in load-bearing applications such as TJR prostheses. Therefore, current research is focused on strengthening these alloys without

significantly increasing the elastic modulus and decreasing the biocompatibility of the resulting alloy (the aim of publication I of this thesis).

1.4.2 Non-metallic materials

Aseptic loosening as a result of wear debris is considered to be the main cause of long-term implant failure in orthopaedic surgery. In order to minimalize wear and subsequent loosening of the prosthesis, non-metallic biomaterials are also used for bearing surfaces manufacturing (like polyethylene or ceramic liners) or for coating metallic bearing surfaces by wear and corrosion resistant layers. Specialized bioactive coatings of implanted stems are also used to improve the bonding of a metallic stem with the host bone.

1.4.2.1 Polymers

Metal-on-metal implants have the longest history dating back to the 30s when stainless steel was first used [20]. Later, to minimize the wear of the bearing surfaces and the subsequent accumulation of metallic ions, a tough but elastic ultra-high-molecular-weight polyethylene (UHMWPE) liner with good wear and corrosion resistance was engaged. However, later studies revealed the susceptibility of the UHMWPE to wear and abrasion caused by third body inclusions resulting in surface delamination, scratch marks, pitting, and folding of the retrieved UHMWPE surface [91, 92]. Furthermore, particles of the UHMWPE have been identified in tissues surrounding metal-on-PE implants [93-95]. These particles have been shown to induce a non-specific macrophage-mediated inflammatory reaction, leading to the release of proinflammatory and bone-resorbing cytokines such as interleukin-1β, interleukin-6, tumour necrosis factor, and prostaglandin E2 leading to periprosthetic osteolysis [96-100].

Indeed, *in vivo* mouse experiments have demonstrated osteoclast recruitment and bone resorption after the administration of UHMWPE particles [101, 102]. Accordingly, in all 160 patients undergoing revision surgery of metal-on-PE prostheses, osteolytic lesions on the acetabulum and femur along with increased atrophy of the gluteus muscle have been found [103]. In addition, overheating of the UHMWPE, mainly due to a lack of sufficient lubrication, has also been reported as a reason for the mechanical failure of metal-on-plastic prostheses [104].

Moreover, wear simulator studies have revealed that metal-on-PE prostheses have around 100 times higher wear than metal-on-metal implants [105-107]. Although a new approach in the manufacture of UHMWPE (consisting of gamma irradiation and vitamin E impregnation) has

decreased the wear of prostheses, a comparison of new highly cross-linked PE with older non-cross-linked PE particles has shown an even higher inflammatory effect of innovated highly cross-linked PE [108].

Recently, another polymer-carbon-fiber-reinforced polyetheretherketone (CFRPEEK) - has been introduced as a low-wear alternative cup-bearing surface. However, *in vivo* experiments have found an increased inflammatory response in a mouse model, comparable with that of UHMWPE particles [109]. Similarly, clinical studies have also shown the limitations of CFRPEEK. [110, 111].

Another polymer used in orthopaedic applications is polymethyl methacrylate (PMMA), commonly referred to as bone cement. Thanks to its low elastic modulus, comparable to that of bone, it is an ideal material for filling small bone defects or for repairing orthopaedic implants. However, PMMA is not suitable for manufacturing load-bearing implants due to its hard but brittle properties and high susceptibility to abrasion and wear caused by third body inclusion [14, 38].

1.4.2.2 Ceramics

Ceramics, mainly alumina (aluminium oxide, Al_2O_3) and zirconia (zirconium dioxide, ZrO_2), are well-known due to their high compressive strength, great wettability, and extremely low wear rate [112, 113]. Although ceramics exhibit great biocompatibility and wear resistance, they also have a high elastic modulus and low tensile strength, which make them very brittle with low crack and fracture resistance. Both alumina and zirconia heads have been repeatedly reported for catastrophic failure and fracture [114-117]. In addition to the high fracture rate of ceramic prostheses, ceramic-on-ceramic combinations often produce unpleasant squeaking sounds [117, 118]. When the ceramic head is combined with a polyethylene cup (ceramic-on-plastic), squeaking is diminished; nevertheless, the wear rate significantly increases [118-120]. Moreover, a recent study has not revealed any beneficial effect of ceramic-on-PE over metal-on-metal prostheses when metal ion levels have been evaluated. Furthermore, a higher incidence of periprosthetic lesions has been observed in patients with ceramic-on-PE implants in comparison with metal-on-metal implants [121].

Other ceramics such as various calcium phosphates, mainly hydroxyapatite (HA), have been widely used as coatings to improve osseointegration due to their favourable osteoconductive and bioactive properties [122, 123]. However, HA has poor mechanical properties, with a bending strength of less than 100 MPa, making it unsuitable for load-bearing implants [124,

125]. Even when used as a coating, mechanical failure and delamination of the HA coating from the metallic stem may occur, causing osteolysis by stimulating bone loss or by migration to the joint space producing third-body wear and subsequent implant failure [126, 127].

Therefore, the stability of the HA coating is the most critical factor in ensuring a successful outcome. Over time, nine common techniques of HA deposition including plasma spray, dip coating, thermal spray, hot isostatic pressing, pulsed laser deposition, electrophoretic deposition, sol–gel suspension, ion beam assisted deposition, and sputtering have been developed [128]. Although numerous studies have reported the beneficial effect of HA-coated implants on healing and osseointegration, most reviews of clinical results have failed to endorse these observations [129-134]. In addition, HA-uncoated roughened implants have often shown better osseointegration than HA-coated implants, suggesting that implant roughness itself has a higher impact than the chemistry of hydroxyapatite [135, 136]. Similarly, clinical studies have revealed no advantage of HA-coated stems over those with porous coated stems without HA [137-142].

1.4.2.3 Carbon-based coatings

Carbon-based materials have recently received great attention due to their unique physicochemical properties including high chemical inertness, mechanical stability, excellent electrical conductivity as well as satisfactory biocompatibility (for more information, see our review about nanocarbon-based materials [143] and our book chapter on fullerenes [144].

One of the materials used for the wear reduction of prosthesis bearing surfaces is diamond-like-carbon (DLC) coating. DLC coating is well known thanks to its unique mechanical properties, as well as its high level of biocompatibility. This coating exhibits great *in vitro* and *in vivo* biocompatibility and is well tolerated by animals with no evidence of chronic inflammatory reaction [145-147]. For more information about the biocompatibility of DLC, see the introduction of the enclosed manuscript in the appendix.

From a mechanical view, DLC coating has been shown to have excellent hardness and to significantly reduce the wear and metal ion release as well as the corrosion rate of metallic bearing surfaces [148-151]. Moreover, the wear of the DLC coating is several times lower than that of ceramic materials, which are substantially better than commonly used PE [152]. Interestingly, DLC-coated implants have been reported to stay undamaged even after aggressive wear tests employing the third-body bone cement particles [153]. Unfortunately, a considerable weakness of DLC coating is its potential delamination caused by the insufficient

adhesion of this layer to a metal substrate [154]. However, engagement of an interlayer could solve the problem and improve the adhesion of the DLC coating [155, 156].

In general, diamond and diamond-like coatings are used in a wide range of biomedical applications thanks to their unique combination of great biocompatibility, hardness, wear and corrosion resistance as well as their favourable electronic, optical, and other mechanochemical properties. Other potential biomedical applications include manufacturing biosensors [157-161]. Nowadays, several impedance biosensors for real-time monitoring of cellular proliferation are commercially available (e.g. xCELLigence system - Roche, ECIS – Electric Cell Substrate Impedance Sensing system - Applied BioPhysics, etc) but they have a number of limitations. The currently available systems are constructed from non-transparent gold interdigitated electrodes, which limit the direct optical observation of cultivated cells. Furthermore, the surface wettability as well as biochemistry of golden electrodes has to be properly controlled and optimized. Therefore, one of the aims of this thesis was to construct a diamond-based impedance biosensor for real-time monitoring of the cellular proliferation without the disadvantages of the currently used systems. For more information see publication IV.

Another carbon-based material with great potential in biomedical applications is fullerene coating. Fullerenes are carbon allotropes with a spherical structure consisting of carbon atoms linked via hexagonal and pentagonal rings. Fullerene C_{60} (also termed Buckminsterfullerene or buckyball) is a remarkably stable cage-like molecule with the ability to withstand high temperatures and pressures. However, the most interesting and promising feature of fullerenes is their strong antioxidant property. An increasing amount of literature is describing the therapeutic effect of fullerenes on osteoarthritis. It has been reported that water-soluble C_{60} administration significantly reduced articular cartilage degeneration in an osteoarthritis rabbit model [162]. Similarly, in arthritis rat models, treatment with water-soluble as well as non-modified fullerene C_{60} led to a decreasing number of osteoclasts together with reduced bone resorption and joint destruction, through the anti-inflammatory and anti-angiogenic effect of C_{60} [163-168]. Similar results have been observed for fullerene derivatives [169, 170]. According to these findings, the coating of orthopaedic implants with a bioactive fullerene layer should also improve the total joint replacement outcome in arthritic patients (amongst others). However, the reactivity of fullerenes may change in time due to the physicochemical changes of molecules in an air atmosphere. Thus, the widely discussed issue of potential fullerene cytotoxicity, resulting from their high reactivity, must be carefully investigated prior to the

clinical use of fullerenes (the aim of publications II and III of this thesis). For more information about fullerenes, see the enclosed publications in the appendix.

2 Objectives of the thesis

The general aim of this thesis was to evaluate the biocompatibility and potential cytotoxicity of promising materials for the manufacturing or coating of total joint replacement prostheses. The specific goals were focused on:

1. Developing a biocompatible beta titanium alloy with increased strength without an excessive increase in the elastic modulus and without a negative effect on the biocompatibility of this alloy. Verifying the biocompatibility and evaluating the osteogenic potential of the manufactured alloys with various Fe and Si additions were also included in our goals.

2. Evaluating the potential cytotoxicity and enhancing the biocompatibility (if needed) of fullerene layers for future use as a bioactive coating for orthopaedic implants.

3. Observing the wear of the Cr-Co-Mo alloy with a Ti gradient adhesive interlayer coated by DLC used for total trapeziometacarpal joint arthroplasty. Evaluating the potential cytotoxicity of wear debris generated by simulated loading was also included in our aims.

4. Developing a biocompatible, label-free, fully optically transparent diamond-based planar biosensor for real-time cell monitoring.

3 Materials and Methods

Author contribution:

All listed methods (chapters 3.2 – 3.8) were performed by the author of this thesis and are described in detail in each publication.

3.1 Materials

Material manufacturing and characterization of the physicochemical properties were performed by our collaborating partners:

- Charles University in Prague, Faculty of Mathematics and Physics (Publication I)
- Institute of Thermomechanics of the Czech Academy of Sciences (Publication I)
- Nuclear Physics Institute of the Czech Academy of Sciences (Publication II and III)
- Institute of Physics of the Czech Academy of Sciences (Publication IV)
- Czech Technical University in Prague, Faculty of Mechanical Engineering (Manuscript)
- Beznoska s.r.o (Manuscript)

3.2 Cells

Various bone cell types were used for different purposes:

Immortalized human osteosarcoma cell lines MG-63 or U-2 OS were utilized for evaluating cell adhesion, morphology, proliferation, viability, and potential membrane damage. Investigating the potential DNA damage of cells was performed on a U-2 OS cell line instead of MG-63, which is p53 deficient. For osteogenic differentiation, human primary osteoblasts HOB-p were employed.

3.3 Cell culture methods

Cell culture methods including cell freezing and thawing as well as passaging, seeding, harvesting, and counting of cells were routinely performed. All cell types were cultured under static or dynamic conditions at 37 °C in a humidified air atmosphere containing 5% of CO_2. Treatment with osteogenic differentiation supplements and a DNA damage inducer was employed.

3.4 Evaluation of cell adhesion and proliferation

In order to evaluate initial cell adhesion and cell proliferation, different methods of cell counting were employed: using a Bürker haemocytometer, Vi-Cell XR analyser, or counting of fixed cells visualised by Texas Red/Hoechst staining. For indirect assessment of cell proliferation, a Cell Proliferation Kit II (XTT assay) measuring the mitochondrial enzymes activity was used. xCELLigence system was utilized for real-time proliferation monitoring by impedance (cell index) measurement.

3.5 Evaluation of cell morphology

Cell morphology during the experiments was observed natively by using an inverted light microscope equipped with a digital camera. Cells fixed in specific time intervals were visualised by Texas Red/Hoechst staining and detected by fluorescence microscopy.

3.6 Evaluation of membrane damage and cell viability

Cell viability and potential membrane damage of the cells were detected by trypan blue staining performed during cell counting in the Vi-Cell XR analyser or by using a LIVE/DEAD Viability/Cytotoxicity Kit.

3.7 Evaluation of DNA damage response

Potential DNA damage was assessed by immunofluorescence staining of the DNA damage response markers, which were analysed by fluorescence microscopy (53BP1) and flow cytometry (gamma-H2AX).

3.8 Evaluation of material’s surface wettability

The wettability of the material’s surface was estimated from the contact angle measured by a material-water droplet system using a reflection goniometer.

4 List of publications

4.1 Publications presented in this thesis

The results presented in this thesis are summarized in four impacted articles and in one already sent manuscript. Individual publications are enclosed at the end of this thesis.

Publication I

Kopova I., Strasky J., Harcuba P., Landa M., Janecek M., Bacakova L.: Newly developed Ti-Nb-Zr-Ta-Si-Fe biomedical beta titanium alloys with increased strength and enhanced biocompatibility. Mater Sci Eng C Mater Biol Appl. 2016 Mar 1;60:230-8.

DOI: 10.1016/j.msec.2015.11.043

$IF_{2014/2015} = 3.088$

Author contribution:

I designed and performed all biological experiments and analysed the obtained data. I wrote the biological part of the manuscript and was the corresponding author.

Publication II

Kopova I., Bacakova L., Lavrentiev V., Vacik J.: Growth and potential damage of human bone-derived cells on fresh and aged fullerene C_{60} films. Int J Mol Sci. 2013 Apr 26;14(5):9182-204.

DOI: 10.3390/ijms14059182

$IF_{2014/2015} = 2.862$

Author contribution:

I designed and performed all biological experiments as well as surface wettability measurements, analysed the obtained data, and also contributed to manuscript writing.

Publication III

Kopova I., Lavrentiev V., Vacik J., Bacakova L.: Growth and potential damage of human bone-derived cells cultured on fresh and aged C_{60}/Ti films. PLoS One. 2015 Apr 15;10(4):e0123680.

DOI: 10.1371/journal.pone.0123680

$IF_{2014/2015} = 3.234$

Author contribution:

I designed and performed all biological experiments as well as the surface wettability measurements and analysed the obtained data. I wrote the major part of the manuscript and was the corresponding author.

Manuscript

Kopova I. *, Kronek J. *, Bacakova L., Fencl J.: The cytotoxicity and wear analysis of a DLC-coated Co-Cr-Mo alloy used for total trapeziometacarpal joint arthroplasty. *Manuscript* (2016)

* equal contribution

Author contribution:

I designed and performed all biological experiments and analysed the obtained data. I wrote the biological part of the manuscript and was the corresponding author.

Publication IV

Izak T., Novotna K., Kopova I., Bacakova L., Rezek B., Kromka A.: H-terminated diamond as optically transparent impedance sensor for real-time monitoring of cell growth. Phys. Status Solidi B 2013;250(12):2741-2746.

DOI: 10.1002/pssb.201300098

$IF_{2014/2015} = 1.489$

Author contribution:

I participated in performing biological experiments, data analysis as well as manuscript writing.

4.2 Other publications

Review

Bacakova L., Kopova I., Stankova L., Liskova J., Vacik J., Lavrentiev V., Kromka A., Potocky S., Stranska D.: Bone cells in cultures on nanocarbon-based materials for potential bone tissue engineering: A review. Phys. Status Solidi A 2014;211(12):2688–2702.

DOI: 10.1002/pssa.201431402

$IF_{2014/2015} = 1.616$

Chapters in books

Bacakova L., Kopova I., Vacik J., Lavrentiev V. Interaction of fullerenes and metal-fullerene composites with cells. In: Fullerenes: Chemistry, Natural Sources and Technological Applications. Edited by Ellis S.B., Nova Science Publishers, Inc., Hauppauge, New York, USA, 2014, pp 1-33. ISBN 978-1-63321-386-9.

Bacakova L., Filova E., Liskova J., Kopova I., Vandrovcova M., Havlikova J.: Nanostructured materials as substrates for the adhesion, growth and osteogenic differentiation of bone cells. In: Nanobiomaterials in hard tissue engineering; Applications of nanobiomaterials, Volume 4. Edited by Grumezescu A.M., Elsevier Inc., William Andrew Publishing, Oxford, Cambridge, 2016, Chapter 4, pp. 103-153, ISBN 978-0-323-42862-0.

5 Results

5.1 Objective No. 1 – Biocompatible beta titanium alloy

Publication I: Newly developed Ti-Nb-Zr-Ta-Si-Fe biomedical beta titanium alloys with increased strength and enhanced biocompatibility

The aim of this study was to develop a new biocompatible Ti-Nb-Zr-Ta alloy of increased strength without an excessive increase in the elastic modulus and without a negative effect on the biocompatibility of this alloy. In order to increase the relatively low strength (around 550 MPa) of this alloy, 5 combinations of small Fe and/or Si atoms additions to a benchmark Ti-35Nb-7Zr-6Ta alloy were used. This approach should increase the strength of the alloy without an excessive increase in the elastic modulus and without negatively affecting the biocompatibility of this alloy. To evaluate the biocompatibility and osteogenic potential of the Ti-Nb-Zr-Ta alloy with Fe and/or Si additions, adhesion, proliferation (under static as well as dynamic conditions), and differentiation of cells were performed in this study.

Indeed, the Fe and Si additions caused a significant increase in strength (from 550 MPa to 850 MPa) but also in the elastic modulus of the Ti-35Nb-7Zr-6Ta alloy. However, even the highest achieved elastic modulus (up to 85 GPa) was still much lower than that of the widely used Ti–6Al–4V alloy (around 115 GPa). The initial biological experiments showed that human osteoblast-like U-2 OS cells adhered more strongly on all six manufactured Ti-35Nb-7Zr-6Ta alloys (especially on TNZT and TNZT with the addition of 1Si, 2Fe or 0.5Si + 1Fe). The metabolic activity of the U-2 OS cells (proportional to the cell number and proliferation) cultured on all β Ti alloys under static conditions was higher than the metabolic activity of cells grown on the reference Ti-6Al-4V alloy. Differentiation experiments revealed significantly higher population densities and collagen I production of the primary human osteoblast cells (HOB-p) grown on TNZT alloys with 2 wt. % of Fe and 0.5 wt.% of Si additions in comparison with the Ti–6Al–4V alloy.

Overall, all manufactured alloys proved to be highly biocompatible. Fe and Si additions increased not only the strength of the benchmark TNZT alloy, but also promoted the adhesion, proliferation, and osteogenic differentiation of human cells. Therefore, the alloy with the composition Ti-35Nb-7Zr-6Ta-2Fe-0.5Si was chosen as a viable candidate for use in load-bearing implants.

5.2 Objective No. 2 – Biocompatibility of fullerene layers

<u>Publication II:</u> Growth and potential damage of human bone-derived cells on fresh and aged fullerene C_{60} films

<u>Publication III:</u> Growth and potential damage of human bone-derived cells cultured on fresh and aged C_{60}/Ti films

In these two publications, the dependence between the age of the fullerene coating (from one week to one year) and the initial adhesion, proliferation, viability, and metabolic activity of the human osteoblast-like cells was evaluated. We also monitored potential membrane and DNA damage as well as morphological changes of the cells.

Our first study, performed on pure fullerene C_{60} films, revealed lower initial adhesion, cell numbers, metabolic activity and viability of MG-63 cells cultured on fresh C_{60} layers. Moreover, the cells cultivated on the fresh C_{60} coating were poorly spread with a rounded morphology; however, no cytotoxic morphological changes, such as enlarged cells or cytosolic vacuole formation were observed. All investigated parameters (including cell adhesion, density, viability, and spreading) markedly improved with the aging of the C_{60} layers. Although the fullerene C_{60} coatings, particularly the fresh ones, attenuated cell growth, experiments performed on human osteoblast-like U-2 OS cells did not reveal any DNA damage response, as evaluated by gamma-H2AX (phosphorylated histone H2AX) and 53BP1 (p53-binding protein). In conclusion, aged C_{60} films provided a better support for the adhesion and growth of MG-63 cells than the corresponding fresh layers.

In our second study, fullerene C_{60} coating was enriched with titanium atoms in order to improve the mechanochemical stability and biocompatibility of the fullerene layers. The results, indeed, showed that the presence of Ti atoms led to an improvement in the fullerene coating properties (particularly the fresh ones), which became more suitable for cell cultivation. No negative influence of fresh or aged C_{60}/Ti films on cell adhesion, proliferation, viability, morphology, or metabolic activity was observed. As on pure C_{60} layers, the cells cultured on both fresh and aged C_{60}/Ti films showed no markers of a DNA damage response.

In conclusion, co-deposition of the C_{60} molecules with Ti atoms significantly improved the performance of the cells cultured on the fresh coating and minimalized the negative effects observed on pure C_{60} films.

5.3 Objective No. 3 – Wear and biocompatibility of DLC-coated Co-Cr-Mo alloy

Manuscript: The cytotoxicity and wear analysis of a DLC-coated Co-Cr-Mo alloy used for total trapeziometacarpal joint arthroplasty

The purpose of this study was to observe the wear of a Cr-Co-Mo alloy with a titanium gradient adhesive interlayer coated by DLC used for total trapeziometacarpal joint arthroplasty and to analyse the potential cytotoxicity of wear particles generated by simulated loading.

No visible wear or delamination of the DLC coating was observed after 3 million cycles of increasing loading force of up to 2.5 kN. In order to investigate the potential cytotoxicity of the wear particles, the real-time monitoring xCELLigence system (measuring electrode impedance, displayed as cell index) was used to evaluate the proliferation of U-2 OS osteoblast-like cells cultivated in different wear particles solutions. After a 7 day long cultivation, no significant differences among the samples (number of loading cycle) were found. Moreover, no correlation between increasing cycle numbers (with increasing loading force of up to 2.5 kN) and decreasing proliferation of the osteoblast-like cells incubated in the obtained wear suspensions was proven. Therefore, we can conclude that during the simulated loading of the DLC-coated Co-Cr-Mo alloy with the Ti gradient adhesive interlayer, no cytotoxic wear debris was formed.

5.4 Objective No. 4 – Biocompatible and transparent biosensor

Publication IV: H-terminated diamond as optically transparent impedance sensor for real-time monitoring of cell growth

Impedance sensors have attracted great attention as powerful characterization tools for real-time, non-invasive, label-free cell monitoring. However, current commercially available systems have several limitations including the restriction of the available area for direct optical observation of the cultivated cells due to the use of non-transparent gold electrodes.

In this study, we successfully invented a biocompatible, fully optically transparent diamond-based planar biosensor with uniform intrinsic edges-free morphology for non-invasive (label-free), real-time monitoring of cell cultivation. The real-time proliferation as well as cell morphology of human osteoblast-like MG-63 cells seeded in various concentrations was evaluated. The commercially available xCELLigence sensor from Roche was used as a reference impedance system. Our diamond-based impedance sensor showed that the morphology and proliferation rate of MG-63 cells was comparable to that of the reference gold-based system. Time-dependent impedance measurements at 1 kHz exhibited similar profiles for the diamond and reference gold sensors.

6 Discussion

Currently used prostheses for total joint replacement still have numerous disadvantages including a too high stiffness or elastic modulus of the metallic bulk material; this causes stress shielding which can result in bone loss with subsequent host bone fractures and implant loosening [8]. Over the decades, several β-type titanium alloys with various Ti, Nb, Zr, and Ta compositions and a low elastic modulus have emerged; nevertheless, the fatigue strength of these alloys is much lower than that of those currently used in load-bearing applications such as hip endoprostheses. Therefore, one of the aims of this thesis was to develop a biocompatible beta titanium alloy with increased strength without an excessive increase in the elastic modulus and without compromising the biocompatibility of this alloy.

Indeed, the result of the first study of this thesis showed that small additions of iron (Fe) and silicon (Si) to a benchmark Ti-35Nb-7Zr-6Ta alloy significantly increased the ultimate strength from 550 MPa to 850MPa. Another study using alloying by combination of Fe and Si additions also observed an increase in tensile strength; however, this study was not performed on a β Ti alloy, but only on the α-type [171]. A detailed macrostructure analysis revealed that Si atoms contributed to alloy hardening via the creation of dispersed precipitates of silicide particles, which were additionally enriched by zirconium. A similar compound formation has been previously reported in other zirconium containing titanium alloys [172]. The hardening effect of iron worked *via* simple solution strengthening, as iron is considered to be a strong β-stabilizer [59, 63]. The elastic modulus of the benchmark Ti-35Nb-7Zr-6Ta alloy (up to 65 GPa) was in accordance with the literature [173]. Although the elastic modulus increased with increasing Fe and Si content, even the highest achieved elastic modulus (up to 85 GPa) was still significantly lower than the value of the widely used Ti–6Al–4V alloy (around 115 GPa). In addition, Fe content also increased the plastic deformation of the resulting alloys.

In vitro biological experiments proved that all TNZT alloys are biocompatible and promote stronger adhesion as well as a higher proliferation of human osteoblast-like U-2 OS cells cultured under static conditions than the reference Ti–6Al–4V alloy. Our observations are in accordance with the literature: When cultured with extracts of similar alloys (Ti–29Nb–13Ta–4.6Zr, Ti-10Zr-8Nb-2Ta-0.2Pd and Ti-15Zr-4Nb-2Ta-0.2Pd) as opposed to cultivation in the extract solution of a Ti-6Al-4V alloy, a higher proliferation of L929 and MC3T3-E1 cells was found [174, 175]. Correspondingly, the proliferation of various cell types was also higher on the Ti–15Zr–4Nb–4Ta, as well as the Ti-35Nb-2Ta-3Z alloy than on the Ti-6Al-4V alloy [21, 176]. In contrast to another study using small boron addition in a similar Ti–35Nb–5.7Ta–7.2Zr

alloy which resulted in a decreased attachment of the human osteoblast-like MG-63 cells [177], our findings revealed that Fe and Si additions even enhanced the already strong adhesion of the U-2 OS cells on the Ti-35Nb-7Zr-6Ta alloy.

Aside from the stronger attachment of osteoblast-like cells, the Si and Fe additions to our benchmark TNZT alloy also promoted the proliferation and osteogenic differentiation of the primary human osteoblast (HOB-p). The beneficial effect of specific iron concentrations on the proliferation and collagen I synthesis of various cell types was also reported in the literature [178-181]. Similarly, Si-containing materials were found to promote the proliferation and osteogenic differentiation of various cell types [182-186].

In our first study, we developed the Ti-35Nb-7Zr-6Ta alloy with Fe and Si additions, which significantly increases strength as well as overall biocompatibility. Thanks to its lower elastic modulus and better osteogenic potential, the better integration of the implant into the host bone should be achieved. This alloy is therefore promising material for the manufacture of total joint replacement prostheses.

Another strategy to improve the integration of metallic implants, which in general do not exhibit high osteoinductivity, is the employment of various bioactive coatings. The fullerene layer is a great candidate for coating orthopaedic implants due to the therapeutic potential of fullerenes in arthritis prevention and treatment [162-168]. The widely discussed potential cytotoxicity of fullerenes was investigated in the second study of this thesis. Because of the high reactivity of the fullerene molecules, the effect of the C_{60} layers' age (from one week to one year) on their biocompatibility was investigated.

Although the fullerene C_{60} films, particularly the fresh ones, attenuated the adhesion and proliferation of osteoblast-like cells, no cytotoxic morphological changes (such as enlarged cells or cytosolic vacuole formation) or DNA damage response were found. In contrast to our results, numerous studies have described fullerenes and their derivatives as cytotoxic and genotoxic agents, causing oxidative DNA damage, polyploidy, inflammation, and inhibition of the detoxificatory and antioxidant enzymes, as well as premature cell senescence and apoptosis [187-193]. However, recently tetrahydrofuran (THF), which was widely used as a solvent of fullerenes, was found to be cytotoxic. Thus, the toxic side products (γ-butyrolactone, 2-hydroxytetrahydrofuranol and formic acid) created during the preparation of C_{60} suspension are probably responsible for the cytotoxicity previously attributed to fullerenes, whereas fullerenes themselves have no harmful effect [194-196]. Likewise, Kepney has recently written to the

editors of Toxicological sciences, questioning the purity of the fullerenes used in the previously published study which asserted the cytotoxicity of fullerenes [197]. He claims that many studies are not observing data relevant to C_{60} exposure, but rather the data from a mixture of fullerenes plus solvent, which together make completely new molecular entities with different cytotoxicity. Correspondingly, our unpublished experiments, where MG-63 cells were treated with C_{60} suspended in a cell culture medium (concentration ranging from 0.15 μg to 30 μg/mL) for seven days, showed no reduction in proliferation or cytotoxic morphologic changes. The fullerene suspension was prepared without using THF. In order to prevent the formation of aggregates, dimethylsulfoxid and sonification were used instead of THF [198]. An *in vivo* toxicity experiment in rodents revealed similar results: Not only did the aqueous C_{60} suspension prepared without using any polar organic solvent not cause any toxicity, but this treatment even had a protective effect on rodents' livers in a dose-dependent manner [199]. In addition, other *in vivo* studies have not observed any skin or eye irritation, allergic reaction, or tumour formation [200-202]. Furthermore, the beneficial effects of fullerene and their derivatives on cognitive behaviour and the lifespan of rodents have been reported [203, 204].

Aged C_{60} layers in our study provided a better support for the adhesion and growth of MG-63 cells, as all investigated parameters (including cell adhesion, density, viability, proliferation and cell spreading) improved markedly with the aging of C_{60} layers. The better cell performance can be attributed to changes in the physicochemical properties of the fullerene films during aging, such as fragmentation, oxidation, polymerization and graphitization (revealed by Raman spectroscopy and X-ray Photoelectron Spectroscopy - XPS). These changes probably decreased fullerene reactivity, modified the chemistry and enhanced the nanoscale roughness of the C_{60} layers, thus facilitating cell adhesion and proliferation [205, 206].

In order to improve the mechanochemical stability and biocompatibility of the fullerene coating, co-deposition of C_{60} with titanium atoms was used in the third study of this thesis. The introduction of a suitable metallic component was expected to stabilize the fullerene films in terms of reducing the release of free C_{60} and their penetration into cells, thus eliminating the potential negative effects of fullerenes. Titanium was chosen as this metallic component due to its biocompatibility, which has been proven in numerous long-lasting experimental and clinical applications. Similar C_{60}-gold nanoparticle films have exhibited good chemical and ultrasonic stability [207]. The results, indeed, showed that the Ti addition improved the properties of the fullerene coatings (particularly the fresh ones). No significant differences in cell adhesion, viability, and growth between the fresh and aged layers were observed. In fact, the behaviour

of cells cultured on both the fresh and aged coating was comparable to the behaviour of cells grown on reference glass coverslips and no DNA damage response or cytotoxic cellular morphology was found. The beneficial effect of the Ti addition on the biocompatibility and bioactivity of the coating has also been reported for DLC layers [208]. At the same time, the Ti presence improved the adhesion of the DLC layer to the underlying substrate and decreased the residual stress as well as the wear rate of the DLC coating [209-211]. Moreover, the excellent wear resistance of the Ti-doped DLC coating thanks to the graphitization of the DLC surface was observed [212]. Similarly, the Ti addition to other carbon-related coatings, including amorphous carbon and the hydrocarbon plasma polymer, also enhanced the adhesion, spreading, and growth of osteoblast-like MG-63 cells [213, 214].

The difference between the pure C_{60} coating and Ti-enriched layers can be explained by the fact that the above-mentioned changes in the fullerene molecules (like fragmentation, polymerization, and oxidation) occurred not only with the aging of the coatings but even during C_{60} and Ti co-deposition by the mutual interaction of these molecules and atoms (confirmed by Raman spectroscopy and XPS). The Ti-enriched C_{60} coating can therefore be considered as a promising material for orthopaedic implant coating with osteoprotective potential [163-168].

Apart from the insufficient mechanical properties and weak integration of total joint replacement prostheses, the accumulation of metallic ions caused by the wear of bearing surfaces is the main reason for implant failure [11]. In order to reduce both the wear and the corrosion of the prostheses, various coatings of bearing surfaces have been investigated. In the fourth study of this thesis, the wear of the DLC-coated Cr-Co-Mo alloy for total trapeziometacarpal joint arthroplasty was evaluated. A titanium gradient adhesive interlayer was employed for enhanced adhesion of the DLC coating on the Cr-Co-Mo substrate [155, 156]. Our results from simulated loading revealed the great wear resistance of the DLC coating with no visible wear or delamination after 3 million cycles. These findings are in accordance with other studies, where the DLC coating significantly reduced the wear and enhanced the scratch resistance of the Cr-Co-Mo alloy [149, 150, 215, 216]. Moreover, the DLC-coated implant has been reported to stay undamaged even after aggressive wear tests employing third-body bone cement particles [153]. Additionally, the results of a simulated body fluid experiment performed for 2 years have shown a 100,000 times lower corrosion rate of the DLC-coated Cr-Co-Mo alloy in comparison with the uncoated alloy [151]. Aside from great corrosion resistance, the DLC coating deposited on the Mg alloy also exhibited excellent blood compatibility by inhibiting platelet adhesion [217]. The engagement of the Ti gradient

interlayer showed better adhesion and stability than the nitride interlayer used in other studies [216, 218].

An evaluation of the potential cytotoxicity of wear debris did not reveal any correlation between the increasing loading cycles (with increasing loading force of up to 2.5 kN) and decreasing proliferation of osteoblast-like cells incubated in obtained wear suspensions. Correspondingly, numerous studies have shown great biocompatibility of the DLC films, supporting the growth and viability of many cell types without any signs of cytotoxicity [147, 219-221]. Furthermore, *in vivo* experiments have proven good acceptance of DLC-coated implants by surrounding tissues [145, 146]. Our study focused on the simulated loading of a DLC-coated Co-Cr-Mo alloy with a Ti gradient interlayer (used for total trapeziometacarpal joint arthroplasty) and proved the great wear resistance of the DLC coating without any cytotoxic debris formation.

In our last project presented in this thesis, we successfully developed a biocompatible, label-free, fully optically transparent diamond-based impedance biosensor for real-time monitoring of cellular proliferation. Our sensor showed similar profiles to the commercially available xCELLigence gold-based sensor. Another significant advantage of our sensor compared with the commercial alternatives is the wide frequency range of the impedance measurement (from 100 Hz up to 100 kHz) which allows detailed study of different cellular processes. For low-frequency measurements (<10 kHz), the current flows through gaps between the cells (paracellular flow), therefore the impedance is sensitive to cell density, growth, and movements. If the measurement frequency is high enough (>40 kHz), current can flow through the cell membrane (transcellular flow), which means that the impedance is more sensitive to cell adhesion and less sensitive to cell population [222]. Moreover, our diamond-based impedance sensor may also be suitable for *in vitro* testing of various drugs and cytotoxic agents.

7 Conclusion

The issue of disadvantages of currently used total joint replacement prostheses were addressed in this thesis, consisting of four impacted publications and one already sent manuscript:

1. Considering the insufficient mechanical properties of commonly used orthopaedic alloys, five new low-rigidity Ti-35Nb-7Zr-6Ta alloys, with various Fe and Si additions which significantly increase the tensile strength and enhance the biocompatibility and osteoconductivity of the benchmark alloy were developed. The alloy with a final composition of Ti-35Nb-7Zr-6Ta-2Fe-0.5Si exhibited the best combination of mechanical and biological properties and was therefore chosen as the most promising candidate for manufacturing load-bearing implants.

2. In order to improve the integration of the implant into the host bone, a fullerene coating with osteoprotective potential was investigated. Although no cytotoxicity or DNA damage was observed in osteoblast-like cells grown on fresh C_{60} layers, we improved the biocompatibility of the fresh fullerene coating by co-deposition of C_{60} molecules with Ti atoms.

3. Another carbon-related coating was used for the reduction of the Co-Cr-Mo wear rate. A DLC-coated Co-Cr-Mo with a Ti gradient adhesive interlayer exhibited no visible wear or delamination. Moreover, the safety of the DLC coating was proven by no observed correlation between the increasing cycles of simulated loading and the decreasing proliferation of the osteoblast-like cells incubated in the obtained wear suspensions.

4. Finally, a biocompatible, fully optically transparent diamond-based planar biosensor with uniform intrinsic edges-free morphology for non-invasive (label-free), real-time monitoring of cell cultivation with a wide range of applications was successfully invented.

8 References

1. Bonfigli M, Jeter WS. Immunological responses to bone. Clinical Orthopaedics and Related Research 1972(87):19-&.
2. Langer R, Vacanti JP. Tissue engineering. Science 1993;260(5110):920-926.
3. Alford AI, Kozloff KM, Hankenson KD. Extracellular matrix networks in bone remodeling. International Journal of Biochemistry & Cell Biology 2015;65:20-31.
4. Pivonka P, Buenzli PR, Dunstan CR. A systems approach to understanding bone cell interactions in health and disease. Cell Interaction: InTech; 2012.
5. Boskey AL. Bone composition: relationship to bone fragility and antiosteoporotic drug effects. BoneKEy reports 2013;2:447.
6. Lamoureux F, Baud'huin M, Duplomb L, Heymann D, Redini F. Proteoglycans: key partners in bone cell biology. Bioessays 2007;29(8):758-771.
7. Hutmacher DW, Schantz JT, Lam CXF, Tan KC, Lim TC. State of the art and future directions of scaffold-based bone engineering from a biomaterials perspective. Journal of Tissue Engineering and Regenerative Medicine 2007;1(4):245-260.
8. Huiskes R, Weinans H, Vanrietbergen B. The relationship between stress shielding and bone-resorption around total hip stems and the effects of flexible materials. Clinical Orthopaedics and Related Research 1992(274):124-134.
9. Niinomi M. Mechanical biocompatibilities of titanium alloys for biomedical applications. Journal of the Mechanical Behavior of Biomedical Materials 2008;1(1):30-42.
10. Chaturvedi TP. An overview of the corrosion aspect of dental implants (titanium and its alloys). Indian journal of dental research : official publication of Indian Society for Dental Research 2009;20(1):91-8.
11. Vermes C, Chandrasekaran R, Jacobs JJ, Galante JO, Roebuck KA, Glant TT. The effects of particulate wear debris, cytokines, and growth factors on the functions of MG-63 osteoblasts. The Journal of Bone & Joint Surgery 2001;83(2):201-201.
12. Goodman SB. Wear particles, periprosthetic osteolysis and the immune system. Biomaterials 2007;28(34):5044-5048.
13. Williams DF. On the mechanisms of biocompatibility. Biomaterials 2008;29(20):2941-2953.
14. Navarro M, Michiardi A, Castano O, Planell JA. Biomaterials in orthopaedics. Journal of the Royal Society Interface 2008;5(27):1137-1158.
15. Pilliar RM, Lee JM, Maniatopoulos C. Observations on the effect of movement on bone ingrowth into porous-surfaced implants. Clinical Orthopaedics and Related Research 1986(208):108-113.
16. Qiu Q, Sayer M, Kawaja M, Shen X, Davies JE. Attachment, morphology, and protein expression of rat marrow stromal cells cultured on charged substrate surfaces. J Biomed Mater Res 1998;42(1):117-27.
17. Chesmel KD, Clark CC, Brighton CT, Black J. Cellular responses to chemical and morphologic aspects of biomaterial surfaces. II. The biosynthetic and migratory response of bone cell populations. J Biomed Mater Res 1995;29(9):1101-10.
18. Healy KE, Thomas CH, Rezania A, Kim JE, McKeown PJ, Lom B, Hockberger PE. Kinetics of bone cell organization and mineralization on materials with patterned surface chemistry. Biomaterials 1996;17(2):195-208.
19. Geetha M, Singh AK, Asokamani R, Gogia AK. Ti based biomaterials, the ultimate choice for orthopaedic implants – A review. Progress in Materials Science 2009;54(3):397-425.

20. Wiles P. The surgery of the osteo-arthritic hip. British Journal of Surgery 1958;45(193):488-497.

21. Okazaki Y. A new Ti-15Zr-4Nb-4Ta alloy for medical applications. Current Opinion in Solid State & Materials Science 2001;5(1):45-53.

22. Katti KS. Biomaterials in total joint replacement. Colloids Surf B Biointerfaces 2004;39(3):133-42.

23. Wen X, Wang R, Jia X, Tang J, He X. In Vitro Cytotoxicity Study of Nickel Ion. Chinese journal of medical instrumentation 2015;39(3):212-5.

24. Amel-Farzad H, Peivandi MT, Yusof-Sani SMR. In-body corrosion fatigue failure of a stainless steel orthopaedic implant with a rare collection of different damage mechanisms. Engineering Failure Analysis 2007;14(7):1205-1217.

25. Tavares SSM, Mainier FB, Zimmerman F, Freitas R, Ajus CMI. Characterization of prematurely failed stainless steel orthopedic implants. Engineering Failure Analysis 2010;17(5):1246-1253.

26. Saito M, Arakaki R, Yamada A, Tsunematsu T, Kudo Y, Ishimaru N. Molecular mechanisms of nickel allergy. International Journal of Molecular Sciences 2016;17(2).

27. Caicedo M, Jacobs JJ, Reddy A, Hallab NJ. Analysis of metal ion-induced DNA damage, apoptosis, and necrosis in human (Jurkat) T-cells demonstrates Ni2+, and V3+ are more toxic than other metals: Al3+, Be2+, Co2+, Cr3+, Cu2+, Fe3+, Mo5+, Nb5+, Zr2+. Journal of Biomedical Materials Research Part A 2008;86A(4):905-913.

28. Au A, Ha J, Hernandez M, Polotsky A, Hungerford DS, Frondoza CG. Nickel and vanadium metal ions induce apoptosis of T-lymphocyte Jurkat cells. Journal of Biomedical Materials Research Part A 2006;79A(3):512-521.

29. Jasmin G, Riopelle JL. Renal carcinomas and erythrocytosis in rats following intrarenal injection of nickel subsulfide. Lab Invest 1976;35(1):71-8.

30. Shibata M, Izumi K, Sano N, Akagi A, Otsuka H. Induction of soft-tissue tumors in F344 rats by subcutaneous, intramuscular, intra-articular, and retroperitoneal injection of nickel sulfide (NI3S2). Journal of Pathology 1989;157(3):263-274.

31. Doll R, Mathews JD, Morgan LG. Cancers of lung and nasal sinuses in nickel workers - reassessment of period of risk. British Journal of Industrial Medicine 1977;34(2):102-105.

32. Andersen A, Berge SR, Engeland A, Norseth T. Exposure to nickel compounds and smoking in relation to incidence of lung and nasal cancer among nickel refinery workers. Occupational and Environmental Medicine 1996;53(10):708-713.

33. Horie M, Nishio K, Fujita K, Kato H, Nakamura A, Kinugasa S, Endoh S, Miyauchi A, Yamamoto K, Murayama H and others. Ultrafine NiO particles induce cytotoxicity in vitro by cellular uptake and subsequent Ni(II) release. Chemical Research in Toxicology 2009;22(8):1415-1426.

34. Phillips JI, Green FY, Davies JCA, Murray J. Pulmonary and systemic toxicity following exposure to nickel nanoparticles. American Journal of Industrial Medicine 2010;53(8):763-767.

35. Salnikow K, Zhitkovich A. Genetic and epigenetic mechanisms in metal carcinogenesis and cocarcinogenesis: Nickel, arsenic, and chromium. Chemical Research in Toxicology 2008;21(1):28-44.

36. Fragou D, Fragou A, Kouidou S, Njau S, Kovatsi L. Epigenetic mechanisms in metal toxicity. Toxicology Mechanisms and Methods 2011;21(4):343-352.

37. Berry CW, Moore TJ, Safar JA, Henry CA, Wagner MJ. Antibacterial activity of dental implant metals. Implant dentistry 1992;1(1):59-65.

38. Simon JP, Fabry G. An overview of implant materials. Acta orthopaedica Belgica 1991;57(1):1-5.

39. Schaffer AW, Pilger A, Engelhardt C, Zweymueller K, Ruediger HW. Increased blood cobalt and chromium after total hip replacement. Journal of Toxicology-Clinical Toxicology 1999;37(7):839-844.

40. Pazzaglia UE, Minoia C, Gualtieri G, Gualtieri I, Riccardi C, Ceciliani L. Metal-ions in body-fluids after arthroplasty. Acta Orthopaedica Scandinavica 1986;57(5):415-418.

41. Brodner W, Bitzan P, Meisinger V, Kaider A, GottsaunerWolf F, Kotz R. Elevated serum cobalt with metal-on-metal articulating surfaces. Journal of Bone and Joint Surgery-British Volume 1997;79B(2):316-321.

42. Urban RM, Jacobs JJ, Tomlinson MJ, Gavrilovic J, Black J, Peoc'h M. Dissemination of wear particles to the liver, spleen, and abdominal lymph nodes of patients with hip or knee replacement. J Bone Joint Surg Am 2000;82(4):457-76.

43. Hostynek JJ, Hinz RS, Lorence CR, Price M, Guy RH. Metals and the skin. Critical Reviews in Toxicology 1993;23(2):171-235.

44. Bhabra G, Sood A, Fisher B, Cartwright L, Saunders M, Evans WH, Surprenant A, Lopez-Castejon G, Mann S, Davis SA and others. Nanoparticles can cause DNA damage across a cellular barrier. Nature Nanotechnology 2009;4(12):876-883.

45. Kasprzak KS, Zastawny TH, North SL, Riggs CW, Diwan BA, Rice JM, Dizdaroglu M. Oxidative DNA-base damage in renal, hepatic, and pulmonary chromatin of rats after intraperitoneal injection of cobalt(II) acetate. Chemical Research in Toxicology 1994;7(3):329-335.

46. Bagchi D, Hassoun EA, Bagchi M, Stohs SJ. Chromium-induced excretion of urinary lipid metabolites, DNA-damage, nitric-oxide production, and generation of reactive oxygen species in Sprague-Dawley rats. Comparative Biochemistry and Physiology C-Pharmacology Toxicology & Endocrinology 1995;110(2):177-187.

47. Gao M, Binks SP, Chipman JK, Levy LS, Braithwaite RA, Brown SS. Induction of DNA strand breaks in peripheral lymphocytes by soluble chromium compounds. Hum Exp Toxicol 1992;11(2):77-82.

48. Seoane AI, Dulout FN. Genotoxic ability of cadmium, chromium and nickel salts studied by kinetochore staining in the cytokinesis-blocked micronucleus assay. Mutation Research-Genetic Toxicology and Environmental Mutagenesis 2001;490(2):99-106.

49. Figgitt M, Newson R, Leslie IJ, Fisher J, Ingham E, Case CP. The genotoxicity of physiological concentrations of chromium (Cr(III) and Cr(VI)) and cobalt (Co(II)): An in vitro study. Mutation Research-Fundamental and Molecular Mechanisms of Mutagenesis 2010;688(1-2):53-61.

50. Bouchard PR, Black J, Albrecht BA, Kaderly RE, Galante JO, Pauli BU. Carcinogenicity of CoCrMo (F-75) implants in the rat. Journal of Biomedical Materials Research 1996;32(1):37-44.

51. Heath JC. The production of malignant tumours by cobalt in the rat. British Journal of Cancer 1956;10(4):668.

52. Heath JC, Daniel MR. The production of malignant tumours by cobalt in the rat - intrathoracic tumours. British Journal of Cancer 1962;16(3):473-478.

53. Paustenbach DJ, Galbraith DA, Finley BL. Interpreting cobalt blood concentrations in hip implant patients. Clinical Toxicology 2014;52(2):98-112.

54. Andersson MA, Grawe KVP, Karlsson OM, Abramsson-Zetterberg LAG, Hellman BE. Evaluation of the potential genotoxicity of chromium picolinate in mammalian cells in vivo and in vitro. Food and Chemical Toxicology 2007;45(7):1097-1106.

55. Kwon YM, Xia Z, Glyn-Jones S, Beard D, Gill HS, Murray DW. Dose-dependent cytotoxicity of clinically relevant cobalt nanoparticles and ions on macrophages in vitro. Biomedical Materials 2009;4(2).

56. Gaechter A, Alroy J, Andersson GBJ, Galante J, Rostoker W, Schajowicz F. Metal carcinogenesis - study of carcinogenic activity of solid metal-alloys in rats. Journal of Bone and Joint Surgery-American Volume 1977;59(5):622-624.

57. Hininger I, Benaraba R, Osman M, Faure H, Roussel AM, Anderson RA. Safety of trivalent chromium complexes: No evidence for DNA damage in human HaCaT keratinocytes. Free Radical Biology and Medicine 2007;42(12):1759-1765.

58. Christian WV, Oliver LD, Paustenbach DJ, Kreider ML, Finley BL. Toxicology-based cancer causation analysis of CoCr-containing hip implants: a quantitative assessment of genotoxicity and tumorigenicity studies. Journal of Applied Toxicology 2014;34(9):939-967.

59. Long M, Rack HJ. Titanium alloys in total joint replacement—a materials science perspective. Biomaterials 1998;19(18):1621-1639.

60. Li PJ, Ohtsuki C, Kokubo T, Nakanishi K, Soga N, Degroot K. The role of hydrated silica, titania, and alumina in inducing apatite on implants. Journal of Biomedical Materials Research 1994;28(1):7-15.

61. Palmquist A, Jarmar T, Emanuelsson L, Branemark R, Engqvist H, Thomsen P. Forearm bone-anchored amputation prosthesis - A case study on the osseointegration. Acta Orthopaedica 2008;79(1):78-85.

62. Jinno T, Goldberg VM, Davy D, Stevenson S. Osseointegration of surface-blasted implants made of titanium alloy and cobalt-chromium alloy in a rabbit intramedullary model. Journal of Biomedical Materials Research 1998;42(1):20-29.

63. Boyer RR. An overview on the use of titanium in the aerospace industry. Materials Science and Engineering a-Structural Materials Properties Microstructure and Processing 1996;213(1-2):103-114.

64. Ghosh SK, Saha R, Saha B. Toxicity of inorganic vanadium compounds. Research on Chemical Intermediates 2015;41(7):4873-4897.

65. Borowy K-H, Kramer K-H. On the properties of a new titanium alloy (TiAl5Fe2.5) as implant material. In: Titanium'84 Science and Technology, vol. 2. Munich, Deutsche Gesellschaft Fur Metallkunde EV 1995:1381—6.

66. Semlitsch M, Staub F, Weber H. Titanium-aluminium-niobium alloy, development for biocompatible, high strength surgical implants. Biomed Tech (Berl) 1985;30(12):334-9.

67. Shaw CA, Tomljenovic L. Aluminum in the central nervous system (CNS): toxicity in humans and animals, vaccine adjuvants, and autoimmunity. Immunol Res 2013;56(2-3):304-16.

68. Li XW, Hu CW, Zhu YZ, Sun H, Li YF, Zhang ZG. Effects of aluminum exposure on bone mineral density, mineral, and trace elements in rats. Biological Trace Element Research 2011;143(1):378-385.

69. Martinez MD, Bozzini C, Olivera MI, Dmytrenko G, Conti MI. Aluminum bone toxicity in immature rats exposed to simulated high altitude. Journal of Bone and Mineral Metabolism 2011;29(5):526-534.

70. Rogers SD, Howie DW, Graves SE, Pearcy MJ, Haynes DR. In vitro human monocyte response to wear particles of titanium alloy containing vanadium or niobium. J Bone Joint Surg Br 1997;79(2):311-5.

71. Shanbhag AS, Jacobs JJ, Black J, Galante JO, Glant TT. Human monocyte response to particulate biomaterials generated in vivo and in vitro. J Orthop Res 1995;13(5):792-801.

72. Manlapaz M, Maloney WJ, Smith RL. In vitro activation of human fibroblasts by retrieved titanium alloy wear debris. J Orthop Res 1996;14(3):465-72.

73. McKellop HA, Sarmiento A, Schwinn CP, Ebramzadeh E. In vivo wear of titanium-alloy hip prostheses. J Bone Joint Surg Am 1990;72(4):512-7.

74. Choubey A, Basu B, Balasubramaniam R. Tribological behaviour of Ti-based alloys in simulated body fluid solution at fretting contacts. Materials Science and Engineering: A 2004;379(1–2):234-239.

75. Lin D-J, Chuang C-C, Chern Lin J-H, Lee J-W, Ju C-P, Yin H-S. Bone formation at the surface of low modulus Ti–7.5Mo implants in rabbit femur. Biomaterials 2007;28(16):2582-2589.

76. Saulacic N, Bosshardt DD, Bornstein MM, Berner S, Buser D. Bone apposition to a titanium-zirconium alloy implant, as compared to two other titanium-containing implants. Eur Cell Mater 2012;23:273-86; discussion 286-8.

77. Blumenthal NC, Cosma V. Inhibition of apatite formation by titanium and vanadium ions. Journal of Biomedical Materials Research 1989;23(S13):13-22.

78. Buehler WJ, Wang FE. A summary of recent research on the nitinol alloys and their potential application in ocean engineering. Ocean Engineering 1968;1(1):105-120.

79. Eisenbarth E, Velten D, Müller M, Thull R, Breme J. Biocompatibility of β-stabilizing elements of titanium alloys. Biomaterials 2004;25(26):5705-5713.

80. Zhou YL, Niinomi M, Akahori T, Fukui H, Toda H. Corrosion resistance and biocompatibility of Ti-Ta alloys for biomedical applications. Materials Science and Engineering a-Structural Materials Properties Microstructure and Processing 2005;398(1-2):28-36.

81. Mareci D, Chelariu R, Gordin DM, Ungureanu G, Gloriant T. Comparative corrosion study of Ti-Ta alloys for dental applications. Acta Biomater 2009;5(9):3625-39.

82. Xu YF, Xiao YF, Yi DQ, Liu HQ, Wu L, Wen J. Corrosion behavior of Ti-Nb-Ta-Zr-Fe alloy for biomedical applications in Ringer's solution. Transactions of Nonferrous Metals Society of China 2015;25(8):2556-2563.

83. Li SJ, Yang R, Li S, Hao YL, Cui YY, Niinomi M, Guo ZX. Wear characteristics of Ti-Nb-Ta-Zr and Ti-6Al-4V alloys for biomedical applications. Wear 2004;257(9-10):869-876.

84. Khan MA, Williams RL, Williams DF. Conjoint corrosion and wear in titanium alloys. Biomaterials 1999;20(8):765-72.

85. Okazaki Y, Gotoh E. Comparison of metal release from various metallic biomaterials in vitro. Biomaterials 2005;26(1):11-21.

86. Sumitomo N, Noritake K, Hattori T, Morikawa K, Niwa S, Sato K, Niinomi M. Experiment study on fracture fixation with low rigidity titanium alloy: plate fixation of tibia fracture model in rabbit. J Mater Sci Mater Med 2008;19(4):1581-6.

87. Niinomi M, Hattori T, Morikawa K, Kasuga T, Suzuki A, Fukui H, Niwa S. Development of low rigidity beta-type titanium alloy for biomedical applications. Materials Transactions 2002;43(12):2970-2977.

88. Nakada H, Numata Y, Sakae T, Okazaki Y, Tanimoto Y, Tamaki H, Katou T, Ookubo A, Kobayashi K, LeGeros RZ. Comparison of bone mineral density and area of newly formed bone around Ti-15%Zr-4%Nb-4%Ta alloy and Ti-6%Al-4%V alloy implants. Journal of Hard Tissue Biology 2008;17(3):99-108.

89. Okazaki Y, Nishimura E, Nakada H, Kobayashi K. Surface analysis of Ti-15Zr-4Nb-4Ta alloy after implantation in rat tibia. Biomaterials 2001;22(6):599-607.

90. Stenlund P, Omar O, Brohede U, Norgren S, Norlindh B, Johansson A, Lausmaa J, Thomsen P, Palmquist A. Bone response to a novel Ti–Ta–Nb–Zr alloy. Acta Biomaterialia 2015;20:165-175.

91. Liza S, Haseeb A, Abbas AA, Masjuki HH. Failure analysis of retrieved UHMWPE tibial insert in total knee replacement. Engineering Failure Analysis 2011;18(6):1415-1423.

92. Camacho N, Stafford SW, Trueba L. Comparative failure analysis of retrieved UHMWPE tibial components. International ASM.; 2013. 63-68 p.

93. Willert HG, Bertram H, Buchhorn GH. Osteolysis in alloarthroplasty of the hip - the role of ultra-high-molecular-weight polyethylene wear particles. Clinical Orthopaedics and Related Research 1990(258):95-107.

94. Cooper RA, McAllister CM, Borden LS, Bauer TW. Polyethylene debris-induced osteolysis and loosening in uncemented total hip arthroplasty. A cause of late failure. The Journal of arthroplasty 1992;7(3):285-90.

95. Amstutz HC, Campbell P, Kossovsky N, Clarke IC. Mechanism and clinical-significance of wear debris-induced osteolysis. Clinical Orthopaedics and Related Research 1992(276):7-18.

96. Ingram J, Matthews JB, Tipper J, Stone M, Fisher J, Ingham E. Comparison of the biological activity of grade GUR 1120 and GUR 415HP UHMWPE wear debris. Biomed Mater Eng 2002;12(2):177-88.

97. Wooley PH, Morren R, Andary J, Sud S, Yang SY, Mayton L, Markel D, Sieving A, Nasser S. Inflammatory responses to orthopaedic biomaterials in the murine air pouch. Biomaterials 2002;23(2):517-26.

98. Trindade MC, Song Y, Aspenberg P, Smith RL, Goodman SB. Proinflammatory mediator release in response to particle challenge: studies using the bone harvest chamber. J Biomed Mater Res 1999;48(4):434-9.

99. Goodman S, Aspenberg P, Song Y, Knoblich G, Huie P, Regula D, Lidgren L. Tissue ingrowth and differentiation in the bone-harvest chamber in the presence of cobalt-chromium-alloy and high-density-polyethylene particles. J Bone Joint Surg Am 1995;77(7):1025-35.

100. Voronov I, Santerre JP, Hinek A, Callahan JW, Sandhu J, Boynton EL. Macrophage phagocytosis of polyethylene particulate in vitro. J Biomed Mater Res 1998;39(1):40-51.

101. Zhang C, Tang T, Ren W, Zhang X, Dai K. Influence of mouse genetic background on wear particle-induced in vivo inflammatory osteolysis. Inflamm Res 2008;57(5):211-5.

102. Ma T, Huang Z, Ren PG, McCally R, Lindsey D, Smith RL, Goodman SB. An in vivo murine model of continuous intramedullary infusion of polyethylene particles. Biomaterials 2008;29(27):3738-42.

103. Hernigou P, Roussignol X, Delambre J, Poignard A, Flouzat-Lachaniette CH. Ceramic-on-ceramic THA associated with fewer dislocations and less muscle degeneration by preserving muscle progenitors. Clin Orthop Relat Res 2015;473(12):3762-9.

104. Burger NDL, de Vaal PL, Meyer JP. Failure analysis on retrieved ultra high molecular weight polyethylene (UHMWPE) acetabular cups. Engineering Failure Analysis 2007;14(7):1329-1345.

105. Anissian HL, Stark A, Gustafson A, Good V, Clarke IC. Metal-on-metal bearing in hip prosthesis generates 100-fold less wear debris than metal-on-polyethylene. Acta Orthop Scand 1999;70(6):578-82.

106. Tipper JL, Firkins PJ, Ingham E, Fisher J, Stone MH, Farrar R. Quantitative analysis of the wear and wear debris from low and high carbon content cobalt chrome alloys used in metal on metal total hip replacements. Journal of Materials Science-Materials in Medicine 1999;10(6):353-362.

107. St John KR, Zardiackas LD, Poggie RA. Wear evaluation of cobalt-chromium alloy for use in a metal-on-metal hip prosthesis. J Biomed Mater Res B Appl Biomater 2004;68(1):1-14.

108. Illgen RL, 2nd, Bauer LM, Hotujec BT, Kolpin SE, Bakhtiar A, Forsythe TM. Highly crosslinked vs conventional polyethylene particles: relative in vivo inflammatory response. J Arthroplasty 2009;24(1):117-24.

109. Utzschneider S, Becker F, Grupp TM, Sievers B, Paulus A, Gottschalk O, Jansson V. Inflammatory response against different carbon fiber-reinforced PEEK wear particles compared with UHMWPE in vivo. Acta Biomater 2010;6(11):4296-304.

110. Field RE, Rajakulendran K, Eswaramoorthy VK, Rushton N. Three-year prospective clinical and radiological results of a new flexible horseshoe acetabular cup. Hip International 2012;22(6):598-606.

111. Grupp TM, Utzschneider S, Schroder C, Schwiesau J, Fritz B, Maas A, Blomer W, Jansson V. Biotribology of alternative bearing materials for unicompartmental knee arthroplasty. Acta Biomater 2010;6(9):3601-10.

112. Salehi A, Tsai S, Pawar V, Sprague J, Hunter G, Varma S, Namavar F. Wettability analysis of orthopaedic materials using optical contact angle methods. In: Nakamura T, Yamashita K, Neo M, editors. Bioceramics 18, Pts 1 and 2; 2006. p 1199-1202.

113. Nevelos J, Ingham E, Doyle C, Streicher R, Nevelos A, Walter W, Fisher J. Microseparation of the centers of alumina-alumina artificial hip joints during simulator testing produces clinically relevant wear rates and patterns. Journal of Arthroplasty 2000;15(6):793-795.

114. Simon JA, Dayan AJ, Ergas E, Stuchin SA, Di Cesare PE. Catastrophic failure of the acetabular component in a ceramic-polyethylene bearing total hip arthroplasty. Journal of Arthroplasty 1998;13(1):108-113.

115. Hummer CD, Rothman RH, Hozack WJ. Catastrophic failure of modular zirconia-ceramic femoral head components after total hip arthroplasty. Journal of Arthroplasty 1995;10(6):848-850.

116. Needham J, Burns T, Gerlinger T. Catastrophic failure of ceramic-polyethylene bearing total hip arthroplasty. Journal of Arthroplasty 2008;23(4):627-630.

117. Malem D, Nagy MT, Ghosh S, Shah B. Catastrophic failure of ceramic-on-ceramic total hip arthroplasty presenting as squeaking hip. BMJ case reports 2013;2013.

118. Dong YL, Li T, Xiao K, Bian YY, Weng XS. Ceramic on ceramic or ceramic-on-polyethylene for total hip arthroplasty: A Systemic Review and Meta-analysis of Prospective Randomized Studies. Chin Med J (Engl) 2015;128(9):1223-31.

119. Lewis PM, Al-Belooshi A, Olsen M, Schemitch EH, Waddell JP. Prospective randomized trial comparing alumina ceramic-on-ceramic with ceramic-on-conventional polyethylene bearings in total hip arthroplasty. J Arthroplasty 2010;25(3):392-7.

120. Amanatullah DF, Landa J, Strauss EJ, Garino JP, Kim SH, Di Cesare PE. Comparison of surgical outcomes and implant wear between ceramic-ceramic and ceramic-polyethylene articulations in total hip arthroplasty. J Arthroplasty 2011;26(6 Suppl):72-7.

121. Bisseling P, de Wit BWK, Hol AM, van Gorp MJ, van Kampen A, van Susante JLC. Similar incidence of periprosthetic fluid collections after ceramic-on-polyethylene total hip arthroplasties and metal-on-metal resurfacing arthroplasties: Results of a screening metal artefact reduction sequence-MRI study. Bone & Joint Journal 2015;97B(9):1175-1182.

122. Corpe RS, Steflik DE, Whitehead RY, Wilson MD, Young TR, Jaramillo C. Correlative experimental animal and human clinical retrieval evaluations of hydroxyapatite (HA)-coated and non-coated implants in orthopaedics and dentistry. Crit Rev Biomed Eng 2000;28(3 - 4):395-8.

123. Sakkers RJ, Dalmeyer RA, Brand R, Rozing PM, van Blitterswijk CA. Assessment of bioactivity for orthopedic coatings in a gap-healing model. J Biomed Mater Res 1997;36(2):265-73.

124. Dewith G, Vandijk HJA, Hattu N, Prijs K. Preparation, microstructure and mechanical-properties of dense polycrystalline hydroxy apatite. Journal of Materials Science 1981;16(6):1592-1598.

125. Wang C, Ma J, Cheng W, Zhang R. Thick hydroxyapatite coatings by electrophoretic deposition. Materials Letters 2002;57(1):99-105.

126. Watson CJ, Tinsley D, Ogden AR, Russell JL, Mulay S, Davison EM. A 3 to 4 year study of single tooth hydroxylapatite coated endosseous dental implants. British Dental Journal 1999;187(2):90-94.

127. D'Angelo F, Molina M, Riva G, Zatti G, Cherubino P. Failure of dual radius hydroxyapatite-coated acetabular cups. J Orthop Surg Res 2008;3:35.

128. Mohseni E, Zalnezhad E, Bushroa AR. Comparative investigation on the adhesion of hydroxyapatite coating on Ti–6Al–4V implant: A review paper. International Journal of Adhesion and Adhesives 2014;48:238-257.

129. Akilapa O, Gaffey A. Hydroxyapatite pins for external fixation: is there sufficient evidence to prove that coated pins are less likely to be replaced prematurely? Acta Orthopaedica Et Traumatologica Turcica 2015;49(4):410-415.

130. Al-Hamdan K, Al-Moaber SH, Junker R, Jansen JA. Effect of implant surface properties on peri-implant bone healing: a histological and histomorphometric study in dogs. Clin Oral Implants Res 2011;22(4):399-405.

131. de Barros RR, Novaes AB, Jr., Queiroz A, de Almeida AL. Early peri-implant endosseous healing of two implant surfaces placed in surgically created circumferential defects. A histomorphometric and fluorescence study in dogs. Clin Oral Implants Res 2012;23(12):1340-51.

132. Abrahamsson I, Linder E, Larsson L, Berglundh T. Deposition of nanometer scaled calcium-phosphate crystals to implants with a dual acid-etched surface does not improve early tissue integration. Clin Oral Implants Res 2013;24(1):57-62.

133. Coelho PG, Cardaropoli G, Suzuki M, Lemons JE. Early healing of nanothickness bioceramic coatings on dental implants. An experimental study in dogs. J Biomed Mater Res B Appl Biomater 2009;88(2):387-93.

134. Parvizi J, Sharkey PF, Hozack WJ, Orzoco F, Bissett GA, Rothman RH. Prospective matched-pair analysis of hydroxyapatite-coated and uncoated femoral stems in total hip arthroplasty. A concise follow-up of a previous report. J Bone Joint Surg Am 2004;86-a(4):783-6.

135. Meirelles L, Melin L, Peltola T, Kjellin P, Kangasniemi I, Currie F, Andersson M, Albrektsson T, Wennerberg A. Effect of hydroxyapatite and titania nanostructures on early in vivo bone response. Clin Implant Dent Relat Res 2008;10(4):245-54.

136. Bryington MS, Hayashi M, Kozai Y, Vandeweghe S, Andersson M, Wennerberg A, Jimbo R. The influence of nano hydroxyapatite coating on osseointegration after extended healing periods. Dent Mater 2013;29(5):514-20.

137. Park YS, Lee JY, Yun SH, Jung MW, Oh I. Comparison of hydroxyapatite- and porous-coated stems in total hip replacement. Acta Orthop Scand 2003;74(3):259-63.

138. Rothman RH, Hozack WJ, Ranawat A, Moriarty L. Hydroxyapatite-coated femoral stems. A matched-pair analysis of coated and uncoated implants. J Bone Joint Surg Am 1996;78(3):319-24.

139. Sharp RJ, O'Leary ST, Falworth M, Cole A, Jones J, Marshall RW. Analysis of the results of the C-Fit uncemented total hip arthroplasty in young patients with hydroxyapatite or porous coating of components. J Arthroplasty 2000;15(5):627-34.

140. Lombardi AV, Jr., Berend KR, Mallory TH. Hydroxyapatite-coated titanium porous plasma spray tapered stem: experience at 15 to 18 years. Clin Orthop Relat Res 2006;453:81-5.

141. Gandhi R, Davey JR, Mahomed NN. Hydroxyapatite coated femoral stems in primary total hip arthroplasty: a meta-analysis. J Arthroplasty 2009;24(1):38-42.

142. Goosen JH, Kums AJ, Kollen BJ, Verheyen CC. Porous-coated femoral components with or without hydroxyapatite in primary uncemented total hip arthroplasty: a systematic review of randomized controlled trials. Arch Orthop Trauma Surg 2009;129(9):1165-9.

143. Bacakova L, Kopova I, Stankova L, Liskova J, Vacik J, Lavrentiev V, Kromka A, Potocky S, Stranska D. Bone cells in cultures on nanocarbon-based materials for potential bone tissue engineering: A review. Physica Status Solidi a-Applications and Materials Science 2014;211(12):2688-2702.

144. Bacakova L, Kopova I, Vacik J, Lavrentiev V. Interaction of fullerenes and metal-fullerene composites with cells. In: S.B. E, editor. Fullerenes: Chemistry, Natural Sources and Technological Applications. Hauppauge, New York, USA: Nova Science Publisher, Inc.; 2014. p 1-33.

145. Allen M, Myer B, Rushton N. In vitro and in vivo investigations into the biocompatibility of diamond-like carbon (DLC) coatings for orthopedic applications. Journal of Biomedical Materials Research 2001;58(3):319-328.

146. Mohanty M, Anilkumar TV, Mohanan PV, Muraleedharan CV, Bhuvaneshwar GS, Derangere F, Sampeur Y, Suryanarayanan R. Long term tissue response to titanium coated with diamond like carbon. Biomolecular Engineering 2002;19(2-6):125-128.

147. Thomson LA, Law FC, Rushton N, Franks J. Biocompatibility of diamond-like carbon coating. Biomaterials 1991;12(1):37-40.

148. Thorwarth G, Falub CV, Muller U, Weisse B, Voisard C, Tobler M, Hauert R. Tribological behavior of DLC-coated articulating joint implants. Acta Biomater 2010;6(6):2335-41.

149. Fisher J, Hu XQ, Tipper JL, Stewart TD, Williams S, Stone MH, Davies C, Hatto P, Bolton J, Riley M and others. An in vitro study of the reduction in wear of metal-on-metal hip prostheses using surface-engineered femoral heads. Proceedings of the Institution of Mechanical Engineers Part H-Journal of Engineering in Medicine 2002;216(H4):219-230.

150. Roy ME, Whiteside LA, Katerberg BJ. Diamond-like carbon coatings enhance scratch resistance of bearing surfaces for use in joint arthroplasty: hard substrates outperform soft. Journal of Biomedical Materials Research Part B-Applied Biomaterials 2009;89B(2):527-535.

151. Tiainen VM. Amorphous carbon as a bio-mechanical coating - mechanical properties and biological applications. Diamond and Related Materials 2001;10(2):153-160.

152. Ching HA, Choudhury D, Nine MJ, Abu Osman NA. Effects of surface coating on reducing friction and wear of orthopaedic implants. Science and Technology of Advanced Materials 2014;15(1).

153. Santavirta SS, Lappalainen R, Pekko P, Anttila A, Konttinen YT. The counterface, surface smoothness, tolerances, and coatings in total joint prostheses. Clinical Orthopaedics and Related Research 1999(369):92-102.

154. Joyce TJ. Examination of failed ex vivo metal-on-metal metatarsophalangeal prosthesis and comparison with theoretically determined lubrication regimes. Wear 2007;263:1050-1054.

155. Utsumi T, Oka Y, Fujiwara E, Yatsuzuka M. Effect of a hard supra-thick interlayer on adhesion of DLC film prepared with PBIID process. Nuclear Instruments & Methods in Physics Research Section B-Beam Interactions with Materials and Atoms 2007;257:706-709.

156. Wang YX, Pu JB, Wang JF, Li JL, Chen JM, Xue QJ. Interlayer design for the graphite-like carbon film with high load-bearing capacity under sliding-friction condition in water. Applied Surface Science 2014;311:816-824.

157. Sim H, Kim JH, Lee SK, Song MJ, Yoon DH, Lim DS, Hong SI. High-sensitivity non-enzymatic glucose biosensor based on Cu(OH)(2) nanoflower electrode covered with boron-doped nanocrystalline diamond layer. Thin Solid Films 2012;520(24):7219-7223.

158. Zehani N, Fortgang P, Saddek Lachgar M, Baraket A, Arab M, Dzyadevych SV, Kherrat R, Jaffrezic-Renault N. Highly sensitive electrochemical biosensor for bisphenol A detection based on a diazonium-functionalized boron-doped diamond electrode modified with a multi-walled carbon nanotube-tyrosinase hybrid film. Biosensors and Bioelectronics 2015;74:830-835.

159. Stefan-van Staden RI, Nejem RM, van Staden JF, Aboul-Enein HY. Amperometric biosensor based on diamond paste for the enantioanalysis of L-lysine. Biosensors & Bioelectronics 2012;35(1):439-442.

160. Olyaee S, Bahabady AM. Design and optimization of diamond-shaped biosensor using photonic crystal nano-ring resonator. Optik 2015;126(20):2560-2564.

161. Picollo F, Gosso S, Vittone E, Pasquarelli A, Carbone E, Olivero P, Carabelli V. A new diamond biosensor with integrated graphitic microchannels for detecting quantal exocytic events from chromaffin cells. Advanced Materials 2013;25(34):4696-4700.

162. Yudoh K, Shishido K, Murayama H, Yano M, Matsubayashi K, Takada H, Nakamura H, Masuko K, Kato T, Nishioka K. Water-soluble C60 fullerene prevents degeneration of articular cartilage in osteoarthritis via down-regulation of chondrocyte catabolic activity and inhibition of cartilage degeneration during disease development. Arthritis Rheum 2007;56(10):3307-18.

163. Weng CT, Chen SY, Chen YH, Wu CL, Liu MF, Shiau AL, Wang CR. Amelioration of collagen-induced arthritis by water-soluble fullerene C60(OH)(36) nanoparticles through the inhibition of angiogenesis. Arthritis & Rheumatology 2014;66:S1022-S1022.

164. Mamontova TV, Mykytiuk MV, Bobrova NO, Kutsenko LO, Vesnina LE, Kaidashev IP. The anti-inflammatory effect of fullerene C60 on adjuvant arthritis in rats. Fiziol Zh 2013;59(3):102-10.

165. Kaidashev IP, Mamontova TV, Vesnina LE, Mikityuk MV, Bobrova NA, Kutsenko LA, Gordinskaya IL, DuBuske LM. The inhibitory effects of fullerene C60 on the immunopathology of experimental adjuvant arthritis. Annals of Allergy Asthma & Immunology 2012;109(5):A107-A108.

166. Vesnina LE, Mamontova TV, Mikitiuk MV, Bobrova NA, Kutsenko LA, Iaroshenko GA, Kaidashev IP. Fullerene C60 exhibits immunomodulatory activity during adjuvant-induced arthritis in rats. Eksp Klin Farmakol 2012;75(8):15-20.

167. Yudoh K, Karasawa R, Masuko K, Kato T. Water-soluble fullerene (C60) inhibits the development of arthritis in the rat model of arthritis. Int J Nanomedicine 2009;4:217-25.

168. Mamontova TV, Vesnina LE, Mikityuk MV, Bobrova NA, Kutsenko LA, Gordinskaya IL, Kaidashev IP. Fullerene C60 inhibited free radical and destructive processes in connective tissue during adjuvant arthritis in rats. Fiziol Zh 2015;61(2):80-6.

169. Dellinger AL, Cunin P, Lee D, Kung AL, Brooks DB, Zhou Z, Nigrovic PA, Kepley CL. Inhibition of inflammatory arthritis using fullerene nanomaterials. PLoS One 2015;10(4):e0126290.

170. Duarte JH. Experimental arthritis: Fullerene nanoparticles ameliorate disease in arthritis mouse model. Nat Rev Rheumatol 2015;11(6):319.

171. Lee DB, Park KB, Jeong HW, Kim SE. Mechanical and oxidation properties of Ti–xFe–ySi alloys. Materials Science and Engineering: A 2002;328(1–2):161-168.

172. Ankem S, Banerjee D, McNeish DJ, Williams JC, Seagle SR. Silicide formation in Ti-3Al-8V-6Cr-4Zr-4Mo. Metallurgical Transactions a Physical Metallurgy and Materials Science 1987;18(12):2015-2025.

173. Ahmed T, Rack HJ; Low modulus biocompatible titanium base alloys for medical devices patent US 5871595. 1999 Feb. 16, 1999.

174. Ito A, Okazaki Y, Tateishi T, Ito Y. In-vitro biocompatibility, mechanical-properties, and corrosion-resistance of Ti-Zr-Nb-Ta-Pd and Ti-Sn-Nb-Ta-Pd alloys. Journal of Biomedical Materials Research 1995;29(7):893-899.

175. Niinomi M. Fatigue performance and cyto-toxicity of low rigidity titanium alloy, Ti–29Nb–13Ta–4.6Zr. Biomaterials 2003;24(16):2673-2683.

176. Guo Y, Chen D, Cheng M, Lu W, Wang L, Zhang X. The bone tissue compatibility of a new Ti35Nb2Ta3Zr alloy with a low Young's modulus. International Journal of Molecular Medicine 2013;31(3):689-697.

177. Majumdar P, Singh SB, Dhara S, Chakraborty M. Influence of in situ TiB reinforcements and role of heat treatment on mechanical properties and biocompatibility of Ti-alloys. Journal of the Mechanical Behavior of Biomedical Materials 2012;10:1-12.

178. Gardi C, Arezzini B, Fortino V, Comporti M. Effect of free iron on collagen synthesis, cell proliferation and MMP-2 expression in rat hepatic stellate cells. Biochemical Pharmacology 2002;64(7):1139-1145.

179. Zhao G-y, Zhao L-p, He Y-f, Li G-F, Gao C, Li K, Xu Y-j. A comparison of the biological activities of human osteoblast hFOB1.19 between iron excess and iron deficiency. Biological Trace Element Research 2012;150(1):487-495.

180. Dai J, Churg A. Relationship of fiber surface iron and active oxygen species to expression of procollagen, PDGF-A, and TGF- β1 in tracheal explants exposed to amosite asbestos. American Journal of Respiratory Cell and Molecular Biology 2001;24(4):427-435.

181. Gardi C, Calzoni P, Ferrali M, Comporti M. Iron mobilization from crocidolite as enhancer of collagen content in rat lung fibroblasts. Biochemical Pharmacology 1997;53(11):1659-1665.

182. Mieszawska AJ, Fourligas N, Georgakoudi I, Ouhib NM, Belton DJ, Perry CC, Kaplan DL. Osteoinductive silk–silica composite biomaterials for bone regeneration. Biomaterials 2010;31(34):8902-8910.

183. Duan W, Ning C, Tang T. Cytocompatibility and osteogenic activity of a novel calcium phosphate silicate bioceramic: Silicocarnotite. Journal of Biomedical Materials Research Part A 2013;101A(7):1955-1961.

184. Qiu X, Wan P, Tan L, Fan X, Yang K. Preliminary research on a novel bioactive silicon doped calcium phosphate coating on AZ31 magnesium alloy via electrodeposition. Materials Science and Engineering: C 2014;36:65-76.

185. Keeting PE, Oursler MJ, Wiegand KE, Bonde SK, Spelsberg TC, Riggs BL. Zeolite a increases proliferation, differentiation, and transforming growth factor β production in normal adult human osteoblast-like cells in vitro. Journal of Bone and Mineral Research 1992;7(11):1281-1289.

186. Byun I-S, Sarkar SK, Jyoti MA, Min Y-K, Seo H-S, Lee B-T, Song H-Y. Initial biocompatibility and enhanced osteoblast response of Si doping in a porous BCP bone graft substitute. Journal of Materials Science-Materials in Medicine 2010;21(6):1937-1947.

187. Moller P, Folkmann JK, Danielsen PH, Jantzen K, Loft S. Oxidative stress generated damage to DNA by gastrointestinal exposure to insoluble particles. Curr Mol Med 2012;12(6):732-45.

188. Vesterdal LK, Danielsen PH, Folkmann JK, Jespersen LF, Aguilar-Pelaez K, Roursgaard M, Loft S, Moller P. Accumulation of lipids and oxidatively damaged DNA in hepatocytes exposed to particles. Toxicol Appl Pharmacol 2014;274(2):350-60.

189. Ferreira JL, Lonne MN, Franca TA, Maximilla NR, Lugokenski TH, Costa PG, Fillmann G, Antunes Soares FA, de la Torre FR, Monserrat JM. Co-exposure of the organic nanomaterial fullerene C(6)(0) with benzo[a]pyrene in Danio rerio (zebrafish) hepatocytes: evidence of toxicological interactions. Aquat Toxicol 2014;147:76-83.

190. Honma M, Takahashi T, Asada S, Nakagawa Y, Ikeda A, Yamakage K. In vitro clastogenicity and phototoxicity of fullerene (C(60)) nanomaterials in mammalian cells. Mutat Res 2012;749(1-2):97-100.

191. Gao J, Wang HL, Shreve A, Iyer R. Fullerene derivatives induce premature senescence: a new toxicity paradigm or novel biomedical applications. Toxicol Appl Pharmacol 2010;244(2):130-43.

192. Rebecca M, Hsing-Lin W, Jun G, Srinivas I, Gabriel MA, Jennifer M, Andrew SP, Yuping B, Chun-Chih W, Zhong C and others. Impact of physicochemical properties of engineered fullerenes on key biological responses. Toxicol Appl Pharmacol 2009;234(1):58-67.

193. Rouse JG, Yang J, Barron AR, Monteiro-Riviere NA. Fullerene-based amino acid nanoparticle interactions with human epidermal keratinocytes. Toxicol In Vitro 2006;20(8):1313-20.

194. Lucafo M, Gerdol M, Pallavicini A, Pacor S, Zorzet S, Da Ros T, Prato M, Sava G. Profiling the molecular mechanism of fullerene cytotoxicity on tumor cells by RNA-seq. Toxicology 2013;314(1):183-92.

195. Johnston HJ, Hutchison GR, Christensen FM, Aschberger K, Stone V. The biological mechanisms and physicochemical characteristics responsible for driving fullerene toxicity. Toxicol Sci 2010;114(2):162-82.

196. Trpkovic A, Todorovic-Markovic B, Trajkovic V. Toxicity of pristine versus functionalized fullerenes: mechanisms of cell damage and the role of oxidative stress. Arch Toxicol 2012;86(12):1809-27.

197. Kepley C, Dellinger A. Study examining fullerene toxicity raises questions as to the purity of the nanomaterials and erroneous experimental conclusions. Toxicological sciences : an official journal of the Society of Toxicology 2014;141(2):326-7.

198. Kim KT, Jang MH, Kim JY, Kim SD. Effect of preparation methods on toxicity of fullerene water suspensions to Japanese medaka embryos. Sci Total Environ 2010;408(22):5606-12.

199. Gharbi N, Pressac M, Hadchouel M, Szwarc H, Wilson SR, Moussa F. [60]fullerene is a powerful antioxidant in vivo with no acute or subacute toxicity. Nano Lett 2005;5(12):2578-85.

200. Huczko A, Lange H, Calko E. Fullerenes: Experimental evidence for a null risk of skin irritation and allergy. Fullerene Science and Technology 1999;7(5):935-939.

201. Nelson MA, Domann FE, Bowden GT, Hooser SB, Fernando Q, Carter DE. Effects of acute and subchronic exposure of topically applied fullerene extracts on the mouse skin. Toxicol Ind Health 1993;9(4):623-30.

202. Sayes CM, Marchione AA, Reed KL, Warheit DB. Comparative pulmonary toxicity assessments of C60 water suspensions in rats: few differences in fullerene toxicity in vivo in contrast to in vitro profiles. Nano Lett 2007;7(8):2399-406.

203. Quick KL, Ali SS, Arch R, Xiong C, Wozniak D, Dugan LL. A carboxyfullerene SOD mimetic improves cognition and extends the lifespan of mice. Neurobiol Aging 2008;29(1):117-28.

204. Baati T, Bourasset F, Gharbi N, Njim L, Abderrabba M, Kerkeni A, Szwarc H, Moussa F. The prolongation of the lifespan of rats by repeated oral administration of [60]fullerene. Biomaterials 2012;33(19):4936-46.

205. Bacakova L, Svorcik V. Cell colonization control by physical and chemical modification of materials. Nova Science Publisher, Inc.; 2009.

206. Bacakova L, Filova E, Parizek M, Ruml T, Svorcik V. Modulation of cell adhesion, proliferation and differentiation on materials designed for body implants. Biotechnology Advances 2011;29(6):739-767.

207. Ko WB, Yun JM, Jo SW, Shon YS. Ultrasonic, chemical stability and preparation of self-assembled fullerene[C60]-gold nanoparticle films. Ultrasonics 2006;44 Suppl 1:e363-6.

208. Joska L, Fojt J, Cvrcek L, Brezina V. Properties of titanium-alloyed DLC layers for medical applications. Biomatter 2014;4.

209. Dwivedi N, Kumar S, Malik HK. Nanostructured titanium/diamond-like carbon multilayer films: deposition, characterization, and applications. ACS Appl Mater Interfaces 2011;3(11):4268-78.

210. Tsai PC, Chiang JY, Hwang YF. Characteristics and mechanical properties of titanium-containing diamond like carbon films deposited by cathodic arc evaporation. J Nanosci Nanotechnol 2008;8(5):2516-21.

211. Popa AC, Stan GE, Husanu MA, Pasuk I, Popescu ID, Popescu AC, Mihailescu IN. Multi-layer haemocompatible diamond-like carbon coatings obtained by combined radio frequency plasma enhanced chemical vapor deposition and magnetron sputtering. J Mater Sci Mater Med 2013;24(12):2695-707.

212. Tan D, Dai MJ, Fu WB, Lin SS, Wei CB, Zhao MC. Performance of CoCrMo alloy with me-doped DLC coatings prepared by a magnetron sputtering method. Rare Metal Materials and Engineering 2015;44(12):2982-2986.

213. Bacakova L, Stary V, Kofronova O, Lisa V. Polishing and coating carbon fiber-reinforced carbon composites with a carbon-titanium layer enhances adhesion and growth of osteoblast-like MG63 cells and vascular smooth muscle cells in vitro. J Biomed Mater Res 2001;54(4):567-78.

214. Grinevich A, Bacakova L, Choukourov A, Boldyryeva H, Pihosh Y, Slavinska D, Noskova L, Skuciova M, Lisa V, Biederman H. Nanocomposite Ti/hydrocarbon plasma polymer films from reactive magnetron sputtering as growth support for osteoblast-like and endothelial cells. J Biomed Mater Res A 2009;88(4):952-66.

215. Madej M, Ozimina D, Kurzydlowski K, Plocinski T, Wiecinski P, Styp-Rekowski M, Matuszewski M. Properties of diamond-like carbon coatings deposited on CoCrMo alloys. Transactions of Famena 2015;39(1):79-88.

216. Liu J, Wang X, Wu BJ, Zhang TF, Leng YX, Huang N. Tribocorrosion behavior of DLC-coated CoCrMo alloy in simulated biological environment. Vacuum 2013;92:39-43.

217. Wei YL, Huang LL, Han LJ, Chen YS. Corrosion resistance and surface biocompatibility of diamond-like carbon coating on AZ31D magnesium alloy. International Journal of Surface Science and Engineering 2016;10(2):101-115.

218. Liu H, Leng Y, Tang J, Wang S, Xie D, Sun H, Huang N. Tribological performance of ultra-high-molecular-weight polyethylene sliding against DLC-coated and nitrogen ion implanted CoCrMo alloy measured in a hip joint simulator. Surface and Coatings Technology 2012;206(23):4907-4914.

219. Allen M, Law F, Rushton N. The effects of diamond-like carbon coatings on macrophages, fibroblasts and osteoblast-like cells in vitro. Clinical Materials 1994;17(1):1-10.

220. Hinuber C, Kleemann C, Friederichs RJ, Haubold L, Scheibe HJ, Schuelke T, Boehlert C, Baumann MJ. Biocompatibility and mechanical properties of diamond-like coatings on cobalt-chromium-molybdenum steel and titanium-aluminum-vanadium biomedical alloys. Journal of Biomedical Materials Research Part A 2010;95A(2):388-400.

221. Mitura E, Mitura S, Niedzielski P, Has Z, Wolowiec R, Jakubowski A, Szmidt J, Sokolowska A, Louda P, Marciniak J and others. Diamond-like carbon coatings for biomedical applications. Diamond and Related Materials 1994;3(4-6):896-898.

222. Benson K, Cramer S, Galla H-J. Impedance-based cell monitoring: barrier properties and beyond. Fluids and barriers of the CNS 2013;10(1):5.

9 Appendix

Materials Science and Engineering C 60 (2016) 230–238

Contents lists available at ScienceDirect

Materials Science and Engineering C

journal homepage: www.elsevier.com/locate/msec

Newly developed Ti–Nb–Zr–Ta–Si–Fe biomedical beta titanium alloys with increased strength and enhanced biocompatibility

Ivana Kopova [a,*], Josef Stráský [b], Petr Harcuba [b], Michal Landa [c], Miloš Janeček [b], Lucie Bačákova [a]

[a] Department of Biomaterials and Tissue Engineering, Institute of Physiology of the Czech Academy of Sciences, Videnska 1083, 14220 Prague 4, , Czech Republic
[b] Department of Physics of Materials, Faculty of Mathematics and Physics, Charles University in Prague, Ke Karlovu 5, 121 16 Prague 2, Czech Republic
[c] Institute of Thermomechanics, Academy of Sciences of the Czech Republic, Dolejskova 5, 182 00 Prague 8, Czech Republic

ARTICLE INFO

Article history:
Received 13 February 2015
Received in revised form 16 August 2015
Accepted 16 November 2015
Available online 17 November 2015

Keywords:
Elastic modulus
Alloy hardening
Cell growth
Osteogenic cell differentiation
Bone implants

ABSTRACT

Beta titanium alloys are promising materials for load-bearing orthopaedic implants due to their excellent corrosion resistance and biocompatibility, low elastic modulus and moderate strength. Metastable beta-Ti alloys can be hardened via precipitation of the alpha phase; however, this has an adverse effect on the elastic modulus. Small amounts of Fe (0–2 wt.%) and Si (0–1 wt.%) were added to Ti–35Nb–7Zr–6Ta (TNZT) biocompatible alloy to increase its strength in beta solution treated condition. Fe and Si additions were shown to cause a significant increase in tensile strength and also in the elastic modulus (from 65 GPa to 85 GPa). However, the elastic modulus of TNZT alloy with Fe and Si additions is still much lower than that of widely used Ti–6Al–4V alloy (115 GPa), and thus closer to that of the bone (10–30 GPa). Si decreases the elongation to failure, whereas Fe increases the uniform elongation thanks to increased work hardening. Primary human osteoblasts cultivated for 21 days on TNZT with 0.5Si + 2Fe (wt.%) reached a significantly higher cell population density and significantly higher collagen I production than cells cultured on the standard Ti–6Al–4V alloy. In conclusion, the Ti–35Nb–7Zr–6Ta–2Fe–0.5Si alloy proves to be the best combination of elastic modulus, strength and also biological properties, which makes it a viable candidate for use in load-bearing implants.

1. Introduction

Titanium alloys have been applied extensively in orthopaedics for several decades due to their superior mechanical properties, excellent corrosion resistance and favourable biocompatibility [1,2]. Numerous studies have reviewed the outstanding properties of these materials for medical use. Excellent biocompatibility of titanium has been proven by many authors, both in vitro and in vivo [3,4]. Commercially pure titanium is used in some orthopaedic and dental applications. However, limited strength (up to 500 MPa) disallows its use as a material for orthopaedic endoprostheses, which constitute most of the market for metallic implants [2].

Although Ti–6Al–4V alloy was developed for the aerospace industry, it is still the workhorse of the orthopaedic implants industry [5]. Despite the generally good properties of this alloy, there are several limitations. Special concern relates to the presence of vanadium, because an increasing number of studies have reported a cytotoxic effect of this element [6,7]. The presence of aluminium has been associated with the induction of neurotoxicity and neurodegenerative diseases reviewed in [8]. Moreover, there is a risk of implant-induced oxidative stress and subsequent inflammatory activation caused by Ti–6Al–4V [9].

Another principal adverse property is its excessively high elastic modulus (around 115 GPa for Ti–6Al–4V alloy), which is much higher than the elastic modulus of cortical bone (10–30 GPa) [10]. The load, which is normally applied to the bone is carried by the stiff implant, and the bone tissue atrophies due to lack of functional stimulation. Consequent osteoporosis results in fractures of the surrounding bone or loosening of the implant. For any of these reasons, the lifetime of an orthopaedic implant made of Ti–6Al–4V alloy is usually limited to 15–20 years [11,12]. At the same time, the excessively low elastic modulus causes large amounts of shear motion between the stem and the bone, leading to the formation of fibrous tissue and to failure [13]. Current interest is therefore focused on metastable β-titanium alloys with increased biocompatibility and a moderate elastic modulus [10].

1.1. Metastable beta-Ti alloys

The first metastable β-Ti alloys were developed in the 1960s [14]. The principal advantages of these alloys are their good response to heat treatment, their enhanced ductility, weldability and high strength [15]. The dominant area of application has been in the aerospace industry [16]. However, in the last two decades, specialized biocompatible

* Corresponding author.
E-mail address: ivana.kopova@biomed.cas.cz (I. Kopova).

http://dx.doi.org/10.1016/j.msec.2015.11.043

alloys have also been developed. The most widely-used alloying elements are vanadium, chromium, iron, molybdenum and niobium. Nb and Zr are regarded as biocompatible alloying elements, whereas V, Cr and Co are considered inappropriate due to their potential cytotoxicity [17].

Metastable beta-Ti alloys after quenching from a temperature above the beta transus (typically around 600–800 °C) do not contain the alpha phase. The major hardening mechanism in metastable β-Ti alloys is the formation of omega and alpha phases by subsequent ageing. Underlying phase transitions including schematic phase diagrams for metastable beta-Ti alloys and effects on mechanical properties are overviewed in [18]. It has been shown experimentally and explained theoretically that the Young's modulus of β-phase is lower than the Young's modulus of the alpha phase or the omega phase [19,20]. Ageing treatment therefore increases the elastic modulus of the alloys. Alternative strengthening mechanisms are solid solution strengthening and precipitation strengthening by small dispersed particles. Both of these mechanisms are utilized and investigated in the present study.

1.2. TNZT alloy

Ti–Nb–Zr–Ta based alloys are known as highly biocompatible materials with favourable mechanical properties. Various types of Ti–Nb–Zr–Ta have been developed. The two most widely used and most widely investigated compositions are Ti–29Nb–13Ta–4.6Zr [12] and Ti–35.3Nb–7.3Zr–5.7Ta (in the following text abbreviated as TNZT). TNZT was developed in the 1990s in the USA and was patented in 1999 [21]. This particular composition was used as a benchmark material for experimental investigations in this study. The TNZT alloy contains only biocompatible elements [11], and consists of beta phase only after quenching from temperatures above the beta transus. In this condition, the elastic modulus is as low as 55 GPa. A considerable disadvantage is the relatively low strength of this alloy of around 550 MPa, depending on oxygen content [22].

The aim of this study is to investigate TNZT alloys as an implant material for hip total endoprostheses, which constitute the majority of market. The strength of basic TNZT alloy in solution treated condition does not exceed 500 MPa and as such cannot be used for hip implant. A relatively low bending strength (e.g. in comparison with Ti–12Cr) of Ti–29Nb–13Ta–4.6Zr limits its application in spinal fixation [23]. In another TNZT alloy, i.e. Ti–35Nb–5.7Ta–7.2Zr, attempts were made to improve its strength by small boron addition and TiB formation. However, the presence of boron decreased the attachment of human osteoblast-like MG-63 cells to the material [24] and also deteriorates its wear resistance of the alloy [25].

The strength can be significantly improved by ageing involving alpha precipitation [26]. However, the elastic modulus is increased to above 100 GPa, which is similar to the modulus of widely-used alpha + beta alloys. The purpose of our study is to employ small Fe and Si additions to strengthen TNZT alloy without increasing the elastic modulus excessively, and to assess the effects of Fe and Si on the biocompatibility of the material.

1.3. Fe and Si additions

The solubility of iron in beta-Ti matrix reaches 22 at.% [27]. Iron acts as a strong beta stabilizer and causes simple solution strengthening in beta alloys due to different electron bonding. However, Si has very low solubility in both the alpha and beta phases and contributes to hardening via the creation of dispersed precipitates Ti_5Si_3 [28]. Moreover, the even more stable $(Ti,Zr)_5Si_3$ compound is formed in alloys containing Zr [28]. An Si content of 0.2–0.4 wt.% is often utilized in high-strength and high-temperature alloys in the aerospace industry to increase the strength and to suppress excessive creep [15,29]. The combined effect of Fe and Si was explored by Lee et al. [30] for the alpha phase only. According to Lee et al., Si increases the strength up to 2 wt.% content, and the most pronounced increase is achieved already for 0.5 wt.% content. On the other hand, Si content in excess of 1 wt.% reduces elongation drastically. Fe additions above 2 wt.% increase the strength substantially. As a result, combined alloying by Fe and Si leads to higher strength levels. Kim et al. [31] studied Ti–(18–28)Nb–(0.5–1.5)Si metastable beta Ti alloys. It is reported that an Si content up to 1 wt.% decreases the elastic modulus to 48 GPa. However, this fact is related to the lower concentration of beta stabilizing elements which leads to the lower stability of the beta phase rather than to an intrinsic effect of Si on the beta phase matrix. To the best of our knowledge, no other authors have yet considered combined additions of Fe and Si to a biomedical beta Ti alloy.

Apart from the mechanical properties, the effect of Fe and Si on the cells and tissues of the living organism must be evaluated. In vivo animal experiments on pure iron stents showed good biocompatibility, with no evidence of local or systemic toxicity or of an inflammatory reaction [32,33]. Similarly, porous silicon microparticles studied as a multistage delivery carrier showed biocompatibility with immune cells, endothelial cells, and erythrocytes [34]. Internalization of these microparticles by endothelial cells did not affect cellular integrity, proliferation, viability, mitosis or the release of pro-inflammatory cytokines [35]. Moreover, in vivo studies demonstrated that acute or subchronic intravenous administration of these silicon microparticles produced no obvious changes in blood chemistry, microscopic histology or immunoreactivity in mice [36,37]. In addition, the combination of Fe and Si in silica–iron phosphate nanocomposites exhibited good biocompatibility, and there was no cytotoxicity or reduced viability of the human mesenchymal stem cells, even if the nanocomposites penetrated the cells [38]. Porous silicon is already clinically used for drug delivery, and also by pSivida Corp as a sustained release device for the treatment of chronic eye disease. Moreover, great biocompatibility of different alloys containing Fe (Fe–Mn, Ti–Zr–Nb–Fe, Ti–Fe–Mo–Mn–Nb–Zr, Au–Fe, Fe–Pd) was reported in numerous studies [39–43]. Alloys with silicon additions (Ti–Zr–Pd–Si–(Nb) and Mg–Si) or Si-coating also show good cell proliferation, viability and biocompatibility [44–47]. However to verify these finding, adhesion, proliferation and potential cytotoxicity as well as differentiation of the cells cultivated on all manufactured TNZT–Si–Fe alloys was performed in this study.

2. Material and experimental procedure

2.1. Manufacturing TNZT alloys

Six different alloys were designed and manufactured. A TNZT alloy with chemical composition 51.7Ti–35.3Nb–7.3Zr–5.7Ta (wt.%) or 68.7Ti–24.2Nb–5.1Zr–2.0Ta (at.%) was used as a benchmark. Six tailored alloys with 0–2 wt.% Fe and 0–1 wt.% Si additions are listed in Table 1.

All alloys were prepared by arc melting of pure elements under low pressure of a clean He atmosphere (350 mbar). Each part of the sample was remelted at least six times by the electric arc to ensure homogeneity. Samples approximately 200 g in weight were homogenized at 1400 °C for two hours and were furnace cooled. Before forging into the shape of rods, the material was heated to approximately 1100 °C; however, the forging temperature was not precisely controlled. This is referred to as the as-forged condition. Some samples were sealed into a quartz tube and a beta solution treated at 1000 °C/2 h, followed by water quenching. This is referred to as the solution treated (ST) condition. The final samples (flat rounded discs, 11 mm in diameter) were

Table 1
Manufactured alloys with different amounts of Fe and Si (wt.%).

Ti–35N–7Zr–5Ta	Ti–35N–7Zr–5Ta–0.5Si–1Fe
Ti–35N–7Zr–5Ta–1Si	Ti–35N–7Zr–5Ta–0.5Si–2Fe
Ti–35N–7Zr–5Ta–2Fe	Ti–35N–7Zr–5Ta–1Si–1Fe

polished by common grinding and polishing techniques using grinding papers and alumina.

2.2. Mechanical and microstructural characterization

Samples for observations by scanning electron microscopy were carefully polished using SiC abrasive papers. Subsequently, a three-step procedure using alumina (0.3 μm and 0.05 μm) and colloidal silica on a vibratory polisher (Buehler–Vibromet) was employed to obtain an optimally clean and flat sample surface.

Extensive SEM observations were performed using the FEI Quanta 200F scanning electron microscope with the FEG cathode at an accelerating voltage of 20 kV, and the EDX analyser. The elastic modulus was measured on samples 3 mm in thickness, using a resonant ultrasound spectroscopic pulse-echo method [48]. For the tensile tests, we employed a computer controlled Instron 5882 machine and a strain rate of 10^{-4} s^{-1}.

2.3. Simulated body fluid (SBF)

To evaluate mineralization of TNZT samples, simulated body fluid experiment following Kokubo's protocol was performed [49]. Samples were incubated for 14 days in Hank's Balanced Salt Solution (Life technologies, Cat. No. 14,025,092) at 37 °C in a humidified air atmosphere containing 5% of CO_2. The samples were subsequently analysed by SEM and TF-XRD.

2.4. Cells and culture conditions

TNZT alloys with various Fe and Si additions, and also the benchmark Ti–6Al–4V alloy, were sterilized by autoclaving and were inserted into polystyrene 24-well tissue culture plates (TPP, well diameter 15.4 mm). For the initial experiments (to evaluate cell adhesion and proliferation), sterile samples were seeded with human osteoblast-like U-2 OS cells (ATCC-LGC, Cat. No HTB-96) with an initial density of about 6000 cells/cm^2 and were cultured for 7 days in 1 mL of Dulbecco's Modified Eagle's Medium (D-MEM; Sigma, Cat. No D5648) supplemented with 10% fetal bovine serum (Sebak GmbH,) and gentamicin (40 μg/mL; LEK,). For differentiation experiments, human primary osteoblasts (HOB-p; PromoCell, Cat. No C12760) in an initial density of about 9000 cells/cm^2 were seeded on samples and were grown in the osteoblast growth medium (PromoCell, Cat. No C 27001) to cell confluence. After confluence was reached, the cells were differentiated for 14 days in the osteoblast growth medium with additives promoting osteogenic differentiation: 10 mM β-glycerolphosphate, 2 mM L-glutamin, 1 μM 1,α25dihydroxyvitamin D_3, 100 nM dexamethasone, 280 μM L-ascorbic acid (all purchased from Sigma). Both cell types were cultivated at 37 °C in a humidified air atmosphere containing 5% of CO_2. The SSM1 Mini Orbital Shaker (circular motion with an orbit of 16 mm; Stuart) was used for cultivation under dynamic conditions. The seeding speed was set to 40 rpm for the first 24 h, followed by 90 rpm for the rest of the cultivation. A polystyrene culture dish and Ti–6Al–4V alloy were used as reference materials. Three samples were analysed for each experimental group and time interval.

2.5. Cell adhesion

After 3 and 7 days of cultivation, all samples seeded with U-2 OS cells were vigorously shaken in 0.5 mL of a four times more concentrated trypsin-EDTA solution (2 g porcine trypsin and 0.8 g EDTA per litter of saline; Sigma) for 15 min at 37 °C on the SSM1 Mini Orbital Shaker. The detached cells were washed away with phosphate-buffered saline (PBS; Sigma). The samples with cells, which remained attached to the samples, were fixed with 4% paraformaldehyde (PFA; Sigma) for 20 min, followed by permeabilization with 0.1% Triton X-100 in PBS (Sigma) for 20 min and incubation in propidium iodide (5 μg/mL; Sigma) for 5 min at room temperature (RT). The stained cells were photographed using an Olympus IX-71 epifluorescence microscope equipped with a DP-71 digital camera.

2.6. Evaluation of proliferation and potential cytotoxicity (XTT assay)

The commercial II XTT Cell Proliferation Kit (Roche, Cat. No 11 465 015 001) was used to investigate the proliferation of human osteoblast-like U-2 OS cells. After 3 and 7 days of cultivation, a 1 mL solution of XTT and D-MEM without phenol red (Gibco, Cat. No 11053-028) supplemented with 10% fetal bovine serum (Sebak GmbH) and gentamicin (40 μg/mL; LEK) in the ratio of 1 portion of XTT to 2 portions of D-MEM (according the manufacturer's protocol) were added to each sample. After 4–6 h of incubation at 37 °C, the absorbance of the resulting solution was measured at a wavelength of 470 nm. Solutions from alloys or a polystyrene culture dish without seeded cells were used as the blank samples. Three parallel samples were used for each experimental group and time interval.

2.7. Differentiation study: evaluation of cell number and collagen I staining

After 14 days of differentiation (induced after reaching the confluence of human primary osteoblasts HOB-p), all samples were fixed in 4% PFA (Sigma) for 20 min at RT. Subsequently, the cells were permeabilized with 0.1% Triton X-100 in PBS (Sigma) for 20 min at RT. Primary antibody anti-collagen type I (2.5 μg/mL; Sigma), followed by secondary antibody coupled to Alexa Fluor 488 (4 μg/mL; Invitrogen) for 1 h at RT were used. The nuclei were visualized by DAPI (1 μg/mL; Sigma). To determine the cell numbers, the cell nuclei were counted on the microphotographs that were obtained. For each experimental group, three samples were used, and from each sample, 10 randomly taken microphotographs (homogeneously distributed on the surface of the sample) were evaluated.

2.8. Statistical analysis

The quantitative data were presented as the mean ± S.E.M. (Standard Error of the Mean). Three samples for each experimental group and time interval were evaluated. A comparison between the groups was analysed with the ANOVA, Student–Newman–Keuls method. p-Values equal to or less than 0.05 were considered statistically significant.

3. Results

3.1. SEM observations

Fig. 1a–f shows SEM micrographs of the microstructure of all prepared alloys in as-forged condition. The channelling contrast makes it possible to distinguish between individual grains, thanks to their different crystallographic orientation. The microstructure of the alloys without an Si content (Fig. 1a and c) is very coarse, with grain sizes >100 μm. The iron content has no observable effect on the grain size. However, Si serves as a grain growth inhibitor. The grain size decreases with increasing Si content (compare Fig. 1d and e with Fig. 1b and f). Small black dots in Fig. 1b, d, e and f are silicide intermetallic precipitates and are depicted in greater detail in Fig. 2. Energy dispersive X-ray spectroscopy (EDS) measurements summarized in Table 2 proved that particles observed in Fig. 2 are indeed silicide particles, which are additionally enriched by zirconium. Note that EDS results should be taken only qualitatively. Two types of silicide particles are present in the material. Bigger particles (2–3 μm) are usually formed along grain boundaries that serve as preferential nucleation sites, whereas smaller particles (~1 μm) are distributed more homogeneously.

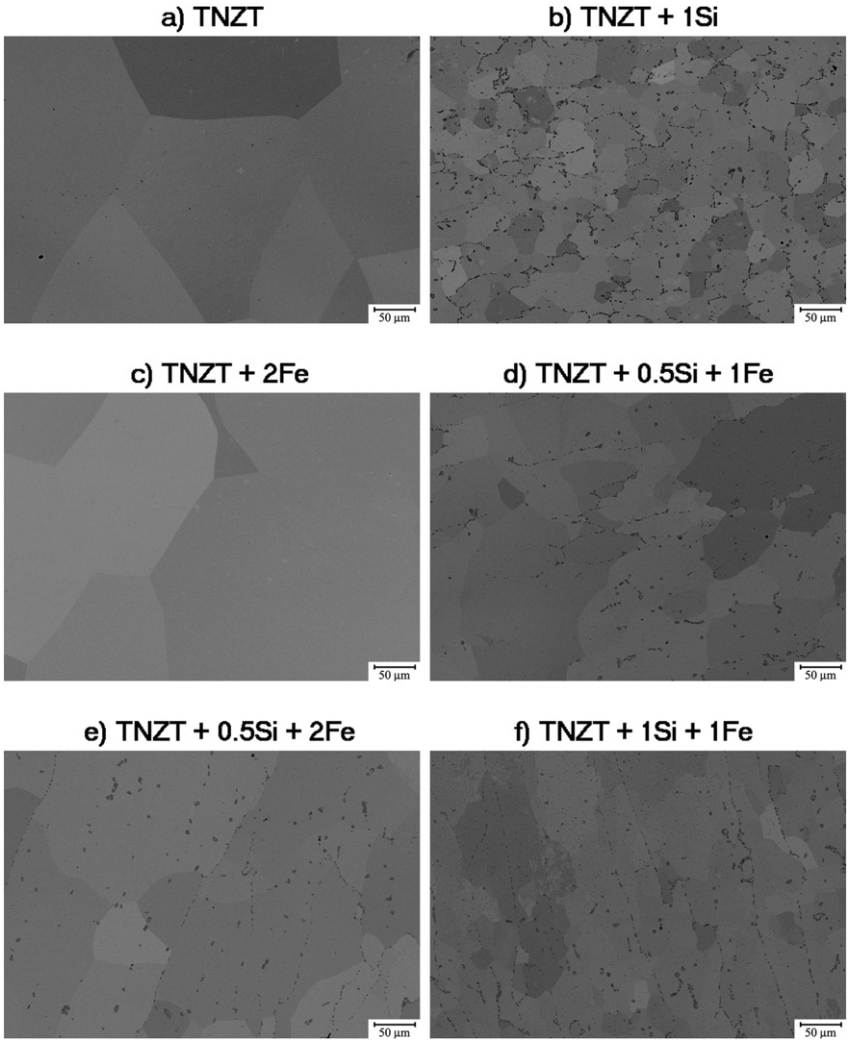

Fig. 1. SEM micrographs of TNZT alloys in as-forged condition (channelling contrast).

3.2. Mechanical properties

The elastic modulus of all alloys was measured by a pulse-echo method for both as-forged and solution treated (ST) conditions. The results of the measurements are summarized in Fig. 3. The elastic modulus of the benchmark TNZT alloy is around 65 GPa, which is in accordance with the literature [21]. The elastic modulus increases with increasing Fe and Si content. The highest elastic modulus is observed for TNZT + 0.5Si + 2Fe alloy. However, the value of 85 GPa is still significantly lower than the value for the widely-used Ti–6Al–4V alloy. Fig. 4 shows the yield stress and the ultimate tensile strength (UTS) of the studied alloys (as-forged condition) determined from the flow curves. The values presented here are the averages from three samples, and the standard deviation is shown by the error bar. The yield stress of the benchmark TNZT alloy is below 500 MPa. Both Fe and Si increase the yield stress and UTS and, moreover, the combined effect of Fe and Si leads to an even higher strength level. TNZT + 0.5Si + 2Fe alloy yields above 700 MPa, and its ultimate strength is higher than 800 MPa. These are relatively high values, considering that the alloy is not hardened by ageing treatment.

Fig. 5a summarizes the total plastic elongation measured after fracture (as-forged condition). All the alloys are ductile at room temperature, but Si significantly reduces the total elongation. Fe content

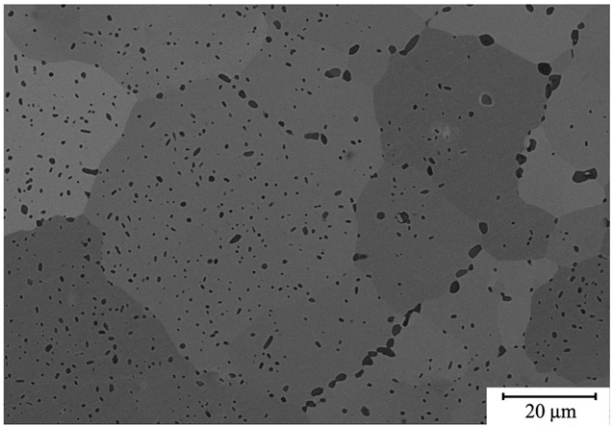

Fig. 2. SEM image of silicides of the TNZT + 1Si alloy.

Table 2
Chemical composition of TNZT + 1Si alloy and composition of silicide particles determined by EDS (qualitative results).

wt.%	Matrix	Particle #1	Particle #2
Ti	46.4	24.8	33.5
Nb	40	11.8	16.7
Zr	7.1	45.7	34.8
Ta	5.5	1.8	3.0
Si	1.0	15.9	12.0

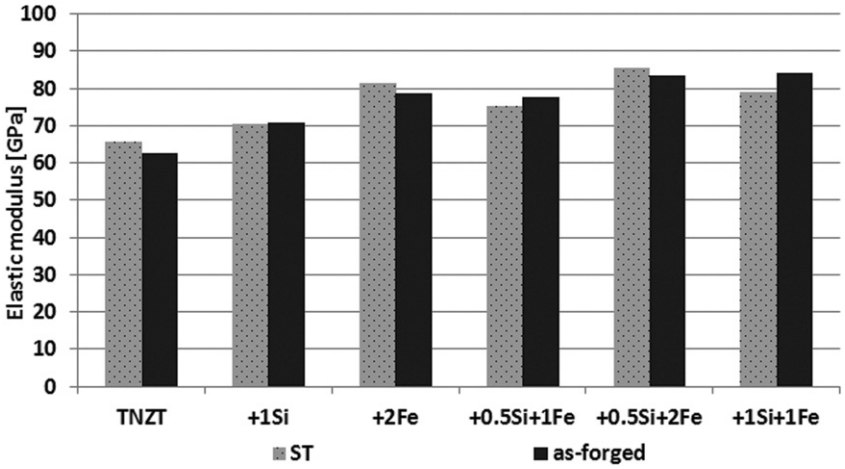

Fig. 3. Elastic modulus measurements of TNZT alloys (solution treated and as-forged condition).

surprisingly increased the total elongation when compared to the benchmark alloy. Flow curves in Fig. 5b show that Fe contrary to Si is responsible for work hardening, which avoids premature necking and therefore increases the overall ductility.

3.3. Cell adhesion

The initial biological experiments showed that human U-2 OS osteoblast-like cells adhered well on all evaluated alloys. Interestingly, stronger adhesion and higher resistance of cells to the detachment by a trypsin-EDTA solution was observed on TNZT alloys (especially on the benchmark TNZT and on TNZT with the addition of 1Si, 2Fe or 0.5Si + 1Fe) than on reference materials, such as Ti–6Al–4V alloy and a polystyrene culture dish (Fig. 6).

3.4. Cell proliferation

In order to investigate the proliferation of human osteoblast-like cells on different alloys, the XXT assay was used to measure the activity of mitochondrial enzymes. This activity is considered to be proportional to the cell number; the XXT assay is therefore often used for evaluating cell proliferation. U-2 OS cells were cultivated for seven days under static or dynamic conditions. The metabolic activity of the cells grown on all tested TNZT alloys under static conditions was comparable to the activity on the reference polystyrene culture dish, and was significantly higher than the metabolic activity of cells cultured on the reference Ti–6Al–4V alloy (Fig. 7 a). These significant differences were not observed on cells cultivated under dynamic conditions, where the metabolic activity of cells cultured on all tested samples was similar (Fig. 7b).

3.5. Cell differentiation study: cell number and collagen I production

The counting of primary human osteoblast HOB-p cells on day 21 after seeding within the cell differentiation study showed significantly higher population densities of HOB-p grown on TNZT with the addition of 2Fe and 0.5Si + 2Fe (wt.%) than on the standard Ti–6Al–4V alloy (Fig. 8). Production of collagen I was used as a marker of the osteogenic differentiation of the cells. Higher collagen I production was observed in cells cultured on TNZT with the addition of 2Fe, 0.5Si + 1Fe and 0.5Si + 2Fe (wt.%) than on the reference polystyrene culture dish. Moreover, TNZT with 0.5Si + 2Fe additions promoted better differentiation of HOB-p cells (evaluated by collagen I production) than the standard Ti–6Al–4V alloy (Fig. 9).

4. Discussion

It follows from the SEM results (Figs. 1 and 2) that Si serves as a grain growth inhibitor. Grain growth suppression during annealing is caused by underpinning the grain boundaries by silicide intermetallic particles. It is known that the composition of intermetallic silicides in zirconium-containing Ti alloys is $(Ti,Zr)_5Si_3$ [28]. EDS analysis summarized in

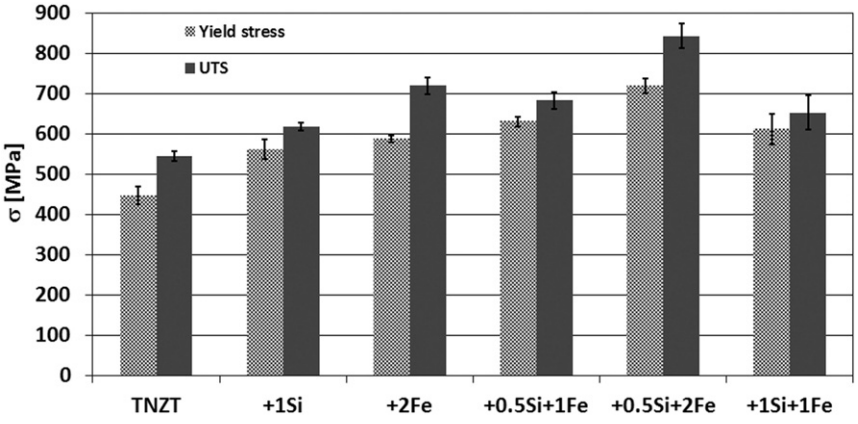

Fig. 4. Yield stress and ultimate tensile strength (UTS) of TNZT alloys (as-forged condition).

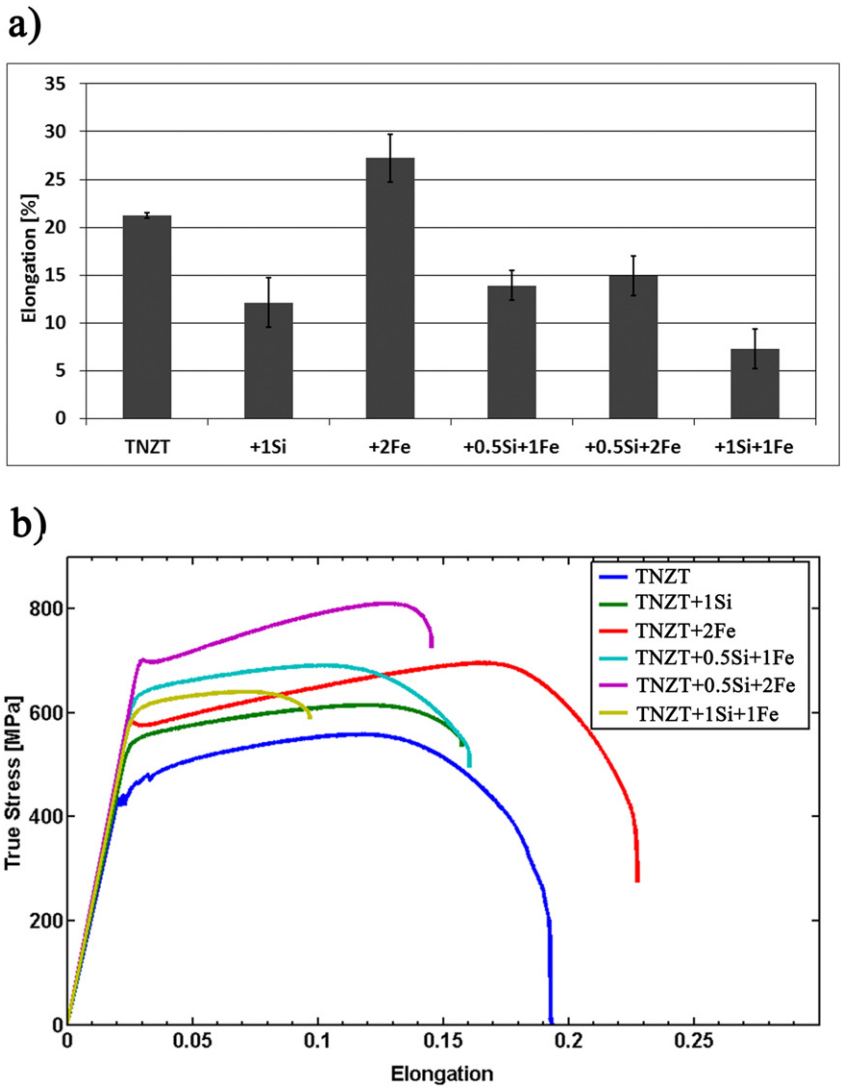

Fig. 5. Total elongation (A5 elongation) (a) and true strain curves (b) of TNZT alloys (as-forged condition).

Table 2 proved that these precipitates are obviously Si enriched and also strongly Zr enriched, which confirms that Zr is preferred for the formation of silicide particles. However, it is impossible to determine the exact chemical composition of these tiny particles by EDS. It has been argued that these particles are also responsible for the increased elastic modulus of Si containing alloys. In addition, these incoherent homogeneously distributed fine particles cause significant precipitation strengthening, as described by the Orowan mechanism [50].

An Fe content of 2 wt.% significantly increased both the elastic modulus and the ultimate strength of the material. The effect on the elastic modulus is related to the strong beta stabilization effect of iron. Two recent approaches relate the e/a ratio and the position in the so-called Bo-Md diagram to the elastic modulus of metastable beta Ti alloys in as-quenched condition [51,52]. The electron per atom ratio, the bonding-order (Bo) and the metal d-orbital energy (Md) values can be calculated simply, and are shown in Table 3 for the benchmark TNZT alloy and TNZT + 2Fe alloy (the effect of the Si additions on the e/a, Bo and Md values is negligible). Fe increases the average electron per atom ratio (e/a ratio) in the alloy, which is associated with an increased elastic modulus [53,54]. Similarly, the beta stabilization effect of Fe decreases the Md value and increases the elastic modulus. This is in excellent agreement with a study by Laheurte et al. [55].

Fe addition also increased the plastic elongation of the material at room temperature, as shown in Fig. 5a. This surprising effect is associated with work-hardening occurring during the tensile test, which is apparent from the flow curves (Fig. 5 b) and also from the difference between the yield stress and the UTS for the TNZT + 2Fe alloy (Fig. 4). More pronounced work-hardening avoids premature necking and increases the uniform elongation. It is argued that Fe atoms (or their clusters) cause dislocation pinning and consequent dislocation multiplication during straining resulting in work hardening. This also explains the sharp yield point observed for alloys containing 2 wt.% of Fe. The dislocation created during hot-working might be pinned in the atmosphere (clusters) of Fe atoms and the macroscopic stress decreases once dislocations are released from Fe atmosphere during yielding.

The biological experiments proved that all TNZT alloys are biocompatible and promote stronger adhesion as well as higher proliferation of U-2 OS cells cultured under static conditions than the standard Ti–6Al–4V alloy. These observations are in accordance with another study comparing a similar TNZT alloy with Ti–6Al–4V alloy, where a higher proliferation of MG-63 cells cultured on Ti–35Nb–3Zr–2Ta was observed [56]. Similarly, higher viability of L-929 cells (proven by MTT assay) when incubated in a solution extracted from Ti–29Nb–13Ta–4.6Zr rather than in a Ti–6Al–4V extract has been reported [57]. The lack of differences in proliferation under dynamic conditions could be explained by the mechanical forces on the cells, and also by better diffusion of oxygen and nutrients associated with circulation of the culture

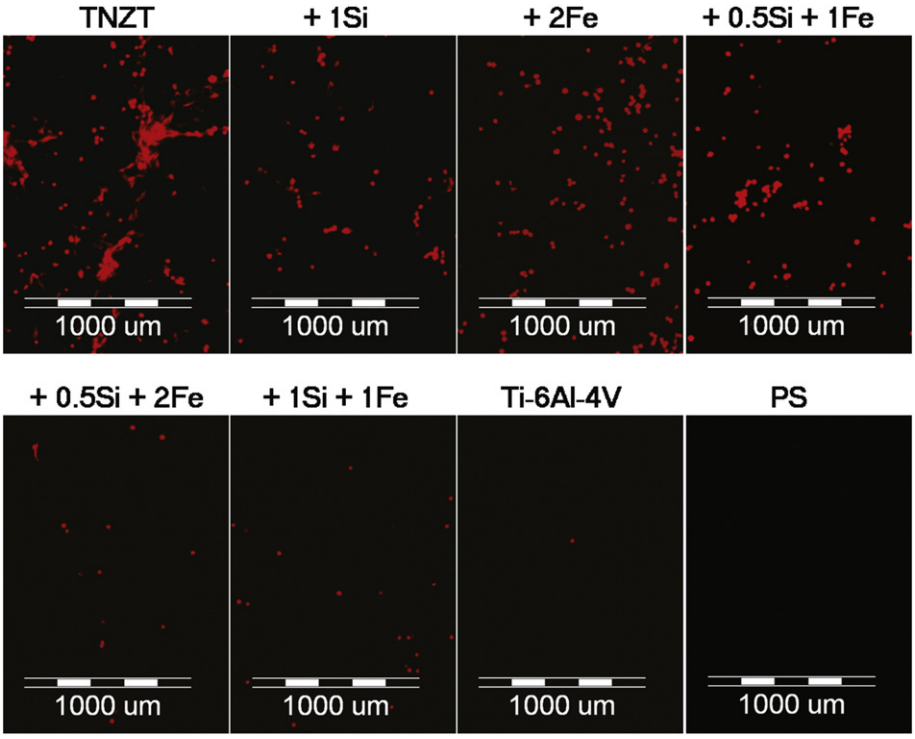

Fig. 6. Adhesion and higher resistance of human U-2 OS osteoblast-like cells to detachment by a four times more concentrated trypsin-EDTA solution from the evaluated materials. Attached cells visualized by propidium iodide. PS — polystyrene culture dish, reference material.

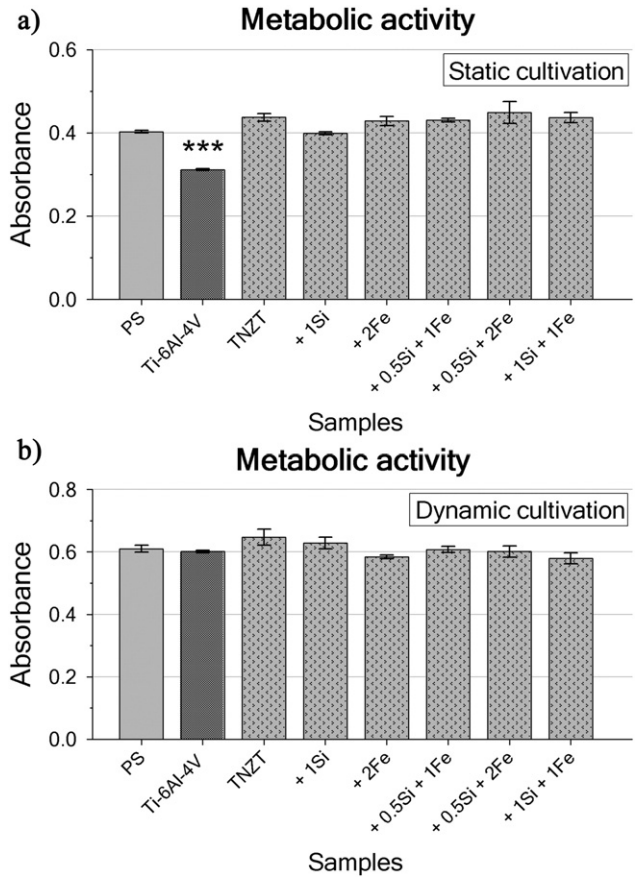

Fig. 7. Metabolic activity measured per culture of human osteoblast-like U-2 OS cells on day seven after seeding cultivated under static (a) and dynamic (b) conditions. PS — polystyrene culture dish, reference material. ***Significant difference from all samples, $p \leq 0.001$.

medium, which are known to enhance cell proliferation [58]. Dynamic cultivation is an approach that better mimics the in vivo environment and therefore promotes the formation of extracellular matrix. This facilitates cell adhesion in the first week of dynamic cultivation [59]. This facilitation may have diminished the effect of the materials on the cells, and may have led to better proliferation of cells cultured on the Ti–6Al–4V alloy.

Our experiments performed on primary human osteoblast (HOB-p) revealed a beneficial effect of Si and Fe additions (especially 0.5Si + 2Fe) to the TNZT alloy on the proliferation and differentiation of these cells. Similarly, in human hFOB1.19 osteoblasts, moderate concentrations of iron in the cell culture media (adjusted with 5 μmol/L of deferoxamine) promoted the proliferation and osteogenic differentiation, manifested by the activity of alkaline phosphatase, expression of collagen I and osteocalcin as well as matrix mineralization. However,

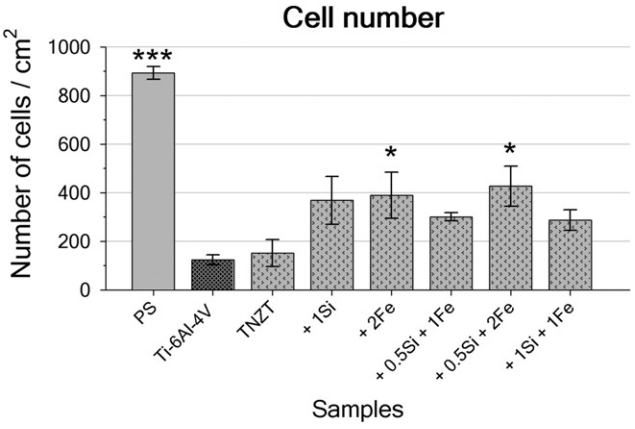

Fig. 8. The number of primary human osteoblast cells (HOB-p) on day 21 after seeding (14 days of differentiation) obtained by counting the cell nuclei. PS — polystyrene culture dish, reference material. ***Significant difference from all samples, $p \leq 0.001$. *Significant difference from Ti–6Al–4V, $p \leq 0.05$.

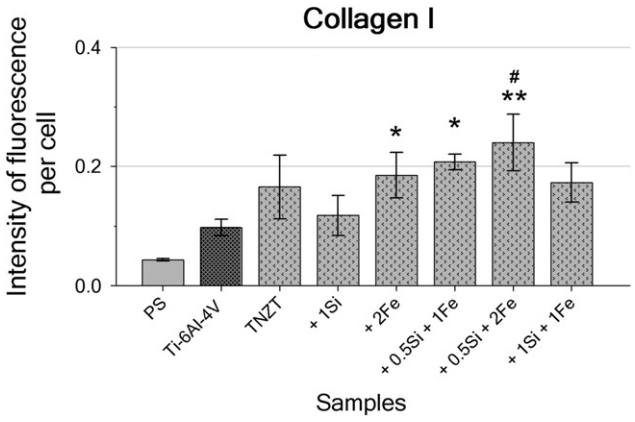

Fig. 9. The amount of collagen I produced by primary human osteoblast cells (HOB-p) after 21 days of cultivation (14 days of differentiation). PS — polystyrene culture dish, reference material. **Significant difference from PS, $p \leq 0.01$. *Significant difference to PS, $p \leq 0.05$. #Significant difference from Ti–6Al–4 V, $p \leq 0.05$.

very low concentrations (at 10–20 μmol/L deferoxamine) or high concentrations of iron (adjusted by 50–200 μmol/L of ferric ammonium citrate) inhibited the growth and differentiation of osteoblasts [60]. Iron also stimulated proliferation and collagen synthesis in other cell types, namely rat lung fibroblasts [61], tracheal cells [62] and rat hepatic stellate cells [63]. As in the case of silicon, Si-containing calcium phosphate [64,65] and silicatein/biosilica substrates [66,67] increased the proliferation of human osteoblast-like MG-63 and Saos-2 cells and rat bone marrow stromal cells, which can be explained e.g. by the increased expression of transforming growth factor beta 1 (TGF-β_1), a potent mitogen for osteoblasts [68]. At the same time, Si-containing materials, such as calcium phosphates, zeolite A, silk–silica composites or silicatein/biosilica matrix, stimulated the expression and synthesis of collagen [66,69] and other markers of osteogenic cell differentiation, such as alkaline phosphatase [65,68], Runx-2, osteopontin, bone sialoprotein, osteocalcin [64,66] and bone morphogenetic protein 2 (BMP-2), an inducer of bone formation [67].

To evaluate potential mineralization of TNZT alloys, in-vitro bioactivity study in simulated body fluid was performed (results not shown). The samples after 14 days of immersion in Hank's Balanced Salt Solution were analysed by scanning electron microscopy (SEM) and Thin Film X-ray diffraction (TF-XRD). All investigated titanium (TNZT) alloys behaved as biologically inert material and no remnants from immersion in SFB were observed.

Unlike the hydroxyapatite scaffolds (intended for degradable implants, which are supposed to be replaced by formation of new bone), where the bioactivity and mineralization is necessary requirement, our TNZT alloys were designed for long-term implantation. In these biostable implants, no extensive mineralization in order to replace the degraded materials is needed. In long-term implantation the great biocompatibility and support of the alloy for cell adhesion and differentiation is more important. It is well known (and our differentiation study also confirmed), that differentiated cells are capable of producing and releasing extracellular matrix components. As mentioned above, the osteoblasts growing on TNZT alloys doped with Si and/or Fe produced more collagen I, which contains binding sites for calcium and phosphate ions, i.e. carboxyl, hydroxyl and amine functional groups. These groups then serve as nucleation sites for formation of hydroxyapatite, and thus for the bone matrix mineralization [70,71].

Table 3
e/a, Bo and Md values computed for benchmark TNZT alloy and TNZT + 2Fe alloy.

Alloy	e/a	Bo	Md
TNZT	4.26	2.887	2.468
TNZT + 2Fe	4.36	2.884	2.434

5. Conclusion

The effect of Fe and Si on the mechanical properties and the biocompatibility of Ti–35Nb–7Zr–6Ta alloy has been evaluated and discussed. All alloys that were developed showed an elastic modulus lower than that of the widely-used Ti–6Al–4V alloy, and a positive effect of Fe and Si on the strength of the alloys was demonstrated.

The newly-developed alloys also displayed superior biocompatibility to that of the widely-used Ti–6Al–4V alloy. The alloy with composition Ti–35Nb–7Zr–6Ta–2Fe–0.5Si provided the best combination of mechanical and biological properties, which makes it a viable candidate for biomedical use in load-bearing bone implants.

Acknowledgements

Financial support from the Czech Science Foundation under grant P107/12/1025 is gratefully acknowledged. We also thank Mr. Robin Healey (Czech Technical University, Prague) for his language revision of the manuscript.

References

[1] M. Geetha, A.K. Singh, R. Asokamani, A.K. Gogia, Ti based biomaterials, the ultimate choice for orthopaedic implants — a review, Prog. Mater. Sci. 54 (2009) 397–425.
[2] M. Long, H.J. Rack, Titanium alloys in total joint replacement — a materials science perspective, Biomaterials 19 (1998) 1621–1639.
[3] Y. Okazaki, E. Gotoh, Comparison of metal release from various metallic biomaterials in vitro, Biomaterials 26 (2005) 11–21.
[4] S. Rao, Y. Okazaki, T. Tateishi, T. Ushida, Y. Ito, Cytocompatibility of new Ti alloy without Al and V by evaluating the relative growth ratios of fibroblasts L929 and osteoblasts MC3T3-E1 cells, Mater. Sci. Eng. C 4 (1997) 311–314.
[5] K.S. Katti, Biomaterials in total joint replacement, Colloids Surf. B 39 (2004) 133–142.
[6] G.C. McKay, R. Macnair, C. MacDonald, M.H. Grant, Interactions of orthopaedic metals with an immortalized rat osteoblast cell line, Biomaterials 17 (1996) 1339–1344.
[7] J.L. Domingo, Vanadium: a review of the reproductive and developmental toxicity, Reprod. Toxicol. 10 (1996) 175–182.
[8] S.C. Bondy, The neurotoxicity of environmental aluminum is still an issue, Neurotoxicology 31 (2010) 575–581.
[9] R. Tsaryk, K. Peters, S. Barth, R.E. Unger, D. Scharnweber, C.J. Kirkpatrick, The role of oxidative stress in pro-inflammatory activation of human endothelial cells on Ti6Al4V alloy, Biomaterials 34 (2013) 8075–8085.
[10] M. Niinomi, M. Nakai, J. Hieda, Development of new metallic alloys for biomedical applications, Acta Biomater. 8 (2012) 3888–3903.
[11] M. Abdel-Hady Gepreel, M. Niiomi, Biocompatibility of Ti-alloys for long-term implantation, J. Mech. Behav. Biomed. Mater. 20 (2013) 407–415.
[12] D. Kuroda, M. Niinomi, M. Morinaga, Y. Kato, T. Yashiro, Design and mechanical properties of new β type titanium alloys for implant materials, Mater. Sci. Eng. A 243 (1998) 244–249.
[13] M. Niinomi, Mechanical biocompatibilities of titanium alloys for biomedical applications, J. Mech. Behav. Biomed. Mater. 1 (2008) 30–42.
[14] G. Lütjering, J.C. Williams, Titanium, Springer, 2007.
[15] G. Welsch, R. Boyer, E.W. Collings, Materials Properties Handbook: Titanium Alloys, ASM International, 1993.
[16] C. Leyens, M. Peters (Eds.), Titanium and Titanium Alloys, Wiley-VCH Verlag GmbH & Co. KGaA, 2003.
[17] S.G. Steinemann, Titanium — the material of choice? Periodontol. 17 (1998) 7–21.
[18] I. Weiss, S.L. Semiatin, Thermomechanical processing of beta titanium alloys—an overview, Mater. Sci. Eng. A 243 (1998) 46–65.
[19] J. Sun, Q. Yao, H. Xing, W.Y. Guo, Elastic properties of β, α″ and ω metastable phases in Ti–Nb alloy from first-principles, J. Phys. Condens. Matter 19 (2007) 486215.
[20] J. Zhao, H. Duan, H. Li, Microstructure and mechanical properties of biomedical Ti–27Nb–8Zr alloy with low elastic modulus, Rare Metal Mater. Eng. 39 (2010) 1707–1710.
[21] Ahmed T, Rack, HJ Low modulus biocompatible titanium base alloys for medical devices. United States Patent, 5,871,595, 1999.
[22] J.I. Qazi, B. Marquardt, L.F. Allard, H.J. Rack, Phase transformation in Ti–35Nb–7Zr–5Ta–(0.06–0.68)O alloys, Mater. Sci. Eng. 25 (2005) 389–397.
[23] H. Liu, M. Niinomi, M. Nakai, J. Hieda, K. Cho, Bending springback behavior related to deformation-induced phase transformations in Ti–12Cr and Ti–29Nb–13Ta–4.6Zr alloys for spinal fixation applications, J. Mech. Behav. Biomed. Mater. 34 (2014) 66–74.
[24] P. Majumdar, S.B. Singh, S. Dhara, M. Chakraborty, Influence of in situ TiB reinforcements and role of heat treatment on mechanical properties and biocompatibility of β Ti-alloys, J. Mech. Behav. Biomed. Mater. 10 (2012) 1–12.
[25] P. Majumdar, S.B. Singh, M. Chakraborty, The influence of heat treatment and role of boron on sliding wear behaviour of β-type Ti–35Nb–7.2Zr–5.7Ta alloy in dry condition and in simulated body fluids, J. Mech. Behav. Biomed. Mater. 4 (2011) 284–297.

[26] J.I. Qazi, H.J. Rack, B. Marguardt, High-strength metastable beta-titanium alloys for biomedical applications, JOM 11 (2004) 49–51.
[27] J. Matyka, F. Faudot, J. Bigot, Study of iron solubility in α titanium, Scr. Metall. 13 (1979) 645–648.
[28] S. Ankem, D. Banerjee, D.J. McNeish, J.C. Williams, S.R. Seagle, Silicide formation in Ti–3Al–8V–6Cr–4Zr–4Mo, Metall. Trans. A 18 (1987) 2015–2025.
[29] K. Chaudhuri, J.H. Perepezko, Microstructural study of the titanium alloy Ti–15Mo–2.7Nb–3Al–0.2Si (TIMETAL 21S), Metall. Mater. Trans. A 25 (1994) 1109–1118.
[30] D.B. Lee, K.B. Park, H.W. Jeong, S.E. Kim, Mechanical and oxidation properties of Ti–xFe–ySi alloys, Mater. Sci. Eng. 328 (2002) 161–168.
[31] H.S. Kim, W.Y. Kim, S.H. Lim, Microstructure and elastic modulus of Ti–Nb–Si ternary alloys for biomedical applications, Scr. Mater. 54 (2006) 887–891.
[32] M. Peuster, C. Hesse, T. Schloo, C. Fink, P. Beerbaum, C. von Schnakenburg, Long-term biocompatibility of a corrodible peripheral iron stent in the porcine descending aorta, Biomaterials 27 (2006) 4955–4962.
[33] R. Waksman, R. Pakala, R. Baffour, R. Seabron, D. Hellinga, F.O. Tio, Short-term effects of biocorrodible iron stents in porcine coronary arteries, J. Interv. Cardiol. 21 (2008) 15–20.
[34] B. Godin, J. Gu, R.E. Serda, S. Ferrati, X. Liu, C. Chiappini, T. Tanaka, P. Decuzzi, M. Ferrari, Multistage mesoporous silicon-based nanocarriers: biocompatibility with immune cells and controlled degradation in physiological fluids, Controll. Release Newsl. 25 (2008) 9–11.
[35] R.E. Serda, S. Ferrati, B. Godin, E. Tasciotti, X. Liu, M. Ferrari, Mitotic trafficking of silicon microparticles, Nanoscale 1 (2009) 250–259.
[36] Q. He, Z. Zhang, F. Gao, Y. Li, J. Shi, In vivo biodistribution and urinary excretion of mesoporous silica nanoparticles: effects of particle size and PEGylation, Small 7 (2011) 271–280.
[37] T. Tanaka, B. Godin, R. Bhavane, R. Nieves-Alicea, J. Gu, X. Liu, C. Chiappini, J.R. Fakhoury, S. Amra, A. Ewing, Q. Li, I.J. Fidler, M. Ferrari, In vivo evaluation of safety of nanoporous silicon carriers following single and multiple dose intravenous administrations in mice, Int. J. Pharm. 402 (2010) 190–197.
[38] J. Athinarayanan, V.S. Periasamy, A.A. Alshatwi, Biogenic silica–metal phosphate (metal = Ca, Fe or Zn) nanocomposites: fabrication from rice husk and their biomedical applications, J. Mater. Sci. Mater. Med. 25 (2014) 1637–1644.
[39] A. Drynda, T. Hassel, F.W. Bach, M. Peuster, In vitro and in vivo corrosion properties of new iron–manganese alloys designed for cardiovascular applications, J. Biomed. Mater. Res. B Appl. Biomater. 103 (3) (2015) 649–660.
[40] P. Xue, Y. Li, K. Li, D. Zhang, C. Zhou, Superelasticity, corrosion resistance and biocompatibility of the Ti–19Zr–10Nb–1Fe alloy, Mater. Sci. Eng. C 50 (2015) 179–186.
[41] S.R. Yu, X.P. Zhang, Z.M. He, Y.H. Liu, Z.H. Liu, Effects of Ce on the short-term biocompatibility of Ti–Fe–Mo–Mn–Nb–Zr alloy for dental materials, J. Mater. Sci. Mater. Med. 15 (6) (2004) 687–691.
[42] V. Amendola, S. Scaramuzza, L. Litti, M. Meneghetti, G. Zuccolotto, A. Rosato, E. Nicolato, P. Marzola, G. Fracasso, C. Anselmi, M. Pinto, M. Colombatti, Magneto-plasmonic Au–Fe alloy nanoparticles designed for multimodal SERS-MRI-CT imaging, Small 10 (12) (2014) 2476–2486.
[43] U. Allenstein, Y. Ma, A. Arabi-Hashemi, M. Zink, S.G. Mayr, Fe–Pd based ferromagnetic shape memory actuators for medical applications: biocompatibility, effect of surface roughness and protein coatings, Acta Biomater. 9 (3) (2013) 5845–5853.
[44] A. Hynowska, A. Blanquer, E. Pellicer, J. Fornell, S. Suriñach, M.D. Baró, A. Gebert, M. Calin, J. Eckert, C. Nogués, E. Ibáñez, L. Barrios, J. Sort, Nanostructured Ti–Zr–Pd–Si–(Nb) bulk metallic composites: novel biocompatible materials with superior mechanical strength and elastic recovery, J. Biomed. Mater. Res. B Appl. Biomater. (2014).
[45] X. Gu, Y. Zheng, Y. Cheng, S. Zhong, T. Xi, In vitro corrosion and biocompatibility of binary magnesium alloys, Biomaterials 30 (4) (2009) 484–498.
[46] Y. Xin, J. Jiang, K. Huo, G. Tang, X. Tian, P.K. Chu, Corrosion resistance and cytocompatibility of biodegradable surgical magnesium alloy coated with hydrogenated amorphous silicon, J. Biomed. Mater. Res. A. 89 (3) (2009) 717–726.
[47] M.A. Arenas, E. Frutos, L. Saldaña, A. Conde, L. Labajos-Broncano, M.L. González-Martín, J.L. González-Carrasco, N. Vilaboa, Corrosion behaviour and biocompatibility of a novel Ni-free intermetallic coating growth on austenitic steel by hot dipping in an Al–12.6%Si alloy, J. Mater. Sci. Mater. Med. 22 (4) (2011) 1005–1014.
[48] M. Landa, J. Plesek, Contrast enhancement of ultrasonic imaging of internal stresses in materials, Ultrasonics 40 (2002) 531–535.
[49] T. Kokubo, H. Takadama, How useful is SBF in predicting in vivo bone bioactivity? Biomaterials 27 (2005) 2907–2915.
[50] E. Orowan, Zur Kristallplastizität, Z. Phys. 89 (1934) 605–659.
[51] M. Morinaga, M. Kato, T. Kamimura, M. Fukumoto, I. Farada, K. Kubo, Theoretical design of β-type titanium alloys, Titanium 1992, Science and Technology, Proc. 7th Int. Conf. on Titanium, San Diego, CA, USA, vol. 1992 1992, pp. 276–283.
[52] M. Abdel-Hady, K. Hinoshita, M. Morinaga, General approach to phase stability and elastic properties of β-type Ti-alloys using electronic parameters, Scr. Mater. 55 (2006) 477–480.
[53] C.A. Luke, R. Taggart, D.H. Polonis, Electronic factors and the metastable constitution of quenched alloys based on titanium and zirconium, J. Nucl. Mater. 16 (1965) 7–18.
[54] Y.L. Hao, S.J. Li, S.Y. Sun, C.Y. Zheng, R. Yang, Elastic deformation behaviour of Ti–24Nb–4Zr–7.9Sn for biomedical applications, Acta Biomater. 3 (2007) 277–286.
[55] P. Laheurte, F. Prima, A. Eberhardt, T. Gloriant, M. Wary, E. Patoor, Mechanical properties of low modulus beta titanium alloys designed from the electronic approach, J. Mech. Behav. Biomed. Mater. 3 (2010) 565–573.
[56] Y. Guo, D. Chen, M. Cheng, W. Lu, L. Wang, X. Zhang, The bone tissue compatibility of a new Ti35Nb2Ta3Zr alloy with a low Young's modulus, Int. J. Mol. Med. 31 (2013) 689–697.
[57] M. Niinomi, Fatigue performance and cyto-toxicity of low rigidity titanium alloy, Ti–29Nb–13Ta–4.6Zr, Biomaterials 24 (2003) 2673–2683.
[58] I. Martin, D. Wendt, M. Heberer, The role of bioreactors in tissue engineering, Trends Biotechnol. 22 (2004) 80–86.
[59] J.V. Araujo, C. Cunha-Reis, T. Rada, M.A. da Silva, M.E. Gomes, Y. Yang, N. Ashammakhi, R.L. Reis, A.J. El-Haj, N.M. Neves, Dynamic culture of osteogenic cells in biomimetically coated poly(caprolactone) nanofibre mesh constructs, Tissue Eng. A 16 (2010) 557–563.
[60] G.Y. Zhao, L.P. Zhao, Y.F. He, G.F. Li, C. Gao, K. Li, Y.J. Xu, A comparison of the biological activities of human osteoblast hFOB1.19 between iron excess and iron deficiency, Biol. Trace Elem. Res. 150 (2012) 487–495.
[61] C. Gardi, P. Calzoni, M. Ferrali, M. Comporti, Iron mobilization from crocidolite as enhancer of collagen content in rat lung fibroblasts, Biochem. Pharmacol. 53 (1997) 1659–1665.
[62] J. Dai, A. Churg, Relationship of fiber surface iron and active oxygen species to expression of procollagen, PDGF-A, and TGF-beta(1) in tracheal explants exposed to amosite asbestos, Am. J. Respir. Cell Mol. Biol. 24 (2001) 427–435.
[63] C. Gardi, B. Arezzini, V. Fortino, M. Comporti, Effect of free iron on collagen synthesis, cell proliferation and MMP-2 expression in rat hepatic stellate cells, Biochem. Pharmacol. 64 (2002) 1139–1145.
[64] W. Duan, C. Ning, T. Tang, Cytocompatibility and osteogenic activity of a novel calcium phosphate silicate bioceramic: silicocarnotite, J. Biomed. Mater. Res. A 101 (2013) 1955–1961.
[65] X. Qiu, P. Wan, L. Tan, X. Fan, K. Yang, Preliminary research on a novel bioactive silicon doped calcium phosphate coating on AZ31 magnesium alloy via electrodeposition, Mater. Sci. Eng. C Mater. Biol. Appl. 36 (2014) 65–76.
[66] A.J. Mieszawska, N. Fourligas, I. Georgakoudi, N.M. Ouhib, D.J. Belton, C.C. Perry, D.L. Kaplan, Osteoinductive silk–silica composite biomaterials for bone regeneration, Biomaterials 31 (2010) 8902–8910.
[67] M. Wiens, X. Wang, U. Schlossmacher, I. Lieberwirth, G. Glasser, H. Ushijima, H.C. Schröder, W.E. Müller, Osteogenic potential of biosilica on human osteoblast-like (SaOS-2) cells, Calcif. Tissue Int. 87 (2010) 513–524.
[68] P.E. Keeting, M.J. Oursler, K.E. Wiegand, S.K. Bonde, T.C. Spelsberg, B.L. Riggs, Zeolite A increases proliferation, differentiation, and transforming growth factor beta production in normal adult human osteoblast-like cells in vitro, J. Bone Miner. Res. 7 (1992) 1281–1289.
[69] I.S. Byun, S.K. Sarkar, M. Anirban Jyoti, Y.K. Min, H.S. Seo, B.T. Lee, H.Y. Song, Initial biocompatibility and enhanced osteoblast response of Si doping in a porous BCP bone graft substitute, J. Mater. Sci. Mater. Med. 21 (2010) 1937–1947.
[70] M. Ngiam, S. Liao, A.J. Patil, Z. Cheng, C.K. Chan, S. Ramakrishna, The fabrication of nano-hydroxyapatite on PLGA and PLGA/collagen nanofibrous composite scaffolds and their effects in osteoblastic behavior for bone tissue engineering, Bone 45 (2009) 4–16.
[71] N. Almora-Barrios, N.H. de Leeuw, A density functional theory study of the interaction of collagen peptides with hydroxyapatite surfaces, Langmuir 26 (18) (2010) 14535–14542.

Int. J. Mol. Sci. **2013**, *14*, 9182-9204; doi:10.3390/ijms14059182

OPEN ACCESS
International Journal of
Molecular Sciences
ISSN 1422-0067
www.mdpi.com/journal/ijms

Article

Growth and Potential Damage of Human Bone-Derived Cells on Fresh and Aged Fullerene C_{60} Films

Ivana Kopova [1], Lucie Bacakova [1,*], Vasily Lavrentiev [2] and Jiri Vacik [2]

[1] Institute of Physiology, Academy of Sciences of the Czech Republic, Videnska 1083, 14220 Prague 4-Krc, Czech Republic; E-Mail: ivana.kopova@biomed.cas.cz

[2] Nuclear Physics Institute, Academy of Sciences of the Czech Republic, 25068 Rez near Prague, Czech Republic; E-Mails: lavrent@ujf.cas.cz (V.L.); vacik@ujf.cas.cz (J.V.)

* Author to whom correspondence should be addressed; E-Mail: lucy@biomed.cas.cz; Tel.: +420-2-9644-3743; Fax: +420-2-9644-2844.

Received: 15 January 2013; in revised form: 10 April 2013 / Accepted: 15 April 2013 / Published: 26 April 2013

Abstract: Fullerenes are nanoparticles composed of carbon atoms arranged in a spherical hollow cage-like structure. Numerous studies have evaluated the therapeutic potential of fullerene derivates against oxidative stress-associated conditions, including the prevention or treatment of arthritis. On the other hand, fullerenes are not only able to quench, but also to generate harmful reactive oxygen species. The reactivity of fullerenes may change in time due to the oxidation and polymerization of fullerenes in an air atmosphere. In this study, we therefore tested the dependence between the age of fullerene films (from one week to one year) and the proliferation, viability and metabolic activity of human osteosarcoma cells (lines MG-63 and U-2 OS). We also monitored potential membrane and DNA damage and morphological changes of the cells. After seven days of cultivation, we did not observe any cytotoxic morphological changes, such as enlarged cells or cytosolic vacuole formation. Furthermore, there was no increased level of DNA damage. The increasing age of the fullerene films did not cause enhancement of cytotoxicity. On the contrary, it resulted in an improvement in the properties of these materials, which are more suitable for cell cultivation. Therefore, fullerene films could be considered as a promising material with potential use as a bioactive coating of cell carriers for bone tissue engineering.

Keywords: carbon nanoparticles; hydrophobicity; osteoblasts; adhesion; morphology; proliferation; cytotoxicity; gamma-H2AX; 53BP1

1. Introduction

Fullerenes, first discovered by Kroto *et al*. in 1985 [1], are carbon allotropes with a spherical structure consisting of more than sixty carbon atoms linked via hexagonal and pentagonal rings. Fullerene C_{60} (also termed Buckminsterfullerene or buckyball) is a remarkably stable cage-like molecule with a diameter of approximately 0.7 nm and, thus, can be defined as a nanomaterial. Thanks to their unique physicochemical properties, such as the ability to withstand high temperatures and pressures, as well as the high reactivity of these nanoparticles, fullerenes are expected to have great potential in industry as catalysts for chemical reactions, electronic equipment, additives in lubricants and fuel [2]. Due to their thirty carbon double bonds, to which free radicals can be easily added, fullerenes are considered to be radical scavengers with antioxidant properties. Therefore, they have already been utilized in cosmetics, such as facial creams and sunscreen protection products [3,4].

The structural analogy to clathrin-coated vesicles, together with the antioxidant properties of fullerenes, makes these nanoparticles highly attractive for nanomedicine, for use as drug and gene delivery agents [5–7], as well as for the prevention and treatment of specific neurodegenerative disorders caused by a hyper-production of reactive oxygen species (ROS), in such diseases as Alzheimer's and Parkinson's [8,9]. Furthermore, fullerenes are able to inhibit the release of allergic mediators in human mast cells and peripheral blood basophils *in vitro*, which suggests that fullerenes could control mast cell-dependent diseases, including asthma, inflammatory arthritis, heart disease and multiple sclerosis [10]. On the other hand, C_{60} is not only able to quench, but also to generate ROS after irradiation with ultraviolet or visible light. Overproduction of ROS is known to cause cell damage, such as the disintegration of plasma membrane and cleavage of DNA, which finally leads to cell death. This harmful effect of fullerenes makes them suitable for photodynamic therapies against tumors, viruses and bacteria that are resistant to multiple drugs [11–13].

Despite the promising potential of fullerenes in medicine, numerous studies have reported a toxic effect of these nanoparticles on various animals, organs, cells and microorganisms (for a review, see [14]). However, recently, it has been found that tetrahydrofuran (THF), which was widely used as a solvent of water insoluble fullerene C_{60}, generates cellular toxicity. Thus, the toxic side products, such as γ-butyrolactone, 2-hydroxytetrahydrofuranol and formic acid (created during the preparation of C_{60} suspension), are probably responsible for the cytotoxicity previously attributed to fullerenes, whereas fullerenes themselves have no negative effect [15–17]. In accordance with this finding, an *in vivo* toxicity study has revealed that aqueous C_{60} suspensions prepared without using any polar organic solvent not only cause no acute or subacute toxicity in rodents, but also have a protective effect on their livers in a dose-dependent manner [18]. In addition, no irritation of skin (human volunteers) or eyes (rabbit) nor allergic risks were observed after administration of the fullerene water suspension [19]. Repeated doses of fullerenes in benzene for up to 24 weeks post-initiation also did not cause acute toxic effects, and no benign or malignant skin tumor formation was observed in mice [20]. Furthermore, inhalation experiments in rats demonstrated lower cytotoxic and proinflammatory effects of C_{60} nanoparticles in comparison with quartz particles [21] and relatively low and similar toxicity of C_{60} in both nanoparticle and microparticle forms [22].

Another promising utilization of fullerenes is the prevention and treatment of arthritis. It has been reported that in an osteoarthritis rabbit model (produced by resection of both the medial meniscus and

medial collateral ligament), water soluble fullerene (purchased from Vitamin C_{60}) significantly reduced articular cartilage degeneration [23]. Moreover, in adjuvant-induced arthritic rats, intra-articular treatment led to a decreasing number of osteoclasts together with reduced synovitis and alleviated bone resorption and destruction of the joints, due to the suppressive effect of C_{60} on proinflammatory cytokine production in the synovial inflammation-related cells [24,25]. Recently it has been reported that carbon nanohorns (CNH; another carbon allotrope closely related to the fullerenes), fixated on a porous polytetrafluoroethylene membrane, were used for covering the calvarial bone defect in rats. The results showed the attachment of macrophages to CNHs and acceleration of newly formed bone regeneration in the presence of these nanoparticles [26].

According to these findings mentioned in the preceding paragraph, fullerene materials appear very promising in bone tissue engineering, e.g., for surface treatment of bone implants. This idea is further supported by our earlier studies performed on fullerenes C_{60} and binary C_{60}/Ti composites deposited on carbon-based or glass substrates in the form of continuous and micropatterned films [27–31]. These films provided a good support for the adhesion, growth and phenotypic maturation of human osteoblast-like MG-63 cells. The growth dynamics of these cells cultured on continuous films were similar to the dynamics on standard cell culture polystyrene dishes [29]. However, potential adverse effects of the fullerene films on cells have not been investigated in these studies. These effects could result from possible changes of physicochemical properties of the fullerene films in time, due to the oxidation and polymerization of C_{60} molecules in an air atmosphere. This could lead to changes in the reactivity of these molecules, which could influence the cytotoxicity of fullerenes. Therefore, we have decided to study the dependence between the age of C_{60} layers (from one week to one year), deposited on glass coverslips, and the adhesion, proliferation, viability and metabolic activity of human osteosarcoma cells, in order to develop a potential bioactive coating of bone implants and cell carriers applicable in bone tissue engineering. We have concentrated not only on the positive effects, but also on potential membrane and DNA damage, as well as morphological changes of cells cultivated on fullerene films.

2. Results and Discussion

2.1. Atomic Force Microscopy (AFM)

The surface morphology and thickness of the fresh and aged C_{60} films were analyzed by Atomic Force Microscopy (AFM) (Figure 1). The AFM micrographs exhibit granular nanostructures (formed by C_{60} clusters) with a typical granule size of approximately 50 nm in the fresh films. The analysis revealed that 1 μm area roughness on the prominences, in both cases (3.40 nm on fresh and 4.86 nm on aged layers) is much smaller than the roughness on the grooves (5.93 nm on fresh and 7.12 nm on aged films). The roughness on the prominences, as well as on the grooves, is higher on the aged C_{60} layers, which could be explained by the fullerene polymerization and other changes of the C_{60} films during the aging period, leading to an increased size of the granular nanostructures (Figure 1).

Figure 1. Surface morphology on the prominences (or on the continuous film; **A**,**B**) and on the grooves (**C**,**D**) of fresh (**A**,**C**) and aged (**B**,**D**) C_{60} films, evaluated by Atomic Force Microscopy (AFM).

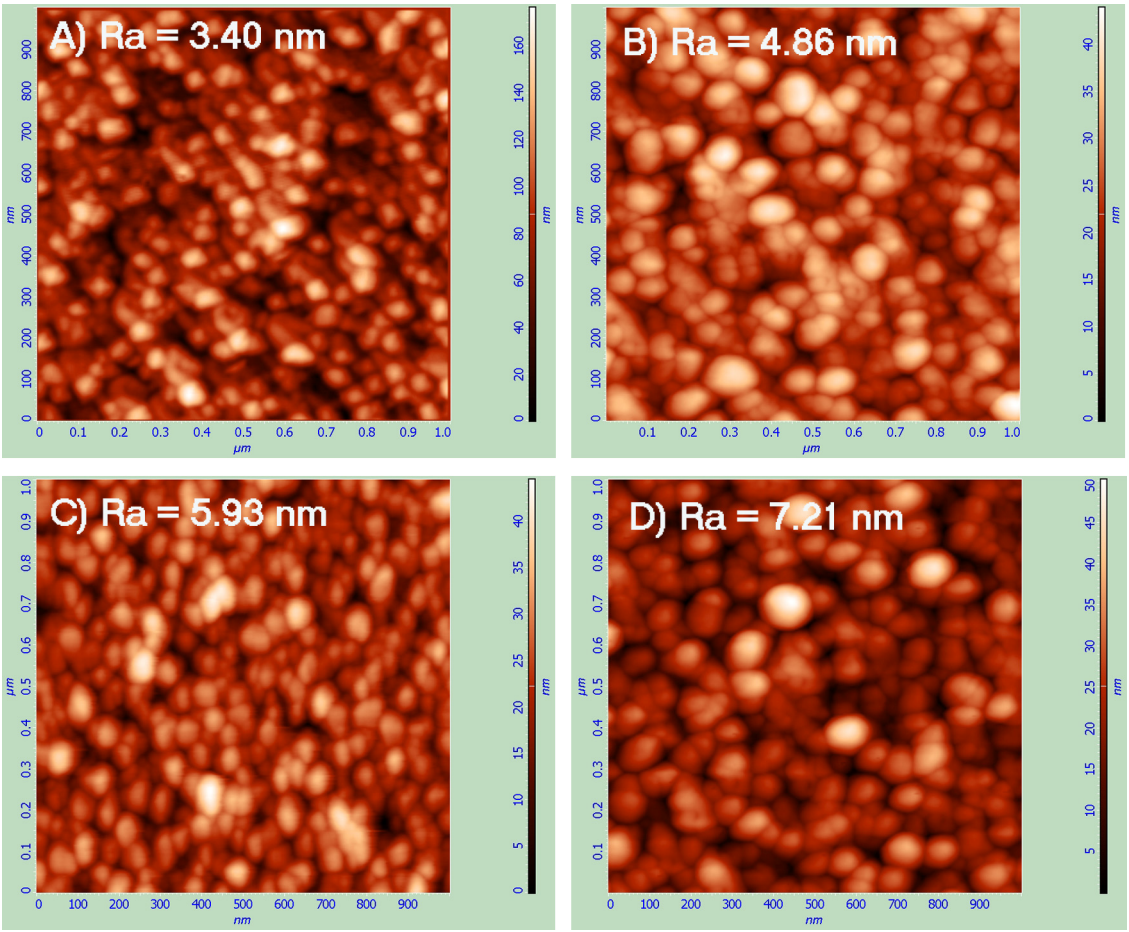

Figure 2. Height of the prominences and the grooves of the micropatterned fresh (**A**) and aged (**B**) C_{60} films.

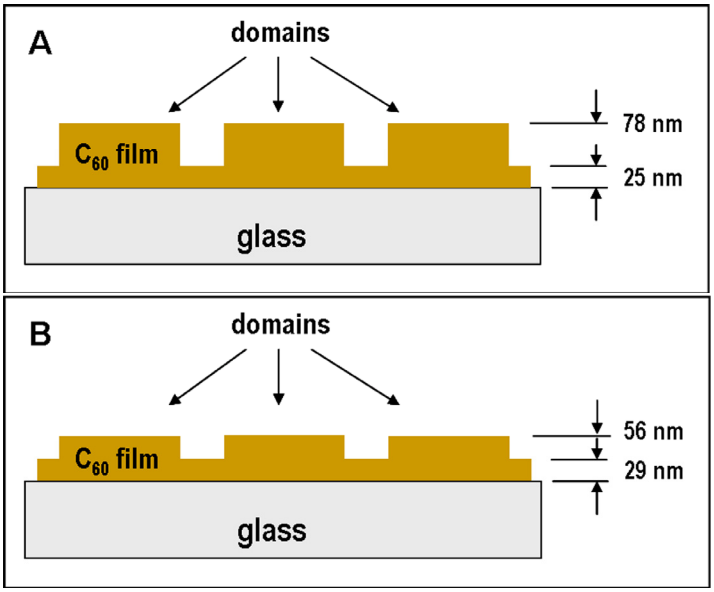

It is also possible to use AFM to scan and analyze the heights of the prominences and grooves. The measurements revealed, in the case of the fresh C_{60} films, that the prominences are about twice as high as the grooves (prominences = 53 nm, grooves = 25 nm), though in the case of the aged layers, the height of the C_{60} prominences are similar to the height of the grooves (prominences = 27 nm, grooves = 29 nm; Figure 2). This decrease in height of the prominences on aged C_{60} films can be explained by post-deposition surface diffusion of the fullerene molecules in time, *i.e.*, during the aging period of fullerene films.

2.2. Raman Spectroscopy

The chemical composition and bonding of the fresh (*i.e.*, one week old) and aged (*i.e.*, one year old) fullerene films were characterized by several techniques, including Raman spectroscopy.

In Figure 3, typical micro-Raman spectra measured on both types of C_{60} films, one-year old and freshly synthesized, are depicted. In both cases, the spectra were measured on the top of the C_{60} bulges. Using the multi-peak Gaussian analysis of the $H_g(7)$, $A_g(2)$ and $H_g(8)$ vibration peaks, area peak ratios $A_g(2)/H_g(7)$ and $A_g(2)/H_g(8)$ for both films were evaluated with the following results:

Fresh C_{60} film: $A_g(2)/H_g(7) = 5.554$, $A_g(2)/H_g(8) = 7.025$

One-year old C_{60} film: $A_g(2)/H_g(7) = 1.675$, $A_g(2)/H_g(8) = 1.613$.

The Raman analysis showed:

(a) Both films (aged and fresh) exhibit typical features of the fullerene films with dominant $H_g(7)$, $A_g(2)$ and $H_g(8)$ peaks.

(b) In the aged samples, however, a main $A_g(2)$ peak (pentagonal pinch mode) dropped down dramatically (see the area peak ratios above) and showed a slight red-shift asymmetry (seen in the detailed examination of the spectrum).

(c) Interestingly, there is also a clear difference in the symmetric (A_g) and asymmetric (H_g) mode changes of the aged sample (in comparison with the fresh one); all symmetric mode peaks decreased in intensity, though the asymmetric modes increased.

Figure 3. Raman spectra of the fresh and aged C_{60} films.

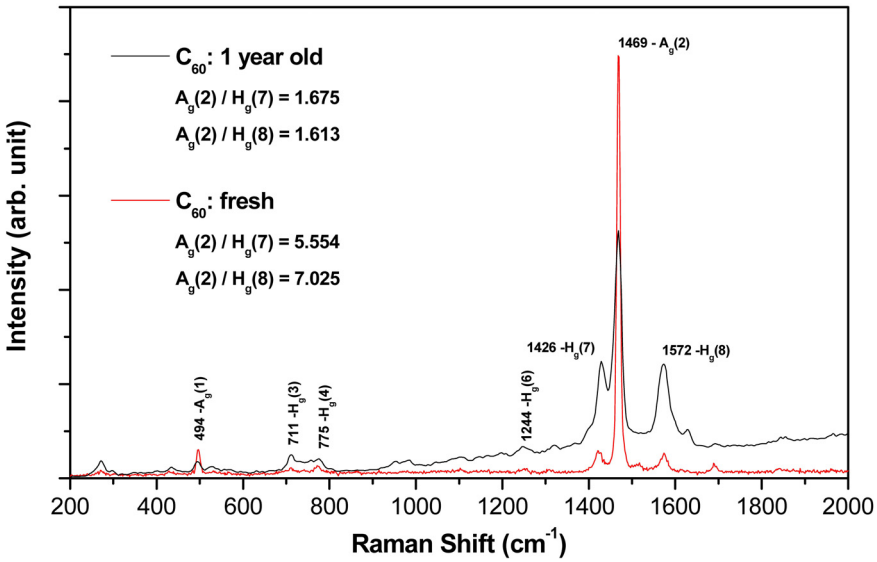

All of these features point to the structural and bonding alterations that have developed in the aged C_{60} film—mainly due to the polymerization and partial oxidation of the fullerene molecules. The aged sample Raman spectrum also showed graphitization of the film, but this effect is rather small.

2.3. X-ray Photoelectron Spectroscopy (XPS)

XPS revealed the presence of C, O, Si and Na in all tested samples (Figure 4). Similarly as Raman spectroscopy, XPS also showed more pronounced changes in the aged fullerene films in comparison to the fresh ones, which is indicated by a missing structure of the bands typical for fullerenes (Figure 5). This can be explained by a degradation of the fullerene molecules and/or spontaneous deposition of carbon compounds, present in the air, on the aged films. Similar carbonaceous contamination has been observed on the surface of Ti and TiNb materials developed for the construction of bone implants [27–32].

Figure 4. Survey XPS spectra of samples under analysis. C 1s, O 1s Si 2s, Si 2p and Na 1s are core-level photoelectron spectra from carbon, oxygen, silicon and sodium atoms. C KLL, O KLL and Na KLL are Auger transitions from carbon, oxygen and sodium atoms.

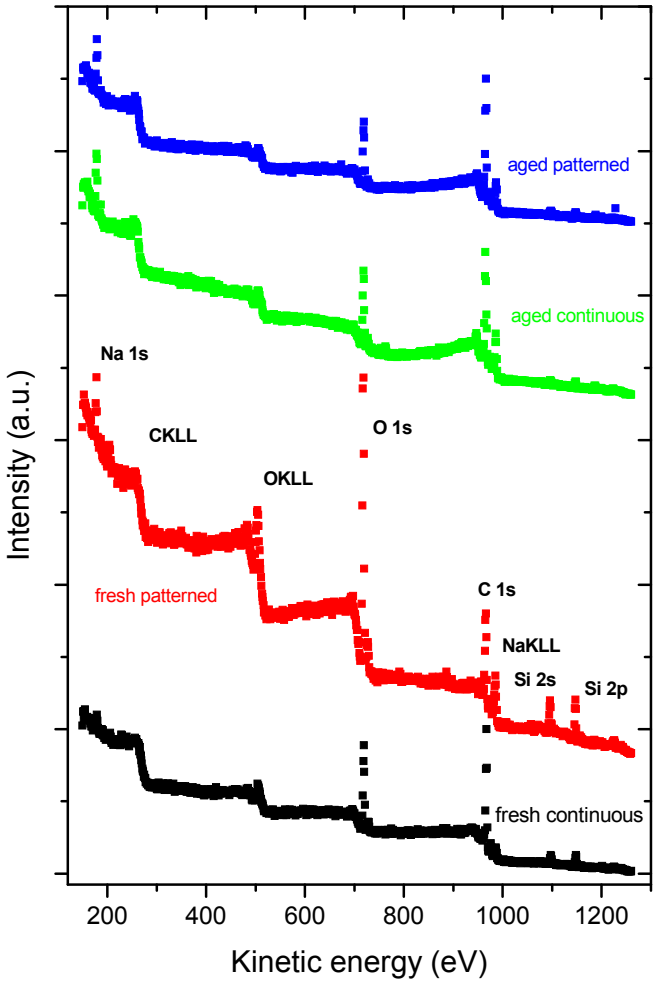

The concentration of oxygen, measured by XPS, was higher in fresh than in aged fullerene films (Tables 1 and 2). This finding might be inconsistent with the results of Raman spectroscopy, which showed that the alterations of fullerene films, such as polymerization, graphitization and partial

oxidation of the fullerene molecules, were more pronounced in the aged films. However, it should be taken into account that the Raman spectroscopy measures the changes throughout the whole thickness of the films, while XPS only measures changes on the very thin surface of these films. The mean value of the inelastic mean free path of electrons is ~2–3 nm for fullerenes C_{60} and C 1s electrons of the energy of ~1000 eV). The informational depth of the method is about three times higher, *i.e.*, 6 to 9 nm. As shown by AFM, the fullerene films are much thicker, *i.e.*, from 25 to 50 nm. In addition, the presence of oxygen on the surface of the aged films could be masked by the carbonaceous contamination mentioned above.

Figure 5. Photoemission from occupied valence bands induced by Mg Kα radiation (1253.6 eV). The spectra of fresh prepared samples show oscillations typical for fullerenes. For aged samples, the spectral features are more complex, indicating strong degradation of the fullerene molecular structure or a surface contamination by a carbon-containing species from air.

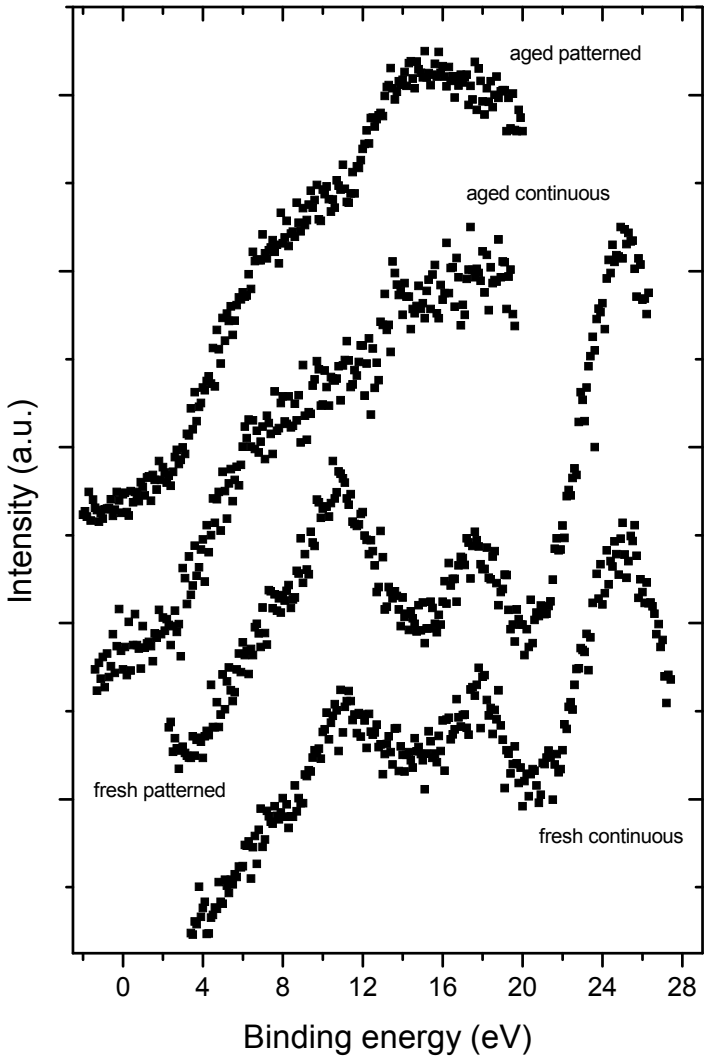

Interestingly, the concentration of oxygen measured by XPS was higher in fresh micropatterned films than in fresh continuous films (Figure 6, Tables 1 and 2). This can be explained by the fact that the materials with prominences and grooves have a larger surface than the flat continuous films and,

thus, these surfaces can accommodate a larger number of oxygen-containing structures. As shown by AFM, on the aged materials, the height of the prominences was lower; thus, the surface of these materials became smaller and the oxygen content of both continuous and micropatterned aged surfaces equilibrated.

Figure 6. High-resolution C 1s lines recorded from fresh deposited samples. Both spectra were corrected for surface charging with respect to the Si 2p line at 103.0 eV. The shape of the bottom spectrum is similar to that of fullerene while the top spectrum is highly asymmetric due to C-O bonding states.

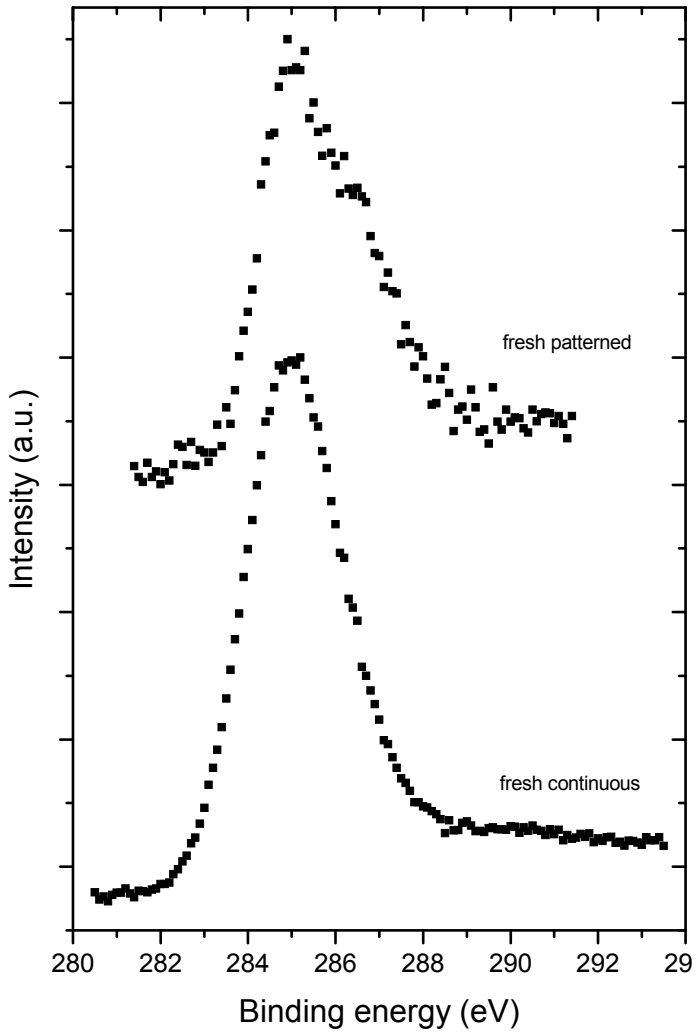

Table 1. Quantitative analysis of the surface of the tested samples.

Sample	C (at.%)	O (at.%)	Si (at.%)	Na (at.%)	F (at.%)
Fresh, continuous	57.2	29.3	11.3	2.3	-
Fresh, micropatterned	43.8	36.1	16.4	3.6	-
Aged, continuous	72.2	16.4	3.8	7.6	-
Aged, micropatterned	73.7	15.6	4.9	5.8	-
Glass substrate	21.9	49.4	22.4	4.1	2.3

Table 2. Correction of the data from Table 1 performed on an assumption that Si and Na originate from the glass substrate and are in the oxide state (*i.e.*, SiO_2, Na_2O).

Sample	C (at.%)	O (at.%)
Fresh, continuous	91	9.0
Fresh, micropatterned	80.0	20.0
Aged, continuous	93.5	6.5
Aged, micropatterned	96.2	3.8
Fullerene powder	95.2	4.8

One should take into account also the fact that there exists competition between oxidation (fast process) and polymerization (lengthy process) and that in time, polymerization as a chemically alteration process will prevail. This may partially explain the situation why the amount of oxide is at aged samples smaller than at fresh ones.

As for the presence of Si and Na in the tested samples, angular measurements of photoemission (not shown) indicated that Si and Na are localized below the fullerene layers, *i.e.*, in the underlying glass coverslips. As the spectra were recorded from a relatively large area (specifically 1 cm^2), these results suggest non-homogeneous coating of the glass substrates with fullerenes, *i.e.*, the absence of these films on some places or the presence of regions covered with a very thin fullerene film (~4 to 5 nm).

Figure 7. Hydrophobicity of micropatterned (**A**) or continuous (**B**) fresh and aged fullerene films.

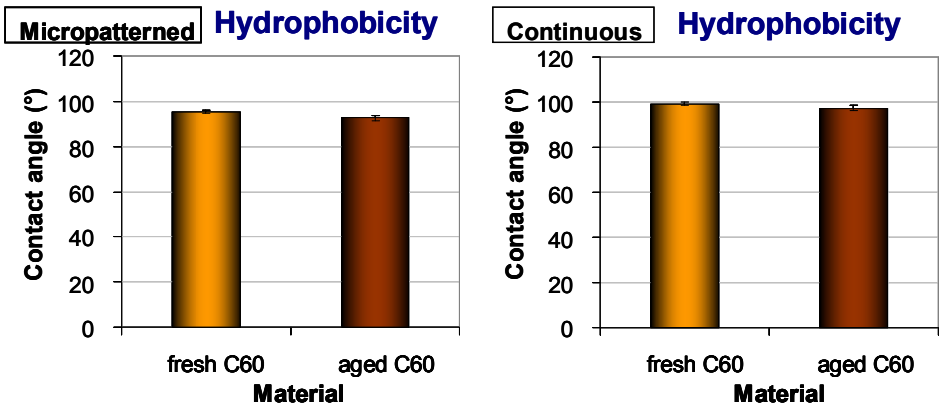

2.4. Hydrophobicity of Fullerene C_{60} Layers

The continuous and micropatterned layers were at a relatively high hydrophobic level. The water drop contact angles of fresh materials were 95.3° on micropatterned films and 99.3° on continuous films. Similar results were obtained in our earlier studies performed on continuous and micropatterned C_{60} films of various thicknesses [28,29]. A slight decrease of the water contact angle was observed in the aged fullerene films (92.7° on micropatterned and 97.2° on continuous films); however, this reduction was not proven to be statistically significant (Figure 7). This tendency to increase in surface wettability could be due to the changes of the fullerene films during aging, such as their polymerization, oxidation, graphitization and degradation, as revealed by the Raman spectroscopy and

XPS (Figures 3 and 5). In our earlier studies, similar changes were observed on fullerene films exposed to 70% ethanol used for material sterilization ([28]; for a review, see [14]).

2.5. Initial Adhesion, Proliferation and Morphology of Cells on Fullerene C_{60} Layers

2.5.1. Comparison of Cell Behavior on Fresh and Aged Fullerene Films

The initial adhesion of human osteoblast-like MG-63 cells seeded on fresh (*i.e.*, one week old) micropatterned and continuous fullerene films was significantly lower in comparison with the aged (*i.e.*, one year old) C_{60} layers, as well as with the reference microscopic glass coverslips (Figure 8). After three and seven days of cultivation, cells growing on both types of fresh fullerene films reached significantly lower population densities than those on the aged layers and control glass coverslips. In addition, the cells cultivated on the fresh C_{60} films were poorly spread with a rounded morphology (Figure 9).

Figure 8. Growth curves of human osteoblast-like MG-63 cells on micropatterned (**A**) or continuous (**B**) fresh and aged fullerene films. GS, microscopic glass coverslips, reference material; * significant difference to GS; + significant difference to C_{60} aged. $p \leq 0.001$ (***/+++); $p \leq 0.01$ (**/++); $p \leq 0.05$ (*/+).

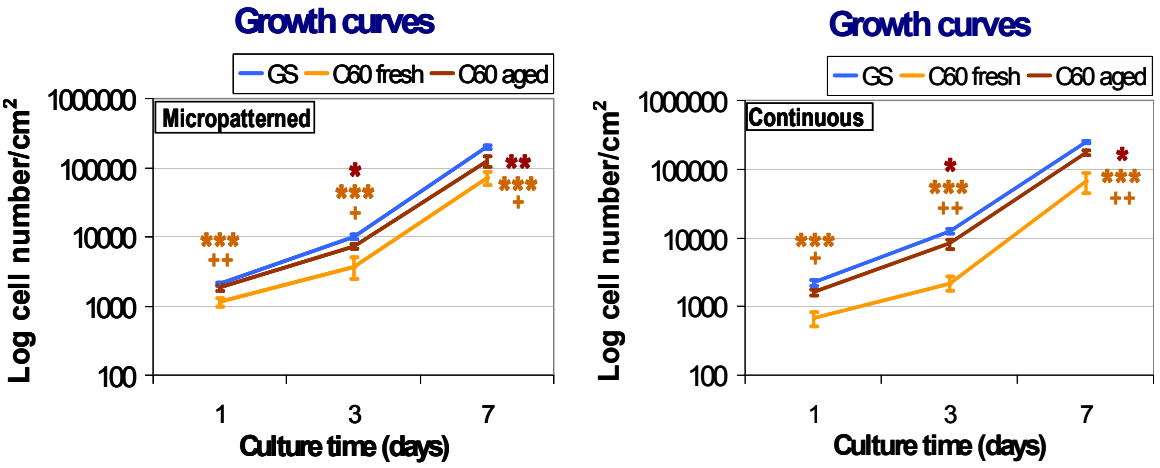

From day one to three after seeding, the cells on fresh fullerene films proliferated more slowly than on control glass coverslips. The cell population doubling times on fresh micropatterned and continuous C_{60} films were 27.9 and 28.0 h, respectively, while on control glass coverslips, it was only 20.9 and 19.4 h. As a result of the reduced initial adhesion and growth dynamics, the cells cultured on fresh fullerene films reached significantly lower population densities on day three after seeding (Figure 8). However, after three days of cultivation, the cells on fresh fullerene films proliferated with similar growth dynamics compared to the cells on the reference material. The doubling times were 22.6 h on fresh micropatterned films, 19.5 h on fresh continuous films and 22.4 and 22.3 h on reference glass coverslips. Although the differences in growth dynamics disappeared between days three and seven, the cell population densities reached on day seven still remained significantly lower on fresh fullerene films than on glass coverslips (Figure 8). Therefore, the lower population densities on day seven can

be explained by combination of a lower number of initially attached cells and reduced growth dynamics during first three days of cultivation.

Figure 9. The morphology and preferential growth of human osteoblast-like MG-63 cells on micropatterned or continuous fresh and aged fullerene films on day 3 after seeding. GS, microscopic glass coverslips, reference material.

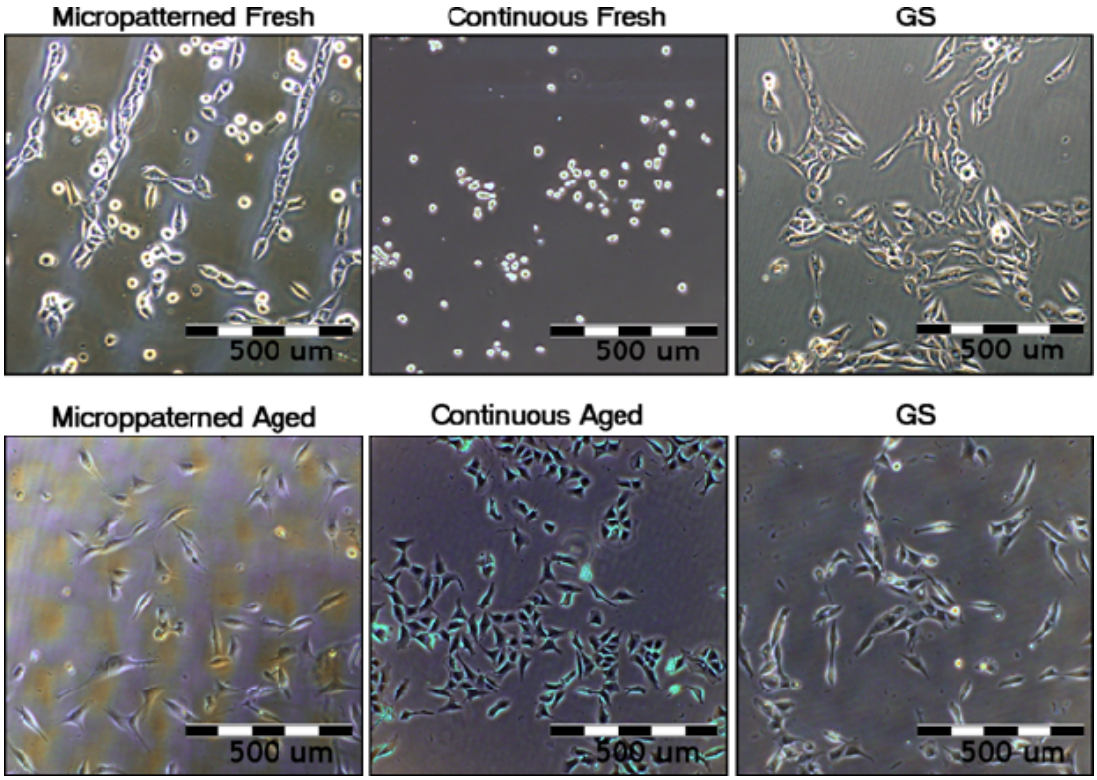

Aged (*i.e.*, one year old) fullerene films provided a better support for the adhesion and growth of MG-63 cells than the fresh films. On both aged micropatterned and continuous C_{60} layers, the number of initially adhered cells was higher than on the corresponding fresh films and similar to the values found on control glass coverslips (Figure 8). Cells on both aged films were well spread, *i.e.*, of polygonal or spindle-like morphology (Figure 9).

The subsequent growth dynamics of cells cultured on aged C_{60} films were closer to those found on the control glass coverslips than in the case of fresh films. From day one to three after seeding, the doubling times on aged micropatterned and continuous C_{60} films were 24.2 and 20.6 h, respectively, and on the control glass coverslips, the values were 20.9 and 19.4 h. Between days three and seven, the doubling times on aged fullerene films (23.3 h on micropatterned and 21.9 h on continuous films) became fully comparable with the values on glass coverslips (22.4 and 22.3 h). Nevertheless, the cell population densities on days three and seven after seeding on aged fullerene films remained still lower than on the reference glass coverslips, although they were significantly higher than on fresh fullerene films (Figure 8). This can be due to the fact that even after aging, the surface hydrophobicity of C_{60} films still remained relatively high (Figure 7) when compared to the microscopic glass coverslips (Menzel Glaser, Germany) used in this study. The water drop contact angle on these coverslips cleaned with ethanol and deionized water was about 60° (data not shown here). Thus, the glass surface was

moderately hydrophilic, which is considered as optimal for the cell adhesion. Similarly as nanostructured surfaces, also the moderately hydrophilic surfaces adsorb the cell adhesion-mediating molecules in an active geometrical conformation, well recognized by the cell adhesion receptors. On the contrary, on hydrophobic materials (*i.e.*, with contact angle more than 90°, which is the case of all fullerene films investigated in this study), the cell adhesion-mediating molecules are adsorbed in a rigid and denatured form, which reduces their accessibility for the cell adhesion receptors. In addition, hydrophobic surfaces preferentially adsorb albumin, which is non-adhesive for cells (for a review, see [33,34]).

The improved adhesion, morphology and proliferation of MG-63 cultured on aged C_{60} films are likely due to the changes in the fullerene films during aging, such as fragmentation, oxidation, polymerization and graphitization of fullerenes in an air atmosphere (Figures 3 and 5). These changes could lead not only to the modification of the chemical properties and the polarity of the material surface, but also to its enhanced nanoscale roughness. These factors together could result in the facilitation and enhancement of cell adhesion (for a review, see [14,33–35]). For example, substrates with nanoscale irregularities promote the adsorption of cell adhesion-mediating extracellular matrix molecules (e.g., fibronectin, vitronectin) present in the serum supplement of the culture media, in an appropriate geometrical conformation, which enables good accessibility of specific sites in these molecules (*i.e.*, RGD-containing oligopeptides) for cell adhesion receptors. In addition, these surfaces adsorb preferentially vitronectin, which is recognized mainly by osteoblasts compared to other cell types [36].

The oxygen present in the fullerene films can also play an important role in cell adhesion and growth. It has been repeatedly shown that the formation of oxygen-containing chemical functional groups on the material surface supports the cell adhesion (for a review, see [32–35]). However, on the fresh fullerene films, which contained more oxygen on their surface, the initial cell adhesion was poorer than on the aged film with a lower surface oxygen concentration. It can be supposed that on freshly deposited films, the oxygen structures (as well as the fullerenes themselves) could be present in more reactive forms harmful for cells. In accordance with this, the cell viability, measured by a trypan-blue exclusion test, was reduced on fresh fullerene films compared to the aged films and uncoated glass coverslips (see below, section 2.6). On the other hand, no DNA damage response was found in cells grown on both fresh and aged fullerene films (section 2.7).

The fresh fullerene films might be also more prone to the release of fullerene micro- and nano-particles, which can enter and damage the cells. However, in our earlier unpublished experiments, MG-63 cells were treated with fullerenes C_{60} suspended in the cell culture medium (concentration range from 0.15 μg to 30 μg/mL) for seven days. The fullerene suspensions were prepared by dissolving C_{60} in DMSO and by sonicating the suspensions for 3 h in order to prevent the formation of aggregates [37]. The results showed no reduction in proliferation after seven days long treatment with dispersed fullerenes C_{60}. In addition, we did not observe any cytotoxic morphological changes, such as enlarged cells or cytosolic vacuole formation. Thus, even if the fullerenes were released from the films, most likely this release was not the main reason for the lower cell colonization of these films in comparison with control glass coverslips.

2.5.2. Comparison of Cell Behavior on Micropatterned and Continuous Fullerene Films

Cells cultivated on fresh micropatterned films adhered and preferentially grew in grooves among the prominences of C_{60} (Figure 9). Similar cell behavior was also observed in our earlier studies performed on micropatterned C_{60} and hybrid C_{60}/Ti films [28–31]. This has been explained by a synergistic action of certain physical and chemical properties of the fullerene bulges less appropriate for cell adhesion, such as their hydrophobicity, a relatively steep rise, as well as the tendency of spherical ball-like fullerene C_{60} molecules to diffuse out of the prominences [28]. However, on aged micropatterned C_{60} films, the preferential adhesion and growth of cells in grooves among the prominences almost disappeared (Figure 9). This could be mainly due to a decrease in the height of the prominences after diffusion of the fullerenes (Figure 2) and also due to the other changes of the fullerenes during aging, mentioned above.

Interestingly, the cell morphology and spreading was poorer on fresh continuous than on fresh micropatterned films (Figure 9). However, cytotoxic morphological changes, such as enlarged cells or cytosolic vacuole formation, were not observed on both forms of fresh C_{60} films. Thus, these differences could be explained by a different morphology of the films. In our earlier studies, the cell attachment, spreading and growth on a terpolymer of polytetrafluoroethylene, polyvinyl difluoride and polypropylene (PTFE/PVDF/PP) was markedly improved after the addition of carbon nanotubes to these polymers, which was attributed to the increased micro- and nano-scale surface roughness. At the same time, the material surface hydrophobicity was relatively high and did not differ significantly between the pure and nanotube-modified terpolymers [14,27]. Similarly, in the present study, the microscale surface roughness of the micropatterned fullerene film, hierarchically combined with a nanostructure, could compensate, at least to a certain degree, a relatively high hydrophobicity of the fullerene films.

2.6. Metabolic Activity and Viability of Cells on Fullerene C_{60} Layers

In order to investigate the metabolic activity of fresh and aged C_{60} films, the XTT assay, measuring the activity of mitochondrial enzymes, was performed. This activity is considered to be proportional to the cell number; therefore, this assay is often used for evaluation the cell proliferation. Thus, proportionally to the lower cell number, MG-63 cultivated for seven days on both forms of C_{60} layers (micropatterned and continuous) showed significantly reduced metabolic activity in comparison with cells grown on control glass coverslips. As in the case of population densities, the fresh materials caused a much lower metabolic activity of cells than aged C_{60} films (Figure 10). Similar results were obtained after three days of cultivation (data not shown).

Cell viability was analyzed by trypan blue staining. This dye penetrates through the damaged cell membrane and stains non-viable cells. We found that the cells growing on all tested fullerene films were highly viable (over 85%). The viability of MG-63 was reduced on both forms of fresh C_{60} layers in comparison with glass coverslips and with aged fullerene films. However, the viability of cells growing on aged C_{60} layers was comparable to that on the reference glass coverslips (Figure 11).

Figure 10. Metabolic activity measured per cultures of human osteoblast-like MG-63 cells on day seven after seeding on micropatterned (**A**) or continuous (**B**) fresh and aged fullerene films. GS, microscopic glass coverslips, reference material; * significant difference to GS; + significant difference to C_{60} aged. $p \leq 0.001$ (***/+++); $p \leq 0.01$ (**/++).

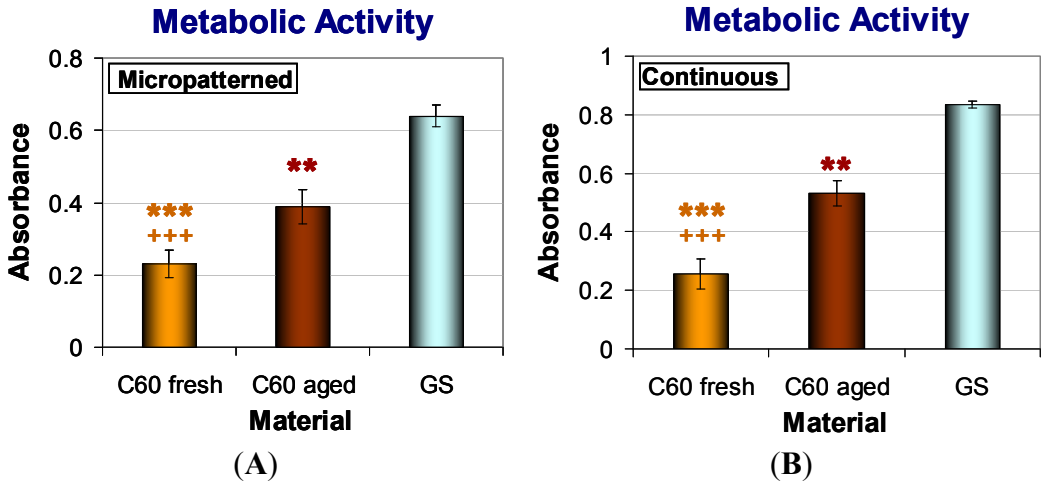

Figure 11. Viability of human osteoblast-like MG-63 cells after seven days of cultivation on micropatterned (**A**) or continuous (**B**) fresh and aged fullerene films. GS, microscopic glass coverslips, reference material; * significant difference to GS; + significant difference to C_{60} aged. $p \leq 0.05$ (*/+).

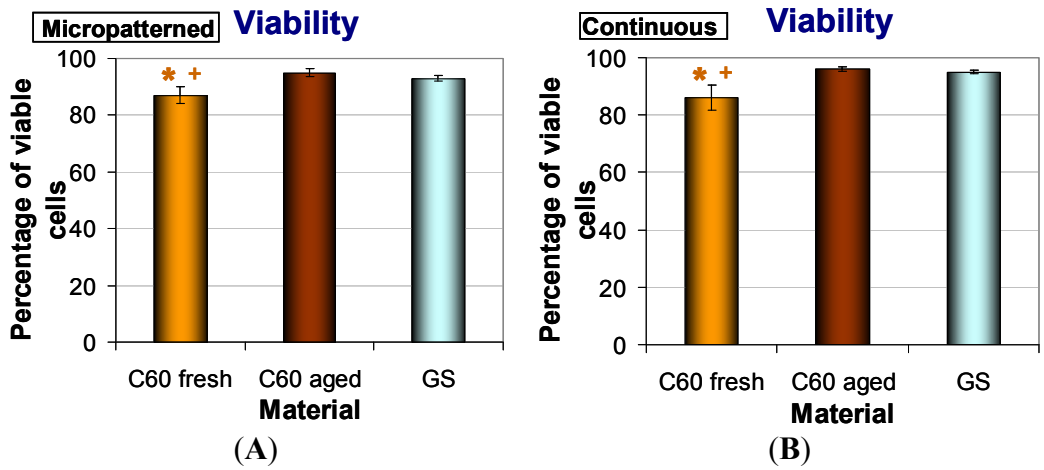

2.7. DNA Damage Response

It has been reported that fullerenes are able to bind directly to the minor and major grooves of double-strand DNA and form a stable complex, which may have a negative impact on the self-repairing process of the dsDNA, leading to the potential cytotoxic effect of fullerenes [38,39]. Therefore, we have studied the DNA damage response (DDR) of cells growing on fullerene films, by markers of DNA double strand breaks. For this purpose, the osteosarcoma cell line U-2 OS was used rather than MG-63, which is p53-deficient. Gamma-HA2X (phosphorylated histone H2AX, a marker of early DDR) and 53BP1 (p53 binding protein), whose focal recruitment depend on a number of upstream factors, were evaluated. After three and seven days of cultivation on both types of fresh and

aged fullerene films, the level of gamma-H2AX phosphorylation was analyzed by flow cytometry. The results show no increase in the percentage of cells with enhanced phosphorylation of histone H2AX cultured either on fresh or aged fullerene films in comparison to the reference glass coverslips (Figure 12). Furthermore, the visualization of both DDR markers by immunofluorescence staining also revealed no increased recruitment and formation of either gamma-H2AX or 53BP1 foci (Figure 13).

Figure 12. Flow cytometry of a marker of DNA damage response: gamma-H2AX in human osteoblast-like U-2 OS cells on micropatterned or continuous fresh and aged fullerene films after seven days of cultivation. GS, microscopic glass coverslips, reference material; GS + NCS, positive control to phosphorylation of histone H2AX (gamma-H2AX), induced by 1 h incubation of U-2 OS cells in neocarzinostatin (NCS; 700 ng/mL). M12 defines the percentage of cells with no increase of DNA damage (obtained from cells growing on reference material, GS); M13 defines the percentage of cells with increased DNA damage response represented by enhanced phosphorylation of histone H2AX (obtained from cells incubated with NCS).

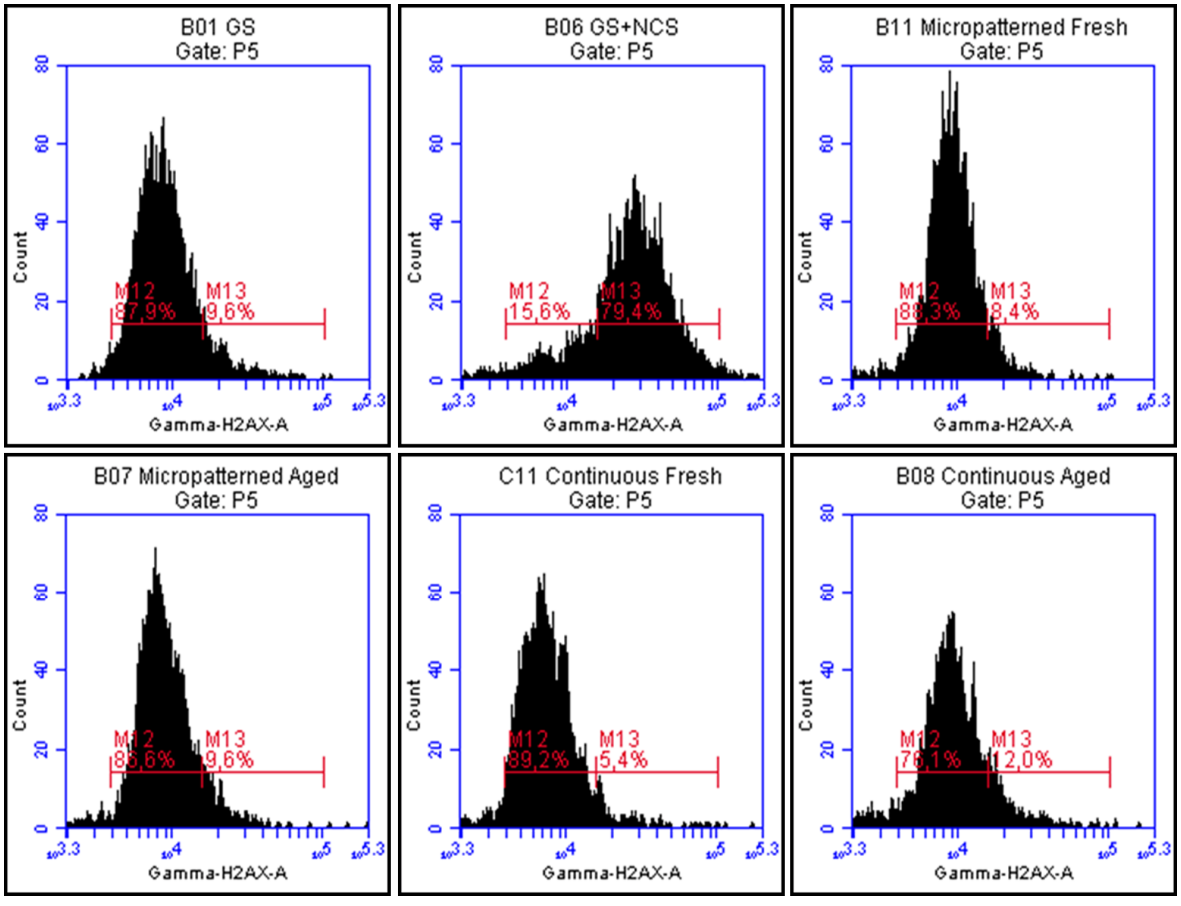

Figure 13. Immunofluorescence staining of markers of DNA damage response: 53BP1 (green) and gamma-H2AX (red) in human osteoblast-like U-2 OS cells on micropatterned or continuous fresh and aged fullerene films after seven days of cultivation. GS, microscopic glass coverslips, reference material; GS + NCS, positive control to DNA damage response, induced by 1 h incubation of U-2 OS cells in neocarzinostatin (NCS; 700 ng/mL).

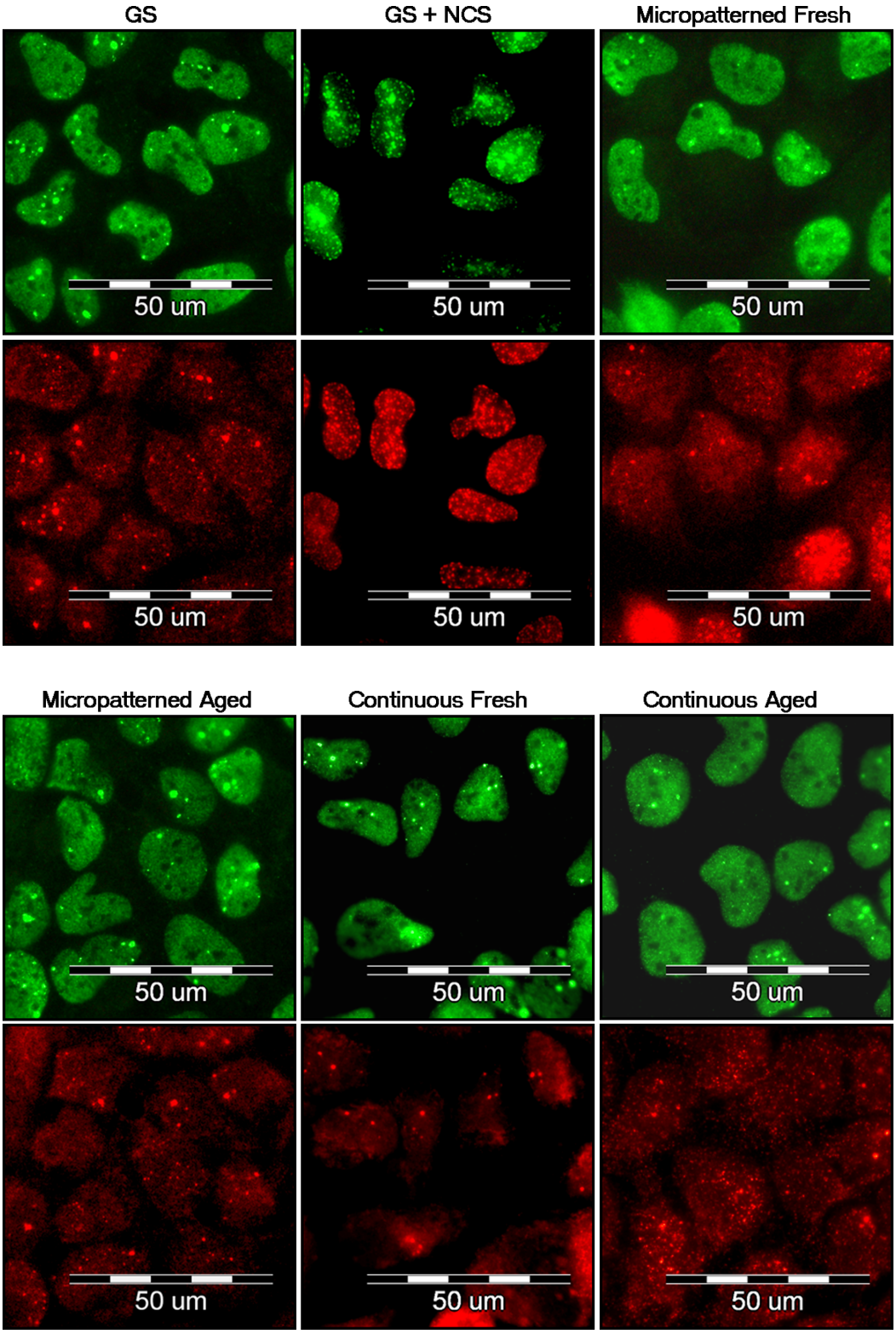

3. Experimental Section

3.1. Material Deposition and Storage Condition

Thin C_{60} fullerene films were synthesized in the Molecular Beam Epitaxy (MBE) systems (in NPI ASCR Rez) by evaporation of the C_{60} phase under certain deposition kinetics: background pressure during deposition ~5×10^{-7} Torr; deposition rate of the C_{60} phase DR(C_{60}) ~5 nm/min; temperature of the substrates during deposition ~room temperature. The fullerene layers were deposited on the selected glass coverslips (Menzel Glaser, Braunschweig, Germany; diameter 12 mm) either as continuous films or through a metallic mesh with regular rectangular openings (100 μm × 150 μm) as a micropatterned array of prominences and grooves. To vaporize the C_{60} phase material, resistive filament heating of the 99.99% pure C_{60} powder was used. The samples were stored in air atmosphere at room temperature in a dark and dry place and evaluated either one week after deposition (fresh samples) or after one year (aged samples).

3.2. Atomic Force Microscopy (AFM)

Surface morphology and thickness of the C_{60} films were analyzed by an Atomic Force Microscopy (AFM microscope NTEGRA, NT-MDT) using a static (contact) mode. The scanning area was selected either as 1000 nm or 100 μm (the presented micrographs, see Figure 1A,B show only 1000 nm scans).

3.3. Raman Spectroscopy

For analysis of the C_{60} films, a Renishaw 2000 imaging microscope (using the 514 nm Ar laser) was applied. The measurements were performed using the low laser power, *i.e.*, (<1 mW) in order to avoid fragmentation of the C_{60} molecules. The spectra were measured on the top of the C_{60} prominences, using the multi-peak Gaussian analysis of the $H_g(7)$, $A_g(2)$ and $H_g(8)$ vibration peaks. Area peak ratios $A_g(2)/H_g(7)$ and $A_g(2)/H_g(8)$ were evaluated.

3.4. X-ray Photoelectron Microscopy (XPS)

The XPS photoelectron spectra were recorded using an angle-resolved photoelectron spectrometer ADES 400 (VG Scientific, East Grinstead, England) operating at a base pressure of 1×10^{-10} Torr. The system is equipped with an X-ray excitation source and a rotatable hemispherical electron energy analyzer. The spectra were recorded using Mg Kα radiation with the pass energy of 100 eV and 20 eV; the incidence angle was 70° with respect to the sample surface normal and the emission angle along the surface normal. The overall energy resolution was 1.2 eV. An area of 1 × 1 cm on the material surface was exposed to X-rays; thus, the spectra represented a mean value of the signal from this area.

The surface composition of the materials was determined from photoelectron peak areas after Shirley's inelastic background subtraction. Assuming a simple model of a semi-infinite solid of homogeneous composition, the peak areas were corrected for the photoelectric cross-sections [40], electron inelastic mean free paths [41] and transmission function of the spectrometer used [42]. Experimental uncertainties accompanied with XPS quantitative analysis, assessed on separate experiments with several standard materials, were estimated to be below 7%. The value covers overall

uncertainties of the method that are mostly introduced by the background subtraction and the procedure used for the calculation of concentrations from intensities of spectral lines. High-energy resolution C 1s photoelectron spectra were recorded at the pass energy of 20 eV.

3.5. Measurement of Wettability

The surface wettability of the fullerene films was estimated from the contact angle measured by a material-water droplet system using a reflection goniometer (SEE System, Masaryk University, Brno, Czech Republic). Data were presented as the mean ± standard error of the mean (SEM) obtained from 10 measurements.

3.6. Cells and Culture Conditions

Since the samples were prepared under aseptic conditions (assured by the high temperature), sterilization was not performed in order to avoid potential damage to the fullerene molecules by irradiation, heating or chemicals. The fullerene-coated glass coverslips were inserted into polystyrene 24-well tissue culture plates (TPP, Trasadingen, Switzerland; diameter 15.4 mm and growth surface 1.862 cm^2, according to the manufacturer's data) and repeatedly rinsed in phosphate-buffered saline (PBS; Sigma, St. Louis, MO, USA). The samples were seeded with human osteosarcoma cell lines MG-63 (European Collection of Cell Cultures, Salisbury, England) in the initial density of 5370 cells/cm^2 (10,000 cells per well) or U-2 OS cell line (ATCC-LGC, Cat. No. HTB-96; Manassas, VA, USA) in densities ranging from 4300 cells/cm^2 (8000 cells per well) to 16,100 cells/cm^2 (30,000 cells per well). Both cell lines were cultured for 7 days in 1 mL of Dulbecco's Modified Eagle's Medium (Sigma, St. Louis, MO, USA, Cat. No. D5648), supplemented with 10% fetal bovine serum (Sebak GmbH, Ingelheim, Germany) and gentamicin (40 μg/mL; LEK, Ljubljana, Slovenia) at 37 °C in a humidified air atmosphere containing 5% of CO_2. Uncoated microscopic glass coverslips (Menzel Glaser, Braunschweig, Germany; diameter 12 mm) were used as reference material. Data from three separate experiments were evaluated. For each experimental group and time interval, three samples were analyzed.

3.7. Evaluation of Cell Morphology, Initial Adhesion and Proliferation (Growth Curves)

MG-63 cells were cultured for 7 days (seeding density 5370 cells/cm^2; 10,000 cells per well). The evaluation of cell morphology was performed on days 1, 3 and 7 after seeding by using an IX-71 microscope equipped with a DP-71 digital camera (Olympus, Shinjuku, Tokyo, Japan). Immediately after that, each sample was transferred to fresh polystyrene 24-well tissue culture plates and rinsed with PBS. The cells were detached by a trypsin-EDTA solution (Sigma, St. Louis, MO, USA, Cat. No. T4174) and counted using a Bürker haemocytometer (days 1 and 3) or Vi-Cell XR analyzer on day 7 (Beckman Coulter, Fullerton, CA, USA). The obtained cell numbers were expressed as cell population densities/cm^2 and used for the construction of growth curves and calculation of the cell population doubling time according the following formula:

$$DT = \log 2 \frac{t - t_0}{\log N_t - \log N_{t_0}}$$

where t_0 and t represent earlier and later time intervals after seeding, respectively, and N_{t0} and N_t the number of cells at these intervals.

Data from three separate experiments were analyzed. For each experimental group and time interval, three parallel samples were evaluated.

3.8. Evaluation of Cell Metabolic Activity

In order to investigate the metabolic activity of cells (which is an indirect measure of the cell proliferation activity), the commercial Cell Proliferation Kit II XTT (Roche, Basel, Switzerland, Cat. No. 11 465 015 001) was used. This is a colorimetric assays based on the cleavage of the yellow tetrazolium salt XTT (2,3-bis(2-methoxy-4-nitro-5-sulphophenyl)-2*H*-tetrazolium-5-carboxanilide) to a soluble orange formazane derivate by mitochondrial enzymes from metabolically active cells. The formazane dye is directly quantified by a spectrophotometer. After 3 and 7 days of cultivation, all samples were transferred to fresh polystyrene 24-well tissue culture plates and rinsed with PBS. To each sample, 1 mL solution of XTT and Dulbecco's Modified Eagle's Medium without Phenol Red (Gibco, Cat. No 11053-028) supplemented with 10% fetal bovine serum (Sebak GmbH, Ingelheim, Germany) and gentamicin (40 μg/mL; LEK, Ljubljana, Slovenia) in the ratio of 1 XTT to 2 DMEM was added (according the manufacturer's protocol). After 4–6 h of incubation at 37 °C in a humidified air atmosphere containing 5% of CO_2, absorbance of the resulting solution was measured at a wavelength of 470 nm against the reference value of 650 nm.

As the blank samples, a solution from C_{60} coated, as well as uncoated microscopic glass coverslips without seeded cells was used. Data from three separate experiments were analyzed. For each experimental group and time interval, three parallel samples were used and the solution from each well was divided into 8 parallel wells.

3.9. Evaluation of Membrane Damage and Cell Viability

On day 7 after seeding, cell viability and membrane damage of the cells were detected by trypan blue staining performed during cell counting in the Vi-Cell XR analyzer (Beckman Coulter, Fullerton, CA, USA). Data from three separate experiments were analyzed. For each experimental group 50 images from three parallel samples were evaluated.

3.10. Evaluation of DNA Damage Response

In order to investigate potential DNA damage of cells, osteosarcoma cell line U-2 OS was used instead of MG-63, which is p53 deficient. After 3 and 7 days of cultivation, DNA damage response was evaluated by immunofluorescence staining analyzed by fluorescence microscopy and flow cytometry.

The samples for microscopy were rinsed with PBS and fixed with 4% paraformaldehyde (PFA; Sigma, St. Louis, MO, USA) for 20 min at room temperature. Subsequently, the cells were permeabilized with 0.1% Triton X-100 in PBS (Sigma, St. Louis, MO, USA) for 20 min at room temperature. This solution also contained 1% bovine serum albumin for blocking non-specific binding sites for antibodies. The samples were incubated with primary antibodies anti-53BP1 (0.2 μg/mL; Santa Cruz Biotech, Dallas, TX, USA; clone H-300) and anti-H2A.X-Phosphorylated Ser139

(0.4 μg/mL; Millipore, Billerica, MA, USA; clone JBW301) for 1 h, followed by secondary antibodies coupled to Alexa Fluor 488 and 546 (4 μg/mL; Invitrogen, Molecular Probes, Eugene, OR, USA) for 1 h. Cells were then mounted with microscopic glass coverslips using a Gel/Mount permanent fluorescence-preserving aqueous mounting medium (Biomeda Corporation, Foster City, CA, USA) and evaluated under the epifluorescence microscope IX-71 (Olympus, Shinjuku, Tokyo, Japan) equipped with the digital camera DP-71 (Olympus, Shinjuku, Tokyo, Japan).

The samples analyzed by flow cytometry were prepared using the same protocol as those for microscopy, except that all steps were performed in suspension, not on microscopic glass coverslips. After 3 and 7 days of cultivation, three parallel samples from each experimental group were transferred to new polystyrene 24-well tissue culture plates and rinsed with PBS. The cells were detached by a trypsin-EDTA solution. The suspensions of three parallel samples were mixed together into one tube. For flow cytometry, an Alexa Fluor 488 anti-H2A.X-Phosphorylated (Ser139) antibody (5 μg/L million cells; BioLegend, San Diego, CA, USA; clone 2F3) was used. After 1 h of incubation with antibody, cells were rinsed and resuspended in PBS. The samples were analyzed by Accuri C6 Flow Cytometer (BD Biosciences, Franklin Lakes, NJ, USA).

U-2 OS treated with neocarzinostatin (NCS; 700 ng/mL; Sigma, St. Louis, MO, USA) for 1 h were used as a positive control for markers of DNA damage response. The cells were fixed 3 h after treatment with NCS. In order to confirm the results, the immunofluorescence staining, as well as flow cytometry analysis was repeated twice.

3.11. Statistical Analysis

Data were presented as the mean ± SEM (Standard Error of the Mean) obtained from three separate experiments. Three samples for each experimental group and time interval were evaluated. A comparison between three groups was analyzed with the ANOVA, Student–Newman–Keuls Method. In the case of two groups, the Student's *t*-test for unpaired data was used. *p*-values less than 0.05 were considered statistically significant.

4. Conclusions

Our study revealed that the colonization of fullerene C_{60} films with human osteoblast-like MG 63 cells was lower in comparison with control microscopic glass coverslips, which served as substrates for the fullerene deposition. This was indicated by lower cell numbers and lower metabolic activity, measured by XTT test, of cells on the C_{60} films. On C_{60} films with micropatterned morphology, the cells adhered preferentially in grooves among the prominences. All these differences were more pronounced on fresh (*i.e.*, one week old) than on aged (*i.e.*, one year old) fullerene films. On the fresh films, also the cell viability, measured by a trypan blue exclusion test, was lower than on control glass coverslips and aged fullerene layers. Nevertheless, studies performed on human osteoblast-like U-2 OS cells revealed no DNA damage response of these cells cultivated on fresh or aged fullerene films. The increasing age of the fullerene films resulted in an improvement of the physicochemical properties of these materials, which became more suitable for cell cultivation. Therefore, fullerene films could be considered as promising materials in bone tissue engineering, namely for potential coating of bone implants.

Acknowledgments

This study was supported by the Grant Agency of the Czech Republic (grant No. P107/11/1856). Sherryl Ann Vacik (P&A Consultants, Angel Fire, NM, USA) is gratefully acknowledged for her language revision of the manuscript.

References

1. Kroto, H.W.; Heath, J.R.; Obrien, S.C.; Curl, R.F.; Smalley, R.E. C60: Buckminsterfullerene. *Nature* **1985**, *318*, 162–163.
2. Aitken, R.J.; Chaudhry, M.Q.; Boxall, A.B.A.; Hull, M. Manufacture and use of nanomaterials: Current status in the UK and global trends. *Occup. Med.* **2006**, *56*, 300–306.
3. Kato, S.; Taira, H.; Aoshima, H.; Saitoh, Y.; Miwa, N. Clinical evaluation of fullerene-C60 dissolved in squalane for anti-wrinkle cosmetics. *J. Nanosci. Nanotechnol.* **2010**, *10*, 6769–6774.
4. Kato, S.; Aoshima, H.; Saitoh, Y.; Miwa, N. Fullerene-C60/liposome complex: Defensive effects against UVA-induced damages in skin structure, nucleus and collagen type I/IV fibrils, and the permeability into human skin tissue. *J. Photochem. Photobiol. B Biol.* **2010**, *98*, 99–105.
5. Foley, S.; Crowley, C.; Smaihi, M.; Bonfils, C.; Erlanger, B.F.; Seta, P.; Larroque, C. Cellular localisation of a water-soluble fullerene derivative. *Biochem. Biophys. Res. Commun.* **2002**, *294*, 116–119.
6. Venkatesan, N.; Yoshimitsu, J.; Ito, Y.; Shibata, N.; Takada, K. Liquid filled nanoparticles as a drug delivery tool for protein therapeutics. *Biomaterials* **2005**, *26*, 7154–7163.
7. Isobe, H.; Nakanishi, W.; Tomita, N.; Jinno, S.; Okayama, H.; Nakamura, E. Nonviral gene delivery by tetraamino fullerene. *Mol. Pharm.* **2006**, *3*, 124–134.
8. Dugan, L.L.; Gabrielsen, J.K.; Yu, S.P.; Lin, T.S.; Choi, D.W. Buckminsterfullerenol free radical scavengers reduce excitotoxic and apoptotic death of cultured cortical neurons. *Neurobiol. Dis.* **1996**, *3*, 129–135.
9. Dugan, L.L.; Lovett, E.G.; Quick, K.L.; Lotharius, J.; Lin, T.T.; O'Malley, K.L. Fullerene-based antioxidants and neurodegenerative disorders. *Parkinsonism Related Disord.* **2001**, *7*, 243–246.
10. Ryan, J.J.; Bateman, H.R.; Stover, A.; Gomez, G.; Norton, S.K.; Zhao, W.; Schwartz, L.B.; Lenk, R.; Kepley, C.L. Fullerene nanomaterials inhibit the allergic response. *J. Immunol.* **2007**, *179*, 665–672.
11. Tabata, Y.; Murakami, Y.; Ikada, Y. Photodynamic effect of polyethylene glycol-modified fullerene on tumor. *Jpn. J. Cancer Res.* **1997**, *88*, 1108–1116.
12. Tegos, G.P.; Demidova, T.N.; Arcila-Lopez, D.; Lee, H.; Wharton, T.; Gali, H.; Hamblin, M.R. Cationic fullerenes are effective and selective antimicrobial photosensitizers. *Chem. Biol.* **2005**, *12*, 1127–1135.
13. Käsermann, F.; Kempf, C. Photodynamic inactivation of enveloped viruses by buckminsterfullerene. *Antivir. Res.* **1997**, *34*, 65–70.
14. Bacakova, L.; Grausova, L.; Vandrovcova, M.; Vacik, J.; Frazcek, A.; Blazewicz, S.; Kromka, A.; Rezek, B.; Vanecek, M.; Nesladek, M.; *et al.* Carbon Nanoparticles as Substrates for Cell Adhesion and Growth. In *Nanoparticles: New Research*; Lombardi, S.L., Ed.; Nova Science Publishers, Inc.: Hauppauge, NY, USA, 2008; pp. 39–107.

15. Spohn, P.; Hirsch, C.; Hasler, F.; Bruinink, A.; Krug, H.F.; Wick, P. C60 fullerene: A powerful antioxidant or a damaging agent? The importance of an in-depth material characterization prior to toxicity assays. *Environ. Pollut.* **2009**, *157*, 1134–1139.
16. Kovochich, M.; Espinasse, B.; Auffan, M.; Hotze, E.M.; Wessel, L.; Xia, T.; Nel, A.E.; Wiesner, M.R. Comparative toxicity of C60 aggregates toward mammalian cells: Role of tetrahydrofuran (THF) decomposition. *Environ. Sci. Technol.* **2009**, *43*, 6378–6384.
17. Henry, T.B.; Menn, F.-M.; Fleming, J.T.; Wilgus, J.; Compton, R.N.; Sayler, G.S. Attributing effects of aqueous C60 nano-aggregates to tetrahydrofuran decomposition products in larval zebrafish by assessment of gene expression. *Environ. Health Perspect.* **2007**, *115*, 1059–1065.
18. Gharbi, N.; Pressac, M.; Hadchouel, M.; Szwarc, H.; Wilson, S.R.; Moussa, F. [60]fullerene is a powerful antioxidant *in vivo* with no acute or subacute toxicity. *Nano Lett.* **2005**, *5*, 2578–2585.
19. Huczko, A.; Lange, H.; Calco, E. Fullerenes: Experimental evidence for a null risk of skin irritation and allergy. *Full. Sci. Technol.* **1999**, *7*, 935–939.
20. Nelson, M.A.; Domann, F.E.; Bowden, G.T.; Hooser, S.B.; Fernando, Q.; Carter, D.E. Effects of acute and subchronic exposure of topically applied fullerene extracts on the mouse skin. *Toxicol. Ind. Health* **1993**, *9*, 623–630.
21. Sayes, C.M.; Marchione, A.A.; Reed, K.L.; Warheit, D.B. Comparative pulmonary toxicity assessments of C60 water suspensions in rats: Few differences in fullerene toxicity *in vivo* in contrast to *in vitro* profiles. *Nano Lett.* **2007**, *7*, 2399–2406.
22. Baker, G.L.; Gupta, A.; Clark, M.L.; Valenzuela, B.R.; Staska, L.M.; Harbo, S.J.; Pierce, J.T.; Dill, J.A. Inhalation toxicity and lung toxicokinetics of C60 fullerene nanoparticles and microparticles. *Toxicol. Sci.* **2008**, *101*, 122–131.
23. Yudoh, K.; Shishido, K.; Murayama, H.; Yano, M.; Matsubayashi, K.; Takada, H.; Nakamura, H.; Masuko, K.; Kato, T.; Nishioka, K. Water-soluble C60 fullerene prevents degeneration of articular cartilage in osteoarthritis via down-regulation of chondrocyte catabolic activity and inhibition of cartilage degeneration during disease development. *Arthrit. Rheum.* **2007**, *56*, 3307–3318.
24. Yudoh, K.; Karasawa, R.; Masuko, K.; Kato, T. Water-soluble fullerene (C60) inhibits the development of arthritis in the rat model of arthritis. *Int. J. Nanomed.* **2009**, *4*, 217–225.
25. Yudoh, K.; Karasawa, R.; Masuko, K.; Kato, T. Water-soluble fullerene (C60) inhibits the osteoclast differentiation and bone destruction in arthritis. *Int. J. Nanomed.* **2009**, *4*, 233–239.
26. Kasai, T.; Matsumura, S.; Iizuka, T.; Shiba, K.; Kanamori, T.; Yudasaka, M.; Iijima, S.; Yokoyama, A. Carbon nanohorns accelerate bone regeneration in rat calvarial bone defect. *Nanotechnology* **2011**, *22*, 065102.
27. Bacakova, L.; Grausova, L.; Vacik, J.; Fraczek, A.; Blazewicz, S.; Kromka, A.; Vanecek, M.; Svorcik, V. Improved adhesion and growth of human osteoblast-like MG 63 cells on biomaterials modified with carbon nanoparticles. *Diam. Related Mater.* **2007**, *16*, 2133–2140.
28. Grausova, L.; Vacik, J.; Bilkova, P.; Vorlicek, V.; Svorcik, V.; Soukup, D.; Bacakova, M.; Lisa, V.; Bacakova, L. Regionally-selective adhesion and growth of human osteoblast-like MG 63 cells on micropatterned fullerene C60 layers. *J. Optoelectron. Adv. Mater.* **2008**, *10*, 2071–2076.
29. Grausova, L.; Vacik, J.; Vorlicek, V.; Svorcik, V.; Slepicka, P.; Bilkova, P.; Vandrovcova, M.; Lisa, V.; Bacakova, L. Fullerene C60 films of continuous and micropatterned morphology as substrates for adhesion and growth of bone cells. *Diam. Related Mater.* **2009**, *18*, 578–586.

30. Vandrovcova, M.; Vacik, J.; Svorcik, V.; Slepicka, P.; Kasalkova, N.; Vorlicek, V.; Lavrentiev, V.; Vosecek, V.; Grausova, L.; Lisa, V.; *et al.* Fullerene C60 and hybrid C60/Ti films as substrates for adhesion and growth of bone cells. *Phys. Status Solidi A* **2008**, *205*, 2252–2261.
31. Vacik, J.; Lavrentiev, V.; Novotna, K.; Bacakova, L.; Lisa, V.; Vorlicek, V.; Fajgar, R. Fullerene (C60)–transitional metal (Ti) composites: Structural and biological properties of the thin films. *Diam. Related Mater.* **2010**, *19*, 242–246.
32. Jirka, I.; Vandrovcova, M.; Frank, O.; Tolde, Z.; Plsek, J.; Luxbacher, T.; Bacakova, L.; Stary, V. On the role of Nb-related sites of an oxidized β-TiNb alloy surface in its interaction with osteoblast-like MG-63 cells. *Mater. Sci. Eng. C* **2013**, *33*, 1636–1645.
33. Bacakova, L.; Svorcik, V. Cell Colonization Control by Physical and Chemical Modification of Materials. In *Cell Growth Processes: New Research*; Kimura, D., Ed.; Nova Science Publishers, Inc.: Hauppauge, NY, USA, 2008; pp. 5–56.
34. Bacakova, L.; Filova, E.; Parizek, M.; Ruml, T.; Svorcik, V. Modulation of cell adhesion, proliferation and differentiation on materials designed for body implants. *Biotechnol. Adv.* **2011**, *29*, 739–767.
35. Bacakova, L.; Grausova, L.; Vacik, J.; Kromka, A.; Biederman, H.; Choukourov, A.; Stary, V. Nanocomposite and Nanostructured Carbon-based Films as Growth Substrates for Bone Cells. In *Advances in Diverse Industrial Applications of Nanocomposites*; Reddy, B., Ed.; InTech: Vienna, Austria, 2011; pp. 399–435.
36. Webster, T.J.; Ergun, C.; Doremus, R.H.; Siegel, R.W.; Bizios, R. Specific proteins mediate enhanced osteoblast adhesion on nanophase ceramics. *J. Biomed. Mater. Res.* **2000**, *51*, 475–483.
37. Kim, K.T.; Jang, M.H.; Kim, J.Y.; Kim, S.D. Effect of preparation methods on toxicity of fullerene water suspensions to Japanese medaka embryos. *Sci. Total Environ.* **2010**, *408*, 5606–5612.
38. Zhao, X.; Striolo, A.; Cummings, P.T. C60 binds to and deforms nucleotides. *Biophys. J.* **2005**, *89*, 3856–3862.
39. Xu, X.; Wang, X.; Li, Y.; Wang, Y.; Yang, L. A large-scale association study for nanoparticle C60 uncovers mechanisms of nanotoxicity disrupting the native conformations of DNA/RNA. *Nucleic Acids Res.* **2012**, *40*, 7622–7632.
40. Band, I.M.; Kharitonov, Yu, I.; Trzhaskovskaya, M.B. Photoionization cross sections and photoelectron angular distributions for X-ray line energies in the range 0.132–4.509 keV targets: $1 \leq Z \leq 100$. *At. Data Nuclear Data Tables* **1979**, *23*, 443–505.
41. Tanuma, S.; Powell, C.J.; Penn, D.R. Calculations of electron inelastic mean free paths. IX. Data for 41 elemental solids over the 50 eV to 30 keV range. *Surf. Interface Anal.* **2011**, *43*, 689–713.
42. Jiricek, P. Measurement of the transmission function of the hemispherical energy analyzer of ADES 400 electron spectrometer. *Czechoslov. J. Phys.* **1994**, *44*, 261–267.

PLOS | ONE

RESEARCH ARTICLE

Growth and Potential Damage of Human Bone-Derived Cells Cultured on Fresh and Aged C_{60}/Ti Films

Ivana Kopova[1]*, Vasily Lavrentiev[2], Jiri Vacik[2], Lucie Bacakova[1]

1 Institute of Physiology, Czech Academy of Sciences, Videnska 1083, 142 20, Prague, 4—Krc, Czech Republic, **2** Nuclear Physics Institute, Czech Academy of Sciences, 250 68, Rez near Prague, Czech Republic

* ivana.kopova@biomed.cas.cz

Citation: Kopova I, Lavrentiev V, Vacik J, Bacakova L (2015) Growth and Potential Damage of Human Bone-Derived Cells Cultured on Fresh and Aged C_{60}/Ti Films. PLoS ONE 10(4): e0123680. doi:10.1371/journal.pone.0123680

Academic Editor: Juha Tuukkanen, University of Oulu, FINLAND

Received: May 2, 2014

Accepted: March 6, 2015

Published: April 15, 2015

Data Availability Statement: Tha data underlying our findings is available either freely in the manuscript in the form of pictures (qualitative data) or in the form of Mean ± S.E.M. The data from which these values was calculated is available upon request.

Funding: This research was supported by the Grant Agency of the Czech Republic (grants No. P107/11/1856 and P108/12/1168) and CANAM infrastructure (NPI ASCR Rez).

Competing Interests: The authors have declared that no competing interests exist.

Abstract

Thin films of binary C_{60}/Ti composites, with various concentrations of Ti ranging from ~ 25% to ~ 70%, were deposited on microscopic glass coverslips and were tested for their potential use in bone tissue engineering as substrates for the adhesion and growth of bone cells. The novelty of this approach lies in the combination of Ti atoms (i.e., widely used biocompatible material for the construction of stomatological and orthopedic implants) with atoms of fullerene C_{60}, which can act as very efficient radical scavengers. However, fullerenes and their derivatives are able to generate harmful reactive oxygen species and to have cytotoxic effects. In order to stabilize C_{60} molecules and to prevent their possible cytotoxic effects, deposition in the compact form of Ti/C_{60} composites (with various Ti concentrations) was chosen. The reactivity of C_{60}/Ti composites may change in time due to the physicochemical changes of molecules in an air atmosphere. In this study, we therefore tested the dependence between the age of C_{60}/Ti films (from one week to one year) and the adhesion, morphology, proliferation, viability, metabolic activity and potential DNA damage to human osteosarcoma cells (lines MG-63 and U-2 OS). After 7 days of cultivation, we did not observe any negative influence of fresh or aged C_{60}/Ti layers on cell behavior, including the DNA damage response. The presence of Ti atoms resulted in improved properties of the C_{60} layers, which became more suitable for cell cultivation.

Introduction

Fullerenes are spheroidal hollow cage-like carbon nanoparticles with diverse biological activities. Due to their unique physicochemical properties, e.g. the ability to withstand high temperatures and pressures, and also the high reactivity of these nanoparticles, fullerenes are expected to have great potential in a wide range of fields including medicine. The high reactivity of these molecules has been explained by bending of sp^2-hybridized carbon atoms, which produces angle strain, and by the presence of double bonds, which can react with radical species. Fullerenes C_{60} and their derivatives are therefore considered to be the world's most efficient radical

scavengers with strong antioxidant properties (for a review, see [1, 2]). For example, fullerene C_{60} and its derivative fullerol has been reported to antagonize the oxidative stress generated by dexamethasone therapy, and thus to prevent osteonecrosis [3, 4]. By quenching oxygen radicals, fullerenes C_{60} also inhibit the differentiation of osteoclasts and the production of matrix metalloproteases, and can thus inhibit the destruction of bone and cartilage tissue in arthritis [5, 6]. Complexes of fullerenes with polyvinylpyrrolidone (with fullerene C_{60} as the major component) displayed photoprotective effects on keratinocytes against ultraviolet B irradiation [7].

However, fullerenes are able not only to quench, but also to generate dangerous reactive oxygen species (ROS). Numerous studies have described fullerenes as a cytotoxic and genotoxic agent, causing oxidative DNA damage [8, 9], inhibition of detoxificatory and antioxidant enzymes [10], polyploidy [11], premature cell senescence [12], apoptosis [13] and inflammation [14]. The biological response to fullerenes is profoundly influenced by their physical and chemical properties, such as water solubility [15]; for a review, see [16], functionalization with various chemical groups [17], electronic behavior, degree of agglomeration [13], and also concentration [14]. For example, increased water solubility was associated with decreased cytotoxicity of C_{60}. On the other hand, certain solvents can enhance fullerene toxicity (for a review, see [16]). The carboxylate derivatization of fullerenes was the determining factor in their ability to induce apoptosis in human monocytic THP1 cells [13]. At lower concentrations (less than 0.04mg/ml), fullerene-based amino acid nanoparticles 0.04 mg/mL initiated less cytokine activity and maintained the viability of human keratinocytes, while at higher concentrations (0.04 to 0.4 mg/ml) these nanoparticles were cytotoxic and pro-inflammatory [14].

In order to prevent possible cytotoxic effects of fullerenes, deposition of these molecules in the form of compact and stable layers, well-adhering to the underlying substrate, was chosen. We supposed that the fullerene films could be strengthened by introducing a biocompatible metallic component into the films. Fullerene C_{60}-gold nanoparticle films, self-assembled on silanized glass coverslips, showed good chemical and ultrasonic stability, as revealed by their immersion in 0.1 M HCl and by their exposure to ultrasonic irradiated surrounding [18]. The introduction of a suitable metallic component was expected to stabilize the fullerene films in terms of reducing the release of free C_{60}, their penetration into cells, and thus to eliminate the potential negative effects of fullerenes. Titanium was chosen as this metallic component, due its biocompatibility, which has been proven in its numerous and long-lasting experimental and clinical applications. Titanium is a metal that has been widely used for constructing stomatological implants and, in the form of alloys, such as Ti-6Al-4V or newly developed beta-titanium alloys, also for orthopedic implants, such as load-bearing joint replacements [19–22]; for a review, see [23]. Titanium was also tested with positive results in our earlier studies as a potential component of carbon-based coatings of bone implants, namely amorphous carbon with titanium [24] or hydrocarbon plasma polymers enriched with Ti [25]. Specifically, the presence of Ti in these coatings enhanced the adhesion, spreading, growth and production of osteocalcin in human osteoblast-like MG-63 cells. The presence of Ti in diamond-like carbon (DLC) coatings also increased their bioactivity compared to pure DLC. This was manifested by precipitation of compounds containing calcium and phosphorus, i.e., basic components of the bone apatite, and by increased colonization of Ti-doped DLC with human osteoblast-like MG 63 cells [26]. At the same time, the addition of Ti into DLC coatings improved their mechanical properties, namely by increasing their adhesion to the underlying substrates [27], by decreased their residual stress and friction coefficient, and by modulating their hardness to appropriate values [28, 29].

The construction of C_{60}/Ti composites in this study was also inspired by our earlier studies and by studies by other authors, in which C_{60} was combined with transitional metals, namely Ni, Fe, Nb, Pt and Pd [30–34]. These composites showed interesting structural, electrotransport,

electrochemical and photoelectric properties, and are applicable in electronics or photovoltaics [35]; for a review, see [33]. However, with the exception of Nb, which is considered as biocompatible, all metals mentioned here are known to be cytotoxic. To the best of our knowledge, C_{60}/Ti composite films, with the exception of our earlier studies [36, 37], have not yet been constructed and investigated for biomedical purposes by other authors. In our earlier studies, only the adhesion and growth of MG-63 cells, measured by changes in their number in three time intervals, were investigated on C_{60}/Ti composite films, together with regional selectivity of cell colonization, if these films were constructed as micropatterned, i.e. containing grooves and prominences [36, 37]. The novelty of present study lies in the deeper investigation of the cell behavior on C_{60}/Ti films, including not only their adhesion and growth, but also their viability, mitochondrial activity, and potential DNA damage.

Another important factor investigated in our study is the influence of the age of C_{60}/Ti composites on these parameters, as well as on the regional selectivity of the cell colonization on films with a micropatterned morphology. In our earlier study performed on pure fullerene C_{60} films, fresh fullerene films lowered the cell number, viability, growth and metabolic activity, and these parameters improved markedly with aging of the C_{60} films [38]. Moreover, micropatterned fresh fullerene films promoted regionally-selective cell colonization in grooves among the prominences, which almost disappeared on aged fullerene films. These results were attributed to changes in the fullerene films during aging, e.g. fragmentation, oxidation, polymerization and graphitization of fullerenes in an air atmosphere, and thus loss of their reactivity [38].

Last but not least, the C_{60}/Ti fullerene films in the present study were deposited with three different concentrations of Ti, ranging from ~ 25% (i.e., 25 Ti atoms and 75 C_{60} molecules) to ~ 70%, in order to investigate potential differences in their stability and in the cell behavior on these surfaces. On DLC films doped with three concentration levels of Ti (up to 23 at. %), the number of MG-63 cells increased with the increasing Ti concentration. They were highest on DLC with a medium and highest content of Ti [26].

Material and Methods

Material deposition

The C_{60}/Ti composite films were prepared by co-deposition of C_{60} and Ti onto microscopic glass coverslips (Menzel-Gläser, Germany, diameter 12 mm) in the Molecular Beam Epitaxy (MBE) chamber using the Knudsen cell and an e—gun for vaporization of C_{60} and Ti, respectively (**Fig 1**), under certain deposition kinetics: background pressure during deposition ~ 5×10^{-7} Torr; deposition rate ~ 1 nm/min; temperature of the substrates during deposition ~ room temperature (RT). Three C_{60}/Ti systems, with different phase ratios, were fabricated, i.e., with a low concentration (25%, i.e., 25 Ti atoms and 75 C_{60} molecules), medium concentration (45%) and high concentration (70%) of Ti atoms in the composite.

The composites were synthesized with a micropatterned morphology by deposition through a contact mask (a metallic mesh) producing rectangular C_{60}/Ti prominences with an average size of 128 μm per 98 μm (12,500 μm^2) and with 50 μm spacing. However, as revealed by Raman spectroscopy and AFM, these spaces (grooves) also contained a very thin continuous film of C_{60}/Ti composites.

The samples were stored for 1–2 weeks (fresh samples) or for 1 year (aged samples) in an air atmosphere at room temperature in a dark and dry place, and were then evaluated.

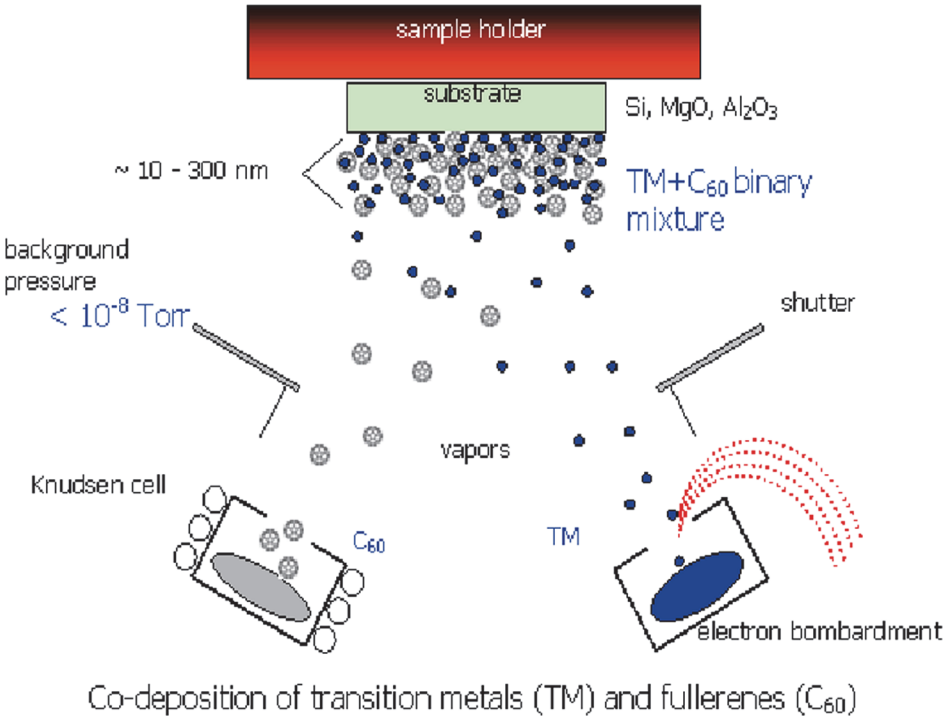

Fig 1. Scheme of the preparation of hybrid fullerene C_{60}/metal composites. Deposition rates: DR(M) = DR(C_{60}) ~ 1 nm/min. Temperatures during deposition: RT.

doi:10.1371/journal.pone.0123680.g001

Raman spectroscopy

A Renishaw 2000 imaging microscope (using a 514 nm Ar laser) was applied for an analysis of the C_{60}/Ti films. The measurements were performed using low laser power, i.e., (< 1 mW) in order to avoid fragmentation of the C_{60} molecules. The spectra were measured on the top of the C_{60}/Ti prominences, using multi-peak Gaussian analysis of the $H_g(7)$, $A_g(2)$ and $H_g(8)$ vibration peaks. Area peak ratios $A_g(2)/H_g(7)$ and $A_g(2)/H_g(8)$ were evaluated.

Atomic force microscopy (AFM)

The surface morphologies of the C_{60}/Ti layers were analyzed by atomic force microscopy (AFM microscope NTEGRA, NT-MDT) using a static (contact) mode. The scanning area was selected as 5 x 5 μm^2.

Stability of C_{60}/Ti coating (potential water dissolution)

All examined C_{60}/Ti coatings with a low, medium and high content of Ti were incubated in 1 ml of deionized water at 37°C in a humidified air atmosphere containing 5% of CO_2 for 24 hours (mimicking the rinsing phase prior to use for all biological experiments; described below in Cells and culture conditions). After 24 hours, the water was transferred from the C_{60}/Ti samples to glass Petri dishes (diameter 2 cm), and fresh deionized water was added to the same C_{60}/Ti samples for further 48 hour-long incubation (mimicking the incubation phase with cells in biological experiments). The water solutions were slowly dried on glass Petri dishes for 2 days. When all water was evaporated, the thin films that had formed on the bottom of the Petri dishes were analyzed by Raman spectroscopy.

Measurement of wettability

The surface wettability of the C_{60}/Ti composites was estimated from the contact angle measured by a material-water droplet system using a reflection goniometer (SEE System, Masaryk University, Brno, Czech Republic). The data was presented as mean ± standard error of the mean (S.E.M.) obtained from 10 measurements.

Cells and culture conditions

Since the samples were prepared under aseptic conditions (assured by the high temperature), sterilization was not performed in order to avoid potential damage to the fullerene molecules by irradiation, heating or chemicals. However, to prevent the potential release of newly deposited C_{60}/Ti molecules into the culture medium, all samples (i.e., glass coverslips coated with C_{60}/Ti films with various Ti concentrations) were incubated in deionized water at 37°C in a humidified air atmosphere containing 5% of CO_2 for 24 hours prior to each biological experiment. The samples were then repeatedly rinsed in phosphate-buffered saline (PBS; Sigma, Missouri, U.S.A.). For studies on cell adhesion, spreading, growth, morphology, viability and metabolic activity, the samples were seeded with human osteoblast-like MG-63 cells (European Collection of Cell Cultures, UK) in an initial density of 5 370 cells/cm^2 (10 000 cells per well). For studies on DNA damage, human osteoblast-like U-2 OS cells (ATCC-LGC, No. HTB-96) were used in densities ranging from 4 300 cells/cm^2 (8 000 cells per well) to 16 100 cells/cm^2 (30 000 cells per well). Both cell lines were cultured for 1, 3 or 7 days in 1 mL of Dulbecco's Modified Eagle's Medium (Sigma, Missouri, U.S.A., Cat. No. D5648) supplemented with 10% fetal bovine serum (Sebak GmbH, Germany) and gentamicin (40 μg/mL; LEK, Slovenia) at 37°C in a humidified air atmosphere containing 5% of CO_2. Uncoated microscopic glass coverslips (Menzel-Gläser, Germany; diameter 12 mm) were used as a reference material. For each experimental group and time interval, 3 samples were analyzed, and the experiment was repeated three times.

Evaluation of cell morphology, initial adhesion and proliferation

The MG-63 cells were cultured for 7 days (seeding density 5 370 cells/cm^2; 10 000 cells per well). An evaluation of the cell morphology was performed on days 1, 3 and 7 after seeding, using an IX-71 microscope equipped with a DP-71 digital camera (Olympus, Japan). Immediately after that, each sample was transferred to fresh polystyrene 24-well tissue culture plates and rinsed with PBS. The cells were detached by a trypsin-EDTA solution (Sigma, Missouri, U.S.A., Cat. No T4174) and were counted using a Bürker haemocytometer (days 1 and 3) or using a Vi-Cell XR analyzer on day 7 (Beckman Coulter, California, U.S.A.). The cell numbers were expressed as cell population densities/cm^2 and were also used for calculating the cell population doubling time according to the following formula:

$$DT = \log 2 \frac{t - t_0}{\log N_t - \log N_{t_0}}$$

where t_0 and t represent earlier and later time intervals after seeding, respectively, and N_{t0} and N_t are the numbers of cells at these intervals.

In order to confirm the validity of the results, the experiments were repeated and data from separate experiments was analyzed. For each experimental group and time interval, three parallel samples were evaluated, and the experiment was repeated three times.

Evaluation of cell metabolic activity

The commercial Cell Proliferation Kit II XTT (Roche, Switzerland, Cat.No.11 465 015 001) was used to investigate the potential cytotoxicity of the C_{60}/Ti films. This is a set of colorimetric assays based on cleavage of the yellow tetrazolium salt XTT (2,3-bis(2-methoxy-4-nitro-5-sulphophenyl)-2H-tetrazolium-5-carboxanilide) to a soluble orange formazane derivate by mitochondrial enzymes from metabolically active cells (an indirect measure of the cell proliferation activity). The formazane dye is directly quantified by a spectrophotometer. After 3 and 7 days of cultivation, all samples were transferred to new polystyrene 24-well tissue culture plates and were rinsed with PBS. A 1 mL solution of XTT and Dulbecco's Modified Eagle's Medium without Phenol Red (Gibco, Cat. No 11053–028), supplemented with 10% fetal bovine serum (Sebak GmbH, Germany) and gentamicin (40 μg/mL; LEK, Slovenia) in the ratio of 1 volume part of XTT to 2 volume parts of DMEM, was added to each sample (according to the manufacturer's protocol). After 4–6 hours of incubation at 37°C in a humidified air atmosphere containing 5% of CO_2, the absorbance of the resulting solution was measured at wavelength 470 nm against the reference value of 650 nm.

Solutions from C_{60}/Ti-coated samples and also from uncoated microscopic glass coverslips without seeded cells were used as blank samples. In order to confirm the validity of the results, the experiment was repeated three times, and the data from separate experiments was analyzed. For each experimental group and time interval within one experiment, three parallel samples were used and the solution from each well was divided into 8 parallel wells.

Evaluation of membrane damage and cell viability

On day 7 after seeding, cell viability and membrane damage to cells were detected by trypan blue staining performed during cell counting in the Vi-CELL XR analyzer (Beckman Coulter, California, U.S.A.). Data from three separate experiments was analyzed. For each experimental group, 50 images from three parallel samples were evaluated within one experiment.

Evaluation of the DNA damage response

In order to investigate potential DNA damage to the cells, osteosarcoma cell line U-2 OS was used instead of MG-63, which is p53 deficient. After 3 and 7 days of cultivation, the DNA damage response was evaluated by immunofluorescence staining analyzed by fluorescence microscopy and flow cytometry.

The samples for microscopy were rinsed with PBS and fixed with 4% paraformaldehyde (PFA; Sigma, Missouri, U.S.A.) for 20 minutes at room temperature. Subsequently, the cells were permeabilized with 0.1% Triton X-100 in PBS (Sigma, Missouri, U.S.A.) for 20 minutes at room temperature. This solution also contained 1% bovine serum albumin for blocking non-specific binding sites for antibodies. The samples were incubated with primary antibodies anti-53BP1 (0.2 μg/mL; Santa Cruz Biotech, California, U.S.A.; clone H-300) and anti-H2A.X-Phosphorylated Ser139 (0.4 μg/mL; Millipore, Massachusetts, U.S.A.; clone JBW301) for 1 hour, followed by secondary antibodies coupled to Alexa Fluor 488 and 546 (4 μg/mL; Invitrogen, Molecular Probes, Oregon, U.S.A.) for 1 hour. The cells were then mounted with a microscopic glass coverslip using a Gel/Mount permanent fluorescence-preserving aqueous mounting medium (Biomeda Corporation, California, U.S.A.) and were evaluated under the IX-71 epifluorescence microscope (Olympus, Japan) equipped with a DP-71 digital camera (Olympus, Japan).

The samples analyzed by flow cytometry were prepared using the same protocol as those for microscopy, except that all steps were performed in a suspension, not on microscopic glass coverslips. Alexa Fluor 488 anti-H2A.X-Phosphorylated (Ser139) antibody (5 μg/1 million cells; BioLegend, California, U.S.A.; clone 2F3) was used for flow cytometry. After 1 hour of incubation

with antibody, the cells were rinsed and resuspended in PBS. The samples were analyzed using an Accuri C6 Flow Cytometer (BD Biosciences, New Jersey, U.S.A.).

U-2 OS treated with neocarzinostatin (NCS; 700 ng/mL; Sigma, Missouri, U.S.A.) for 1 hour were used as a positive control to markers of a DNA damage response. The cells were fixed 3 hours after treatment with NCS. Immunofluorescence staining and also flow cytometry analysis were repeated in order to confirm the results.

Statistical analysis

The data was presented as mean ± S.E.M. (Standard Error of the Mean) or median with interquartile range (IQR) obtained from three separate experiments. Within each experiment, three samples for each experimental group and time interval were evaluated. A comparison between all groups was analyzed by two-way ANOVA, Student-Newman-Keuls Method, to evaluate two factors: the composition of the C_{60}/Ti layers (Ti content—25%, 45%, 70%) and their age (1 week or 1 year). *P*-values less than 0.05 were considered statistically significant.

Results and Discussion

Raman spectroscopy

A study by Raman spectroscopy measured on the top of the prominences revealed a change in both the fresh and aged fullerene films, in comparison with the C_{60} standard. **Fig 2A** depicts the Raman spectra (only relevant details between 1100–1800 cm^{-1}) measured on the fresh (i.e., 1-week-old) C_{60}/Ti composites deposited on glass coverslips at RT with a low (25%), medium (45%) and high (70%) concentration of Ti. For comparison, a Raman spectrum from the C_{60} standard (a film of C_{60} deposited on glass coverslips) is also shown. The main Raman vibration modes for fullerenes: $A_g(2)$, $H_g(7)$ and $H_g(8)$ were inspected. For all fresh layers, a change in the spectra revealed that the intensity of the most important $A_g(2)$ peak (pentagonal pinch mode, characteristic for fullerenes) dropped dramatically down (compared to the neighboring $H_g(7)$ and $H_g(8)$ vibration modes). Moreover, the $A_g(2)$ peak exhibits a significant red shift towards position 1450 cm^{-1}. The $H_g(7)$ and $H_g(8)$ modes remained on the same positions, but the area ratios $H_g(7)/A_g(2)$ and $H_g(8)/A_g(2)$ altered in comparison with the C_{60} standard. These changes are ascribed to alterations in the chemical bonding of C_{60}, such as polymerization (interaction of fullerene molecules into a polymerized network) and oxidation (chemical bonding of oxygen with fullerene molecules) [39]. It is known that $A_g(2)$ is the most sensitive vibration mode—by analyzing this mode one can get information about the C_{60} structural and bonding change (high sensitivity of Ti/C_{60} towards oxidation is described e.g. in [30]). All these changes are more obvious with increasing Ti content. In addition, new vibration modes G appeared in layers with a low and medium Ti content, indicating the formation of graphitic flakes.

An examination of aged (i.e., 1-year-old) C_{60}/Ti composites revealed dramatic difference in comparison with the fresh samples. The most important $A_g(2)$ mode is suppressed for all Ti concentrations, and $H_g(8)$ and G (formation of graphitic flakes and fragmentation of fullerenes) became the most prominent peaks. Another important difference of aged layers is the formation of the D band in films with low and medium Ti content, indicating disordered nanocarbon with sp^3 bonding (**Fig 2B**).

Degradation and oxidation of C_{60} films during aging was also proven by X-ray Photoelectron Spectroscopy (XPS) in our earlier study [38]. Alterations and fragmentation of fullerenes are enhanced in hybrid systems (transition metal/C_{60}) because of the strong catalytic properties of transition metals (including Ti) during co-deposition, which may cause the fullerene decay. The effect of aging was therefore least obvious in the samples with a high Ti concentration.

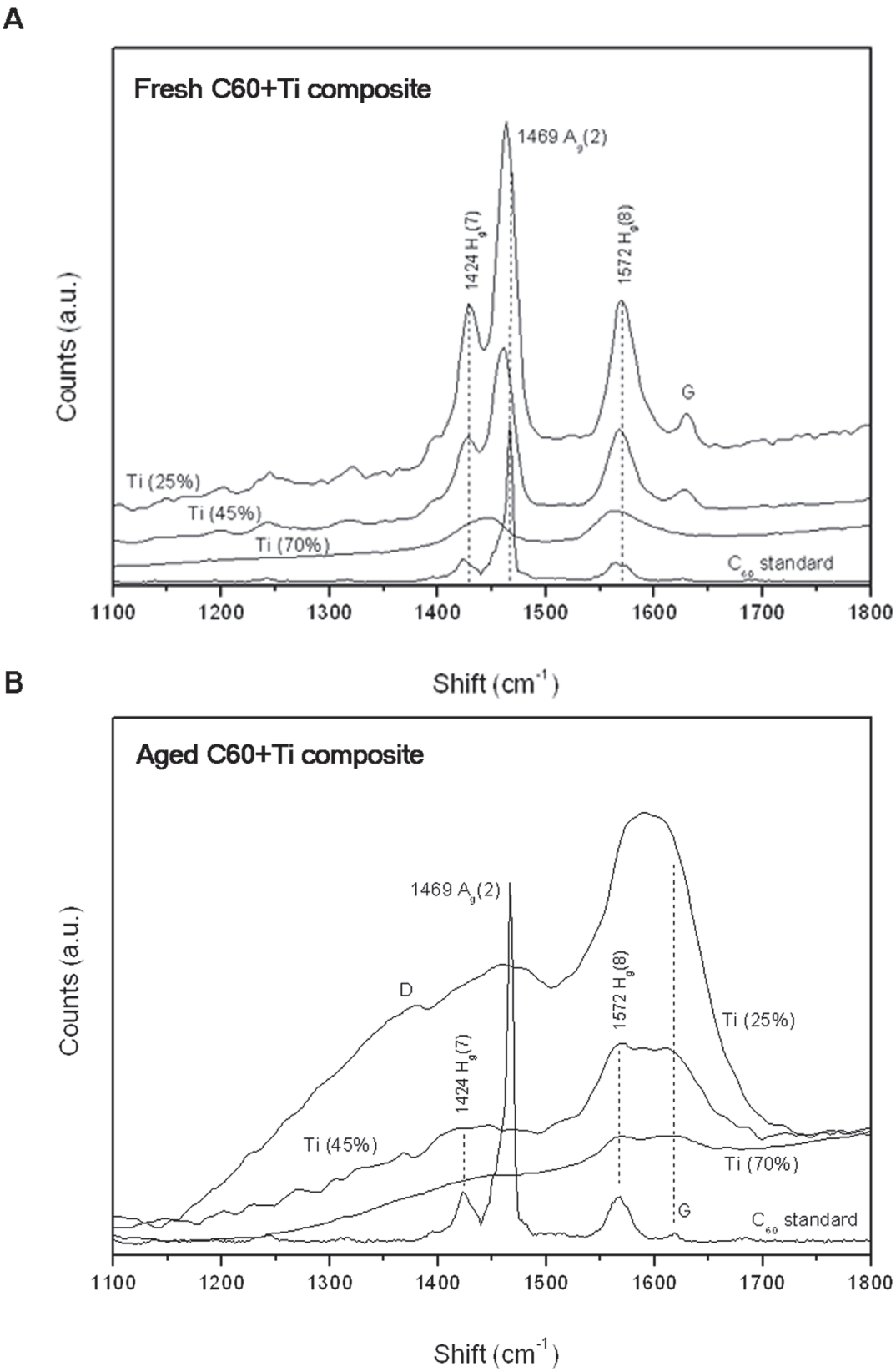

Fig 2. Raman spectra (between 1100–1800 cm^{-1}) of the fresh *(A)* and aged *(B)* C_{60}/Ti composites with various Ti concentrations (low: 25%, medium: 45%, high: 70%). For comparison, a spectrum from the C_{60} standard is shown.

doi:10.1371/journal.pone.0123680.g002

Based on reports from a similar system (with the combination of immiscible phases, i.e., C_{60}/Ni), the transition metal–fullerene hybrid composites, deposited at RT, are structurally stressed and exhibit a tendency toward phase separation [31, 32]. The final structure depends on the ratio of the building blocks (Ti and C_{60}), the thickness of the film and the temperature of preparation. Obviously, the different structure with different chemical bonds and surface morphology can have a different effect on the adhesion and growth of cells in biological systems.

Atomic force microscopy (AFM)

The morphology of the C_{60}/Ti films was analyzed by AFM (Fig 3) in the 5 x 5 μm^2 scanning areas. The thickness of the films varied from 10 nm (in grooves among the prominences) to about 300 nm (on the tops of the prominences). The ratio between the thicknesses of the C_{60}/Ti films at the prominences and in the grooves changed in the course of time, i.e., the ratio became lower in the aged composites (Table 1). This could be explained by a decrease in the height of the prominences after diffusion of the fullerenes, which was also observed in our earlier studies performed on pure micropatterned C_{60} films [38, 40].

In addition, the AFM images from the top of the prominences of all deposited systems with low (25%), medium (45%) and high (70%) atomic concentrations of Ti exhibited an interesting feature—the formation of particles with a different size (*S*) and area density (*D*), see Table 1. These particles, grown on the surface of the samples, were inspected by Raman spectroscopy and it was confirmed that they are large fullerene clusters with a low concentration of the Ti phase (causing only a mild disruption of the $A_g(2)$ pinch mode). This interesting effect was

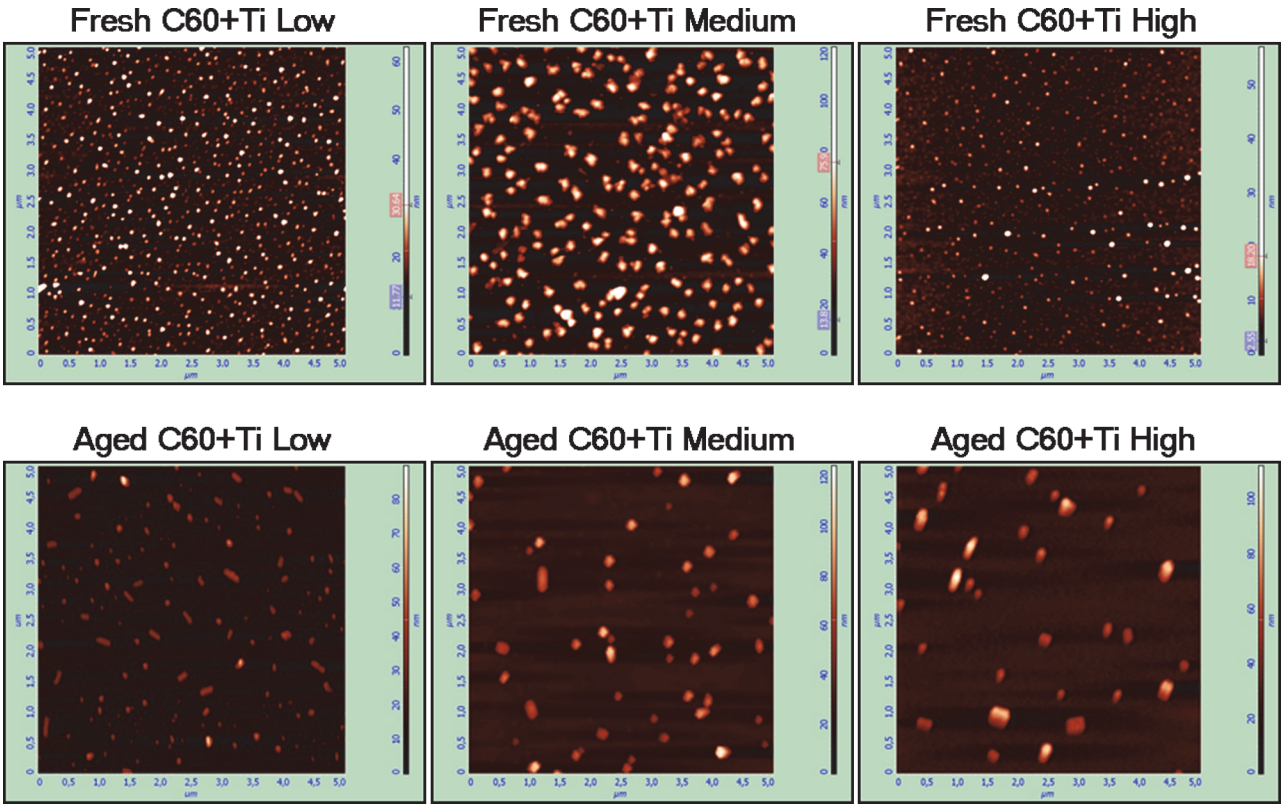

Fig 3. AFM images of the surface morphology on the prominences of the fresh and aged C_{60}/Ti composites with various Ti concentrations (low: 25%, medium: 45%, high: 70%).

doi:10.1371/journal.pone.0123680.g003

Table 1.

Parameter	Fresh C_{60}/Ti films	Aged C_{60}/Ti films
TP_{25} / TG_{25}	~ 8.3	~ 3.5
S_{25} [nm]	50–100	50–200
D_{25} [particles / 25 μm^2]	~ 650	~ 150
TP_{45} / TG_{45}	~ 10	~ 5.3
S_{45} [nm]	100–200	50–200
D_{45} [particles / 25 μm^2]	~ 250	50
TP_{70} / TG_{70}	~ 11.6	~ 4
S_{70} [nm]	25–75	50–150
D_{70} [particles / 25 μm^2]	~ 250	30

Main characteristics of the surface morphology of the prominences for fresh and aged (1-year-old) C_{60}/Ti thin films with various Ti concentrations (low: 25%, medium: 45%, high: 70%). TP/TG—ratio between the thickness of the prominences and the thickness of the grooves, S—particle size, D—particle area density. Scanning areas: 5 x 5 μm^2.

doi:10.1371/journal.pone.0123680.t001

already observed for the C_{60}/Ni hybrid system that was also prepared at RT [34]. The C_{60}/Ni composite was grown as a stressed, supersaturated mixture of two immiscible phases showing a strong proclivity to phase separation and particle network formation. After a year, about 200 particles per mm^{-2} several micrometers in size were formed. Interestingly, in the case of the C_{60}/Ti composites, all the observed particles had become smaller in size, the largest being only about 200 nm. The reason might be a limited reservoir (from a single prominence) for the diffusing fullerene molecules (building blocks for the grown particles), or different stress intensity (in comparison to the C_{60}/Ni system). On the other hand, the size of the C_{60}/Ti particles was larger than the typical granule size observed on pure C_{60} layers (~50 nm) [38]. In both (fresh and aged) cases, however, the morphology of the prominences changed, and this new nonostructural surface may be expected also to affect the biocompatibility of the hybrid system.

In addition, a different density of these clusters was observed on fresh and aged C_{60}/Ti layers. The number of C_{60}/Ti particles was higher on the fresh layers than on the aged films, but the size of the particles was slightly higher in the aged films (**Fig 3**, **Table 1**). This could be explained by fragmentation and diffusion of the fullerene molecules, and also by their polymerization and other changes in the C_{60}/Ti systems during the aging period.

Stability of C_{60}/Ti coating in a water environment

The stability of fresh C_{60}/Ti layers with a low, medium and high content of Ti was evaluated by dissolution in deionized water, and was analyzed by Raman spectroscopy. In the original (as deposited) films, the Raman measurements point to the dominant $A_g(2)$ breathing mode, confirming the presence of fullerenes (**Fig 2**; described above). However, the examination of the dried water in the Petri dishes, taken from the C_{60}/Ti films, did not prove any presence of fullerenes or other carbon allotropes. The Raman spectra showed only a broad luminescence distribution with Si-O-Si and O-H peaks from glass (Petri dish) and H_2O (**Fig 4**). Thus, no dissolution of C_{60} molecules was observed, and all tested C_{60}/Ti films deposited on the glass coverslips were mechanically stable in the water.

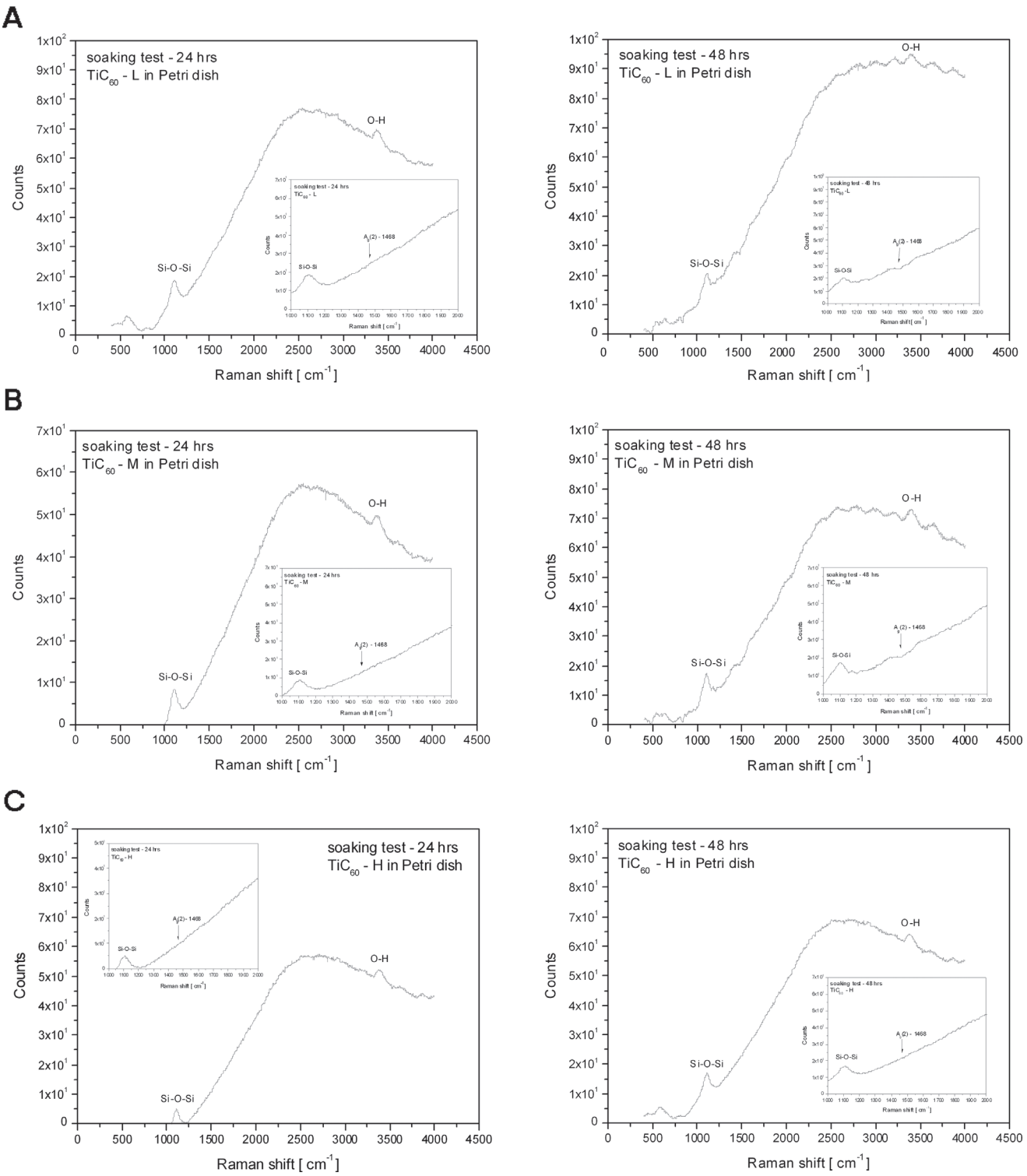

Fig 4. Raman spectrum of thin films formed in Petri dishes by evaporating water solutions after incubation of C_{60}/Ti composites with a low *(A)*, medium *(B)* and high *(C)* content of Ti for 24 hours and then for another 48 hours. No $A_g(2)$ vibration mode (i.e., no presence of C_{60}) was confirmed.

doi:10.1371/journal.pone.0123680.g004

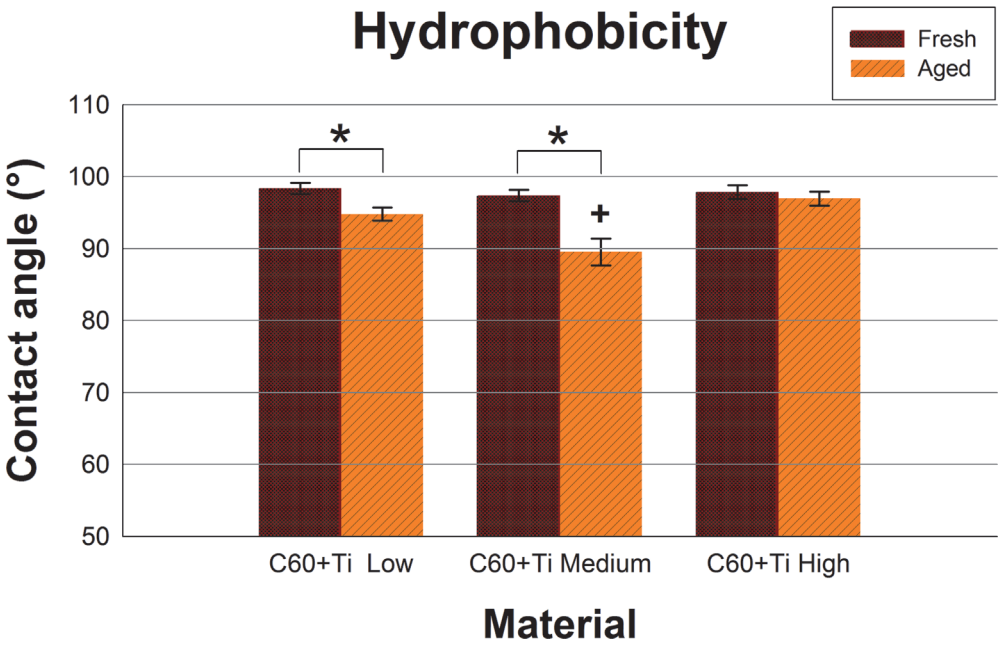

Fig 5. Static water drop contact angle of fresh and aged C_{60}/Ti composites with various Ti concentrations (low: 25%, medium: 45%, high: 70%). * significant difference between fresh and aged layers; $p \leq 0.05$.

doi:10.1371/journal.pone.0123680.g005

Hydrophobicity of C_{60}/Ti layers

Both fresh and aged layers of all C_{60}/Ti composites with various Ti concentrations were at a relatively high hydrophobic level ranging from 89.6° to 98.4°. A significant decrease in the water contact angle was observed during the aging of C_{60}/Ti films with low and medium Ti content (Fig 5, S1 Table, S1 Dataset).

This could be explained by spontaneous physicochemical changes (such as fragmentation, polymerization, oxidation and graphitization) in an air atmosphere (Fig 2; described above). This decline was not observed for aged C_{60}/Ti layers with a high Ti content (Fig 5, S1 Table, S1 Dataset), which is in correlation with the results obtained from Raman spectroscopy, where the spectra of the fresh and aged samples were very similar, and therefore fewer physicochemical changes occurred during their aging (Fig 2; described above). The presence of oxygen and the formation of oxygen-containing chemical functional groups are known to increase the surface wettability of various materials, e.g. synthetic polymers, metals or carbon-based materials (for a review see [1, 2]). In our earlier studies, oxidation and also fragmentation, polymerization and graphitization of fullerenes were observed on fullerene films exposed to 70% cold ethanol used for material sterilization.

Initial adhesion, proliferation and morphology of cells on fullerene C_{60} /Ti layers

The number of initially adhered human osteoblast-like cells MG-63 cells on day 1 after seeding on fresh (i.e., one-week-old) C_{60}/Ti composites with various Ti additions was slightly lower (the decrease correlated positively with the increase in Ti concentration) in comparison with the reference microscopic glass coverslips (Fig 6A, S2A Table, S1 Dataset); however, these reductions were not proven to be statistically significant. Similar results for cell numbers were obtained on day 3 after seeding (Fig 6B, S2B Table, S1 Dataset). The calculation of the cell

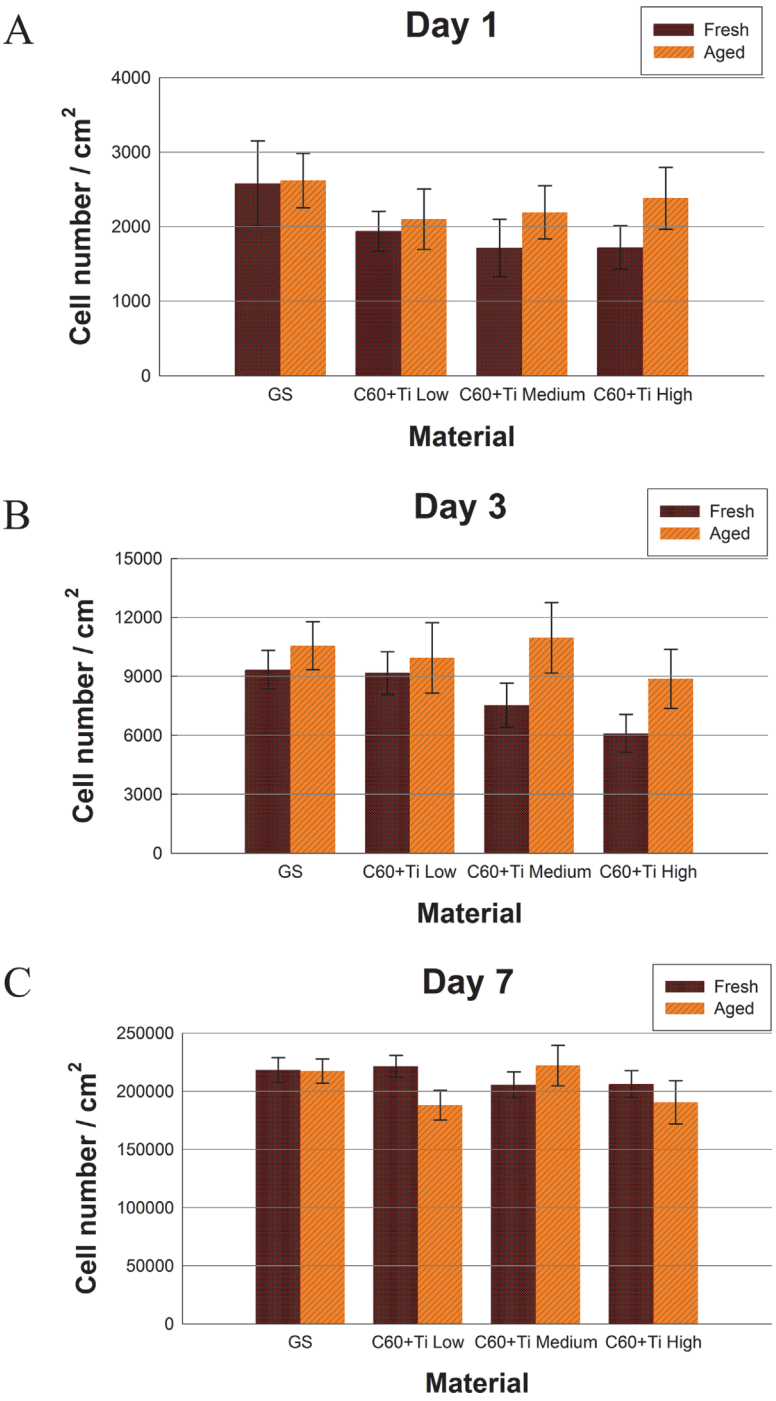

Fig 6. Numbers of human osteoblast-like MG-63 cells on fresh or aged C_{60}/Ti composites with various Ti concentrations (low: 25%, medium: 45%, high: 70%) on day 1 *(A)*, 3 *(B)* and 7 *(C)* after seeding. GS: microscopic glass coverslips, a reference material. No significant differences among the experimental groups were found.

doi:10.1371/journal.pone.0123680.g006

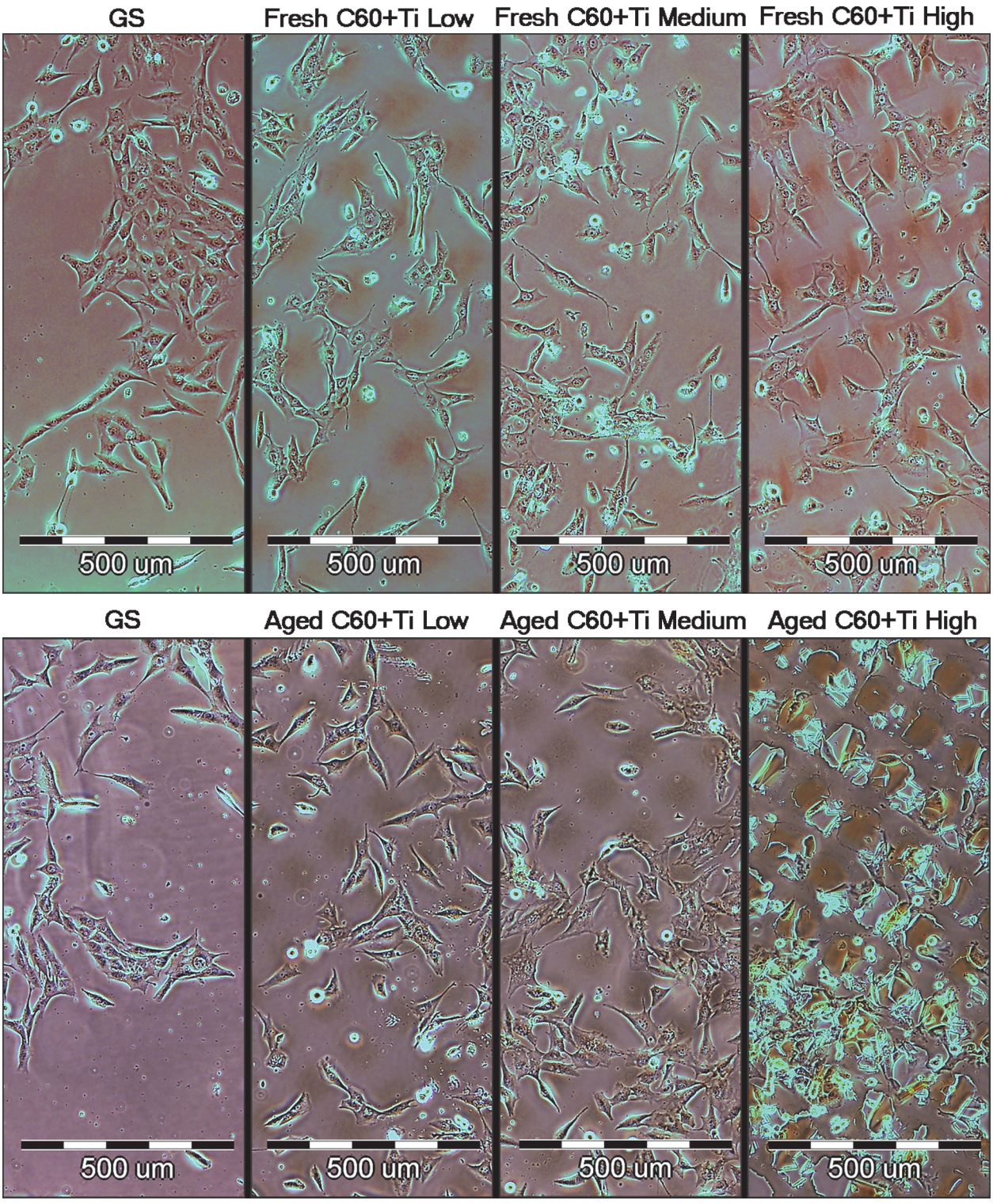

Fig 7. Morphology of human osteoblast-like MG-63 cells on day 3 after seeding on fresh and aged C_{60}/Ti composites with various concentrations of Ti (low: 25%, medium: 45%, high: 70%). GS: microscopic glass coverslips, reference material.

doi:10.1371/journal.pone.0123680.g007

population doubling time also did not reveal any significant decrease in proliferation of cells cultured on fresh C_{60}/Ti films. The doubling times of the cells cultured on all fresh samples were comparable with the reference material (**S1 and S2 Figs, S3 Table, S1 Dataset**).

On the aged C_{60}/Ti films, the initial adhesions as well as the cell numbers on all tested samples were almost the same in all culture intervals (**Fig 6, S2 Table, S1 Dataset**). The growth dynamics of cells cultured on aged composites of all Ti concentrations was also similar to that on the reference material (the doubling times are shown in **S1 and S2 Figs, S3 Table, S1 Dataset**).

In a previous study performed on pure C_{60} layers, lower numbers and slower proliferation of MG 63 cells were found on the fresh films in comparison with the control glass coverslips or with aged C_{60} films [38]. However, on aged C_{60} films, these differences diminished considerably or almost disappeared. This result was explained by changes in C_{60} molecules during their ageing, such as fragmentation, polymerization and oxidation, which decreased the reactivity of fullerenes. Interestingly, the examination of C_{60}/Ti composites in this study showed no significant differences in cell adhesion and growth between the fresh and aged films. Moreover, from this point of view, both fresh and aged layers were comparable to the reference glass coverslips. A possible explanation for this improvement of the fresh C_{60} layers for cell cultivation by co-deposition with Ti could be that fragmentation, polymerization and oxidation of C_{60} occurred during deposition of the composite films by the interaction of C_{60} molecules with Ti atoms, and not only due to the ageing of the C_{60}/Ti films. In other words, the C_{60}/Ti composites exhibited similar biocompatibility as the mix of amorphous carbon and titanium. Similarly, amorphous carbon in the form of films or electrospun nanofibrous scaffolds has been shown to provide good support for the adhesion and proliferation of mouse neuroblastoma N2a cells and rat Schwann RT4-D6P2T cells [41].

The cell morphology was similar on both fresh and aged C_{60}/Ti composites of all Ti concentrations. The cells were generally well-spread, polygonal or spindle-shaped. No cytotoxic morphological changes, such as enlarged cells or cytosolic vacuole formation, were observed on fresh or on aged C_{60}/Ti films with various Ti concentrations (**Fig 7**).

Preferential growth in grooves among the prominences was also apparent, particularly on the fresh composites (**Fig 7**). Similar cell behavior was also observed in our earlier studies performed on micropatterned pure C_{60} as well as hybrid C_{60}/Ti films [36–38, 40]. Nevertheless, on micropatterned pure C_{60} films, the preferential cell colonization in grooves was much more apparent on the fresh films than on the aged films. This was explained by the diffusion of C_{60} molecules from the prominences towards the grooves and thus lowering of the prominences during aging [38]. On the composite C_{60}/Ti films in the present study, prominences and preferential cell colonization in grooves were still apparent on the aged films, particularly those with the highest Ti concentration. This could be attributed to increased stability of the prominences due to the presence of Ti atoms.

Metabolic activity and viability of cells on fullerene C_{60} /Ti layers

In order to investigate the potential cytotoxicity of fresh and aged C_{60}/Ti composites with various Ti additions, an XTT cell proliferation assay was performed. Proportionally to the cell numbers, MG-63 cultivated for 7 days on both fresh and aged C_{60}/Ti layers showed comparable metabolic activity (i.e., activity of mitochondrial enzymes) with cells grown on control glass coverslips (**Fig 8, S4 Table, S1 Dataset**). No significant differences in metabolic activity were found among the various Ti concentrations or the ages of the C_{60}/Ti composites.

Cell viability and potential cell membrane damage were analyzed by trypan blue staining. The cells growing on all tested C_{60}/Ti composites were highly viable (over 80%) and were comparable to the cells on the reference material. No statistically significant differences in viability were observed among the various Ti concentrations or ages of the C_{60}/Ti composites (**Fig 9, S5 Table, S1 Dataset**). The improvement in metabolic activity and also in the viability of cells

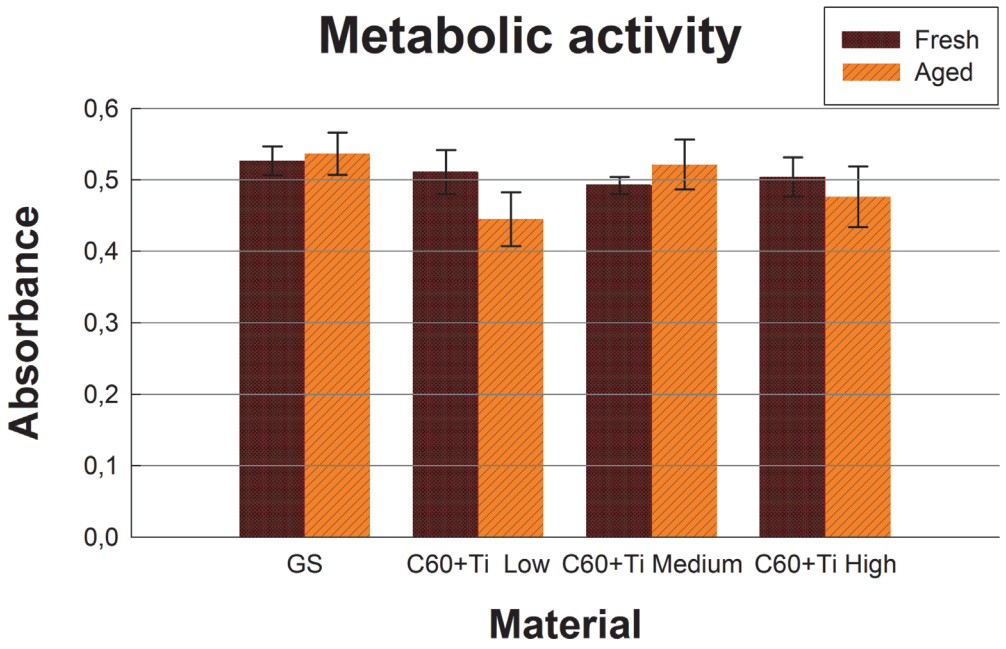

Fig 8. Metabolic activity measured by the XTT test per culture of human osteoblast-like MG-63 cells on day 7 after seeding on fresh and aged C_{60}/Ti composites with various Ti concentrations (low: 25%, medium: 45%, high: 70%). GS: microscopic glass coverslips, a reference material. No significant differences among the experimental groups were found.

doi:10.1371/journal.pone.0123680.g008

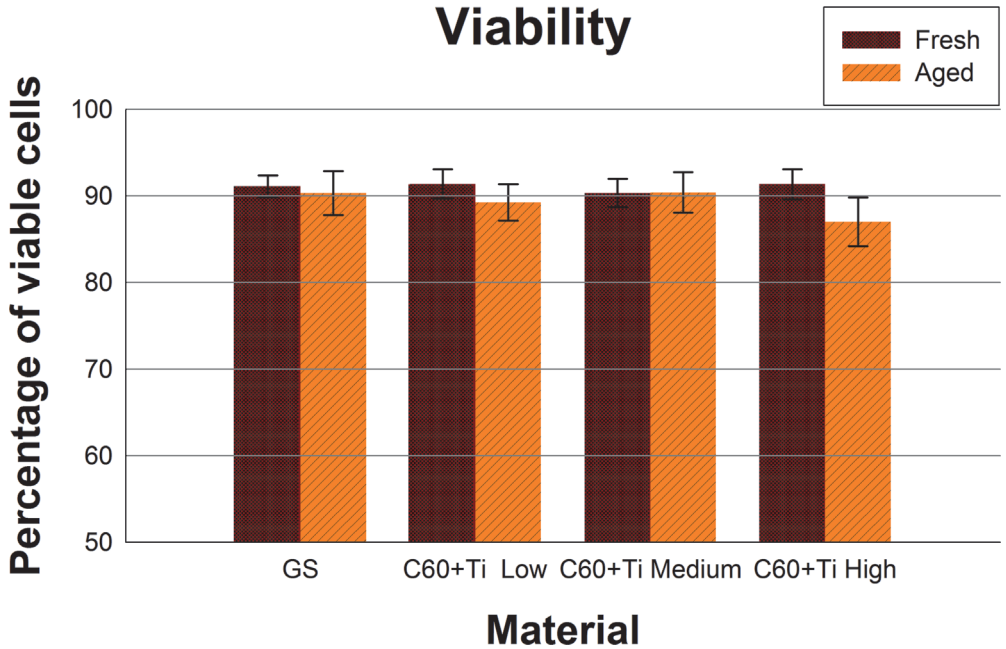

Fig 9. Viability of human osteoblast-like MG-63 cells, measured by the trypan blue exclusion test on day 7 after seeding on fresh and aged C_{60}/Ti composites with various Ti concentrations (low: 25%, medium: 45%, high: 70%). GS: microscopic glass coverslips, reference material. No significant differences among the experimental groups were found.

doi:10.1371/journal.pone.0123680.g009

A

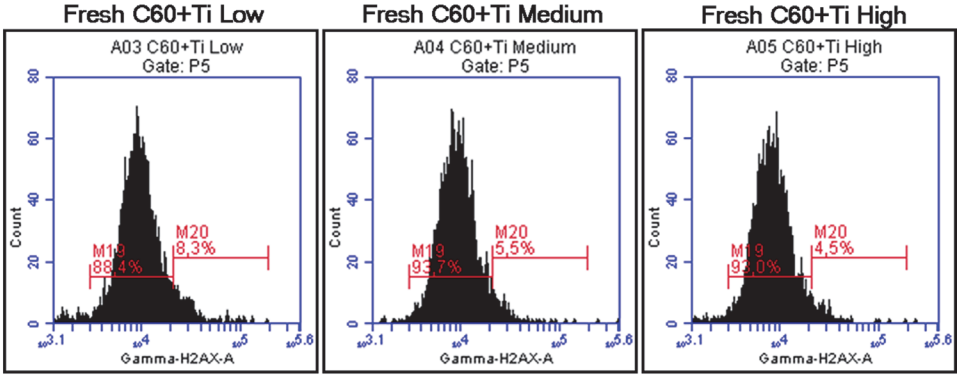
Fresh C60+Ti Low
A03 C60+Ti Low
Gate: P5
M19
88,4%
M20
8,3%
Fresh C60+Ti Medium
A04 C60+Ti Medium
Gate: P5
M19
93,7%
M20
5,5%
Fresh C60+Ti High
A05 C60+Ti High
Gate: P5
M19
93,0%
M20
4,5%
Count
Gamma-H2AX-A

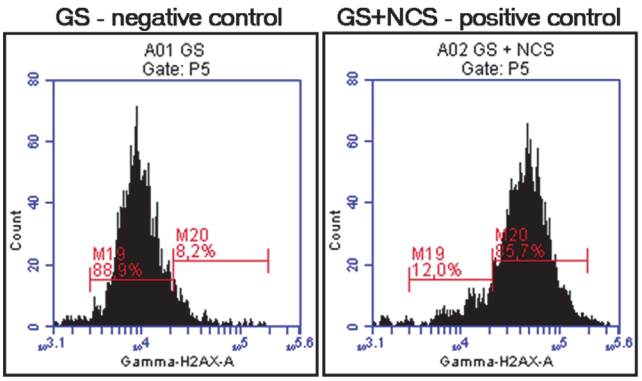
GS - negative control
A01 GS
Gate: P5
M19
88,9%
M20
8,2%
GS+NCS - positive control
A02 GS + NCS
Gate: P5
M19
12,0%
M20
85,7%
Count
Gamma-H2AX-A

B

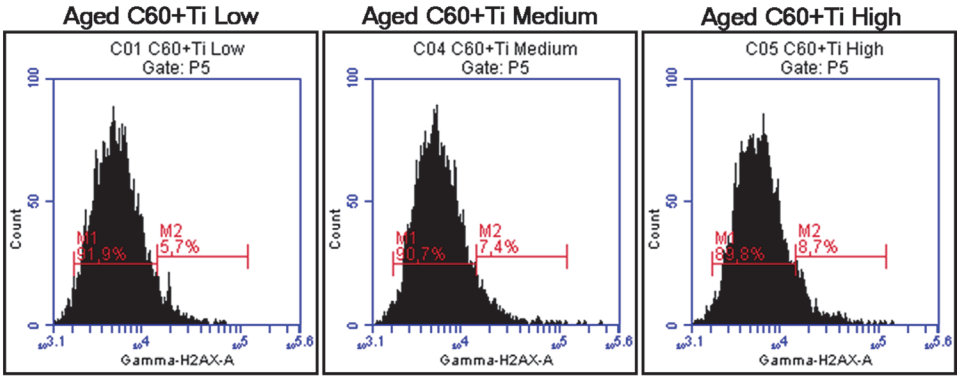
Aged C60+Ti Low
C01 C60+Ti Low
Gate: P5
M1
91,9%
M2
5,7%
Aged C60+Ti Medium
C04 C60+Ti Medium
Gate: P5
M1
90,7%
M2
7,4%
Aged C60+Ti High
C05 C60+Ti High
Gate: P5
M1
89,8%
M2
8,7%
Count
Gamma-H2AX-A

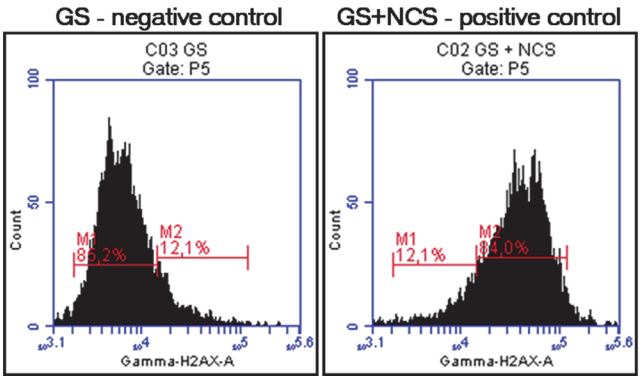
GS - negative control
C03 GS
Gate: P5
M1
86,2%
M2
12,1%
GS+NCS - positive control
C02 GS + NCS
Gate: P5
M1
12,1%
M2
84,0%
Count
Gamma-H2AX-A

Fig 10. Flow cytometry of the marker of DNA damage response: gamma-H2AX in human osteoblast-like U-2 OS cells on fresh (A) and aged (B) C_{60}/Ti composites with various Ti concentrations (low: 25%, medium: 45%, high: 70%). GS: microscopic glass coverslips, reference material; GS+NCS: positive control to phosphorylation of histon H2AX (gamma-H2AX), induced by 1 hour incubation of U-2 OS in neocarzinostatin (NCS; 700ng/mL). M19 and M1 define the percentage of cells with no increase in DNA damage (obtained from cells growing on the reference material, GS); M20 and M2 define the percentage of cells with an increased DNA damage response represented by enhanced phosphorylation of histon H2AX (obtained from cells incubated with NCS).

doi:10.1371/journal.pone.0123680.g010

cultured on C_{60}/Ti layers (especially fresh composites) is obvious when compared to our previous study performed on pure C_{60} layers [38].

DNA damage response

It has been reported that fullerenes are able to bind directly to the minor and major grooves of double-strand DNA and to form a stable complex, which may have a negative impact on the self-repairing process of the dsDNA and may lead to a potential cytotoxic effect of fullerenes [42, 43].

We therefore studied the DNA damage response (DDR) of cells growing on fullerene films, by markers of DNA double strand breaks. For this purpose, osteosarcoma cell line U-2 OS was used instead of MG-63, which is p53-deficient. Gamma-HA2X (phosphorylated histon H2AX, a marker of early DDR) and 53BP1 (p53 binding protein), whose focal recruitment depends on a number of upstream factors, were evaluated. After 3 and 7 days of cultivation on various Ti concentrations of fresh and aged C_{60}/Ti composites, the level of gamma-H2AX phosphorylation was analyzed by flow cytometry. The results show no increase in the percentage of cells with enhanced phosphorylation of histon H2AX cultured on layers with various Ti additions in comparison to the reference glass coverslips. Moreover, there was no effect of the age of the C_{60}/Ti composites on DDR (**Fig 10**). Furthermore, the visualization of both DDR markers by immunofluorescence staining also revealed no increased recruitment or formation of either gamma-H2AX or 53BP1 foci (**Fig 11**). These results are consistent with our previous study focused on C_{60} layers [38]. In accordance with our results, fullerene C_{60} nanoparticles in suspension had no genotoxic ability in the bacterial reverse mutation assay, in the *in vitro* chromosome aberration assay, or in the *in vivo* micronucleus assay [44]. In addition, fullerenol mediated a decrease in the frequency of micronuclei and chromosome aberrations [45].

Conclusions and Further Perspectives

Our study has revealed that both fresh and aged C_{60}/Ti composites are suitable substrates for the adhesion and growth of human bone cells. However, in the case of pure fullerene C_{60} films studied earlier, aged films were better for cell colonization than fresh films, which had a certain negative impact on the cell spreading, proliferation, viability and activity of mitochondrial enzymes. Interestingly, the examination of C_{60}/Ti composites in this study showed no significant differences between fresh and aged films (caused by the improvement in the properties of the fresh layers). This difference between pure fullerene films and C_{60}/Ti composites may lie in the fact that in the composites, changes in the fullerene molecules, such as fragmentation, polymerization, oxidation and graphitization, occur not only due to aging of the material, but immediately during C_{60} and Ti co-deposition due to the interaction of C_{60} molecules and Ti atoms. In addition, studies performed on human osteoblast-like U-2 OS cells revealed no DNA damage response of these cells cultivated on fresh or aged C_{60}/Ti composites. C_{60}/Ti composites can therefore be considered as promising materials in bone tissue engineering, namely for potential coating of bone implants. The connection (association) of C_{60} with Ti may also have promising

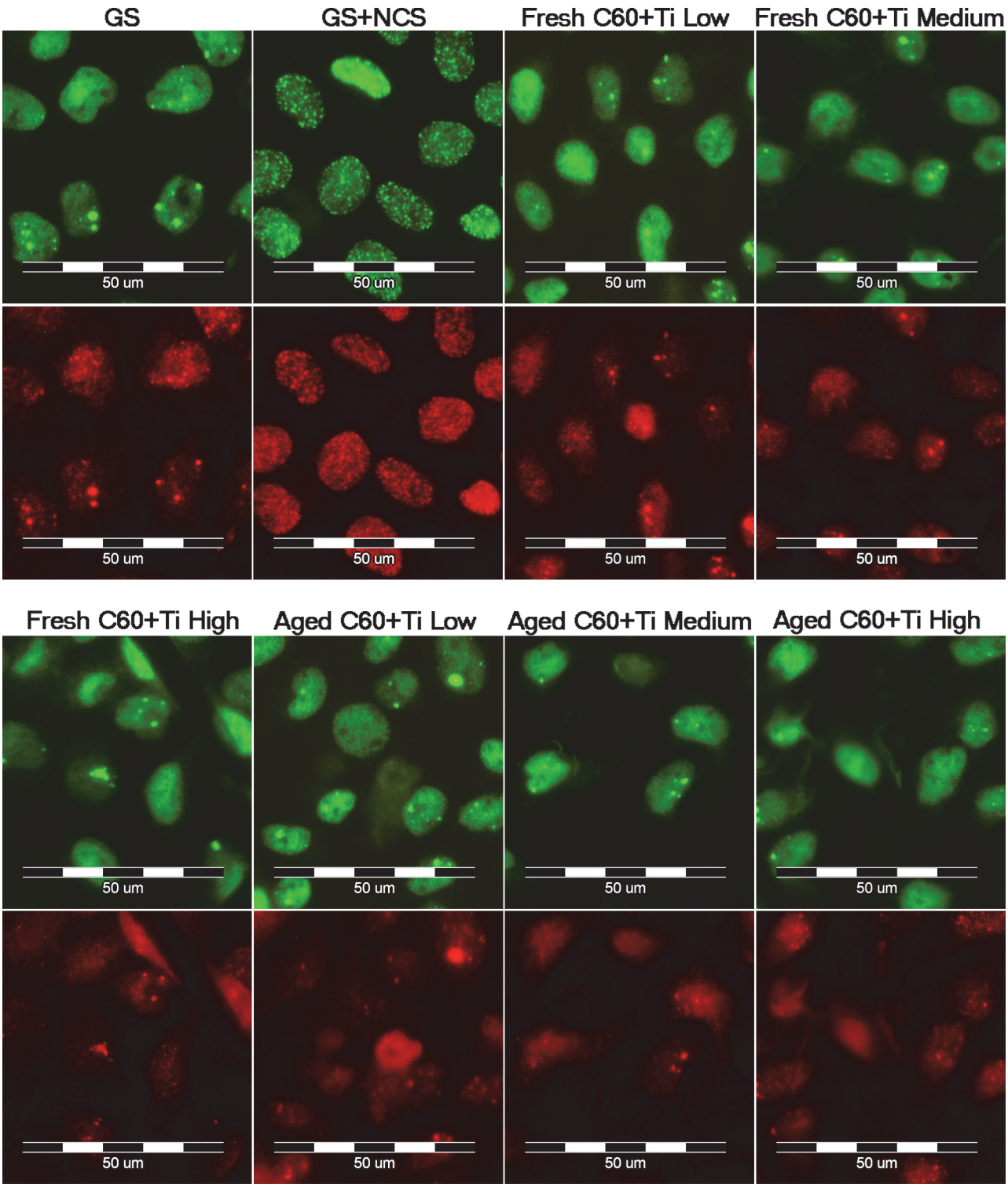

Fig 11. Immunofluorescence staining of markers of a DNA damage response: 53BP1 (green) and gamma-H2AX (red) in human osteoblast-like U-2 OS cells on fresh and aged C_{60}/Ti composites with various Ti concentrations (low: 25%, medium: 45%, high: 70%). GS: microscopic glass coverslips, reference material; GS+NCS: positive control of DNA damage response induced by 1 hour incubation of U-2 OS in neocarzinostatin (NCS; 700ng/mL).

doi:10.1371/journal.pone.0123680.g011

therapeutic potential against oxidative stress-associated conditions and in the treatment of bone and cartilage tissue destruction in arthritis.

Supporting Information

S1 Dataset. Excel sheet of raw data numbers from which the qualitative data, mean ± standard error of the mean (S.E.M) or median with interquartile range (IQR) were calculated.
(XLS)

S1 Fig. Doubling times (in hours) of human osteoblast-like MG-63 cells cultured on fresh or aged C_{60}/Ti composites with various Ti concentrations (low: 25%, medium: 45%, high: 70%). GS: microscopic glass coverslips, reference material. The data from different time intervals (day 1–3 **(A)**, day 3–7 **(B)**) is presented as median with interquartile range (IQR = Q3—Q1) obtained from 3 experiments. No significant differences among the experimental groups were found.
(TIF)

S2 Fig. Summarized doubling time (in hours) of human osteoblast-like MG-63 cells cultured on fresh or aged C_{60}/Ti composites with various Ti concentrations (low: 25%, medium: 45%, high: 70%). GS: microscopic glass coverslips, reference material. The data is presented as median with interquartile range (IQR = Q3—Q1) obtained from 3 experiments. No significant differences among the experimental groups were found.
(TIF)

S1 Table. Static water drop contact angle of fresh and aged C_{60}/Ti composites with various Ti concentrations (low: 25%, medium: 45%, high: 70%). The data is presented as mean ± standard error of the mean (S.E.M.) obtained from 10 measurements. $^{*\text{Aged}}$ significant difference between fresh and aged layers; $^{+\text{Low, High}}$ significant difference to low and high concentration of Ti among the aged samples; $p \leq 0.05$.
(DOC)

S2 Table. Numbers of human osteoblast-like MG-63 cells on fresh or aged C_{60}/Ti composites with various Ti concentrations (low: 25%, medium: 45%, high: 70%) on day 1 (A), 3 (B) and 7 (C) after seeding. The data is presented as mean ± standard error of the mean (S.E.M.) obtained from 3 experiments. GS: microscopic glass coverslips, a reference material. No significant differences among the experimental groups were found.
(DOC)

S3 Table. Doubling times (in hours) of human osteoblast-like MG-63 cells cultured on fresh or aged C_{60}/Ti composites with various Ti concentrations (low: 25%, medium: 45%, high: 70%). GS: microscopic glass coverslips, reference material. The data from different time intervals (day 1–3 **(A)**, day 3–7 **(B),** and summarized day 1–7 **(C)**) is presented as median with interquartile range (IQR = Q3—Q1) obtained from 3 experiments. No significant differences among the experimental groups were found.
(DOC)

S4 Table. Metabolic activity measured by the XTT test per culture of human osteoblast-like MG-63 cells on day 7 after seeding on fresh and aged C_{60}/Ti composites with various Ti concentrations (low: 25%, medium: 45%, high: 70%). The data is presented as mean ± standard error of the mean (S.E.M.) obtained from 3 experiments. GS: microscopic glass coverslips, a reference material. No significant differences among the experimental groups

were found.
(DOC)

S5 Table. Percentage of viable cells (human osteoblast-like MG-63 cells), measured by the trypan blue exclusion test on day 7 after seeding on fresh and aged C_{60}/Ti composites with various Ti concentrations (low: 25%, medium: 45%, high: 70%). The data is presented as mean ± standard error of the mean (S.E.M.) obtained from 3 experiments. GS: microscopic glass coverslips, reference material. No significant differences among the experimental groups were found.
(DOC)

Acknowledgments

The deposition and characterization of the C_{60}/Ti composites were carried out in the laboratories of the CANAM infrastructure (NPI ASCR Rez). Mr. Robin Healey (Czech Technical University in Prague) is gratefully acknowledged for his language revision of the manuscript.

Author Contributions

Conceived and designed the experiments: IK LB. Performed the experiments: IK VL. Analyzed the data: IK JV LB. Contributed reagents/materials/analysis tools: LB JV. Wrote the paper: IK LB JV.

References

1. Bacakova L, Grausova L, Vandrovcova M, Vacik J, Frazcek A, Blazewicz S, et al. (2008) Carbon nanoparticles as substrates for cell adhesion and growth. In: Nanoparticles: New Research (Ed. Lombardi Simone Luca), Nova Science Publishers, Inc., Hauppauge, New York, USA, pp. 39–107, ISBN 978-1-60456-704-5. doi: 10.1002/yd.272 PMID: 18855319
2. Bacakova L, Grausova L, Vacik J, Kromka A, Biederman H, Choukourov A, et al. (2011) Nanocomposite and nanostructured carbon-based films as growth substrates for bone cells. In: Advances in Diverse Industrial Applications of Nanocomposites. (Ed. Reddy Boreddy), Intech, Open Access Publisher, pp. 399–435, ISBN 978-953-307-202-9.
3. Zhang Y, Wang L, Sun Y, Zhu Y, Zhong Z, Shi J, et al. (2013) Conjugation of dexamethasone to C60 for the design of an anti-inflammatory nanomedicine with reduced cellular apoptosis. ACS Appl Mater Interfaces. 5(11): 5291–5297. doi: 10.1021/am401153k PMID: 23669026
4. Liu H, Yang X, Zhang Y, Dighe A, Li X, Cui Q (2012) Fullerol antagonizes dexamethasone-induced oxidative stress and adipogenesis while enhancing osteogenesis in a cloned bone marrow mesenchymal stem cell. J Orthop Res 30: 1051–1057. doi: 10.1002/jor.22054 PMID: 22570221
5. Yudoh K, Shishido K, Murayama H, Yano M, Matsubayashi K, Takada H, et al. (2007) Water-soluble C60 fullerene prevents degeneration of articular cartilage in osteoarthritis via down-regulation of chondrocyte catabolic activity and inhibition of cartilage degeneration during disease development. Arthritis Rheum 56: 3307–3318. PMID: 17907184
6. Yudoh K, Karasawa R, Masuko K, Kato T (2009) Water-soluble fullerene (C60) inhibits the osteoclast differentiation and bone destruction in arthritis. Int J Nanomedicine 4: 233–239. PMID: 19918370
7. Murakami M, Hyodo S, Fujikawa Y, Fujimoto T, Maeda K (2013) Photoprotective effects of inclusion complexes of fullerenes with polyvinylpyrrolidone. Photodermatol Photoimmunol Photomed 29: 196–203. doi: 10.1111/phpp.12050 PMID: 23815352
8. Møller P, Folkmann JK, Danielsen PH, Jantzen K, Loft S (2012) Oxidative stress generated damage to DNA by gastrointestinal exposure to insoluble particles. Curr Mol Med 12: 732–745. PMID: 22292440
9. Vesterdal LK, Danielsen PH, Folkmann JK, Jespersen LF, Aguilar-Pelaez K, Roursgaard M, et al. (2014) Accumulation of lipids and oxidatively damaged DNA in hepatocytes exposed to particles. Toxicol Appl Pharmacol 274: 350–360. doi: 10.1016/j.taap.2013.10.001 PMID: 24121055
10. Ferreira JL, Lonné MN, França TA, Maximilla NR, Lugokenski TH, Costa PG, et al. (2013) Co-exposure of the organic nanomaterial fullerene C60 with benzo[a]pyrene in Danio rerio (zebrafish) hepatocytes: Evidence of toxicological interactions. Aquat Toxicol 147C: 76–83.

11. Honma M, Takahashi T, Asada S, Nakagawa Y, Ikeda A, Yamakage K (2012) In vitro clastogenicity and phototoxicity of fullerene (C(60)) nanomaterials in mammalian cells. Mutat Res 749: 97–100. doi: 10.1016/j.mrgentox.2012.08.006 PMID: 22960459

12. Gao J, Wang HL, Shreve A, Iyer R (2010) Fullerene derivatives induce premature senescence: a new toxicity paradigm or novel biomedical applications. Toxicol Appl Pharmacol 244: 130–143. doi: 10.1016/j.taap.2009.12.025 PMID: 20045429

13. Rebecca M, Hsing-Lin W, Jun G, Srinivas I, Gabriel MA, Jennifer M, et al. (2009) Impact of physicochemical properties of engineered fullerenes on key biological responses. Toxicol Appl Pharmacol 234: 58–67. doi: 10.1016/j.taap.2008.08.021 PMID: 18926839

14. Rouse JG, Yang J, Barron AR, Monteiro-Riviere NA (2006) Fullerene-based amino acid nanoparticle interactions with human epidermal keratinocytes. Toxicol In Vitro 20: 1313–1320. PMID: 16759832

15. Lucafò M, Gerdol M, Pallavicini A, Pacor S, Zorzet S, Da Ros T, et al. (2013) Profiling the molecular mechanism of fullerene cytotoxicity on tumor cells by RNA-seq. Toxicology 314: 183–192. doi: 10.1016/j.tox.2013.10.001 PMID: 24125657

16. Johnston HJ, Hutchison GR, Christensen FM, Aschberger K, Stone V (2010) The biological mechanisms and physicochemical characteristics responsible for driving fullerene toxicity. Toxicol Sci 114: 162–182. doi: 10.1093/toxsci/kfp265 PMID: 19901017

17. Trpkovic A, Todorovic-Markovic B, Trajkovic V (2012) Toxicity of pristine versus functionalized fullerenes: mechanisms of cell damage and the role of oxidative stress. Arch Toxicol 86: 1809–1827. doi: 10.1007/s00204-012-0859-6 PMID: 22562437

18. Ko WB, Yun JM, Jo SW, Shon YS (2006) Ultrasonic, chemical stability and preparation of self-assembled fullerene[C60]-gold nanoparticle films. Ultrasonics. 44 Suppl 1: e363–6. PMID: 16814825

19. Harcuba P, Bacakova L, Strasky J, Bacakova M, Novotna K, Janecek M (2012) Surface treatment by electric discharge machining of Ti-6Al-4V alloy for potential application in orthopaedics. J Mech Behav Biomed Mater 7: 96–105. doi: 10.1016/j.jmbbm.2011.07.001 PMID: 22340689

20. Strasky J, Havlikova J, Bacakova L, Harcuba P, Mhaede M, Janecek M (2013) Characterization of electric discharge machining, subsequent etching and shot-peening as a surface treatment for orthopedic implants. Applied Surface Science 213: 73–78.

21. Jirka I, Vandrovcova M, Frank O, Tolde Z, Plšek J, Luxbacher T, et al. (2013) On the role of Nb-related sites of an oxidized β-TiNb alloy surface in its interaction with osteoblast-like MG-63 cells. Mater Sci Eng C Mater Biol Appl 33: 1636–1645. doi: 10.1016/j.msec.2012.12.073 PMID: 23827618

22. Vandrovcova M, Jirka I, Novotna K, Lisa V, Frank O, Kolska Z, et al. (2014) Interaction of human osteoblast-like Saos-2 and MG-63 cells with thermally oxidized surfaces of a titanium-niobium alloy. PLOS ONE 9(6): e100475. doi: 10.1371/journal.pone.0100475 PMID: 24977704

23. Vandrovcova M, Bacakova L (2011) Adhesion, growth and differentiation of osteoblasts on surface-modified materials developed for bone implants. Physiol Res 60: 403–417. PMID: 21401307

24. Bacakova L, Stary V, Kofronova O, Lisa V (2001) Polishing and coating carbon fibre-reinforced carbon composites with a carbon-titanium layer enhances adhesion and growth of osteoblast-like MG 63 cells and vascular smooth muscle cells in vitro. J Biomed Mater Res 54: 567–578. PMID: 11426603

25. Grinevich A, Bacakova L, Choukourov A, Boldyryeva H, Pihosh Y, Slavinska D, et al. (2009) Nanocomposite Ti/hydrocarbon plasma polymer films from reactive magnetron sputtering as growth support for osteoblast-like and endothelial cells. J Biomed Mat Res A 88: 952–966. doi: 10.1002/jbm.a.31918 PMID: 18384161

26. Joska L, Fojt J, Cvrcek L, Brezina V (2014) Properties of titanium-alloyed DLC layers for medical applications. Biomatter 4. pii: e29505.

27. Popa AC, Stan GE, Husanu MA, Pasuk I, Popescu ID, Popescu AC, et al. (2013) Multi-layer haemocompatible diamond-like carbon coatings obtained by combined radio frequency plasma enhanced chemical vapor deposition and magnetron sputtering. J Mater Sci Mater Med 24(12): 2695–2707. doi: 10.1007/s10856-013-5026-y PMID: 23943017

28. Tsai PC, Chiang JY, Hwang YF (2008) Characteristics and mechanical properties of titanium-containing diamond like carbon films deposited by cathodic arc evaporation. J Nanosci Nanotechnol 8(5): 2516–2521. PMID: 18572676

29. Dwivedi N, Kumar S, Malik HK (2011) Nanostructured titanium/diamond-like carbon multilayer films: deposition, characterization, and applications. ACS Appl Mater Interfaces 3(11): 4268–4278. doi: 10.1021/am200939j PMID: 21942626

30. Talyzin AV, Jansson U (2003) A comparative Raman study of some transition metal fullerides. Thin Solid Films 429(1–2): 96–101.

31. Vacik J, Naramoto H, Narumi K, Yamamoto S, Abe H (2004) Study of the nickel-fullerene nano-structured thin films. Nucl Instrum Meth B 219–220: 862–866.

32. Vacik J, Lavrentiev V, Hnatowicz V, Yamamoto S, Vorlicek V, Stadler H (2009) Spontaneous partitioning of the Ni+C60 thin film grown at RT. J Alloy Compd 483: 374–377.

33. Vacik J, Lavrentiev V, Vorlicek V, Bacakova L, Narumi K (2010) Effect of ion irradiation on structure and thermal evolution of the Ni–C60 hybrid systems. Nucl Instr Meth Phys Res B 268(11–12): 1976–1979.

34. Vacik J, Lavrentiev V, Horak P, Michalcova A, Abe H (2011) Spontaneous growth of the polyhedral fullerene crystals in the supersaturated Ni-C60 composite. J Alloy Compd 509S: S380–S383.

35. Liu X, Jia Y, Guo L, Wang G (2005) Photoelectric investigations of charge-transferring metal-doped [60] fullerenes. Solar Energy Materials and Solar Cells 87(1–4): 5–10.

36. Vandrovcova M, Vacik J, Svorcik V, Slepicka P, Kasalkova N, Vorlicek V, et al. (2008) Fullerene C60 and hybrid C60/Ti films as substrates for adhesion and growth of bone cells. Phys. Status Solidi A 205: 2252–2261.

37. Vacik J, Lavrentiev V, Novotna K, Bacakova L, Lisa V, Vorlicek V, et al. (2010) Fullerene (C60)–transitional metal (Ti) composites: Structural and biological properties of the thin films. Diam Related Mater 19: 242–246.

38. Kopova I, Bacakova L, Lavrentiev V, Vacik J (2013) Growth and potential damage of human bone-derived cells on fresh and aged fullerene C_{60} films. Int J Mol Sci 14: 9182–9204. doi: 10.3390/ijms14059182 PMID: 23624607

39. Dresselhaus MS, Dresselhaus G, Eklund PC (1996) Science of fullerenes and carbon nanotubes, Academic Press, San Diego, CA, ISBN 012-221820-5.

40. Grausova L, Vacik J, Bilkova P, Vorlicek V, Svorcik V, Soukup D, et al. (2008) Regionally-selective adhesion and growth of human osteoblast-like MG 63 cells on micropatterned fullerene C(60) layers. J Optoelectronics Adv Mater 10: 2071–2076.

41. Jain S, Sharma A, Basu B (2013) In vitro cytocompatibility assessment of amorphous carbon structures using neuroblastoma and Schwann cells. J Biomed Mater Res B Appl Biomater 101: 520–531. doi: 10.1002/jbm.b.32852 PMID: 23359403

42. Zhao X, Striolo A, Cummings PT (2005) C_{60} binds to and deforms nucleotides. Biophys J, 89: 3856–3862. PMID: 16183879

43. Xu X, Wang X, Li Y, Wang Y, Yang L (2012) A large-scale association study for nanoparticle C_{60} uncovers mechanisms of nanotoxicity disrupting the native conformations of DNA/RNA. Nucleic Acids Res 40: 7622–7632. doi: 10.1093/nar/gks517 PMID: 22661584

44. Shinohara N, Matsumoto K, Endoh S, Maru J, Nakanishi J (2009) In vitro and in vivo genotoxicity tests on fullerene C60 nanoparticles. Toxicol Lett 191(2–3): 289–296.

45. Mrdanović J, Solajić S, Bogdanović V, Stankov K, Bogdanović G, Djordjevic A (2009) Effects of fullerenol C60(OH)24 on the frequency of micronuclei and chromosome aberrations in CHO-K1 cells. Mutat Res 680: 25–30. doi: 10.1016/j.mrgentox.2009.08.008 PMID: 19733687

The cytotoxicity and wear analysis of DLC coated Co-Cr-Mo alloy used for total trapeziometacarpal joint arthroplasty

Ivana Kopova[1*], Jakub Kronek[2*], Lucie Bacakova[1], Jaroslav Fencl[3]

[1] Department of Biomaterials and Tissue Engineering, Institute of Physiology of the Czech Academy of Sciences, Videnska 1083, 14220 Prague 4, Czech Republic

[2] Department of Mechanics, Mechatronics and Biomechanics, Faculty of Mechanical Engineering, Czech Technical University in Prague, Technicka 4, 166 07 Prague, Czech Republic

[3] Beznoska s.r.o., Delnicka 2727, 272 01 Kladno, Czech Republic

*These authors contributed equally to this work

Abstract

Diamond-like carbon (DLC) coating exhibits excellent mechanical properties improving the smoothness and wear characteristic of the metallic component of total joint replacements. Although DLC is considered to be highly biocompatible, the effect of implant wear debris must be carefully analyzed. Simulated loading can help to mimic the wear of the implant in the human body during the time. Therefore the purpose of this study is to observe the wear of DLC-coated Co-Cr-Mo alloy with titanium gradient interlayer used for total trapeziometacarpal joint arthroplasty and to analyze the potential cytotoxicity of wear particles generated by simulated loading. After 3 million cycles of increasing loading force up to 2.5 kN, no visible wear or delamination of DLC coating was observed. Accordingly, no correlation between increasing number of loading cycles (with increasing loading force) and decreasing proliferation of the osteoblast-like cells incubated in obtained wear suspension was proven. Therefore, we can conclude that during the simulated loading of DLC coated Co-Cr-Mo alloy with Ti gradient interlayer no cytotoxic wear debris was formed.

Introduction

The increasing demand for total joint replacement in younger (more active) patients results in the necessity of understanding the mechanism of the implant failure. Currently, most of the artificial joints consist of ultra-high-molecular-weight polyethylene (UHMWPE) cup and ceramic or metallic head. Unfortunately, mechanical loading of these artificial joints is (Voronov, Santerre et al. 1998) associated with the wear of contact surfaces and a higher debris production, causing the inflammation and bone resorption that may lead to the implant loosening (Willert, Bertram et al. 1990, Voronov, Santerre et al. 1998, Goodman 2007). Moreover, wear simulator studies have revealed that metal-on-polyethylene prostheses have around 100 times higher wear than metal-on-metal implants (Anissian, Stark et al. 1999, Tipper, Firkins et al. 1999, St John, Zardiackas et al. 2004).

Another option is metal-on-metal artificial replacement providing higher wear resistance and lower risk of osteolysis (Chan, Bobyn et al. 1996, St John, Zardiackas et al. 2004). Co–Cr–Mo alloy is widely used due to its biocompatibility and superior mechanical properties such as the fatigue strength, hardness and corrosion resistance. Although the wear particles generated by these prostheses are much smaller than UHMWPE particles (Musib, Rasquinha et al. 2011),

there is still a concern about the adverse biological reactions and potential rejecting by the immune system (Sargeant and Goswami 2006, Sargeant and Goswami 2007) as well as corrosion of these metallic debris (Yan, Neville et al. 2007, Valero Vidal and Igual Munoz 2011). In order to reduce the volume of wear, the concentration of metal debris and the level of metal ion release into the human body, different approaches for surface modification have been developed.

The diamond-like carbon (DLC) coating is well-known thanks to its unique mechanical properties as well as high level of biocompatibility. Various cell types have been grown on DLC under different conditions and cell responses such as cell adhesion, viability, proliferation, differentiation, cell morphology and cytoskeletal architecture have been evaluated. No indication of cytotoxicity or abnormal morphology has been found (Thomson, Law et al. 1991, Allen, Law et al. 1994, Butter, Allen et al. 1995). Moreover, cells adhered and proliferated well with the developed cytoskeleton (Linder, Pinkowski et al. 2002). *In vivo* studies have also proved that DLC coated surfaces are well tolerated by the animals with no evidence of corrosion products or chronic inflammatory reaction (Mitura, Mitura et al. 1994, Butter, Allen et al. 1995, Allen, Myer et al. 2001, Mohanty, Anilkumar et al. 2002).

From the mechanical point of view, DLC coating exhibits high hardness and low frictional coefficient (COF) resulting in the significant reduction of the wear, metal ion release as well as corrosion rate of metallic bearing surfaces. The wear of the DLC coating is several times lower than that of the ceramic materials, which are substantially better than commonly used PE (Ching, Choudhury et al. 2014). The wear rate is very complex variable depending on many factors such as material combination, geometry, loading, temperature, chemical surrounding, and time. According to some studies, the simple way to model the wear rate is to look at it as a time-independent constant (Tuke, Taylor et al. 2010, Abdelgaied, Liu et al. 2011). On the other hand, other publications have reported that even the quality of wear particles (such as shape and dimension) may change during the lifetime of the prosthesis (Catelas, Bobyn et al. 2003). The COF value is dependent on lubricant composition (physiological solution reduces COF more than bovine serum) and an applied load (in the case of lower normal load the COF increases more sharply with a number of slide cycles; (Guo, Zhou et al. 2015)). Good wear behavior together with corrosion resistance, chemical inertness and excellent smoothness match well with the criteria of a good biomaterial for orthopedic implants (reviewed in (Roy and Lee 2007)). Numerous studies have reported that DLC coating significantly reduced the wear and enhanced the scratch resistance of Cr-Co-Mo alloy (Tiainen 2001, Fisher, Hu et al. 2002, Roy, Whiteside et al. 2009, Thorwarth, Falub et al. 2010). Additionally, the results from a simulated body fluid (SBF) experiment performed for 2 years have shown 100,000 times lower corrosion rate of DLC-coated Cr-Co-Mo alloy in comparison with the uncoated alloy (Tiainen 2001).

A risk of potential DLC coating delamination (often observed in various coating materials) could be minimized by an engagement of an interlayer, which has been reported to improve the adhesion of DLC coating to a metal substrate (Utsumi, Oka et al. 2007, Wang, Pu et al. 2014, Kang, Lim et al. 2015). Although the DLC coatings have been known to extend the operational lives of hip and knee prostheses, to our best knowledge no study evaluated the Cr-Co-Mo alloy with titanium gradient adhesive interlayer coated by DLC for the trapeziometacarpal joint total replacement has been published. Therefore the purpose of this study is to observe the wear of DLC-coated Co-Cr-Mo alloy with Ti gradient interlayer and to analyze the potential cytotoxicity of wear particles generated by the simulated loading.

Materials and Methods

Joint samples preparation

Three joint samples were tested. The geometry of the joint samples corresponds with trapeziometacarpal joint (TMCJ) for a total joint arthroplasty. Each joint sample consists of the spherical head articulating in the spherical cup (both spheres with the nominal diameter 7mm). The cup contains a small hole (1mm) at the bottom. The basic material of both head and cup was Co-Cr-Mo alloy commonly used for implants[1]. Contact surfaces were coated by DLC (diamond like carbon) on Ti gradient adhesive interlayer. The conditions of DLC layer deposition and DLC characterization are summarized in the **Tab 1.**

Joint samples simulated loading

Joint samples were cyclically loaded on the simulator KKK ELO 2011 (Franta, Kronek et al. 2011). No standard exists for TMCJ testing, thus parameters of loading cycle were inspired by ISO standard 14 243 (testing of knee replacement). Both cup and head rotated ±8° with sine function (**Fig 1**) and frequency 2Hz. Axis of rotation were perpendicular each other and pass through the center of spheres. Thus the trajectory of the theoretical contact point on the head had the shape of letter "S". Two joint samples were loaded by 1 million cycles and constant loading force 200 N and the third joint sample was loaded by 3 million cycles (with increased loading force up to 2.5 kN; **Tab 2-3**). Experimental space was encapsulated by silicon tube and distilled water was used as lubrication medium, which was heated to constant temperature 37°C. The medium was removed after a number of loading cycles (**Tab 2-3**) to analyze potential cytotoxicity of wear suspension. Reference samples were prepared in compliance with the same conditions, only without loading (without wear particles).

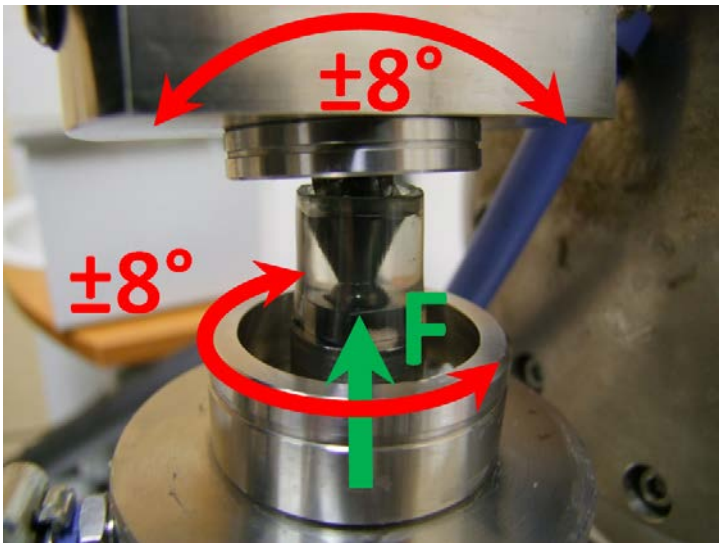

Figure 1. Joint sample in testing machine KKK ELO 2011 consisting of the head (upper) and the cup (lower). Experimental space is defined by a silicone tube. Red arrows show

[1] Accurate weight concentrations of the main three metals (Co, Cr and Mo) and other elements (Fe, Mn, Si, C, N, Co) are prescribed by ISO standard 5832-12 as same as mechanical properties (tensile strength, ductility) of the alloy.

schematically kinematics of loading cycle. The green arrow shows the direction of loading force.

Wear observation

The geometry of joint heads was measured before and after simulating loading to evaluate initial globosity and material loss volume using high accurate (accuracy 1μm) non-contact profilometer (RedLux, Great Britain; (Tuke, Taylor et al. 2010)). Surfaces of the head were scanned by more than 150.000 points. Scans before wear tests were compared to the best-fit sphere and to the scans after wear tests. The contact surfaces of cups were qualitatively observed by microscope during each exchange of lubrication medium.

Samples preparation for evaluation of cytotoxicity

The suspensions of wear particles (samples with different cycle numbers from 10,000 to 3,000,000, listed in **Tab 2-3**) in distilled water were evaporated in hot-air sterilizer at 160 °C for 15 minutes. Before the evaporation, some of the solutions were mixed together (listed in **Tab 2-3).** The dry particles were then re-suspended in sterile Dulbecco's Modified Eagle's Medium (Sigma, Missouri, U.S.A., Cat. No. D5648) supplemented with 10% fetal bovine serum (Sebak GmbH, Germany) and gentamicin (40 μg/mL; LEK, Slovenia).

xCELLigence evaluation

Each sample was divided into four aliquots. Three of them were mixed with human U-2 OS osteoblast-like cells and seeded into the special 96-well plate with microelectrodes covering well bottoms (E-plate-96, Roche, Switzerland) in a density of ~ 2,300 cells per well. The fourth aliquot was used as negative control (suspension without cells). Electric impedance was measured every 30 minutes for 160 hours by xCELLigence system (Roche, Switzerland). This impedance (which is displayed and recorded as cell index (CI) values) is used to monitor cell adhesion, proliferation and viability. Cells grown in DMEM (without wear particles) were used as the proliferation control.

Statistical analysis

The results were presented as real-time cell index curves (mean of nine cell indexes – 3 joint samples evaluated in triplet) obtained from RTCA xCELLigence software (**Supplementary Graphs 1 - 5**). Cell indexes after 24 and 160 hours of incubation were compared to the proliferation control (CTR) and expressed as mean ± S.E.M. (Standard Error of the Mean) obtained from 9 values (3 joint samples evaluated in triplet). A comparison between all groups was analyzed by one-way ANOVA, Student-Newman-Keuls Method. *P*-values less than 0.05 were considered statistically significant.

Results and Discussion

Our investigation revealed that radial deviations in all tested heads were under ±15μm in comparison with best-fit spheres. An example of the deviations of one head can be seen in **Fig 2**. Comparison of scans before and after 1 million of loading cycles with constant loading force of 200 N did not show any DLC coating delamination or any changes in the shape of the joint samples such as wear or plastic deformation. All relevant differences were under the resolution of the method (below 1μm). Considering the thickness of DLC layer 3-4 μm with gradient adhesive interlayer around 2.5 μm, no wear down to the metallic cofe of the implant occurred. Analysis of microscopy pictures confirmed the previous result of no (or very low) wear rate. Similarly, no damage of DLC layer was observed with a naked eye (no shiny metal surface; **Fig**

3) The most of the scratches, which were present before the testing (**Fig 3A**), were still visible even after 1 million of cycles (**Fig 3D**). This scratches were caused by manufactory, not by the wear test and did not reduce the endurance of the DLC coating leading to increased abrasion or breaking of DLC layer.

Moreover, similar results with no visible delamination or wear of the DLC coating were found in the third sample after 3 million of simulated loading cycles with increasing loading force up to 2.5 kN. Correspondingly, numerous studies have shown great wear and scratch resistance of DLC coating deposited on Cr-Co-Mo alloy (Roy, Whiteside et al. 2009, Thorwarth, Falub et al. 2010, Liu, Wang et al. 2013, Guo, Zhou et al. 2015, Madej, Ozimina et al. 2015). In addition, the DLC-coated implant has been reported to stay undamaged even after aggressive wear tests employing the third-body bone cement particles (Santavirta, Lappalainen et al. 1999).

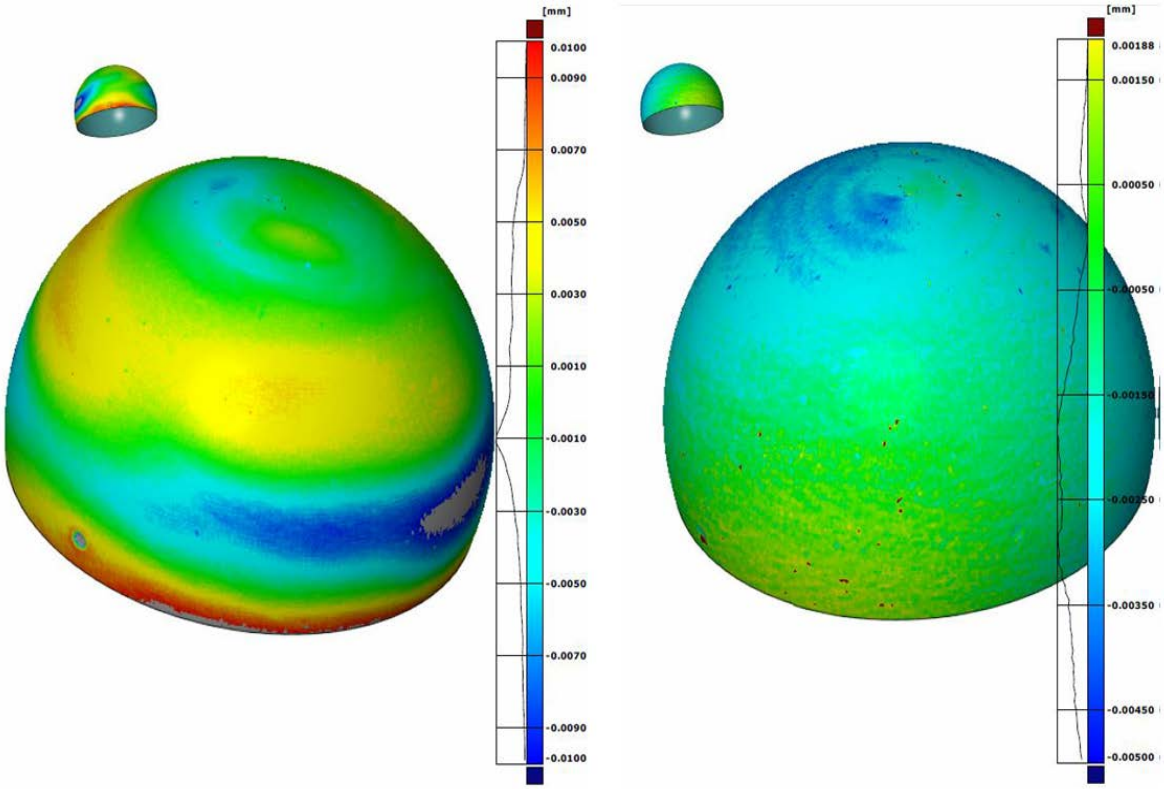

Figure 2. Left: The map of radial deviations between the real surface points and best-fit sphere. Right: deviations between the scan before wear test and the scan after 1 million of loading cycles with constant loading force of 200 N - no visible wear was detected.

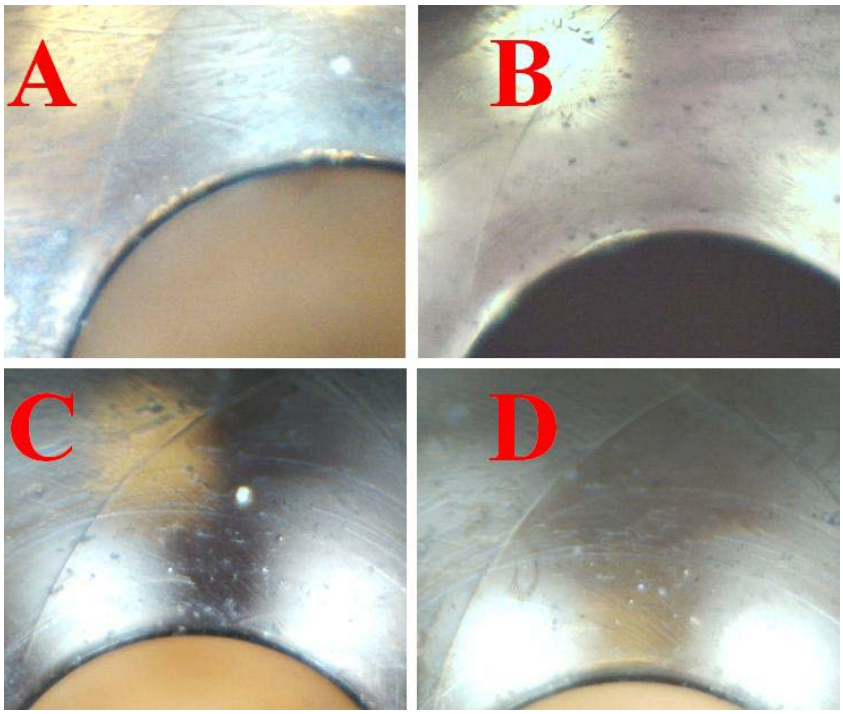

Figure 3. Detail pictures of the same place on the same cup (the place near the small central hole) before wear test (A); after 110,000 cycles (B); after 600,000 cycles (C), and after 1 million cycles (D) with constant loading force of 200 N. The main visible scratch is present from the beginning and was not "rewritten" by other scratches.

In order to investigate potential cytotoxicity of wear particles generated by simulated loading, the xCELLigence system (measuring electrode impedance, displayed as cell index) was used. The real-time proliferation of U-2 OS osteoblast-like cells cultivated in different medium-wear particles solutions was monitored. After 7 days long cultivation, no significant differences among the samples with various loading cycles were found. Cell indexes of all samples were comparable to the cell index of the cell proliferation control **(Fig 4, Supplementary Graph 1-5**, red line). Moreover, the small cell index variations correlated with the trend of differences in the initial adhesion of cells evaluated 24 hours after seeding **(Fig 5).** Therefore the lower cell indexes obtained from 7 day-long cultivation can be attributed to the lower cell indexes from the beginning of experiments on day 1 rather than to the decreased proliferation due to potential cytotoxicity of wear particles. The suspension or wear particles alone (without cells) resuspended in the cell culture medium had no effect on the measurement of the electric impedance (see the negative control in **Supplementary Graph 1- 5**, black line).

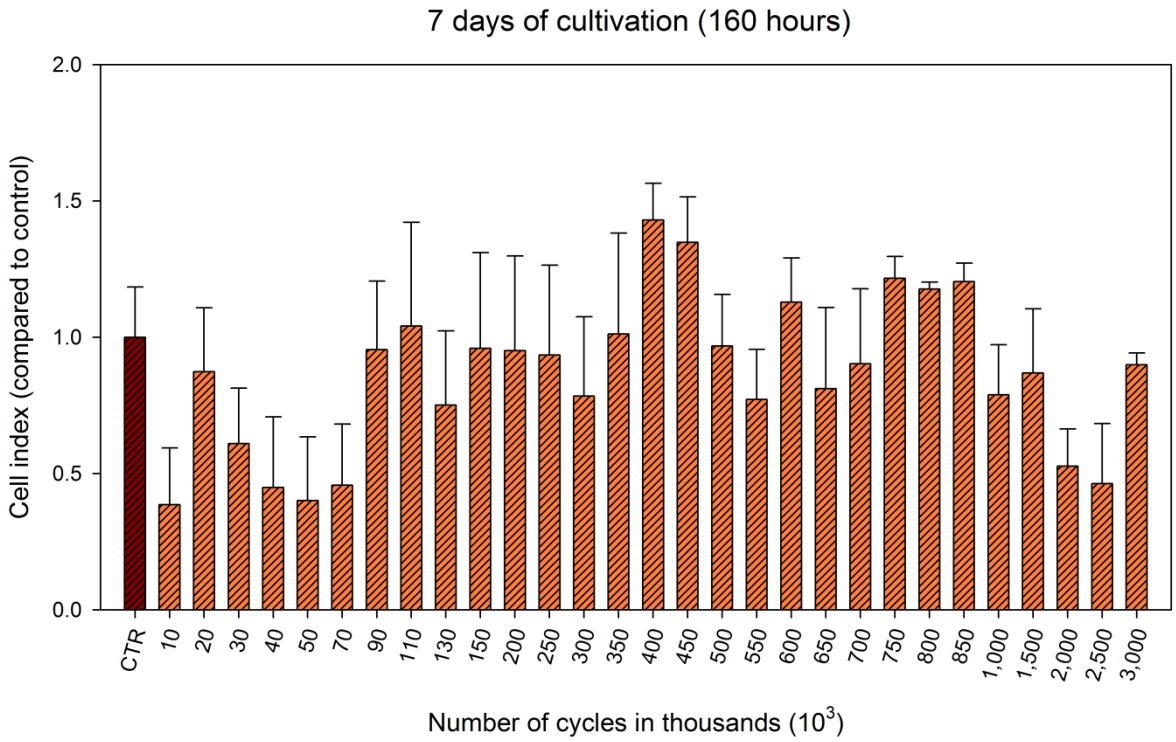

Figure 4. Cell indexes after 7-day long cultivation obtained from xCELLigence system compared to the proliferation control (CTR - cells cultivated in medium without wear particles). Different numbers of cycles (x-axis) from 10,000 to 3 million were evaluated.

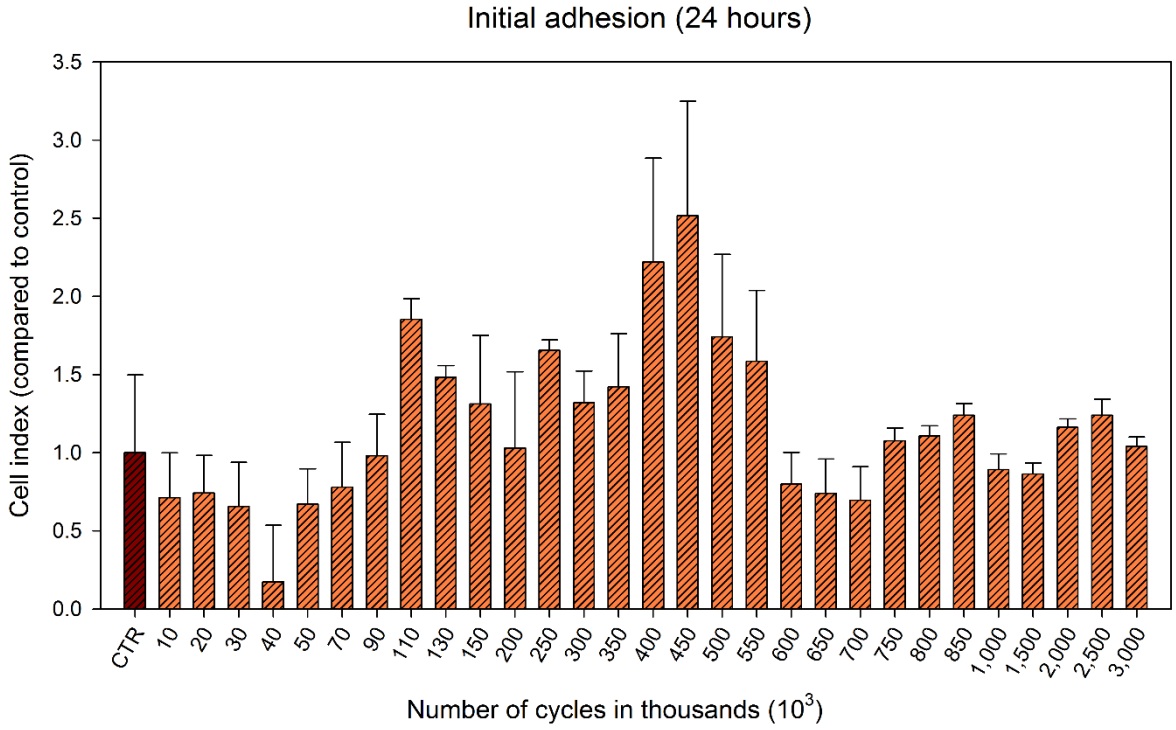

Figure 5. Cell indexes after 24-hour long cultivation obtained from xCELLigence system compared to the proliferation control (CTR - cells cultivated in medium without wear particles). Different numbers of cycles (x-axis) from 10,000 to 3 million were evaluated.

Thus, no correlation between increasing cycle numbers and decreasing proliferation of the cells was proven. The cell indexes were relatively high at intermediate numbers of cycles, and relatively high at both lowest and highest numbers of cycles. At the same time, it can be supposed that the number of wear nanoparticles increased with increasing number of cycles. The cytotoxicity of diamond-like and graphite-like carbon nanoparticles for cell lines derived from of human embryonic kidney, lung carcinoma and breast adenocarcinoma was dose-and time-dependent (Kumar, Meena et al. 2012). Similarly, the proliferation and metabolic activity of macrophages decreased with increasing concentration of synthetic diamond nanoparticles (Thomas, Halloran et al. 2012). Dose-dependent cytotoxicity was also revealed in particulate silicon carbide, i.e. a material used as an interfacial layer between the implant and its DLC coating (Allen, Butter et al. 1995). On the other hand, when a similar material (i.e., amorphous hydrogenated silicon) was deposited in the form of an intermediate layer between glass substrates and DLC, no cytotoxicity for mouse macrophages, human fibroblasts and human osteoblast-like cells was found (Butter, Allen et al. 1995).

Our results are in accordance with earlier reports by other authors on a good biocompatibility and non-cytotoxicity of DLC films. These films deposited on various substrates supported the growth, viability and development of normal morphology of many cell types, including bone-derived cells, without any signs of cytotoxicity (Thomson, Law et al. 1991, Allen, Law et al. 1994, Mitura, Mitura et al. 1994, Hinuber, Kleemann et al. 2010). Materials coated with DLC were also well accepted with the surrounding tissues in vivo (Allen, Myer et al. 2001, Mohanty, Anilkumar et al. 2002). However, many materials that are well-tolerated by cells and tissues in their bulk form, are able to induce toxic reaction if present in particulate form. Our results suggest that it is not the case of DLC. In accordance with this, particles obtained by delamination of a related material, i.e. amorphous hydrogenated carbon (a:C-H) films did not elicit any toxic effect on bone marrow cells in cultures (Bruinink, Schroeder et al. 2005).

Conclusion

Simulated loading mimicking the conditions of the implant in the human body after total trapeziometacarpal joint arthroplasty caused no visible delamination or wear of DLC coating deposited on Co-Cr-Mo alloy with titanium gradient adhesive interlayer. In accordance with very low wear, no correlation between increasing number of loading cycles (with increasing loading force) and decreasing proliferation of the osteoblast-like cells incubated in obtained wear suspension was observed. Thus we can conclude that during the simulated loading of DLC coated Co-Cr-Mo alloy with Ti gradient adhesive interlayer no cytotoxic wear debris was formed.

Acknowledgements

This research was supported by Ministry of Health of the Czech Republic, grant No. 15-31269A.

References

Abdelgaied, A., F. Liu, C. Brockett, L. Jennings, J. Fisher and Z. Jin (2011). "Computational wear prediction of artificial knee joints based on a new wear law and formulation." Journal of Biomechanics **44**(6): 1108-1116.

Allen, M., R. Butter, L. Chandra, A. Lettington and N. Rushton (1995). "TOXICITY OF PARTICULATE SILICON-CARBIDE FOR MACROPHAGES, FIBROBLASTS AND OSTEOLBLAST-LIKE CELLS IN-VITRO." Bio-Medical Materials and Engineering **5**(3): 151-159.

Allen, M., F. Law and N. Rushton (1994). "The effects of diamond-like carbon coatings on macrophages, fibroblasts and osteoblast-like cells in vitro." Clinical Materials **17**(1): 1-10.

Allen, M., B. Myer and N. Rushton (2001). "In vitro and in vivo investigations into the biocompatibility of diamond-like carbon (DLC) coatings for orthopedic applications." Journal of Biomedical Materials Research **58**(3): 319-328.

Anissian, H. L., A. Stark, A. Gustafson, V. Good and I. C. Clarke (1999). "Metal-on-metal bearing in hip prosthesis generates 100-fold less wear debris than metal-on-polyethylene." Acta Orthop Scand **70**(6): 578-582.

Bruinink, A., A. Schroeder, G. Francz and R. Hauert (2005). "In vitro studies on the effect of delaminated a-C : H film fragments on bone marrow cell cultures." Biomaterials **26**(17): 3487-3494.

Butter, R., M. Allen, L. Chandra, A. H. Lettington and N. Rushton (1995). "IN-VITRO STUDIES OF DLC COATINGS WITH SILICON INTERMEDIATE LAYER." Diamond and Related Materials **4**(5-6): 857-861.

Catelas, I., J. D. Bobyn, J. B. Medley, J. J. Krygier, D. J. Zukor and O. L. Huk (2003). "Size, shape, and composition of wear particles from metal-metal hip simulator testing: Effects of alloy and number of loading cycles." Journal of Biomedical Materials Research Part A **67A**(1): 312-327.

Fisher, J., X. Q. Hu, J. L. Tipper, T. D. Stewart, S. Williams, M. H. Stone, C. Davies, P. Hatto, J. Bolton, M. Riley, C. Hardaker, G. H. Isaac, G. Berry and E. Ingham (2002). "An in vitro study of the reduction in wear of metal-on-metal hip prostheses using surface-engineered femoral heads." Proceedings of the Institution of Mechanical Engineers Part H-Journal of Engineering in Medicine **216**(H4): 219-230.

Franta, L., J. Kronek and J. Suchanek (2011). "TKA wear testing input after kinematic and dynamic meta-analysis: Technique and proof of concept." Wear **271**(9-10): 2687-2692.

Goodman, S. B. (2007). "Wear particles, periprosthetic osteolysis and the immune system." Biomaterials **28**(34): 5044-5048.

Guo, F., Z. Zhou, M. Hua and G. Dong (2015). "Effect of aqueous solution and load on the formation of DLC transfer layer against Co-Cr-Mo for joint prosthesis." Journal of the Mechanical Behavior of Biomedical Materials **49**: 12-22.

Hinuber, C., C. Kleemann, R. J. Friederichs, L. Haubold, H. J. Scheibe, T. Schuelke, C. Boehlert and M. J. Baumann (2010). "Biocompatibility and mechanical properties of diamond-like coatings on cobalt-chromium-molybdenum steel and titanium-aluminum-vanadium biomedical alloys." Journal of Biomedical Materials Research Part A **95A**(2): 388-400.

Chan, F. W., J. D. Bobyn, J. B. Medley, J. J. Krygier, S. Yue and M. Tanzer (1996). "Engineering issues and wear performance of metal on metal hip implants." Clinical Orthopaedics and Related Research(333): 96-107.

Ching, H. A., D. Choudhury, M. J. Nine and N. A. Abu Osman (2014). "Effects of surface coating on reducing friction and wear of orthopaedic implants." Science and Technology of Advanced Materials **15**(1).

Kang, S., H.-P. Lim and K. Lee (2015). "Effects of TiCN interlayer on bonding characteristics and mechanical properties of DLC-coated Ti-6Al-4V ELI alloy." International Journal of Refractory Metals and Hard Materials **53, Part A**: 13-16.
Kumar, P., R. Meena, R. Paulraj, A. Chanchal, A. K. Verma and H. B. Bohidar (2012). "Fluorescence behavior of non-functionalized carbon nanoparticles and their in vitro applications in imaging and cytotoxic analysis of cancer cells." Colloids and Surfaces B-Biointerfaces **91**: 34-40.
Linder, S., W. Pinkowski and M. Aepfelbacher (2002). "Adhesion, cytoskeletal architecture and activation status of primary human macrophages on a diamond-like carbon coated surface." Biomaterials **23**(3): 767-773.
Liu, J., X. Wang, B. J. Wu, T. F. Zhang, Y. X. Leng and N. Huang (2013). "Tribocorrosion behavior of DLC-coated CoCrMo alloy in simulated biological environment." Vacuum **92**: 39-43.
Madej, M., D. Ozimina, K. Kurzydlowski, T. Plocinski, P. Wiecinski, M. Styp-Rekowski and M. Matuszewski (2015). "PROPERTIES OF DIAMOND-LIKE CARBON COATINGS DEPOSITED ON CoCrMo ALLOYS." Transactions of Famena **39**(1): 79-88.
Mitura, E., S. Mitura, P. Niedzielski, Z. Has, R. Wolowiec, A. Jakubowski, J. Szmidt, A. Sokolowska, P. Louda, J. Marciniak and B. Koczy (1994). "DIAMOND-LIKE CARBON COATINGS FOR BIOMEDICAL APPLICATIONS." Diamond and Related Materials **3**(4-6): 896-898.
Mohanty, M., T. V. Anilkumar, P. V. Mohanan, C. V. Muraleedharan, G. S. Bhuvaneshwar, F. Derangere, Y. Sampeur and R. Suryanarayanan (2002). "Long term tissue response to titanium coated with diamond like carbon." Biomolecular Engineering **19**(2-6): 125-128.
Musib, M. K., V. Rasquinha and S. Saha (2011). "Identification and characterization of polymeric and metallic wear debris from periprosthetic tissues after total hip revision surgery." Journal of long-term effects of medical implants **21**(4): 281-290.
Roy, M. E., L. A. Whiteside and B. J. Katerberg (2009). "Diamond-Like Carbon Coatings Enhance Scratch Resistance of Bearing Surfaces for Use in Joint Arthroplasty: Hard Substrates Outperform Soft." Journal of Biomedical Materials Research Part B-Applied Biomaterials **89B**(2): 527-535.
Roy, R. K. and K. R. Lee (2007). "Biomedical applications of diamond-like carbon coatings: A review." Journal of Biomedical Materials Research Part B-Applied Biomaterials **83B**(1): 72-84.
Santavirta, S. S., R. Lappalainen, P. Pekko, A. Anttila and Y. T. Konttinen (1999). "The counterface, surface smoothness, tolerances, and coatings in total joint prostheses." Clinical Orthopaedics and Related Research(369): 92-102.
Sargeant, A. and T. Goswami (2006). "Hip implants: Paper V. Physiological effects." Materials & Design **27**(4): 287-307.
Sargeant, A. and T. Goswami (2007). "Hip implants - Paper VI - Ion concentrations." Materials & Design **28**(1): 155-171.
St John, K. R., L. D. Zardiackas and R. A. Poggie (2004). "Wear evaluation of cobalt-chromium alloy for use in a metal-on-metal hip prosthesis." Journal of Biomedical Materials Research Part B-Applied Biomaterials **68B**(1): 1-14.
St John, K. R., L. D. Zardiackas and R. A. Poggie (2004). "Wear evaluation of cobalt-chromium alloy for use in a metal-on-metal hip prosthesis." J Biomed Mater Res B Appl Biomater **68**(1): 1-14.
Thomas, V., B. A. Halloran, N. Ambalavanan, S. A. Catledge and Y. K. Vohra (2012). "In vitro studies on the effect of particle size on macrophage responses to nanodiamond wear debris." Acta Biomaterialia **8**(5): 1939-1947.

Thomson, L. A., F. C. Law, N. Rushton and J. Franks (1991). "BIOCOMPATIBILITY OF DIAMOND-LIKE CARBON COATING." Biomaterials **12**(1): 37-40.
Thorwarth, G., C. V. Falub, U. Muller, B. Weisse, C. Voisard, M. Tobler and R. Hauert (2010). "Tribological behavior of DLC-coated articulating joint implants." Acta Biomater **6**(6): 2335-2341.
Tiainen, V. M. (2001). "Amorphous carbon as a bio-mechanical coating - mechanical properties and biological applications." Diamond and Related Materials **10**(2): 153-160.
Tipper, J. L., P. J. Firkins, E. Ingham, J. Fisher, M. H. Stone and R. Farrar (1999). "Quantitative analysis of the wear and wear debris from low and high carbon content cobalt chrome alloys used in metal on metal total hip replacements." Journal of Materials Science-Materials in Medicine **10**(6): 353-362.
Tuke, M., A. Taylor, A. Roques and C. Maul (2010). "3D linear and volumetric wear measurement on artificial hip joints-Validation of a new methodology." Precision Engineering-Journal of the International Societies for Precision Engineering and Nanotechnology **34**(4): 777-783.
Utsumi, T., Y. Oka, E. Fujiwara and M. Yatsuzuka (2007). "Effect of a hard supra-thick interlayer on adhesion of DLC film prepared with PBIID process." Nuclear Instruments & Methods in Physics Research Section B-Beam Interactions with Materials and Atoms **257**: 706-709.
Valero Vidal, C. and A. Igual Munoz (2011). "Effect of physico-chemical properties of simulated body fluids on the electrochemical behaviour of CoCrMo alloy." Electrochimica Acta **56**(24): 8239-8248.
Voronov, I., J. P. Santerre, A. Hinek, J. W. Callahan, J. Sandhu and E. L. Boynton (1998). "Macrophage phagocytosis of polyethylene particulate in vitro." J Biomed Mater Res **39**(1): 40-51.
Wang, Y. X., J. B. Pu, J. F. Wang, J. L. Li, J. M. Chen and Q. J. Xue (2014). "Interlayer design for the graphite-like carbon film with high load-bearing capacity under sliding-friction condition in water." Applied Surface Science **311**: 816-824.
Willert, H. G., H. Bertram and G. H. Buchhorn (1990). "OSTEOLYSIS IN ALLOARTHROPLASTY OF THE HIP - THE ROLE OF ULTRA-HIGH-MOLECULAR-WEIGHT POLYETHYLENE WEAR PARTICLES." Clinical Orthopaedics and Related Research(258): 95-107.
Yan, Y., A. Neville and D. Blowson (2007). "Biotribocorrosion of CoCrMo orthopaedic implant materials - Assessing the formation and effectof the biofilm." Tribology International **40**(10-12): 1492-1499.

Supplementary Graph 1- 5:

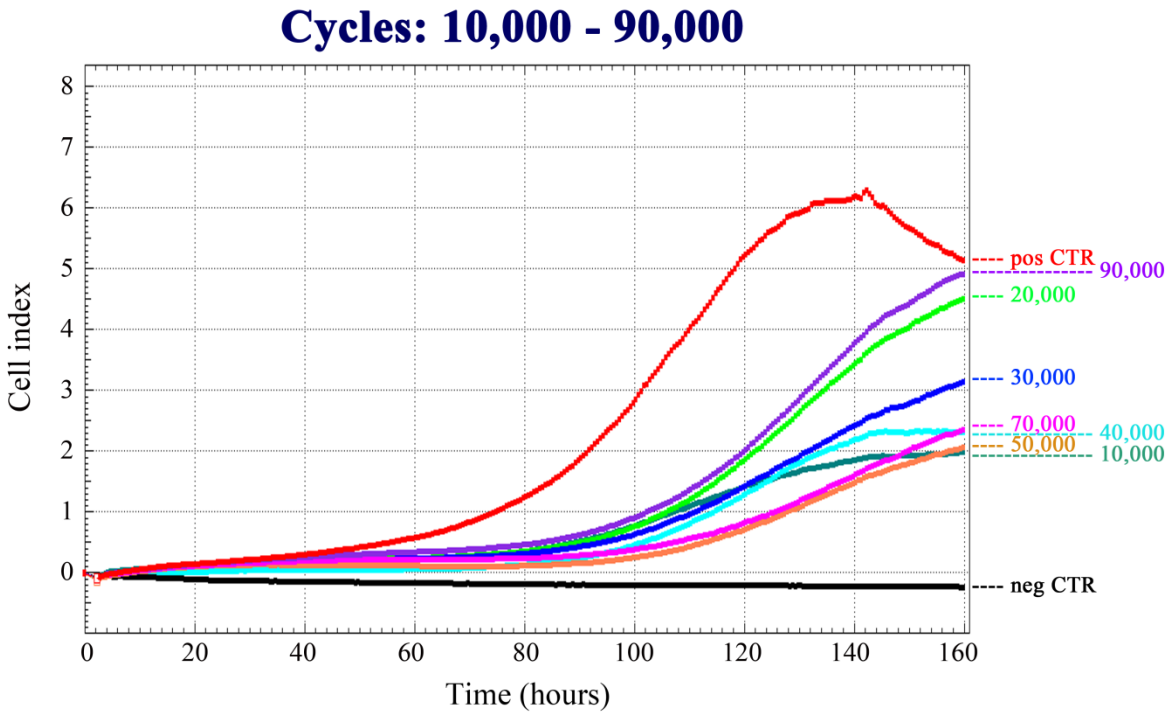

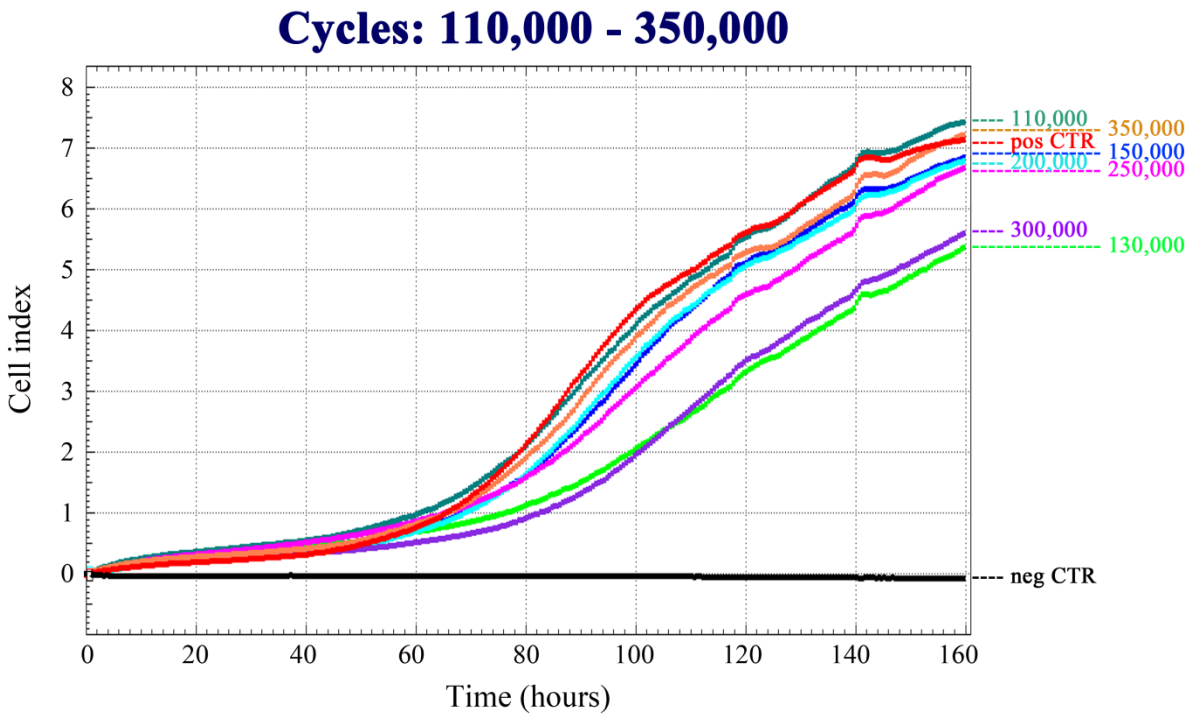

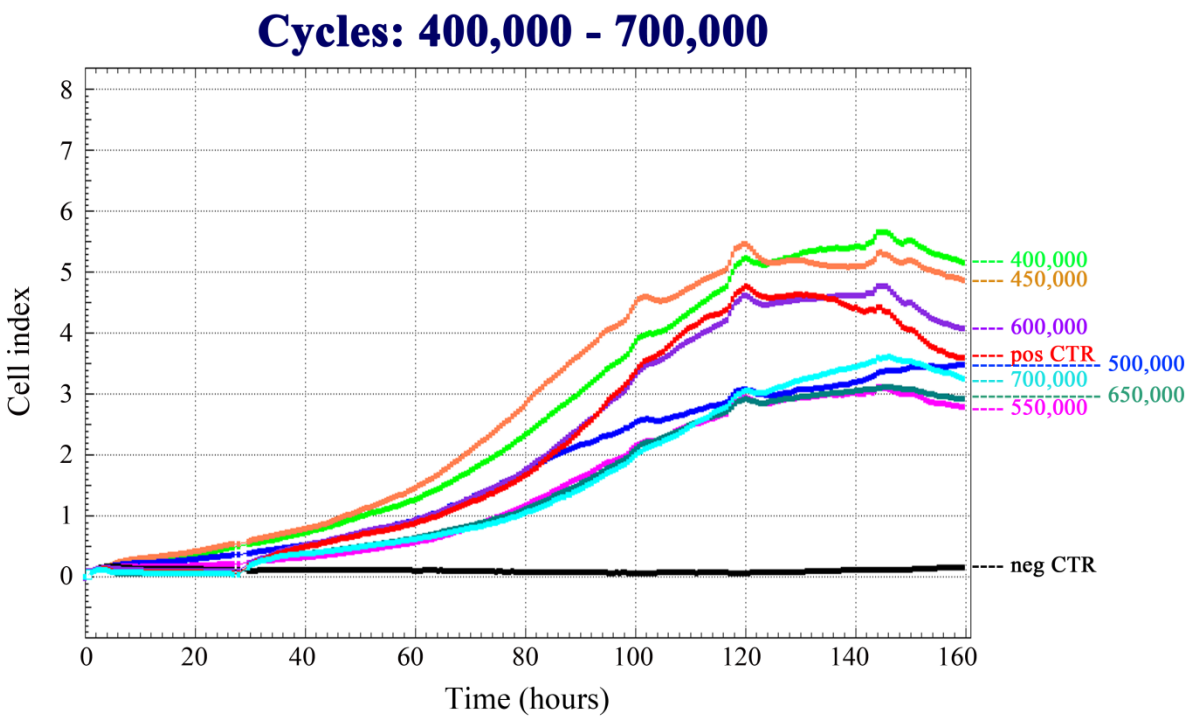
Cycles: 400,000 - 700,000
Cell index
Time (hours)
0
20
40
60
80
100
120
140
160
1
2
3
4
5
6
7
8
400,000
450,000
600,000
pos CTR
500,000
700,000
650,000
550,000
neg CTR

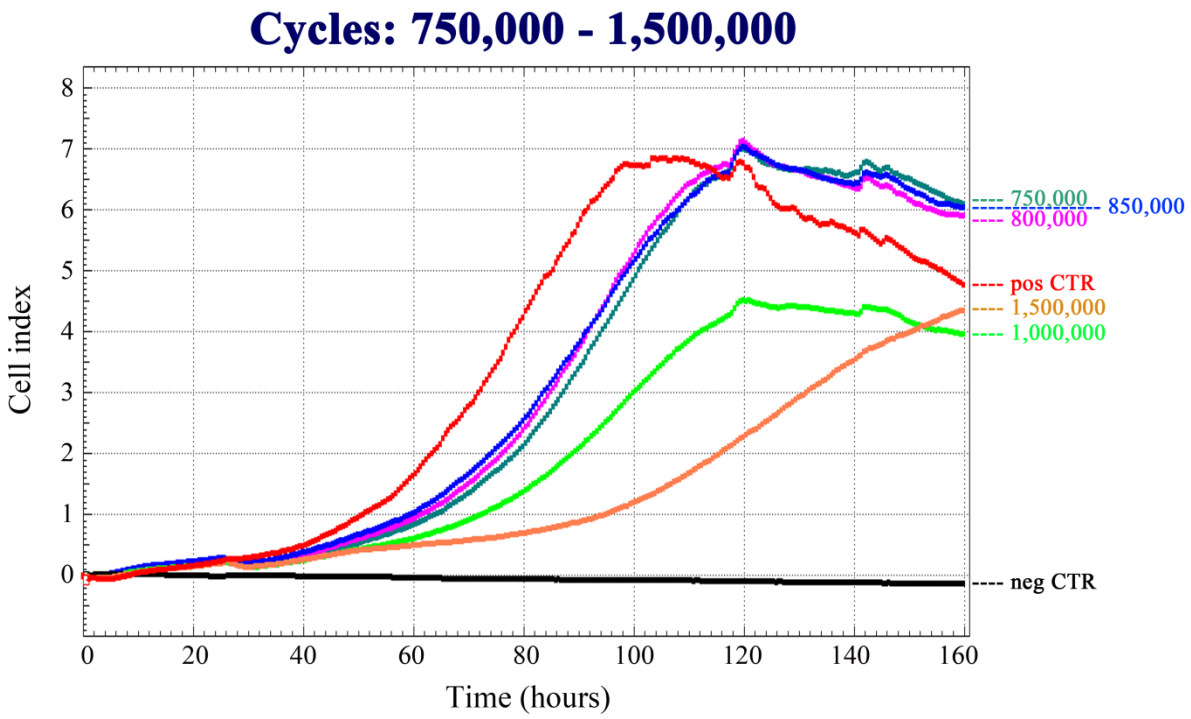
Cycles: 750,000 - 1,500,000
Cell index
Time (hours)
0
20
40
60
80
100
120
140
160
1
2
3
4
5
6
7
8
750,000
850,000
800,000
pos CTR
1,500,000
1,000,000
neg CTR

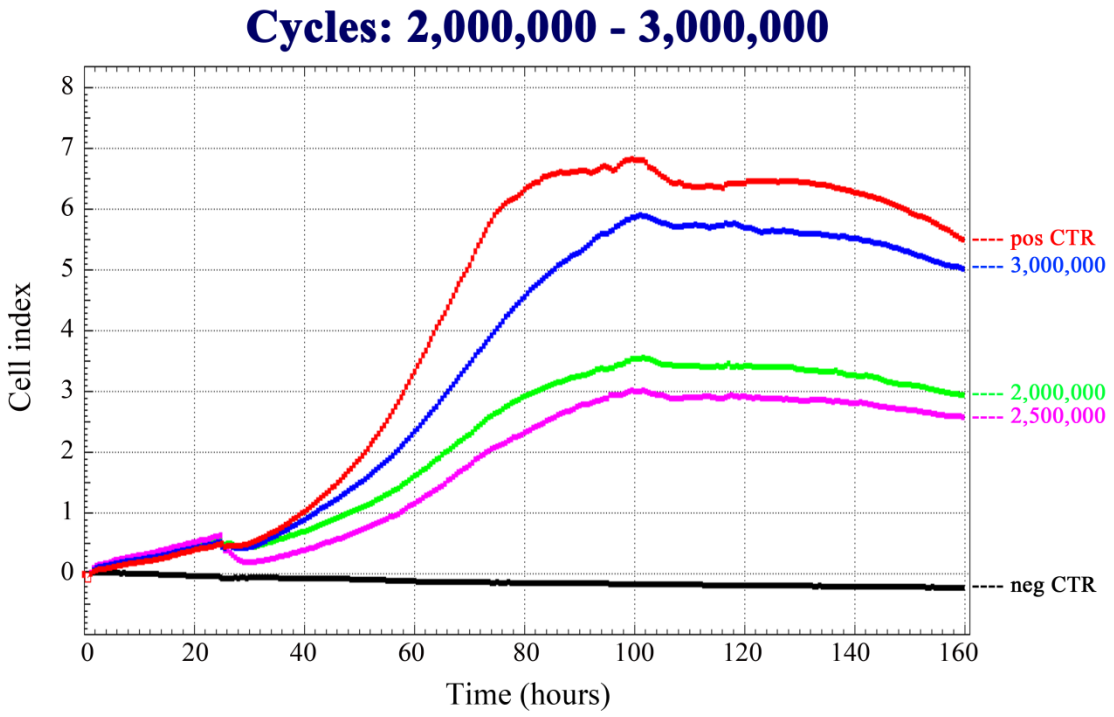

Graph 1-5: Cell index real-time curves of all cycles' samples (from 10,000 to 3 million). Cells grown in DMEM (without wear particles) were used as the proliferation control (pos CTR – the red line). Suspension of DMEM with wear particles without cells was used as the negative control (neg CTR, the black line).

Tables:

Table 1. Conditions of DLC deposition and the physical properties of CLC coating

gradient adhesive interlayer	Ti/Ti-C:H: Ti (0.5 µm): magnetron sputtering from Ti (grade 1) targets Ti-C:H (2 µm) reactive magnetron sputtering from Ti (grade 1) targets and C_2H_2 (99.6%) (Hauzer Flexicoat 1200)
DLC layer	a-C:H (3-4 µm): PACVD technique from C_2H_2 (99.6%), with a pulsed bias ranging from 20 kHz to 100 kHz applied on the substrates holder (Hauzer Flexicoat 1200)
deposition temperature	200°C
deposition pressure	1.0 Pa
microhardness	HV 2200±100 at a load of 20 mN (Fisher PICODENTOR® HM500)
elastic modulus	180-200 Gpa
adhesion[1]	Lc2 ≥ 20 N, Lc3 ≥ 30 N (CSEM Revetest scratch tester)
chemical composition	H (8-12 %), C (88-92 %)
friction coefficient	0.06-0.08 (saline solution) 0.08-0.1 (air) tested at room temperature at a load of 5 N (pin-on-disc tribometer)
wear resistance	~ 5.0E-7 mm^3/Nm (both on air and on saline solution) tested at room temperature at a load of 5 N (pin-on-disc tribometer)
wear resistance	1.805E-5 m^2/N (BAQ kaloMAX NT)
color	black

[1] Parameters of layer adhesion Lc2 and Lc3 mean critical loads according to the standard ENV 1071-3: 1994

Table 2. The loading conditions of three joint samples showing cycle numbers and grouping of samples for cytotoxicity evaluation. The constant loading force of 200 N was used for joint sample 1 and 2. For the third joint sample, 100 N was used till 1 million cycles.

Joint Sample 1	Joint Sample 2	Joint Sample 3	
10,000	10,000	10,000	
20,000	20,000	20,000	
30,000	30,000	30,000	
40,000	40,000	40,000	
50,000	50,000	50,000	
70,000	70,000	70,000	
90,000	90,000	90,000	
110,000	110,000	110,000	
130,000	130,000	130,000	
150,000	150,000	150,000	
200,000	200,000	200,000	
250,000	250,000	250,000	
300,000	300,000	300,000	
350,000	350,000	350,000	
400,000	400,000	400,000	
450,000	450,000	450,000	
500,000	500,000	500,000	
550,000	550,000	550,000	
600,000	600,000	600,000	
650,000	650,000	650,000	
700,000	700,000	700,000	
750,000	750,000	750,000	
800,000	800,000	800,000	
850,000	850,000	850,000	
900,000	900,000	900,000	} grouped together
950,000	950,000	950,000	
1,000,000	1,000,000	1,000,000	

Table 3. The loading conditions of the third joint sample after 1 million cycles showing cycle numbers and grouping of samples for cytotoxicity evaluation. Increasing loading force from 100 N to 2.5 kN was used.

	Joint sample 3	
loading force increased to 110N	1,100,000	grouped together
	1,200,000	
loading force increased to 130N	1,300,000	
	1,400,000	
loading force increased to 150N	1,500,000	
	1,600,000	grouped together
loading force increased to 170N	1,700,000	
	1,800,000	
loading force increased to 180N	1,900,000	
	2,000,000	
loading force increased to 200N	2,100,000	grouped together
	2,200,000	
loading force increased to 500N	2,300,000	
	2,400,000	
	2,500,000	
loading force increased to 1,000N	2,600,000	grouped together
loading force increased to 1,500N	2,700,000	
loading force increased to 2,500N	2,800,000	
	2,900,000	
	3,000,000	

Phys. Status Solidi B **250,** No. 12, 2741–2746 (2013) / **DOI** 10.1002/pssb.201300098

physica status solidi b
www.pss-b.com
basic solid state physics

H-terminated diamond as optically transparent impedance sensor for real-time monitoring of cell growth

Tibor Ižák[1], Katarína Novotná[2], Ivana Kopová[2], Lucie Bačáková[2], Bohuslav Rezek[1], and Alexander Kromka[*,1]

[1] Institute of Physics, ASCR, Cukrovarnická 10, 16200 Prague 6, Czech Republic
[2] Institute of Physiology, ASCR, Videnska 1083, 14220 Prague 4, Czech Republic

Received 19 April 2013, revised 18 August 2013, accepted 7 October 2013
Published online 25 November 2013

Keywords cell cultivation, diamond thin films, impedance measurements, label-free biosensors

[*] Corresponding author: e-mail kromka@fzu.cz, Phone: +420 220 318 437, Fax: +420 233 343 184

Cell-based impedance spectroscopy is a promising method for real-time monitoring of cell cultivation. Here, we present intrinsic diamond film as a material suitable for fully optically transparent impedance biosensor. Conductive interdigitated electrodes are realized in plane by local hydrogen termination of diamond surface, thereby the surface morphology is uniform. The diamond-based impedance sensors are used for real-time electrical (label-free) monitoring of osteoblast-like cells. Fluorescence images confirm that H/O-termination provides a patterned cell colonization at lower cell seeding concentration (16 000 cells cm^{-2}). The cells form a confluent colony across the whole sensor area at higher cell concentrations (>27 000 cells cm^{-2}). Time-dependent impedance measurements at 1 kHz exhibit similar profiles for the diamond and Au reference sensors. Nevertheless, the diamond sensor seems superior in terms of overall transparency, uniform morphology, and sensitivity to the development of the cell cultures.

1 Introduction Non-invasive label-free techniques for *in vitro* monitoring of cell growth are of high interest due to simplicity, fast response in real time, and excluding experiments with animals. Presently, there are two analytic approaches, which employ either optical or electronic signal processing [1]. Both these approaches reached a state of the art in a transducer type, which converts a stimulus-induced cellular response into a quantifiable signal (i.e. biosensor signal) [2]. From the broad family of electronic systems, impedance measurements seem to be one of the simplest and still a powerful method for monitoring of the cellular signals [3, 4]. As shown by many reports, the monitored impedance signal is sensitive not only to ionic currents but also to cell growth stages (i.e. cell attachment, spreading, shape, proliferation, differentiation, and communication) [5–8].

The typical impedance sensors use gold interdigitated electrodes (IDEs), which are deposited on an electrically isolating material (like glass or plastic). Up to now, several sensor systems were developed and are commercially represented by xCELLigence system (Roche/Acea), ECIS – Electric Cell Substrate Impedance Sensing system (Applied BioPhysics), etc. Nevertheless, the use of gold electrodes restricts the available area for a direct optical monitoring of cultivated cells from the sensor backside. This restriction can represent a disadvantage in specific experiments. Moreover, employing any surface biochemistry has to be optimized either to the used gold electrodes or to the carrying substrate. Finally, the sensor surface wettability is not simply controllable.

Using optically transparent IDEs for impedance sensors is not a trivial issue due to requirements on their biocompatibility and chemical resistance to the cell culture media and serums. Diamond can fulfill above-mentioned requirements owing its unique combination of favorable electronic, optical, mechanical, chemical, and biocompatible properties. It has been recognized as a promising material for life sciences including biosensors [9], controlled biointerfaces [10–12], or artificial substrates for cell cultivation [13]. Biological as well as electronic properties of intrinsic diamond can be significantly altered by hydrogen and oxygen atomic surface termination, which results in different properties as electrical conductivity, electron affinity, and surface wettability. Most of these properties are characteristic not only for single crystalline diamond but also for

synthetic diamond films consisting of micro- and nano-sized grains. Our previous studies have confirmed that films consisting of nano-sized diamond grains (<200 nm) are of high enough quality for fabrication of fully operational electronic devices [4].

In this paper, we use intrinsic polycrystalline diamond thin film as an optically transparent, functional, and electrically active layer for fabrication of impedance biosensor. Electrically conductive interdigitated electrodes were fabricated from locally hydrogen-terminated diamond surface. The real-time impedance curves are compared with the reference commercial sensor based on gold electrodes.

2 Experimental

2.1 Growth of diamond films Diamond thin films were grown on fused quartz silica substrates in size $10 \times 10 \times 0.7\,mm^3$. At first, substrates were seeded by diamond powder (diameter 5–10 nm, New Metals and Chemicals Corp. Ltd., Kyobashi) [14]. Then, diamond thin films (thickness 250–350 nm) were grown by plasma enhanced chemical vapor deposition (CVD) using an ellipsoidal resonator [15]. Process parameters were as follow: 1% methane diluted in hydrogen, microwave power 1500–2500 W, total gas pressure 50 mbar, substrate temperature $T_s \approx 480\,^{\circ}C$. After the CVD growth, diamond films were exposed to hydrogen plasma for 10 min. Hydrogen-terminated diamond reveals the surface conductivity only after its exposure to air where a water layer is absorbed. New equilibrium conditions result in the charge transfer (i.e. transport of electrons) from diamond bulk to this interface. The remaining holes are accumulated below the diamond surface and give rise to p-type conductivity of otherwise intrinsic highly resistive diamond films.

Surface morphology, grain size and thickness of the deposited coatings were characterized by scanning electron microscopy in top and cross section views (SEM, e_LiNE writer, Raith GmbH,). Diamond character of the films was determined by Raman spectroscopy (Renishaw In Via Reflex Raman spectrometer, excitation at 325 nm).

2.2 Diamond-based impedance sensors After the CVD growth, the IDEs structures were realized by selectively created hydrogen- and oxygen-terminated diamond surface using an optical lithography. O-terminated surface was achieved by inductively coupled oxygen plasma (3 min, 13.56 MHz, power 300 W, time 3 min) on the masked substrate and it represents a non-conductive part. The width of the H-terminated IDEs structure was 100 μm for rectangular-shape IDE and 100 μm in diameter for circular-type (see Fig. 1c–e). Au layer (100 nm) was used for fabrication of external contact pads.

Impedance measurements were conducted at voltage of 500 mV, frequency of 100 Hz–100 kHz using LCR meter HIOKI 3522-50 LCR HiTESTER. The measurement system is fully automated. It enables data collection for several days and can operate up to eight sensor units in a parallel configuration via USB-GPIB interface using LabView.

As a reference, commercially available xCELLigence sensor (circular-shape Au IDE structure) was used from Roche Applied Science [16]. This sensor provides the so-called cell index, which represents a dimension-less parameter. In the first approximation, it is defined as $(Z_i - Z_0)$/const, where Z_i is the impedance measured at time i and Z_0 is the starting impedance. In reality, the cell index value is more complex and is calculated from measurements done at different discrete frequencies (in the case of Roche system at 10, 25, and 50 kHz).

2.3 Cells and culture conditions The tested impedance biosensors were sterilized with 70% ethanol for 1 h, placed into 24-well polystyrene well plates (diameter 1.5 cm; TPP, Trasadingen, Switzerland) and then let dry in air for 12 h in a sterile flowbox. Samples were seeded with human osteoblast-like MG 63 cells (European Collection of Cell Cultures, Salisbury, UK). The cells were cultured in Dulbecco's modified Eagle's Minimum Essential Medium (DMEM; Sigma, Cat. No. D5648) supplemented with 10% fetal bovine serum (FBS; Gibco, Cat. No. 10270-106) and gentamicin ($40\,\mu g\,ml^{-1}$, LEK, Slovenia) in humidified air with 5% CO_2. The cells were cultured in 1.5 ml of the culture medium for 50 h (set 1) or 70 h (set 2) and cell seeding density was 30 000 cells $well^{-1}$ (about 16 000 cells cm^{-2}; set 1) and 50 000 cells $well^{-1}$ (about 27 000 cells cm^{-2}; set 2). For the fluorescence microscopy evaluation, the cells were rinsed with phosphate-buffered saline, fixed with cold 70% ethanol (−20 °C, 5 min) and visualized with combination of the fluorescent dyes Hoechst #33342 (nuclear dye, Sigma-Aldrich, Cat. No. B2261) and Texas Red C_2-maleimide (membrane dye, Molecular Probes, Invitrogen, Cat. No. T6008). The stained cells were photographed using an epifluorescence microscope (Olympus IX 51, Japan, obj. 20×) equipped with a digital camera (DP 70, Japan).

3 Results and discussion

3.1 Diamond film properties Figure 1 shows SEM image and Raman spectrum of the diamond films used for the impedance biosensor. The film morphology consists of diamond crystals in sizes from 100 to 250 nm with root-mean-square surface roughness of 20 nm. The representative Raman spectrum of the diamond films reveals a characteristic spectrum with one sharp peak (i.e. sp^3 bonded carbon in diamond) centered at frequency of $1330\,cm^{-1}$ and a broad band centered at $1575\,cm^{-1}$ which represents graphitic sp^2 carbon phases (graphite-band) (Fig. 1b). Moreover, there are two additional carbon-related bands: one broad band at $1380\,cm^{-1}$ attributed to disordered carbon bonds (D-band) and second band at $1175\,cm^{-1}$ corresponding to trans-polyacetylene-like groups [17]. Bands centered at ∼440 and $\sim 800\,cm^{-1}$ are assigned to the glass substrate [18].

The sensor part is fully optically transparent in the whole VIS region. Interdigitated electrodes are not detectable under the optical microscope. They become visible in SEM as observed in Fig. 1c–e. The H-terminated diamond surface exhibits negative electron affinity and thus, it emits electrons

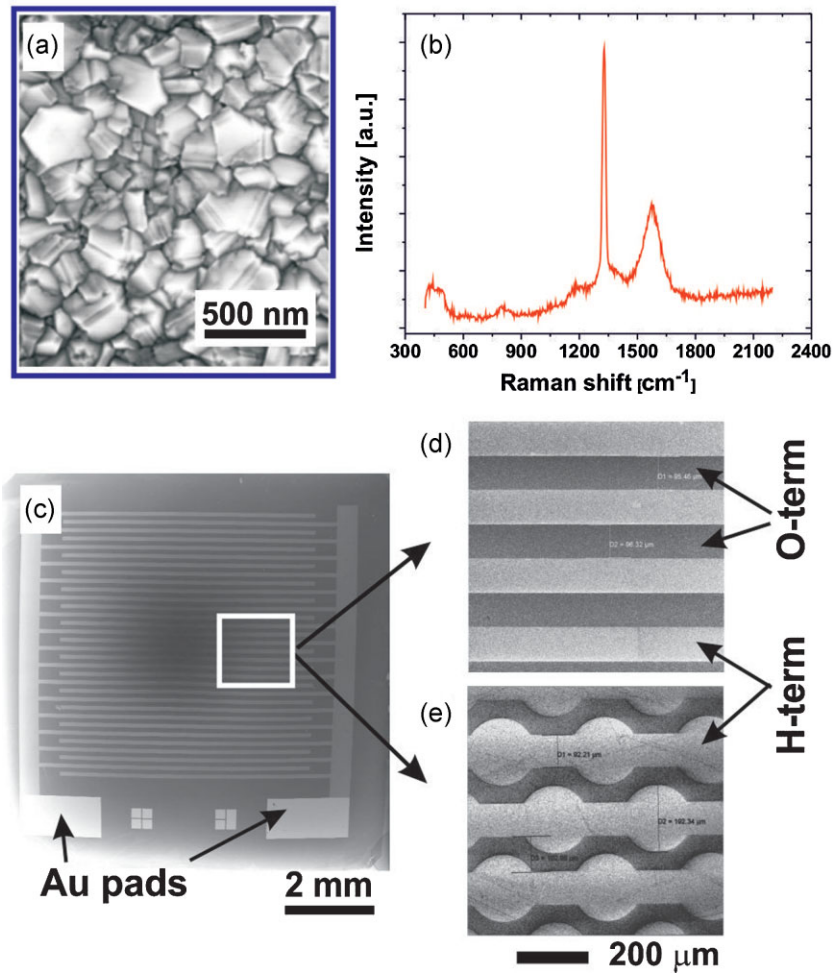

Figure 1 (a) SEM image of diamond film morphology and (b) its Raman spectrum. (c) SEM image of the sensor active diamond film area with H-terminated interdigitated electrodes and Au contact pads. The magnified SEM images visualize H/O-diamond sensor patterns in (d) rectangular and (e) circular form.

easier than oxygen terminated surface (darker regions) [19]. Thus, the brighter regions correspond to the H-terminated diamond surface, which induces p-type surface conductivity even on intrinsic diamond [20–22], and represent the IDEs. O-terminated surface is resistive and electrically isolates and separates the electrodes. From morphological point of view, both surface termination are identical (i.e. they are of the same surface roughness and crystal size).

3.2 Cell growth Fluorescence measurements of cell cultures were obtained after *in situ* electrical monitoring of the cell culture process. Figure 2a–d shows fluorescence images of the cell cultures after 50 h (set 1). Images of cells cultivated for 70 h (set 2) are summarized in Fig. 2e–f. In both cases, osteoblast-like MG 63 cells feature similar properties on diamond film, commercial sensor and polystyrene substrate (i.e. the reference substrate).

The main difference is observed in cell densities occupying the diamond surface for low cell concentration of 16 000 cells cm^{-2} (set 1). In this case, osteoblast-like MG 63 cells preferentially occupy linear patterns (Fig. 2a). A systematic scanning of the diamond surface clearly confirmed that the cells preferentially colonize the O-terminated diamond. Cells try to keep patterns and they "stretch" across the O-/H-terminated border area. Moreover, for H-termination patterns the cells over-bridge the H-patterns. In contrast to this observation, experiments done at higher cell concentration (27 000 cells cm^{-2}, set 2) do not exhibit such patterned cell growth (Fig. 2e). Cells also grow on H-terminated diamond because they create a confluent colony that does not differentiate on the local surface properties.

Present observations are in a good agreement with previous studies. It was shown that H/O-terminated diamond patterns induced a selective growth of osteoblasts, fibroblasts, and cervical carcinoma cells via different surface wettability [23]. The patterned cell growth was observed only for low cell concentration. Applying higher concentration resulted in a colonization of the whole surface. The patterned cell colonization was not observed for experiments

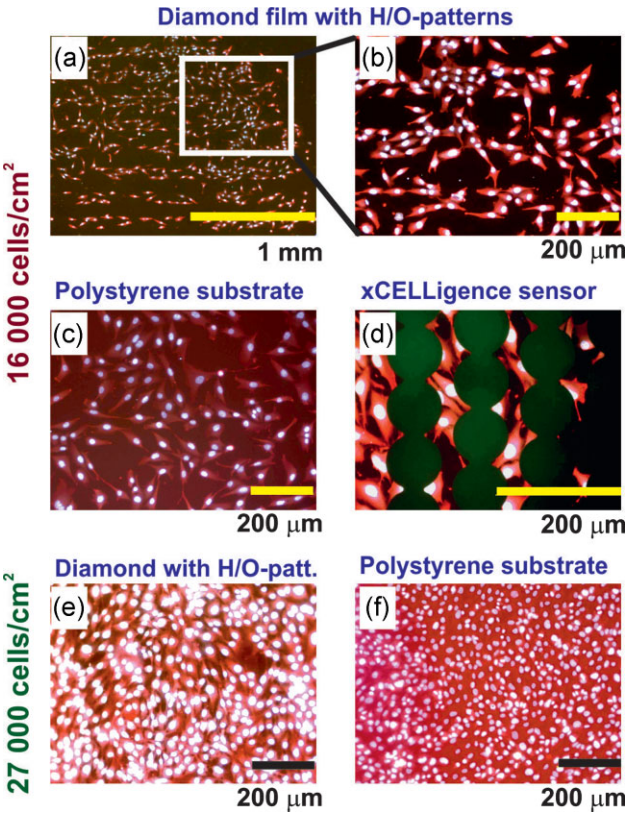

Figure 2 Fluorescence images of cells cultured for 50 h (set 1) on H/O-terminated diamond (a,b) compared with polystyrene substrate (c) and reference xCELLigence sensor (d). Fluorescence images of cells cultured for 70 h (set 2) on H/O-terminated diamond (e) compared with polystyrene dish (f).

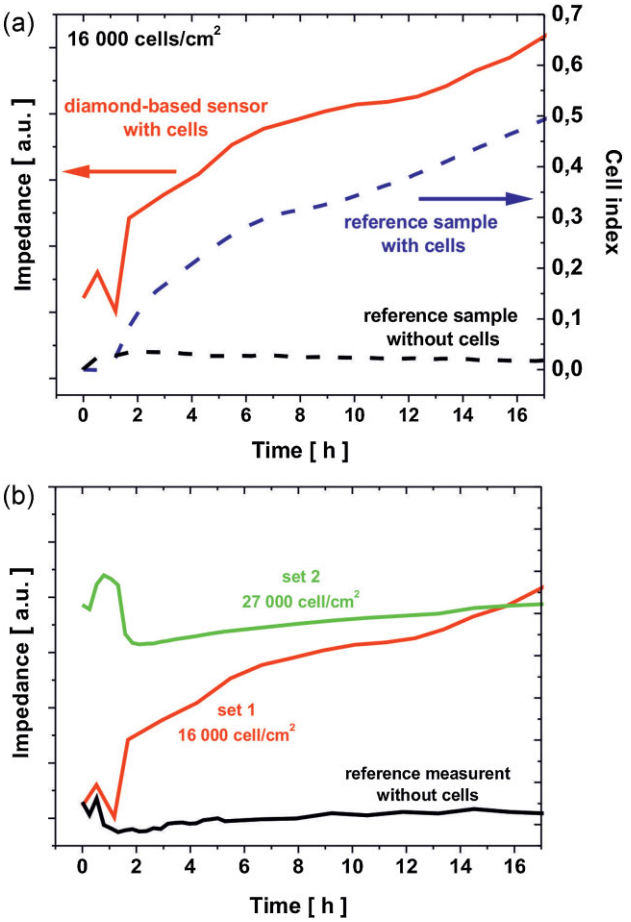

Figure 3 Absolute impedance as a function of time measured at 1 kHz for (a) low cell concentration (16 000 cells cm^{-2}) and corresponding reference measurements utilized with xCELLigence sensor and (b) a comparison of impedance measurements for diamond-based sensor for the low and high cell concentrations (high 27 000 cells cm^{-2}) and its reference measurement without cell.

done without the FBS serum. Atomic force microscopy confirmed that the geometrical conformation of proteins adsorbed from the cell culture serum is influenced and controlled by the diamond surface termination [24]. The patterned cell colonization was not observed for polystyrene well plates or for substrates with bare Au electrodes. This result indicates that the H/O-terminated diamond surface extends the sensor functionality. Another advantage of H-terminated diamond electrodes is their full optical transparency allowing *in situ* monitoring of cells by optical or fluorescence microscopy. A limitation of using gold interdigitated electrodes is shown in Fig. 2d. Here, gold IDEs (greenish color) obscure fluorescence measurements in the inverted microscope measurement set-up. Observing the living cells from top is also problematic due to a free surface of cell medium. It should be mentioned that we did not observe any negative influence of Au electrodes on the cell growth.

3.3 Impedance measurements Absolute impedance as a function of time measured at 1 kHz in parallel setup with low initial cell concentration (set 1) is shown in Fig. 3a. Although the impedance was measured for a broader frequency range, the measurement at 1 kHz is chosen as the representative spectrum with a good compromise between sensor response and noise level. The impedance measurement starts at the moment of insertion into the incubator. For comparison, the time dependence of the cell index on Au electrodes by xCELLigence sensor is added as the reference measurement together with the background measurement without the cells. The values of absolute impedance as well as cell index generally increase with time and follow about the same profile. Nevertheless it is noticeable, that the diamond-sensor profile is not as smooth and provides more detailed features (modulations) along the profile.

Figure 3b compares the impedance measurements for the low and high cell concentrations. It is evident that except for the settling region at the beginning (<2 h) only a monotonic, almost linear increase of absolute impedance is observed for the high cell concentration (set 2). The profile shape more or less follows that of the reference measurement without cells for the same diamond-based sensors, albeit with overall

higher impedance due to cell presence (Fig. 3b). The profile at the low cell concentration displays some kind of modulations or fluctuations.

Exact interpretation of the measured impedance profiles is a complex issue. First, cellular plasma membrane acts as an insulating barrier, which influences the pathways for current flow during the electrical measurements. For low frequency impedance measurements (<10 kHz), the current first flows through an extracellular matrix layer, passing a gap between cells, and continues through electrolyte (cultivation serum). This current flow is called as the paracelullar flow [25, 26]. The impedance is sensitive to the cell density, growth and cell movements. If the measurement frequency is high enough (>40 kHz), current can flow through cell membrane and is labeled as transcellular flow [27]. In this case, the impedance characteristic should be more sensitive to the cell adhesion and less to the cell population. However, the exact value of optimal frequency range depends on parameters such as sensor design, electrode material, cell type, cultivation conditions, etc. Some data were presented in a mathematical model, which describes the correlation between the electrical impedance value and the stage of cell growth [28].

Our impedance curves are presented for the low frequency range (1 kHz). In this case, the electrical current flow will be blocked by attachment of cells to IDEs, by their spreading over the IDEs, or by cell enlargements (growth). We propose that in the first hours, osteoblast-like MG 63 cells cover the electrodes, which results in the increasing impedance. However, the exact correlation of cell growth with the impedance changes is not trivial, especially for low cell concentrations when patterned cell colonization is observed on the O-patterns. Presently, we cannot ascertain how the cells follow or move across the patterns, how long does the cell redistribution take, etc.

Nevertheless, there is no doubt that patterned cell colonization will additionally affect the character of monitored impedance. Benson et al. [26] presented results on the smaller scale of cell movement. The impedance can be also modulated by the change of cell spreading across interdigitated electrodes. This situation can occur during mitosis when cell splits into two daughter cells [29].

As the detailed modulations are not visible in the cell index profile on Au electrodes, the diamond sensor response seems sensitive to the development of the cell culture when the initial cell concentration is lower.

The situation seems to be more straightforward for the high cell concentration (set 2). In this case, the impedance curve shows less fluctuations which can be attributed to full coverage of the sensor by cells and correspondingly lower sensitivity to cell motility and proliferation. The increasing impedance in the blank medium may be attributed to adsorption of proteins on diamond from the medium [30].

All the above-mentioned factors still need to be elucidated in more detail. For instance, simultaneous optical monitoring of cell growth will be helpful for a direct correlation between our impedance measurements and cell growth stages.

4 Conclusions We have proved that intrinsic diamond thin film can be used as biocompatible, fully transparent planar biosensor for *in situ* electronic (label-free) monitoring of cell cultures. Generally, the sensor response is well comparable to the reference Au sensors provided commercially. In the case of diamond, the sensing principle is based on impedance measurements employing conductive H-terminated surface regions as in-plane electrodes that were separated by resistive oxidized surface regions. Thereby, the sensor is fully transparent in the visible range including low fluorescence background. Moreover, any possible and unwanted geometrical effects of metal electrodes (like step edges) were avoided as purely surface atom modifications defined and induced the p-type diamond surface conductivity. In comparison to the commercial Au electrode systems, the diamond sensor exhibited small modulation, which should correspond to the development of the cell culture, probably due to the preferential growth of cells on oxidized diamond regions. Future experiments with *in situ* optical monitoring through the transparent sensor may elucidate correlation between electronic data and cell culture condition. The diamond-based impedance sensor may be useful for real-time monitoring of cell cultivation as well as for *in vitro* testing of drugs and cytotoxic agents.

Acknowledgements This work was financially supported by the GACR research projects P108/12/G108 (TI, LB, AK) and P108/12/0996 (BR). This work was carried out in the frame of LNSM infrastructure.

References

[1] Y. Fang, Int. J. Electrochem. **2011**, 1 (2011).
[2] Y. Fang, Drug Discov. Today Technol. **7**, e5 (2010).
[3] T. Sakata, I. Makino, and S. Kita, Eur. Biophys. J. **40**, 699 (2011).
[4] M. Krátká, A. Kromka, E. Ukraintsev, M. Ledinský, A. Brož, M. Kalbacova, and B. Rezek, Sens. Actuators B, Chem. **166–167**, 239 (2012).
[5] I. Giaever and C. R. Keese, Proc. Natl. Acad. Sci. USA **81**, 3761 (1984).
[6] L. T. Hall, C. D. Hill, J. H. Cole, B. Stadler, F. Caruso, P. Mulvaney, J. Wrachtrup, and L. C. L. Hollenberg, Proc. Natl. Acad. Sci. USA **107**, 18777 (2010).
[7] P. O. Bagnaninchi and N. Drummond, Proc. Natl. Acad. Sci. USA **108**, 6462 (2011).
[8] I. Giaever and C. R. Keese, Nature **366**, 591 (1993).
[9] L. Grausova, A. Kromka, Z. Burdikova, A. Eckhardt, B. Rezek, J. Vacik, K. Haenen, V. Lisa, and L. Bacakova, PLoS ONE **6**, e20943 (2011).
[10] W. Yang, O. Auciello, J. E. Butler, W. Cai, J. A. Carlisle, J. E. Gerbi, D. M. Gruen, T. Knickerbocker, T. L. Lasseter, J. N. Russell, L. M. Smith, and R. J. Hamers, Nature Mater. **1**, 253 (2002).
[11] B. Rezek, D. Shin, H. Uetsuka, and C. E. Nebel, Phys. Status Solidi A **204**, 2888 (2007).

[12] A. Hartl, E. Schmich, J. A. Garrido, J. Hernando, S. C. R. Catharino, S. Walter, P. Feulner, A. Kromka, D. Steinmuller, and M. Stutzmann, Nature Mater. **3**, 736 (2004).
[13] M. Kalbacova, L. Michalikova, V. Baresova, A. Kromka, B. Rezek, and S. Kmoch, Phys. Status Solidi B **245**, 2124 (2008).
[14] A. Kromka, S. Potocký, J. Cermák, B. Rezek, J. Potmesil, J. Zemek, and M. Vanecek, Diam. Relat. Mater. **17**, 1252 (2008).
[15] S. Potocky, A. Kromka, J. Potmesil, Z. Remes, V. Vorlicek, M. Vanecek, and M. Michalka, Diam. Relat. Mater. **16**, 744 (2006).
[16] Roche Applied Science, Biochem. Newsl. 2009 (n.d.).
[17] H. Kuzmany, R. Pfeiffer, N. Salk, and B. Günther, Carbon **42**, 911 (2004).
[18] D. W. Matson, S. K. Sharma, and J. A. Philpotts, J. Non-Cryst. Solids **58**, 323 (1983).
[19] F. Maier, J. Ristein, and L. Ley, Phys. Rev. B **64**, 165411 (2001).
[20] H. Kawarada, Surf. Sci. Rep. **26**, 205 (1996).
[21] F. Maier, M. Riedel, B. Mantel, J. Ristein, and L. Ley, Phys. Rev. Lett. **85**, 3472 (2000).
[22] V. Chakrapani, J. C. Angus, A. B. Anderson, S. D. Wolter, B. R. Stoner, and G. U. Sumanasekera, Science **318**, 1424 (2007).
[23] L. Michalikova, B. Rezek, A. Kromka, and M. Kalbacova, Vacuum **84**, 61 (2009).
[24] B. Rezek, E. Ukraintsev, A. Kromka, M. Ledinský, A. Brož, L. Nosková, H. Hartmannová, and M. Kalbacova, Diam. Relat. Mater. **19**, 153 (2010).
[25] F. Asphahani, K. Wang, M. Thein, O. Veiseh, S. Yung, J. Xu, and M. Zhang, Phys. Biol. **8**, 015006 (2011).
[26] K. Benson, S. Cramer, and H.-J. Galla, Fluids Barriers CNS **10**, 5 (2013).
[27] X. Huang, D. Nguyen, D. W. Greve, and M. M. Domach, IEEE Sens. J. **4**, 576 (2004).
[28] S. Cho, J. Nanosci. Nanotechnol. **12**, 5228 (2012).
[29] H. Curtis and N. S. Barnes, Biology, fifth ed. (W. H. Freeman, New York, 1989).
[30] B. Rezek, L. Michalíková, E. Ukraintsev, A. Kromka, and M. Kalbacova, Sensors **9**, 3549 (2009).

